Università degli Studi Roma TRE

e

Consorzio Nazionale Interuniversitario per le Scienze Fisiche della Materia

Dottorato di Ricerca in Scienze Fisiche della Materia
XXVI ciclo

Dissipative and fluctuating effects in $Ba(Fe_{1-x}Rh_x)_2As_2$ iron-based superconductors.

Tesi di dottorato della dott. ssa Lucia Bossoni

Supervisore
Prof. Pietro Carretta

Coordinatore Dottorato
Prof. Settimio Mobilio

a. a. 2013/2014

إِلي محمود

To Mahmoud

The most beautiful sea hasn't been crossed yet.
The most beautiful child hasn't grown up yet.
Our most beautiful days we haven't seen yet.
And the most beautiful words I wanted to tell you I haven't said yet.

Nazim Hikmet

Preamble

Motivations and Organization of the thesis

This thesis deals with dissipative and fluctuating mechanisms, taking place both in the superconducting, and in the normal phase of the Rh-doped family of 122 iron-based superconductors. These novel materials have been holding the stage of superconductivity, and renewing the interest in high temperature superconductors, for the last six years.
Iron-pnictides are extremely type-II superconductors, with a Ginzurg-Landau parameter $\kappa \sim 100$, and extremely high upper critical fields, that can reach up to 100 T! Such large values of H_{c2} result from their short coherence lengths $\xi = 1-3$ nm. On the other hand, the lower critical field H_{c1} is of the order of few mT, so there is a very broad range of magnetic fields in which the behavior of the vortex matter can vary significantly.
Nuclear Magnetic Resonance (NMR) is the more widely employed experimental tool in this thesis, given its microscopic nature, and the sensitivity to kHz-MHz fluctuations, that well match the vortices dynamic timescale. However, not many NMR studies concerning the dynamic in the iron-pnictides of the vortex lattice have been carried out, so far. One possible reason may be that the vortex dynamic is strongly related to technological applications, whereas NMR usually probes the equilibrium state, namely the limit $J \to 0$. Even though from a technological point of view this regime is not very appealing, it can anyhow help to grasp some information about the nature of the solid vortex phase.

The experimental data discussed here, have been collected in several research laboratories. The main part of the NMR measurements has been carried out in the NMR laboratory of the University of Pavia, and of the Northwestern University (Illinois), while the NMR experiments at high field have been done at the LNCMI of Grenoble (France), and the NHMFL of Tallahasse (Florida). The Magnetic characterization of the sample has been done by a SQUID magnetometer, at

the University of Pavia, while the ac-susceptibility measurements were performed at the University of Parma. The cantilever magnetometry study, presented in the last chapter, has been carried out at Poggio Lab, at the University of Basel (Switzerland).

The thesis is organized as follows:

- **Part I** includes the first two chapters. The first chapter presents an overview of structural, electronic and magnetic properties of the materials. A whole section reports the main NMR results obtained on 122 iron-pnictides, up to now. The second chapter presents the basic aspects of NMR, which are needed to understand the experimental results.

- **Part II** includes chapters 3-7. The third chapter discusses the onset of unconventional fluctuative phenomena of the order parameter, taking place above T_c. Chapter 4 debates an NMR study of the anomalous enhancement of the spin-spin decay rate, in the normal state. The phenomenology of these systems becomes even more rich, below the transition temperature, where the vortex lattice dynamic, in equilibrium condition (Chapter 5), and out-of-equilibrium (Chapter 6) can be investigated by NMR. Finally, chapter 7 deals with novel methodologies to study the vortex lattice melting transition.

- **Part III** is devoted to the appendices, which describe both the experimental equipment employed, as well as some theoretical background.

Contents

Part I
Introductive remarks

Chapter 1

Iron-Based superconductors at a glance

The response of the worldwide scientific community to the discovery of superconductivity at 26 K in an iron-based compound ($LaFeAsO_{1-x}F_x$) has been very enthusiastic [1]. This experimental finding polarized the attention of the scientific research so much that, in few years after the discovery, new iron-based materials were identified and hundreds of papers were published. Since the very beginning, it was clear that the iron-based superconductors display unconventional superconductivity, and also share some similarities with cuprate superconductors. For instance, superconductivity takes place in the FeAs layers, while the ions intercalated between the layers act as charge reservoirs. Additionally, superconductivity can be induced by chemical doping or external pressure. The isotope effect has been found in both the families of superconductors, and their phase diagrams suggest the coexistence of superconductivity with magnetism.
After 28 years from the discovery of the high-T_c materials however, the microscopic mechanism responsible for superconductivity has not been found yet. As a consequence of the similarities among the materials, many scientists think that the study of the iron-based superconductors may shed light on the cuprates, as well. Nevertheless, after 6 years from the discovery of iron-based superconductors, a zoology of theories and models has been formulated, but the crucial experimental evidence which is able to discriminate among all of them has not been found yet. Some of the more intriguing theories involve plasmonic excitation, in Josephson coupled layered superconductor [2]. Although the scenario may appear quite confusing, there are some fixed points that have been understood.
This thesis begins by listing some basic structural and electronic properties of the

iron-based superconductors, with particular attention to the so-called 122 family. In the following, an overview concerning the Nuclear Magnetic Resonance (NMR) phenomenology of these compounds is given.

The name *iron-pnictides* comes from the FePn structure common to all compounds, where Pn is the pnictogen atom.[1] This FePn group forms a two-dimensional (2-D) layer which is contained into a tetragonal crystal structure, for all the compounds, at room temperature. The low-dimensionality of the systems plays an important role in determining their physical properties, as in other superconductors like the cuprates, ruthenates and cobaltates. The iron-pnictides are customary divided into four families that are presented below, in order of discovery.

1111 family

The discovery made in February 2008 of a new superconductor, $LaFeAsO_{1-x}F_x$, with a critical temperatures as high as 26 K, was a clear indication that a new chapter of the story of superconductivity has begun. T_c could be raised if the compound was put under pressure, reaching 43 K, and even higher transition temperatures (up to 55 K) could be found in other rare earth members [3, 4]. This family, called "1111", presents the crystal structure of ZrCuSiAs-like (space group $P4/nmm$) and its formula is written as RTMPnO, where R is the rare earth element, TM the transition metal, Pn the pnictogen atom. The parent compound shows a simultaneous, first-order, structural/ antiferromagnetic phase transition at 150 K, which gives rise to a low-temperature, orthorhombic, antiferromagnetic phase. The first superconducting element of this family emerges when at least the 3% of oxygen is replaced by F. To this family belong more than 300 compounds, among which the critical temperature record holder $SmFeAs(O_{1-x}F_x)$, exhibits $T_c = 55$ K [4].

122 family

Few months later, in May 2008, $Ba_{1-x}K_xFe_2As_2$ was found to superconduct at temperatures approaching 40 K [5]. The parent compound of the so-called "122" family, $BaFe_2As_2$, has the $ThCr_2Si_2$-type structure and is a poor Pauli-paramagnetic metal which undergoes a structural and magnetic phase transition at 140 K. The parent compounds LaFeAsO and $BaFe_2As_2$ both share similar structural features, namely a square planar Fe layer, which is included (on the top and in the bottom) by As layers. On the other hand, $BaFe_2As_2$ and $LaFeAsO_{1-x}F_x$ compounds differ in the oxygen content. As a consequence of that, it was clear that FeAs layer was the structural *leit motif* in these materials and that the superconductivity in RFeAsO (R=rare earth element) materials

[1] To the pnictogen group belong the chemical elements in group 15 of the periodic table. This group is also known as the nitrogen family. It consists of the elements nitrogen (N), phosphorus (P), arsenic (As), antimony (Sb) and bismuth (Bi).

was not uniquely associated with oxide physics. Furthermore, the fact that the compounds of the second family are made solely of metallic elements, was a great advantage with respect to the growing techniques. Indeed, the 122 compounds can be grown using conventional intermetallic, solution growth techniques, of which Sn-flux and self-flux techniques give the best results [6].

A third important discovery was posted in July 2008: superconductivity could be stabilized in both 1111 and 122 families, by substitution of Co for Fe [7], in contrast to the cuprates, where atomic substitution tends to hinder superconductivity. The two 122 sub families, share the same unit AFe_2As_2 ($I4/mmm$): the $B^+(A_{1-x}B_x)Fe_2As_2$ (with A= Ba, Rs, Ca and B=K,Cs,Na), which induces superconductivity via hole doping and $A(Fe_{1-x}TM_x)_2As_2$, which is electron doped, instead. These compounds show a similar antiferromagnetic ordering, in the underdoped region of the phase diagram, which is not first order like the 1111, and it can coexist with superconductivity.

The third structure was reported in superconducting LiFeAs ($P4/nmms$) [8]. It shows the Cu_2Sb-type tetragonal structure, containing the FeAs layer with an average iron valence of +2, like those for the 1111 or 122 parent compounds, and it is named 111. Noticeably, the parent compound shows superconductivity itself at 18 K, with electron-like carriers but it can also be induced by Li-deficiency and high pressure. There are recent evidences showing that the 111 family displays a triplet state superconductivity [9].

111 family

In the end of the same year, superconductivity has been found in a α-PbO-type structure, which is called "11" and has the same planar structure found in the other four families, but it is a chalcogenide instead of a pnictides. This last family shows superconductivity in case of Se deficiency in FeSe systems, or Te substitution of Fe. Se-deficient FeSe has a rather small transition temperature, namely 9 K, which can be raised up to 27 K, by applying a pressure larger than 1 GPa. It was also found that Te substitution for Se enhances T_c up to 15.2 K in $FeSe_{0.5}Te_{0.5}$ [10]. The four families are sketched in Fig. 1.1.

11 family

Later on, in March 2013 Kudo *et al.* [11] showed that T_c in $CaFe_2As_2$ could be enhanced, up to 45 K, if the sample was doped with P and La, thus reaching a new record for the 122 family.

Finally in November 2013 the discovery of a new superconductor family has been announced by Katayama *et al.* [12]. Superconductivity has been found in $Ca_{1-x}La_xFeAs_2$, which is a monoclinic iron-pnictide with arsenic forming zig-zag bonds.

As it has been stated before, the iron-based materials are unconventional

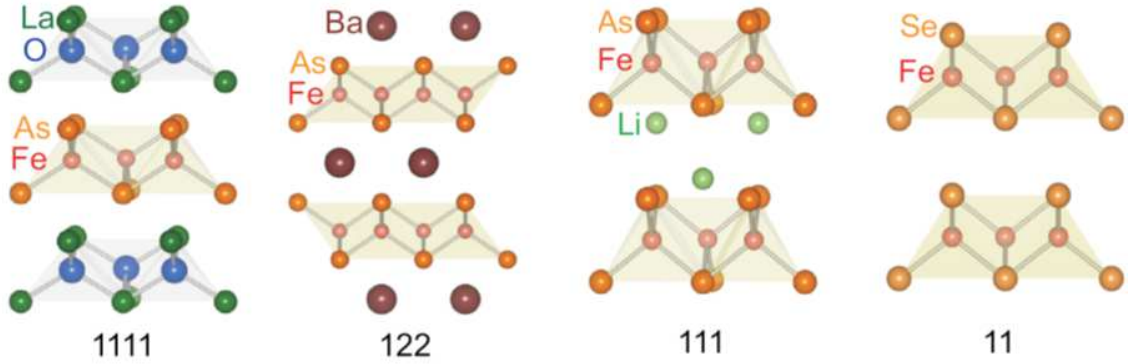

Figure 1.1: The four families of iron-based superconductors, as described in the text above. The figure is adapted form Ref. [13].

superconductors, where the microscopic interaction cannot be explained only by electron-phonon coupling, as in the BCS theory. It is widely accepted that the isotope effect on T_c provides a strong evidence for the role of electron-phonon interaction. Basically, such law claims that the Debye frequency, as well as the transition temperature, scales with the α-th power of the isotopic mass M:

$$M^{\alpha} T_c = \text{const} \tag{1.1}$$

where $\alpha = 0.5$. In case of phonon-coupling superconductivity, it is reasonable to assume that the relevant effect of isotopic substitution is just to change the Debye frequency, leaving essentially unchanged all the other parameters concerning the electronic part of the problem. In fact, in the Debye model for simple lattices, ω_D is proportional to $\sqrt{M}$. Some transition metals, like mercury, verify this effect very well, but the actual phenomenology is much more complex. In the iron-pnictides the complete (namely $\alpha = 0.5$) isotopic effect has not been clearly found. Liu *et al.* [14] reported the effect of isotropic substitution on T_c and on the antiferromagnetic transition temperature T_N in $SmFeAsO_{1-x}F_x$, by replacing ^{16}O with isotope ^{18}O, and $Ba_{1-x}KFe_2As_2$ by replacing ^{56}Fe with isotope ^{54}Fe. T_N and T_c were found to change by approximately 0.61% and 0.75%, for oxygen isotope exchange in the first compound, and changes are 1.39% and 1.34% for Fe isotope exchange in the second compound, with x = 0 and 0.4 respectively. The effect of the oxygen isotope is much smaller than that of the iron isotope, which suggests that the FeAs layer is responsible for superconductivity [13]. However an iron isotope effect in both T_c and T_N suggests that the electron-phonon interaction plays an important role in superconductivity and in the magnetic interaction as well [15]. Up to now there is no general consensus about the mechanism leading

Isotope effect

to superconductivity, in these materials. However, the electron-phonon interaction *alone* is too weak to produce such a high transition temperature [16]. On the other hand explicit involvement of the spin degree of freedom leads to an enhancement of electron-phonon coupling [17]. One of the most prominent mechanism was suggested by Mazin *et al.* [18] and it was inspired by the shape of the Fermi surface and of the $s^{\pm}$ topology of the superconducting gap (as explained subsequently), having different sign on the hole and electron-like sheets forming the Fermi Surface. Mazin suggested that superconductivity can be driven by a strong repulsive interband interaction, and spin fluctuations are appealing candidates for that. That is why the role of the spin fluctuations has been deeply investigated since the discovery of those novel materials.

1.1 Are the iron-pnictides good candidates for applications?

In order to answer to such a question, one has to look at some key properties of the materials. At first, the critical field versus temperature reveals some insights into the microscopic behavior of these systems [19]. In fact, at some doping levels, the H_{c2} curves show a linear dependence on the temperature which is reminiscent to the standard Werthamer-Helfand-Hohenberg (WHH) theory. On the other hand, it is sometimes observed a positive curvature which is considered a hallmark of multiband superconductivity. This difference may be related to the complex multisheet Fermi surfaces of these materials, suggesting the involvement of other bands. Even though the multiband superconductivity is quite widely agreed, in the present work $H_{c2}(0)$ was determined from the ordinary single-band Ginzburg-Landau relations for the upper critical field, which is derived from the single-band Werthamer-Helfand-Hohenberg (WHH) expression [20]: $H_{c2} = -0.69 T_c |dH_{c2}/dT|_{Tc}$.

A first SQUID characterization of the compounds $Ba(Fe_{1-x}Rh_x)_2As_2$ for $x = 7$ %, showed $|dH_{c2}^{ab}/dT| = 2.85 \pm 0.1$ T/K and $|dH_{c2}^{c}/dT| = 2.6 \pm 0.1$ T/K. From those values it has been derived $H_{c2}^{\|c} = 40.5$ T and $H_{c2}^{\|ab} = 51.5$ T, which matches the values found by Ni *et al.* [21] (Fig. 1.2). From the upper critical fields, the

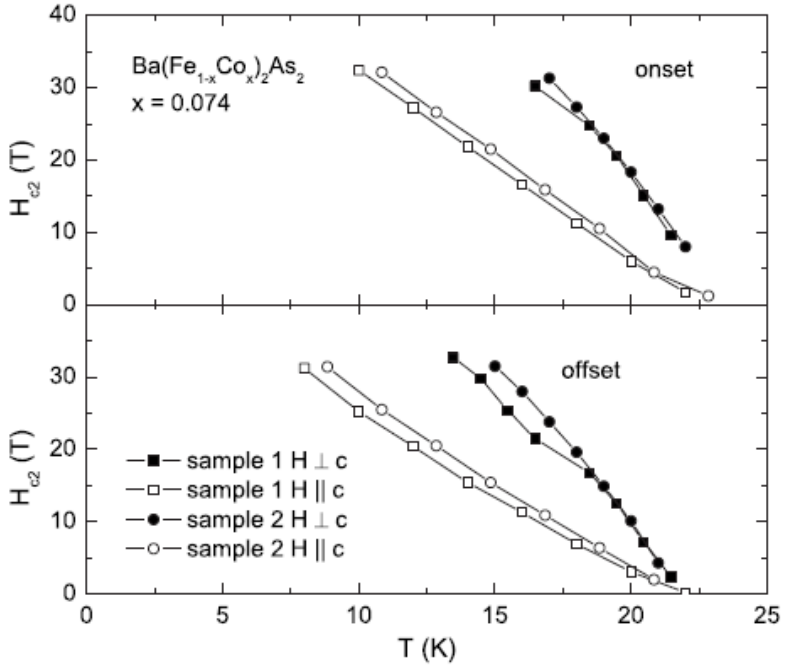

Figure 1.2: Upper critical field curves determined for two single crystalline samples of $Ba(Fe_{1-x}Co_x)_2As_2$ (x=0.074), and for $\mathbf{H} \parallel c$ and $\mathbf{H} \perp c$. The figure is adapted form Ref. [21].

coherence lengths for the two field orientations can be obtained [22]

$$\begin{aligned} \xi_{ab}^2 &= \frac{\Phi_0}{2\pi H_{c2}^{\parallel c}} \\ \xi_c &= \frac{\Phi_0}{2\pi \xi_{ab} H_{c2}^{\parallel ab}} \end{aligned} \tag{1.2}$$

In the same compound the correlation lengths become $\xi_{ab} = 2.85 \pm 0.15$ nm and $\xi_c = 2.24 \pm 0.2$ nm.
Surprisingly, the K-doped family of Ba122 can reach upper critical fields up to 100 T, which is extremely appealing for the applications! [23] Among the four most representative families of iron-pnictides, the 122 seems to have the largest values of H_{c2} [24].

Being said that, another important aspect to mention is the value of the anisotropy of H_{c2}, which is defined as $\gamma = \xi_{ab}/\xi_c$ (Fig. 1.3). In the limit of very low temperature, these compounds show nearly isotropic magnetic behavior, despite the layered structure. Together with the high critical fields and the low

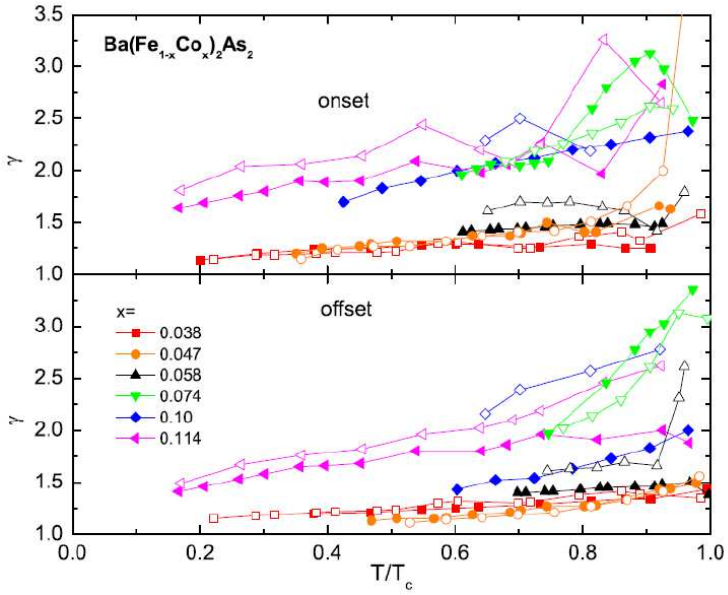

Figure 1.3: Anisotropy ratio, as a function of effective temperature, T/T_c, for $Ba(Fe_{1-x}Co_x)_2As_2$ single crystals. Upper panel: onset criterion; lower panel: offset criterion. The "onset" and "offset" criterion are explained in Ref. [21], from which the picture is adapted.

anisotropy, also the critical currents of these materials are very promising. In fact the critical current densities J_c can reach up to $10^5 - 10^6$ A/cm^2 at 5 K [24], which is comparable to the high-T_c and MgB_2 superconductors. Note that the absolute value of J_c has roughly increased of 1 order of magnitude in two years. Another interesting marker of the "effectiveness" of a superconductors is the Ginzburg number:

$$G_i = \left(\frac{2\pi^2 \lambda^2 k_B T_c}{c \xi \Phi_0^2} \right)^2 \tag{1.3}$$

where k_B is the Boltzmann constant, $\Phi_0 = 2.05 \times 10^{-7}$ Gcm^2 is the magnetic quantum flux, λ the London penetration depth and ξ the coherence length. Such number quantifies the extent of thermal fluctuations, which are detrimental for the applications. In the iron-pnictides G_i is in the range of $G_i < 10^{-4} - 10^{-2}$, suggesting that different phases of vortex matter can be found, ranging from glassy/liquid transition to the conventional Abrikosov Vortex lattice [19]. Note that the family with the smallest G_i value is the Ba122 one.
In the following section, particular attention will be paid to the $Ba(Fe_{1-x}Co_x)_2As_2$ and $Ba(Fe_{1-x}Rh_x)_2As_2$ families.

1.2 The $Ba(Fe_{1-x}Co_x)_2As_2$ and $Ba(Fe_{1-x}Rh_x)_2As_2$ families

Superconductivity can be induced in the $Ba(Fe_{1-x}TM_x)_2As_2$ materials when the structural/antiferromagnetic phase transitions are suppressed to sufficiently low temperatures, and the number of extra electrons added by the TM-doping is within a specific window. Fe is typically substituted with some transition metals, as Co, Rh, Ni and Pd....

Much experimental and theoretical efforts have been focused on the Co-doped family, given its superior homogeneity as compared to the K-doped one. Even if, at a glance (Fig. 1.4), the phase diagrams of Co and Rh-doped compounds[2] are equivalent, which might be firstly ascribed to the fact that Co and Rh are isoelectronic dopant pairs (like Ni and Pd) as a matter of fact, there is a substantial difference on the way they affect the c lattice parameter and the c/a, upon doping. In fact, while Co dopes the compound with $3d$ electrons, Rh provides

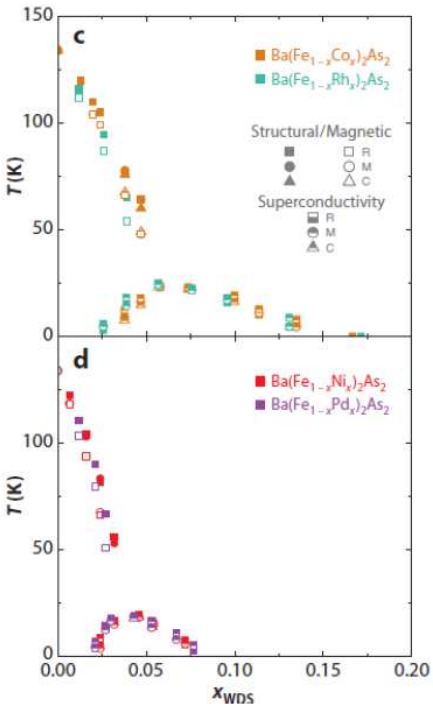

Figure 1.4: T-x phase diagrams for Co and Rh-doping (upper panel) and for Ni and Pd doping (lower panel). Figure adapted from Ref. [6].

[2]The transition temperature is usually derived as the onset of the superconducting transition, in the magnetization measurement, and the offset of the resistive transition, in the transport measurements.

$4d$ electrons. For $3d$ substitution it is found that the c lattice parameter and the c/a ratio do scale with x, and additionally c/a scales very well with the extra conduction electron e, added by the dopant per Fe/M site. Co and Rh add just one extra electron, while Ni and Pd provide two extra electronic charges. On the other hand, for the $4d$-doping the same parametrization does not apply. Doping issues

It has been proposed that some other parameters, such as bonding angles associated with the As position, might be a better alternative to parameterize the transition temperatures [25].

Other curious effects are observed when the superconducting domes are compared. In fact, the underdoped side of the phase diagram shows a finite spread among different curves. In Fig.1.5 it is clear that the Rh-doped compounds suppress the magnetic transition at the lowest doping, as compared to the other compounds, and accordingly, they also show superconductivity at the lowest doping. In fact, superconductivity starts to arise from $x = 0.026$[3].

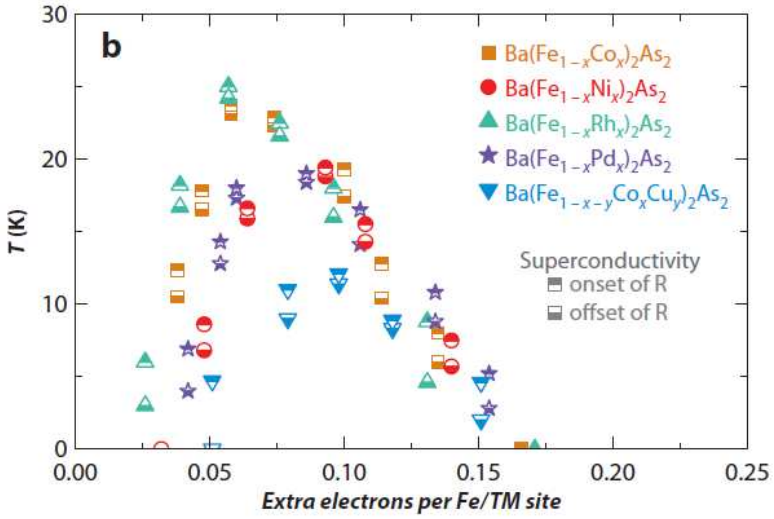

Figure 1.5: T-e phase diagram enlargement, showing just the superconducting dome for Co-, Rh-, Ni-, Pd-, Cu-, and Cu/Co-dopings of $BaFe_2As_2$. The phase diagrams have been derived by the analysis of electrical transport, magnetization, and specific heat measurements data, whereas the actual doping concentration was detected by means of wavelength dispersive x-ray spectroscopy (WDS). From the latter techniques, it has been inferred that no impurity phases are present. Figure adapted from Ref. [6].

Moreover the optimally doped compound of this family emerges at $x = 0.057$, and it has a maximum temperature of 24 K, with $\Delta T_c = 0.7$ K [26]. On the overdoped side of the phase diagram, the critical field data merge together onto a universal curve, regardless the dopant element. This evidence is not understood

[3]At this doping rate for the Rh doped compound, it has been found that $T_c = 3$ K.

yet.

All the techniques employed to build the phase diagram (see caption Fig. 1.5), detect a magnetic/structural transition (in the underdoped region of the phase diagram), and a superconductive transition.
Resistivity and magnetization data show the apparent coexistence of the higher temperature structural antiferromagnetic phase transition, with lower temperature superconductivity for the lower Rh-doping levels [6]. This intriguing aspect has been vastly investigated by microscopic techniques, like NMR [13] and μSR [27].

1.3 Self-flux growth procedure

$Ba(Fe_{1-x}Rh_x)_2As_2$ samples have been prepared by Canfield's group at Ames laboratory, by self-flux using conventional high-temperature solution growth techniques. Hereafter the growth procedure is described, as reported in Ref. [21].
Small Ba chunks, FeAs powder, and CoAs powder were mixed together according to the ratio Ba:FeAs:CoAs=1:4(1−x):4x. The mixture was placed into an alumina crucible. A second catch crucible containing quartz wool was placed on top of this growth crucible and both were sealed in a quartz tube under 1/3 atm Ar gas. The sealed quartz tube was heated up to 1180 °C, stayed at 1180 °C for 2 h, and then cooled to 1000 °C over 36 h. Afterwards, the excess of FeAs/CoAs was decanted from the platelike single crystals. The FeAs and CoAs powders used as part of the self-flux were synthesized by reacting Fe or Co powder and As powder after they were mixed together and pressed into pellets. Single crystal dimension grown by this technique can reach 12 x 8 x 0.8 mm^3 (Fig. 1.6).

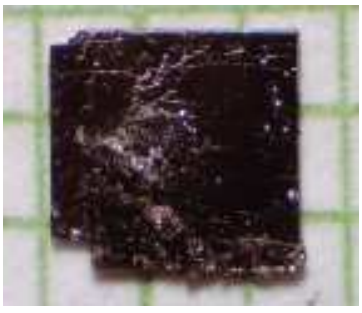

Figure 1.6: Single crystal of $BaFe_2As_2$ is shown against a millimeter grid. The figure is adapted from Ref. [6].

1.4 The electronic properties

The parent compounds of iron-pnictide superconductors show (quite bad) metallic behavior in electric resistivity, differently from the insulating parent compounds of cuprate superconductors. Magnetic measurements have evidenced the occurrence of antiferromagnetism in the undoped systems, with critical vector equal to $(\pi, 0)$ and $(0, \pi)$ which corresponds to a stripe-type, or columnar, or sometimes also called nematic antiferromagnetic structure. The relationship between the Fermi surface nesting and the magnetic correlations within the parent compound, is very important to unveil the origin of magnetism in these novel materials. *Ab initio* calculations can be compared with experimental techniques, as Angle-resolved photoemission spectroscopy (ARPES), or Scanning Transmission Microscopy (STM) or Point-contact Andreev reflection, to understand the physical origin of magnetism and, hopefully, also superconductivity [28]. Local density approximation (LDA) of the density functional theory (DFT) allows one to calculate the band dispersion, the density of states (DOS), as well as the Fermi surface. Singh [29] reported for $BaFe_2As_2$ that hole Fermi surfaces appear around the center of the Brillouin zone (Γ point), and are generally derived from heavier bands, namely lower velocity, than the electron surfaces, which are around the zone corner M point in a primitive tetragonal zone (Fig. 1.7). The underdoped compounds share some similarities with the parent compound, namely (1) small Fermi surfaces, with hole cylinders at the zone centers and electron cylinders at the corner, (2) high DOS at the Fermi level, and a strongly enhancement of the DOS below the Fermi level. This may suggest that in underdoped compounds ferromagnetic spin fluctuations, rising from the hole band, may break the singlet superconductivity. Additionally, Singh showed that the Spin Density Wave (SDW) is the best candidate for the ground state: he calculated a magnetic moment of $1.75\mu_B$/Fe, quite far from the measured value of $0.35\mu_B$/Fe [30]. The high sensitivity of the Fe moment to the ordering, and the fact that the SDW state is so much lower in energy, would favor the scenario of itinerant magnetism, with a spin-density wave state driven by the structure of the Fermi surface. On the other hand, the local moment framework, which is related to the Heisenberg-type exchange coupling, is less favored. Nevertheless, as will be discussed later, the Hubbard-like scenario is able to predict some remarkable behaviors.

DFT calculations

LDA calculations predict a robust magnetic moment across the entire phase diagram. Experimentally what happens is different, in fact the compounds become paramagnetic and then superconducting, above a certain doping level. The Fermi

The challenge of the magnetic moment

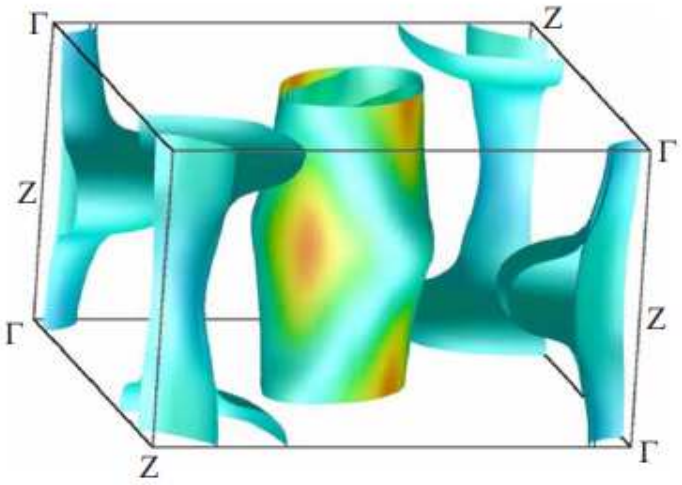

Figure 1.7: LDA Fermi surface of $BaFe_2As_2$. The color refers to band velocity, as described in Ref. [29].

surface of the $BaFe_2As_2$, calculated by density functional theory, is similar to the parent compound of 1111 family, but the hole Fermi surface at the Z point is flattened out, suggesting a more three-dimensional character than that in the 1111 and 11 structures. Remarkably, cylinders at the Γ and M points are nearly nested at (π, π), in the folded Brillouin zone. This can lead to *enhanced spin fluctuations* at critical wavevectors equal to the nesting one. Now it has been suggested that, if these fluctuations are sufficiently strong, they can cause stripe-type Spin-Density-Wave ordering [13].
Moreover, the more the doping, the less the degree of nesting of the Fermi sheets. Figure 1.8 shows a comparison of the size of the low-temperature Γ and X pockets. These data suggest that the overdoped side of the superconducting dome is governed by relative Fermi surface size, which is controlled by e-value in the case of TM-doping. When the electron doping increases, the hole pocket shrinks, thus hindering the nesting between the electron and hole pockets and potentially suppressing the spin fluctuations [31]. To corroborate the nesting effect, ARPES measurements made by Ding *et al.* have found, in $Ba_{0.6}K_{0.4}Fe_2As_2$, two superconducting gaps, which are nearly isotropic, and which close simultaneously at the bulk T_c. The authors claim that the pairing mechanism originates from the interband interaction between the hole and the electron nested Fermi surface sheets [32].
Very recently Tai et al. [33] developed a minimal multiorbital tight-binding model for hole and electron doped $BaFe_2As_2$ compounds. Interestingly, by lowering the

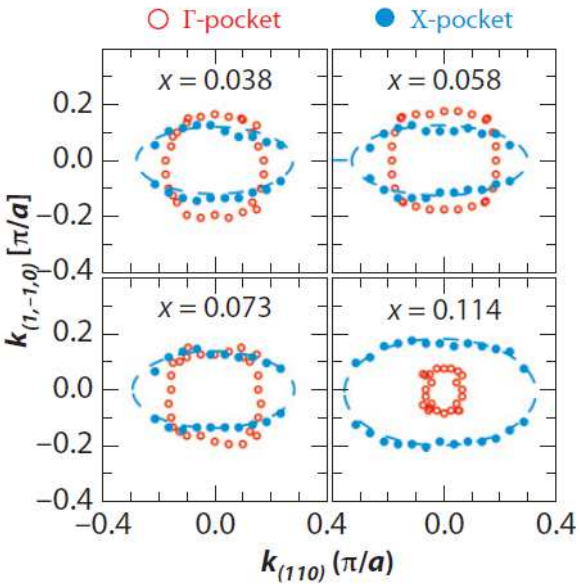

Figure 1.8: Γ and X pockets location of the low-temperature data, extracted through the peak position of the momentum distribution curves in $Ba(Fe_{1-x}Co_x)_2As_2$, as measured from angle-resolved photo emission spectroscopy. x is the Co concentration. Figure adapted from Ref. [31].

crystal symmetry from C_4 to D_{2d} an accurate description of the Fermi surface evolution with doping is naturally found. Furthermore such model is in agreement with the experimental ARPES results. The authors claim that the upper anion atom mediates the overlap between the Fe $3d_{xz}$ orbital and the $4p$ As orbital. Likewise, the lower anion atom mediates the overlap between the Fe $3d_{yz}$ orbital and the $4p$ As orbital. Moreover they suggest that the symmetry breaking, and the competing interactions in the multiorbital mean-field Hamiltonian, are responsible for the rising of a small $d-$wave pairing, in addition to the more robust extended $s-$wave scenario. This admixture can give rise to quasiparticles which behave like nodal excitation.

1.5 Spin fluctuations and magnetic properties from an experimental viewpoint

Since the discovery of iron-pnictide superconductors, many NMR experiments have been carried out to investigate the magnetic and superconducting properties of these systems, from a microscopic viewpoint. In this paragraph, an overview

of the most significant achievements obtained by NMR, and their contribution to the vastly debated topic of spin fluctuations is given. Indeed quantum magnetism in the iron-pnictides is a "hot topic", as there are many issues that the scientists fail to reconcile. Some examples are:

- The small measured value of Fe magnetic moment, as opposed to the theoretical calculation;
- The interplay between superconductivity and magnetism: whether they are competing or precursors;
- The correct scenario to interpret the iron magnetic moments: whether they are strongly delocalized, or localized;
- The role of frustration and its effects on reducing the magnetic moment, facilitating the formation of superconductivity, and spin fluctuations.
- The role of orbital currents.

NMR spectroscopy can contribute to solve this puzzle. The first aspect concerns the Knight-shift measurements in the superconducting state. In the iron-pnictides the Shift decreases continuously (see Fig. 1.9), below T_c, indicating a monotonic decrease of the spin expectation value, suggesting that these materials show a spin-singlet state. Moreover, an accurate Knight shift study over temperature in principle allows one to make quantitative considerations on the magnitude and on the symmetry of the gap [34].

The Knight Shift

An even more intriguing result was found in the temperature dependence of the Knight Shift, in the normal state. The shift follows an Arrhenius-like trend, that is still a matter of debate. Tentative explanations will be given in Chapter 4.

While the Knight Shift is sensitive to static fields and spin excitations at $\mathbf{q} = 0$, the spin-lattice relaxation time T_1 is able to probe the spin dynamics at all wavevectors, and in the limit of low-energies:

$1/T_1$

$$\frac{1}{T_1} \sim T \sum_{\mathbf{q}} |A(\mathbf{q})|^2 \frac{\chi''(\mathbf{q}, \omega_0)}{\omega_0} \tag{1.4}$$

where $A(\mathbf{q})$ is the $\mathbf{q}$-dependent form factor, and $\chi''(\mathbf{q}, \omega_0)$ is the dynamical susceptibility, at the Larmor frequency ω_0. The sum is taken over the first Brillouin zone. The spin-lattice relaxation rate $1/T_1$ is often measured in the superconducting state to study the nature of the coupling, and sometimes also the gap

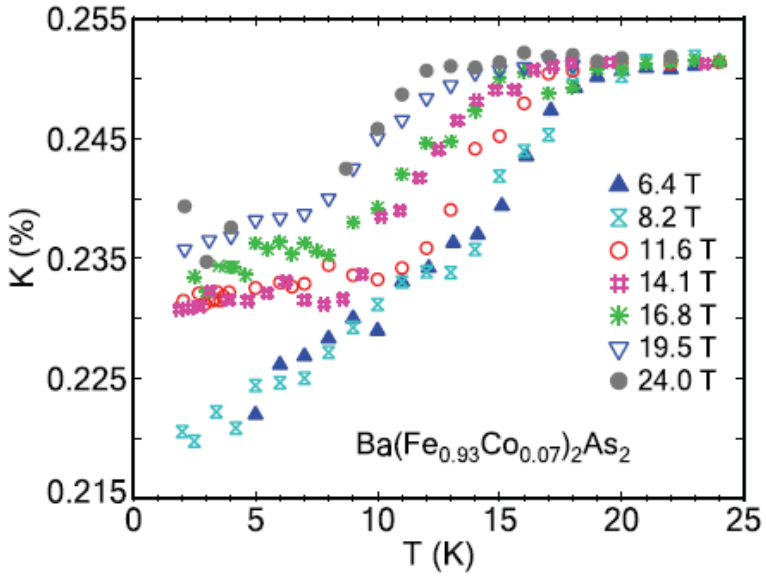

Figure 1.9: Knight shifts measured at several magnetic fields, in $Ba(Fe_{1-x}Co_x)_2As_2$ with x=7.4%. The figure is adapted from Ref. [35].

symmetry.

The first remarkable finding in $1/T_1$ is the absence of a coherence peak, which rules out the pure s-wave scenario (see Chapter 2 for further explanations). On the other hand, a power law trend $1/T_1 \sim T^3$ has been observed [36], suggesting the presence of an anisotropic superconducting gap, in partial disagreement with other experimental techniques. Nevertheless the occurrence of a power-law behavior in $1/T_1T$ is not necessarily due to the presence of a nodal gap. In fact, impurity scattering in various strengths, is sufficient to produce a wide variety of power-law behavior in many thermodynamic quantities, even in the near-Born limit [37, 38]. In the extended s-wave state, interband impurities are even more effective in creating such a behavior.

In fact, one of the gap symmetry that has been more supported is the $s^{\pm}$-wave, which considers the presence of two gaps, with an inversion of the gap sign. In such a case, the peak in the $1/T_1$ is not expected [37], in agreement with the experimental results (Fig. 1.10). Another way to extract the symmetry and the value of the superconducting gap is to observe the temperature dependence of the London penetration depth λ which is related to the density of the Copper pairs n_s, via

$$\lambda^2 = \frac{m}{4\pi n_s e^2} \tag{1.5}$$

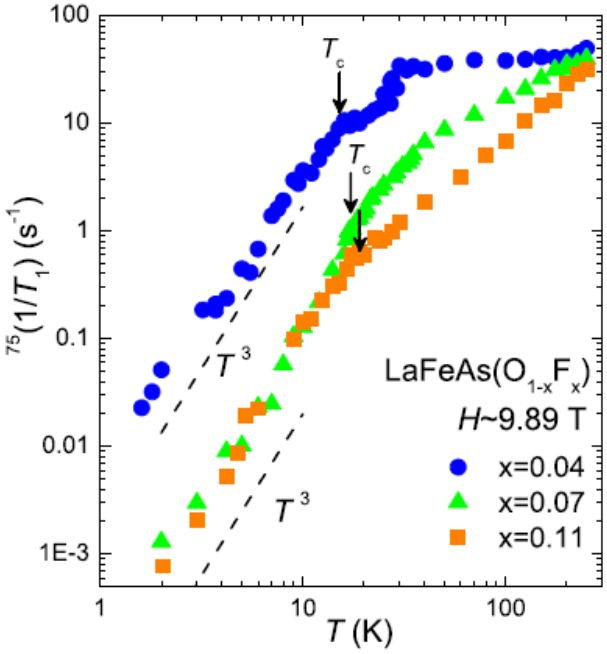

Figure 1.10: Temperature dependence of $1/T_1$, for $\mathbf{H} \parallel ab$, in LaFeAS($O_{1-x}F_x$). The figure is adapted from Ref. [39].

However, NMR is not the best technique, in this regard, because the vortex supercurrents can provide diamagnetic screening which does not effectively cancel in the intervortex region. On the other hand, muon spin rotation (μSR) can provide more reliable data.[4]

Furthermore, in the undoped LaFeAsO and $BaFe_2As_2$, a strong enhancement of the $1/T_1T$ rate has been observed and ascribed to stripe-type magnetic fluctuations [13]. Remarkably, in the 1111 family the fluctuations are suppressed by increasing the doping concentration [39]. Indeed in $LaFeAsO_{1-x}F_x$, at x=0.04 a weak magnetic anomaly occurs at 30 K, and superconductivity sets in at 16 K. Upon F doping, significant AFM fluctuations observed for x=0 and 0.04 are suppressed systematically, and pseudogap behavior appears for x=0.11 and 0.14 without pronounced AFM fluctuations. Indeed $1/T_1T$ measurements of LaFeAsO, display an activated temperature dependence:

The pseudo-gap

$$\frac{1}{T_1T} = a + b\exp\left(\frac{-\Delta}{T}\right) \tag{1.6}$$

which is reminiscent of the pseudo-gap Δ. Such behavior increases upon the F (electron)-doping, that is opposite to what observed in the cuprate super-

[4] See [27] for a recent review.

conductors, in which the pseudogap behavior is significant in the underdoped region. However, Oka and coworkers [40] reported a systematic study by ^{75}As nuclear-quadrupole resonance in the same compound, where antiferromagnetic spin fluctuations were found above the magnetic ordering temperature and from 0.04<x<0.08 doping, where superconductivity sets in. Moreover, the spin-lattice relaxation rate, below T_c decreases exponentially down to $0.13T_c$, which unambiguously indicates that the energy gaps are fully opened. The temperature variation of $1/T_1$ becomes nonexponential for other dopings, by impurity scattering. The situation in Ba122 compounds is rather different, as reported by Nakai and coworkers [41]. With this respect Ning *et al.* [42] published a study of the $Ba(Fe_{1-x}Co_x)_2As_2$ family, where $1/T_1T$ behaves in such a way that, upon increasing the doping concentration, a suppression of the spin fluctuations occurred until the systems behaves like a Fermi liquid, with a peculiar Korringa's law behavior. No pseudogap-trend has been observed, and a Curie-Weiss relation (see Fig. 1.11) fits quite well the experimental data for $1/T_1T$. They observed that, as the level of doping is decreased across x=0.15, a hole Fermi surface emerges in the center of the Brillouin zone, inducing a strong enhancement of antiferromagnetic spin fluctuations associated with interband transitions, at a critical wavevector $\mathbf{Q_c} = (\pi, 0)$. The superconducting critical temperature is maximum when these spin fluctuations are enhanced, until the SDW ordering does not set in.
Therefore, Kitawaga *et al.* [43] found a remarkable difference in $1/T_1T$ of $BaFe_2As_2$, depending on the orientation of the sample, with respect to the field, namely an enhancement in $1/T_1T$ was observed when the external field was laying in the *ab* plane. The authors concluded that the observed anisotropy was due to spin-space anisotropy of the stripe-type (nematic) spin fluctuations, and suggested that such anisotropy might also be observed in the tetragonal doped superconducting compositions, and indeed might have an important role in superconductivity.

Magnetic frustration

As far as the magnetic moment discrepancy is concerned, one possible reason may be found in magnetic frustration. The key feature here is that in the FeAs unit, not only the Fe atoms form a square lattice, but also each As atom lays at an equal distance from each of the four adjacent Fe atoms. Superexchange interactions develop between a pair of nearest-neighbor Fe spins J_1, and a pair of next-nearest-neighbor spins J_2. Fig. 1.12 shows the process contributing to the NNN superexchange interaction, between a pair of $3d_{x^2-y^2}$ electrons, mediated by $4p$ orbitals, and the process contributing to the NN superexchange interaction, between a pair of $3d_{x^2-y^2}$ electrons together with two orthogonal $4p$ orbitals, lead-

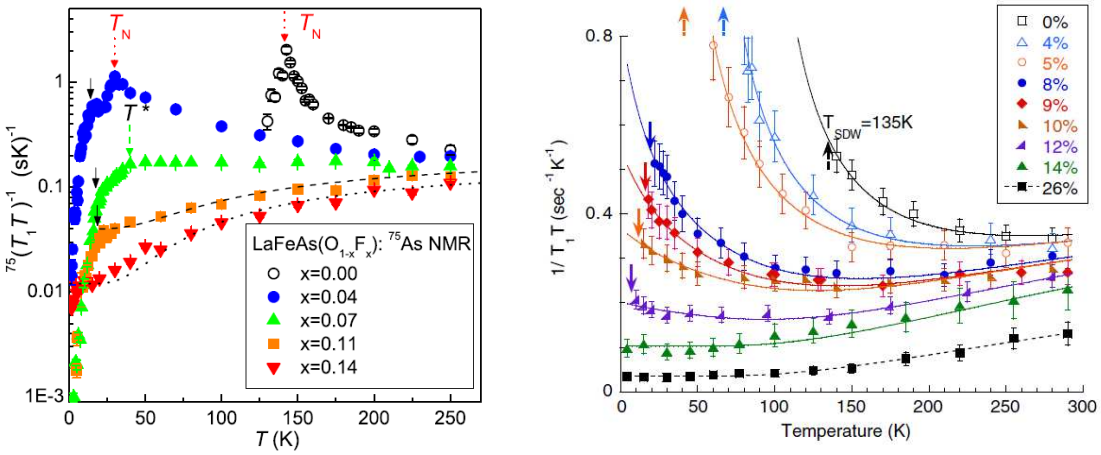

Figure 1.11: (left figure) Temperature dependence of the $1/T_1T$ for different compounds of the 1111 family. Figure adapted from [39]. (right figure) $1/T_1T$ for in $Ba(Fe_{1-x}Co_x)_2As_2$, with magnetic field applied along the ab plane. Solid and dashed arrows mark T_c and T_{SDW}, respectively. Solid and dashed curves are the best fits to the Curie-Weiss law, rising from antiferromagnetism. Figure adapted from Ref. [42].

ing to a ferromagnetic J_1, and an antiferromagnetic J_2. In the undoped parent compound, these frustrated interactions lead to a two-sublattice collinear antiferromagnet with a reduced magnitude of the ordered moment. Electron or hole doping, together with the frustration effect, suppress the magnetic ordering and allows a superconducting state. This idea has been proposed by Si *et al.* in 2008 [44]. The authors suggest that magnetic frustration may have two roles in

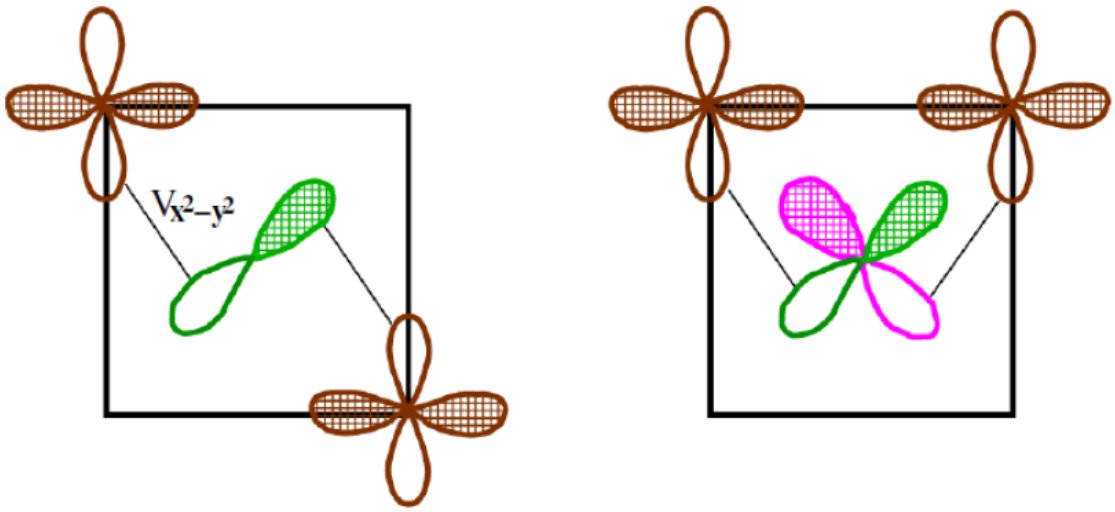

Figure 1.12: The orbital hybridization as a source of exchange interaction. J_2 interaction is given by the hybridization shown in the left panel, while J_1 arises from the hybridization shown in the right panel. The figure is adapted from Ref. [44].

these systems: at first it is responsible to suppress the magnetic ordering, and secondly to accumulate entropy at low temperatures, the relief of which can turn into a superconducting gap opening. However Fang *et al.* [30] showed that, in a quantum Heisenberg spin-localized model, frustration is not sufficient to account for the experimentally observed small magnitude of the ordered moment.
Other authors supporting the spin-fluctuation scenario, as Mazin *et al.* [18, 45], state that spin fluctuations can induce only a triplet superconductivity, or a singlet superconductivity, with the order parameter changing sign over the Fermi surface. The $s^{\pm}$-wave is a good candidate, with a gap $\Delta(k_x, k_y) \sim \cos(k_x)+cos(k_y)$ (Fig. 1.13). According to these authors, the spin fluctuations spectrum in the

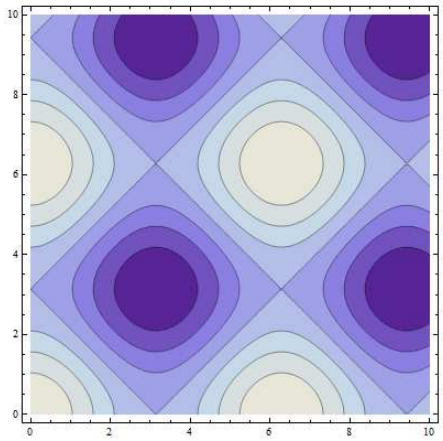

Figure 1.13: Contour plot of the $s^{\pm}$-wave gap. The horizontal axis denotes k_x, while the vertical axis denotes k_y. The color map shows sign reversion of the gap.

parent compound of 1111 family may have three different origins: (1) the system is relatively close to a Stoner ferromagnetic instability, (2) there is a nearest-neighbor antiferromagnetic (AFM) superexchange path, which can give rise to frustration and (3) there may be a nesting of the Fermi surfaces, leading to SDW fluctuation, at wave vectors connecting the electron and hole pockets. The latter seems to be the most supported hypothesis, also considered that such effect may induce a strong pairing, provided that the order parameters on the two sets of the Fermi sheets have opposite signs. Moreover spin fluctuations and fluctuating magnetic domain boundaries persist up to the paramagnetic state and the over-doped part of the phase diagram. This observation may pave the way for the interpretation of the anomalous T_2 data, presented in Chapter 4.

Spin fluctuations

A recent NMR study [46] seems to support this framework, suggesting that antiferromagnetic spin fluctuations could be responsible for the "glue" binding the Cooper pairs. The authors believe that NMR spin-lattice relaxation rate, elec-

trical resistivity, inelastic neutron scattering data, in the paramagnetic phase of $BaFe_2(As_{1-x}P_x)_2$ and $Ba(Fe_{1-x}Co_x)_2As_2$, can be understood quantitatively in the framework of the self-consistent renormalization spin-fluctuation theory. A consistent description of these physical properties suggests a cross-over between a non-Fermi liquid towards a Fermi-liquid behavior, which emerges upon increasing the doping concentration.

The presence of spin fluctuations has been studied very recently also by other authors [47]. Hammerath *et al.* studied the evolution of low-energy spin dynamics in F-doped LaFeAsO, over a broad doping, temperature, and magnetic field range. An enhanced spin-lattice relaxation rate divided by temperature, in underdoped superconducting samples, suggests the presence of unconventional antiferromagnetic spin fluctuations, which are strongly reduced in optimally doped (x = 0.10) and completely absent in overdoped (x = 0.15) samples.

IN spectroscopy

Together with NMR, also inelastic neutron scattering (INS) is used to probe the collective spin excitation. For instance, Lester *et al.* [48] studied the near optimally doped superconductor $Ba(Fe_{1-x}Co_x)_2As_2$. Prior measurements on the antiferromagnetically ordered parents of this material, showed a strongly anisotropic spin-wave velocity. Lester and coworkers measured the magnetic excitations up to 80 meV, and observed a magnetic anisotropy of the excitations persisting for superconducting compositions (Fig. 1.14). Moreover from the spin wave velocity and the Heisenberg model they succeed in extracting the exchange couplings: $J_1 = 43 \pm 7$ meV, and $J_2 = 30 \pm 3$ meV, on the compound $Ba(Fe_{0.935}Co_{0.065})_2As_2$. Even though there is no static magnetic order, this system is close to the antiferromagnetic quantum critical point. In fact, it has been shown [49] that 2D square-lattice systems, described by the J_1-J_2 Hamiltonian, develop a stripe-like order of the type observed in the ferropnictides for $J_2/J_1 > 1/2$. In this case, the *order out of disorder* mechanism [50] predicts the formation of collinear state described by two interpenetrating Néel sublattices.

Few months ago, Chaloupka and coworker [51] proposed a model describing the magnetic behavior of Fe-based superconductors, based on a dynamical mixing of quasidegenerate spin states of the iron ion, by intersite electron hopping, resulting in an effective local spin S_{eff}. They suggested that the $Fe^{2+}(d^6)$ ion, in a covalent compound, is characterized by a competition between the Hund's rule and the covalency, that is responsible of a ground state which is a coherent superposition of a triplet and a singlet state. The resulting effective spin expectation value S_{eff}, depends on pressure and similar parameters. The process generating the dynamical mixing of triplets and singlets is shown in figure 1.15. They claim to have

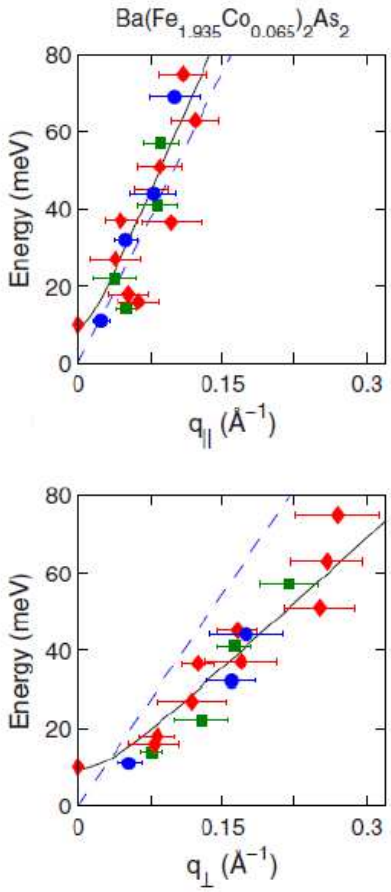

Figure 1.14: The dispersion of magnetic excitations in $Ba(Fe_{1-x}Co_x)_2As_2$ with x = 6.5 %, for T = 7 K. The comparison shows a dispersive behavior of the spin fluctuations, and a marked anisotropy. The figure is adapted from Ref. [48].

solved the puzzle of large, but fluctuating, Fe moments by invoking magnonic exitations, taking place across the whole phase diagram. Their model allows one to predict the temperature-activated behavior of the spin susceptibility. The authors found that the effective moment S_{eff} is a function of the thermal expansion coefficient. Moreover, while the ordered moment vanishes at certain doping, the effective moment remains almost constant, corresponding to a fluctuating magnetic moment of $\sim 1\mu_B$.

When the spin fluctuations issue is addressed from the "NMR viewpoint", the quantity that is typically studied is $1/T_1$. However also the spin-spin relaxation time T_2, turns very versatile to investigate the low-frequency spin dynamics. $1/T_2$ is particularly effective in revealing the spin dynamics that involves the longitudinal component of the local field probed by the nucleus. T_2 study

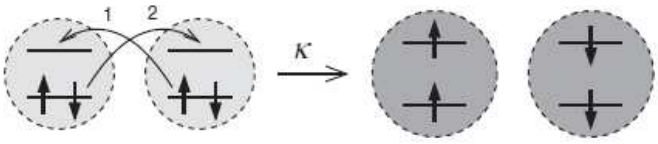

Figure 1.15: The process κ, as described by Chaloupka *et al.*, is given by the hopping of two electrons in the d-levels of iron Fe^{2+} ions. Two configurations are dynamically created: a spin singlet S =0 state, and a spin triplet S=1 state. The ground state is a mixture of the two pure states. The figure is adapted from Ref. [51].

In fact, Oh *et al.* [35] studied Hahn Echo and Carr-Purcell-Meiboom-Gill (CPMG), on the optimally Co-doped Ba122. Measurements of NMR spin-spin relaxation time indicate an anomalously long T_2, that could not be justified in terms of As-As dipolar interaction. The authors suggested that strong indirect exchange interactions among As nuclei play a role, at all temperatures, in increasing the values of T_2. This exchange narrowing effect, in metals, needs to have resonant nuclei, namely the flip-flop processes can happen without changing the nuclei energy. In other words the nuclei must have the same Larmor frequency, within an interval corresponding to the dipolar coupling.
Below the superconducting transition temperature, abrupt changes in vortex dynamics lead to an anomalous dip in T_2 (Fig. 1.16), consistent with vortex freezing/melting, from which the authors obtain the vortex phase diagram up to H =28 T. An earlier study made by Mukhopadhyay *et al.* in 2009 [52] in $Ba_{1-x}K_xFe_2As_2$ and $CaFe_2As_2$ has reported the spin-spin relaxation rate, by means of both Hahn echo and CPMG sequence (Fig. 1.17). They observed that the parent compound $CaFe_2As_2$ has a spin-spin relaxation time comparable with the dipolar calculation, which gives 0.72 ms. On the other hand, $Ba_{1-x}K_xFe_2As_2$ shows an anomalously long T_2, suggesting a quenching of the dipole-dipole interaction. Chapter 4 will address the study of the spin-spin relaxation time, as a probe of spin fluctuations.

Orbital currents

Finally INS measurements have recently discovered two branches of weakly dispersive collective modes, in underdoped cuprates. Polarization analysis revealed that such modes are magnetic excitations. He and coworker [53] have theoretically shown that these branches are originated from orbital current ordering, in the CuO_6 octahedron in Hg1201. Mounce *et al.* [54] have used NMR to infer about the presence of these currents, but surprisingly they didn't find any clue of them, form the study of the spectra of the apical and planar ^{17}O. Mounce proposed that the discrepancy between detection of magnetic ordering by neutrons and NMR measurements is due to the different timescales involved in the experi-

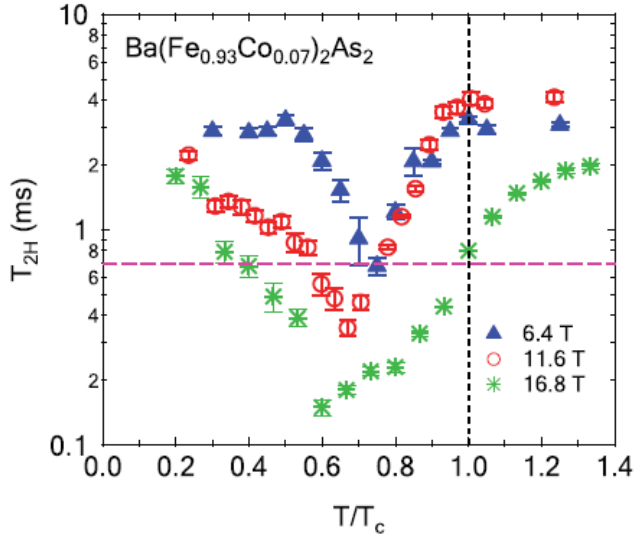

Figure 1.16: ^{75}As NMR Hahn echo decay time for $Ba(Fe_{1-x}Co_x)_2As_2$, for various magnetic fields. At the temperature where T_{2H} displays the minimum, the authors associate the vortex freezing. The figure is adapted from Ref. [35].

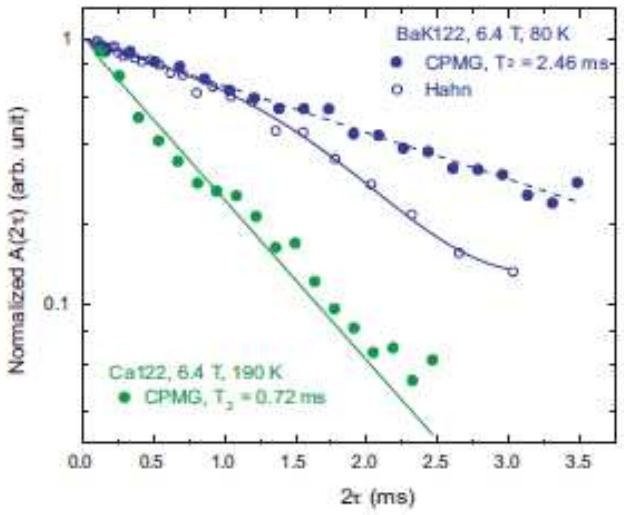

Figure 1.17: ^{75}As NMR Hahn echo and CPMG decays in $Ba_{1-x}K_xFe_2As_2$ and $CaFe_2As_2$. The figure is adapted from Ref. [52].

ments. In essence, neutrons are sensitive to way faster timescales (10^{-11} s), while NMR shifts are sensitive to MHz frequencies. This suggestion may also be an alternative explanation of the "missing magnetic moment" found in experiments on iron-pnictides. Also, the role of orbital currents in inducing superconductivity in the iron-based material is under discussion [55].

1.6 The flux line lattice (FLL)

Since the main part of this thesis focuses on the dynamics occurring in the mixed phase of iron-based materials, it is convenient to spend few words about the Abrikosov's vortices. A. Abrikosov found that type-II superconductor allows some magnetic flux to enter into the specimen body, below T_c, for magnetic field intensity between H_{c1} and H_{c2}. The flux enters in the form of periodic lines or tubes, any of which carries a magnetic quantum flux $\Phi_0 = hc/2e$ =2.05x10^{-7} Gcm^2 [56]. This result came after solving the Ginzburg-Landau equations for a GL parameter $\kappa > 1/\sqrt{2}$, and it found immediate good agreement with Zavaritsii's experimental results on a low-temperature film [57]. This periodic solution is called Flux Line Lattice (FLL) or Abrikosov lattice and it is characterized by lines which have a core of size $\sim \xi$, where the superconductivity is suppressed, and around that a circulating supercurrent $\mathbf{J}(\mathbf{r})$ is responsible for generating a decreasing field $\mathbf{B}(\mathbf{r})$.
The isolated vortex line is a topological excitation of the superconductor characterized by a line singularity in the phase θ of the order parameter. By encircling the vortex line once, the phase θ changes by 2π [58]. As a result, the order parameter is suppressed within the core region extending a length ξ from the singularity. More important is the fact that, the gauge-invariant phase gradient $\nabla\theta$ creates a circular screening current:

$$J = -(2e\hbar/m)|\Psi|^2\nabla\theta \tag{1.7}$$

which extends over a distance λ from the core.
From the purpose of the NMR study one can imagine the Abrikosov vortices like tubes of section $\pi\xi^2$ (Fig. 1.18), in which the magnetic field is close to the external one. The FLL usually forms a triangular arrangement, with an intervortex distance of $l_e = \sqrt{\frac{3\Phi_0}{2H_0}}$, which is about 170 Å, for fields near 10 T. In case of an isolated vortex, Clem and Hao calculated an approximate solution for

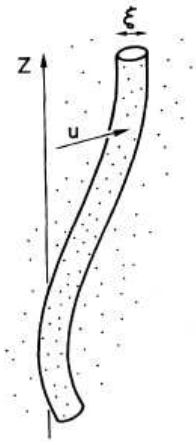

Figure 1.18: Single vortex line, pinned by the collective action of many weak pointlike pinning centers. u is the displacement of the vortex line from the equilibrium position. Figure adapted from Ref. [58].

both the amplitude of the order parameter and the field: [59, 60]

$$|\psi(\mathbf{r})|^2 \sim \frac{1}{1+2\xi^2/r^2} \tag{1.8}$$

$$B(r) \sim \frac{\psi_0}{2\pi\lambda^2} K_0[\sqrt{r^2+2\xi^2}/\lambda] \tag{1.9}$$

where $r^2 = \sqrt{x^2+y^2}$ and $K_0(x)$ is a modified Bessel function. For $r \gg \lambda$ the approximated solution for the wavefuction is $\psi \sim \exp(-r/\lambda)$. Moreover the supercurrent circulating around the vortex core can be found by the Maxwell equation. It can be shown that, for $\kappa \gg 1$, at the center of the vortex, the maximum current is the depairing current J_0 (in S.I. units):

$$J_0 = \psi/(3\sqrt{3}\pi\lambda^2\xi\mu_0). \tag{1.10}$$

When the applied field is increased, more and more flux lines penetrate until they overlap such that ψ vanishes, and the superconductivity disappears. When $H > 0.2H_{c2}$ (which is nearly always verified in the experiments hereafter) the magnetic field is given by a linear superposition of the previous solution, and the second moment of the field distribution is given by:

$$< \Delta^2 B >= c_0\Phi_0^2/\lambda^4 \tag{1.11}$$

where c_0 is a constant depending on the geometry of the lattice. The field profile derived for this case can be seen in figure 1.19. The **minimum field** is found at the **center** of the unit cell of the vortex lattice. The saddle-point field is found midway between two nearest-neighbor vortices, and it is the most likely position. The **maximum field** is found in the vortex core (long tail), with very low probability. The NMR spectrum is directly related to the vortex field distribution, even if such line profile is hardly found in real experiments, as the NMR linewidth is usually a convolution of a Gaussian and the distribution sketched in Fig. 1.19. The Gaussian takes into account the disorder due to the pinning centers or sample impurities. Once the line is de-convoluted, the actual vortex field distribution can be extracted and the vortex lattice properties can be studied selectively on the spectrum. On the contrary, at high inductions, $H > 0.5H_{c2}$, the GL theory gives

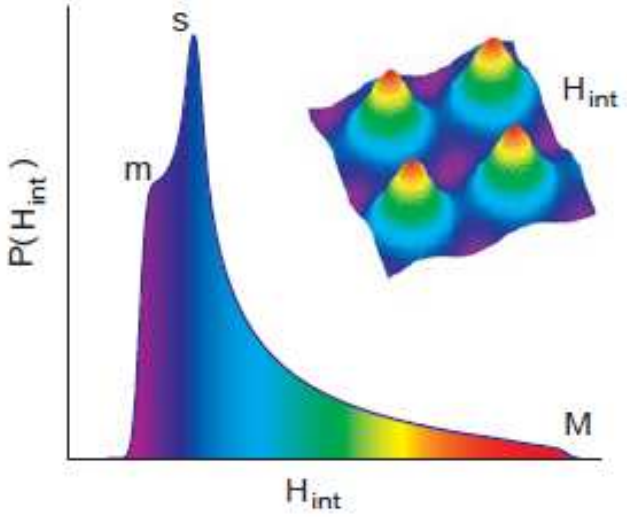

Figure 1.19: Real space magnetic field profile and the corresponding field distribution function. Figure adapted from ref. [61].

a periodic FLL:

$$|\psi(\mathbf{r})|^2 = \frac{1-H/H_{c2}}{1-2/(2\kappa^2)}\beta_A \sum_{\mathbf{K}} a_{\mathbf{K}} \cos(\mathbf{K}\cdot\mathbf{r}) \quad (1.12)$$

$$B(r) = B_a - (\psi_0/4\pi\lambda^2)|\psi(\mathbf{r})|^2 \quad (1.13)$$

where the sum runs over the reciprocal lattice vectors **K**. For a general lattice symmetry the Fourier coefficients $a_{\mathbf{K}}$ and the Abrikosov parameter β_A are:

$$a_{\mathbf{K}} = (-1)^{m+n+mn} \exp(-K_{mn} x_1 y_1 / 8\pi) \quad (1.14)$$

$$\beta_A = \sum_{\mathbf{K}} a_{\mathbf{K}}^2 \quad (1.15)$$

where $x_1 y_1$ is the unit-cell area. Also from the previous values, the free energy and the magnetization can be estimated.

Anyhow, in real systems, when a deviation form the stochiometry occurs (even in the highest quality crystals) the order parameter is suppressed in the vicinity of the defect, thus allowing some magnetic flux to enter the specimen. Such a **point defect**, deforms the free energy profile, creating a metastable minimum, in correspondence to such defect or, in other words, the vortex line will be attracted by the potential well. Thermal energy, as well as external field gradients, will tend to depin the vortex line: at small distances from the vortex core the pinning energy is linear with the distance, resulting into an elastic behavior.

Vortex pinning

Twin plane boundaries are another source of pinning, which is likely found in the orthorombic crystals. In case of a tetragonal structure no many line defects are expected. Moreover, the layered structure is a source of **intrinsic pinning**, since the vortex core can be stuck in the superconducting layers, when the field is aligned along the *ab* plane [22].

In order to prevent the vortices to move and dissipate energy, it is quite customary to induce artificial defects, by bombarding the sample with high-energy beam or heavy ions.

1.7 Conclusions

The basic structural, electronic and magnetic properties of the iron-pnictides are discussed, paying particular attention to the first two families, 1111 and 122. Despite the rich experimental and theoretical efforts, the microscopic mechanism responsible for the superconducting transition is still under debate. Although the electron-phonon scenario may be partially saved, a further mechanism has to be invoked. Some authors propose a spin-fluctuation mediated scenario, while others claim that a coupling with orbital currents must be considered, instead. Open discussions concern the symmetry of the order parameter.

Among all the experimental techniques employed to explore the superconducting state, more attention is given to NMR, as it turns to be very useful to investigate

any dynamic which is able to affect the local magnetic field, in a frequency window of typically kHz-MHz. Moreover, NMR is very sensitive to collective as well as a individual mechanisms. The next chapter will address the basic aspects of NMR.

Chapter 2

Basic aspects of Nuclear Magnetic Resonance

Almost all materials present on Earth contain elements which have a Nuclear Magnetic Resonance active isotope. These nuclei have such small magnetic moments (3 orders of magnitude smaller than the electronic moments), that their interaction with an external magnetic field does not perturb the electrons in the surrounding atoms. However, by virtue of their magnetic moments, nuclei can resonate at radiofrequencies (rf) high enough to allow the scientists to grasp the response of the nuclei interacting with their charge/spin environment. In fact NMR is a local probe which allows one to study individual particles, as well as collective particles phenomena. Additionally, NMR is sensitive to low-frequency spin dynamics (kHz-MHz range), that affect both the longitudinal and transverse local field components.
If on one hand NMR requires rather "cheap" equipment (see appendix D), on the other hand the theoretical background needed to interpret the experimental results is quite intricate. Therefore, new sequences are implemented and invented also in recent times, thus making NMR a state-of-the-art research technique.
Since NMR is the most widely employed experimental tool in this thesis, it is conceivable to devote one whole chapter to the description of its basics. Hereafter the key concepts of pulsed NMR, mainly from a quantum point of view, are reported. It is shown how static interactions among nuclei together with the response of the spin dynamics may affect the NMR linewidth and relaxation times. Finally, the most widely agreed theories used to interpret the NMR results in the superconducting state, will be sketched.

2.1 Semi-classical description

Nuclear Magnetic Resonance is a branch of radio-frequency (rf) spectroscopy with a very broad frequency domain. Magnetic dipole transitions among nuclear levels are induced by an external rf source, after the application of a static magnetic field, which splits the levels, by virtue of the Zeeman interaction. The absorption and emission of radiation does not need to set up a quantum mechanical description of the radiation field, hence the second-quantization of the radiation is not needed. Nonetheless, the complexity of NMR is reflected in its "double" interpretation. From a semi-classical viewpoint, the nuclear magnetization is a vector, which turns back to thermal equilibrium, after a rf pulse has perturbed its initial state. Actually, the "return to equilibrium" contains many physical properties of the system.

Bloch equations

The most intuitive approach to the study of the evolution of nuclear spins in a magnetic field was due to Bloch, who formulated in 1946 a set of phenomenological equations that predict the temporal evolution of the longitudinal and transverse components of nuclear magnetization. When a static magnetic field $\mathbf{H_0}$ is applied along the z axis, the nuclear moments $\mu = \gamma\hbar\mathbf{I}$ tend to line up with the external field, to minimize their magnetic energy. Since the magnetic moment is associated to an angular moment, via the gyromagnetic ratio γ_n, the return to equilibrium is a precessional motion.[1] Indeed the nuclear magnetic moment experiences a net torque $\mathbf{N} = \mu \wedge \mathbf{H}_0$. According to the *second cardinal equation of dynamics*:

$$\frac{d\mathbf{I}}{dt} = \mathbf{N}, \tag{2.1}$$

the magnetic moment will be described by a precessional motion

$$\frac{d\mu}{dt} = \gamma_n \mu \wedge \mathbf{H_0}. \tag{2.2}$$

By solving the equation one realizes that equation (2.2) describes a classical precession of frequency $\omega_0 = -\gamma\mathbf{H}_0$ in clockwise sense. In case of non-interacting spins, equation (2.2) holds also for the expectation value of the magnetization, which is the measured quantity. Then relation (2.2) can be properly modified considering N spins in a volume V. The nuclear magnetization $\mathbf{M}$ is defined as

[1] An accurate description of the Bloch equations can be found in many excellent NMR textbooks, as [62] and [63].

the magnetic moment per unit volume:

$$\mathbf{M} = \frac{1}{V}\sum_i \mu_{\mathbf{i}} \tag{2.3}$$

where i is the spin index. When the nuclear system is out-of-equilibrium, the longitudinal component of the nuclear magnetization evolves with time in such a way that:

$$\frac{dM_z}{dt} = \gamma(\mathbf{M}\times\mathbf{H}_0)_z + \frac{M_0 - M_z}{T_1} \tag{2.4}$$

where T_1, which is called spin-lattice relaxation time, describes the time in which the energy exchange between the spin ensemble and the thermal bath (i.e. electron spins, phonons, magnons etc...) occurs. Moreover $M_0 = \chi_0 H_0$ is the equilibrium magnetization, and χ_0 is the Curie susceptibility, describing the response of a non interacting nuclear spin ensemble, to the application of an external field. On the contrary, to the electronic spins, which can show several magnetic behaviors, as ferromagnetism, antiferromagnetism, diamagnetism or paramagnetism, nuclear spins just experience the last kind of behavior.
As far as the xy components are concerned, naively one can deduce that if the magnetization tends to align to the external field, the transverse component will vanish. Bloch in fact predicted:

$$\frac{dM_{x,y}}{dt} = \gamma(\mathbf{M}\times\mathbf{H}_0)_{x,y} - \frac{M_{x,y}}{T_2} \tag{2.5}$$

where T_2 (called spin-spin relaxation time) quantifies the timing of this process. However the classical approach seems to suggest that $T_1 = T_2$, which is not generally true. The confusion originates from the fact that the nuclear magnetization is *not* a rigid vector, and there is a substantial difference between the T_1 and T_2 mechanisms. Indeed, in the former case the return to equilibrium is due to energy transfer from the spin system to the thermal reservoir, whereas in the latter case, the spin-spin process takes place without exchanging energy with the lattice, and it quantifies the loss of phase coherence on the nuclear spins in the xy plane, during the time. For this reason T_2 is sometimes called dephasing, or decoherence time. One possible mechanism for the T_2 decay is the dipolar interaction. In fact, if a nucleus is at distance r from its nearest neighbor, it will experience a local field $H_{loc} \sim \mu/r^3$. The two nuclei will precess at a slight different frequency (with respect to the Larmor frequency ω_L) separated by $\delta\omega = H_{loc}\gamma$ that, in a time t, turns into a phase difference $\delta\omega t$. The actual presence of many nuclei with many first, second, and n-th neighbors, will result into a big amount of accumulated

phase, and eventually in a big spread of the signal. Solid samples have the largest "spread effect", which reflects into the broadest lines. A rough estimate of T_2 coming from dipolar interaction is $T_2 \sim r^3/(\gamma^2\hbar)$.

If a small field H_1, rotating at frequency ω, and directed perpendicularly to $\mathbf{H_0}$, is added to the external one:

$$\mathbf{H} = H_1(\hat{x}\cos\omega t - \hat{y}\sin\omega t) + H_0\hat{z}, \tag{2.6}$$

the Bloch equations will be modified, accordingly:

$$\frac{dM_x}{dt} = \omega_0 M_y + \omega_1 M_z \sin\omega t - \frac{M_x}{T_2} \tag{2.7}$$

$$\frac{dM_y}{dt} = -\omega_0 M_x + \omega_1 M_z \cos\omega t - \frac{M_y}{T_2} \tag{2.8}$$

$$\frac{dM_z}{dt} = -\omega_1(M_x \sin\omega t + M_y \cos\omega t) + \frac{M_0 - M_z}{T_1} \tag{2.9}$$

Bloch equations in presence of a rotating field

where $\omega_1 = \gamma H_1$ and $\omega_0 = \gamma H_0$ is the Larmor frequency. If the rf field is so small that $\gamma H_1 << 1/\sqrt{T_1 T_2}$, it can be shown that, at resonance ($\omega_1 = \omega_0$), M_z can be tilted in the xy plane. In fact, if one neglects ω_1 and $M_z \approx M_0$, one obtains $\frac{dM_z}{dt} = 0$. A solution for M_x and M_y can be looked for, by exploiting the classical analogy of the spinning top precession problem (Fig. 2.1):

$$\begin{aligned} M_x &= m\cos(\omega t + \varphi) \\ M_y &= -m\sin(\omega t + \varphi) \end{aligned}$$

Signal generation

In an NMR experiment, the signal comes from the time variation of the transverse magnetization itself. In fact, the pick up coil containing the sample, probes the time variation of the magnetic flux, induced by the precessing nuclear magnetization. According to the Faraday law, the magnetic flux is converted into an electromotive force (e.m.f),[2] the magnitude of which is proportional to $M_{x,y}$. To get the amplitude of the signal the sine and cosine functions are expanded:

$$M_{x,y} = m[\hat{x}(\cos\omega t\cos\varphi - \sin\omega t\sin\varphi) - \hat{y}(\sin\omega t\cos\varphi + \cos\omega t\sin\varphi)] \tag{2.10}$$

where $\hat{x}, \hat{y}$ are the versors pointing towards the x and y axes. By collecting the

[2]See Appendix D for the details concerning the NMR equipment.

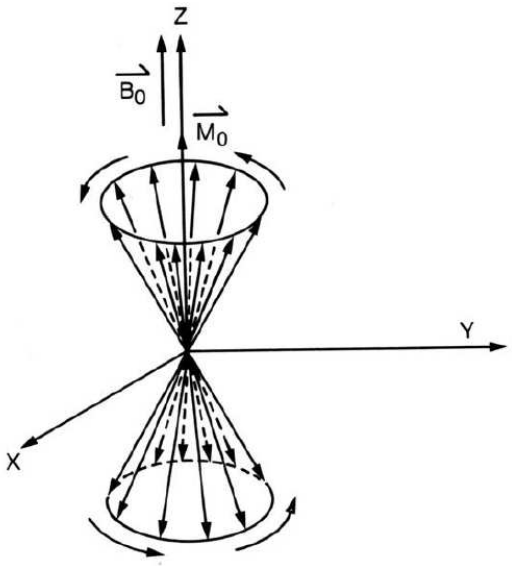

Figure 2.1: Precession of nuclear spins (I = 1/2) at thermal equilibrium, in a stationary magnetic field that defines the z-axis. The angle between the vectors and the z-axis has been exaggerated for illustrative purposes. The picture is adapted from Ref. [64].

terms in $\cos\varphi$ and $\sin\varphi$

$$\mathbf{m}' = m\cos\varphi(\hat{x}\cos\omega t - \hat{y}\sin\omega t) \tag{2.11}$$

$$\mathbf{m}'' = -m\sin\varphi(\hat{x}\sin\omega t + \hat{y}\cos\omega t), \tag{2.12}$$

where the first component is in phase with H_1, while the second is in quadrature with respect to the same field. It is now conceivable to introduce the response function of the nuclear magnetization, under the action of the oscillating external field, $\chi = \chi' + i\chi''$:

$$\chi'(\omega) = \frac{M_0}{H_0}\frac{T_2^2(\omega_0-\omega)\omega_0}{T_2^2(\omega_0-\omega)^2+1} \tag{2.13}$$

$$\chi''(\omega) = \frac{M_0}{H_0}\frac{T_2\omega_0}{T_2^2(\omega_0-\omega)^2+1} \tag{2.14}$$

the real part represents the energy **dispersion**, while the imaginary part represents the energy **dissipation** (or absorption), the latter being a Lorentian (Fig. 2.2) centered at the resonance frequency ω_0, and of width $1/T_2$.

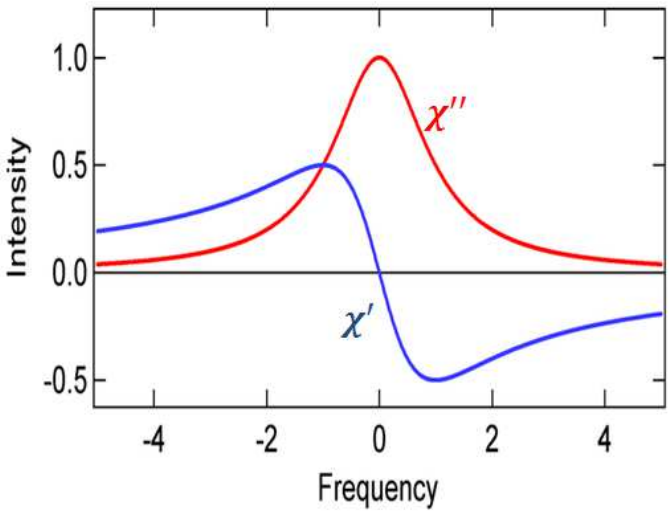

Figure 2.2: A sketch of the dissipative (χ'') and dispersive (χ') parts of the spin susceptibility.

2.2 The Free Induction Decay (FID) signal

A great improvement in the NMR development was introduced when the pulsed technique was employed. Pulsed NMR allows one to study the free induction decay signal (FID) of the nuclear magnetization, after a rf pulse H_1 is applied, along the xy plane, which is in resonance with the Larmor frequency, and which persists for τ. In such a time, the nuclear magnetization will be flipped by a tipping angle $\theta_p = \omega\tau$. The flipping of a $\pi/2$ angle is sketched in Fig 2.3.

From a quantistic point of view, the free induction signal (FID) emerging after a $\pi/2$ pulse, in-resonance with the Larmor frequency, is equal to the auto-correlation function of the transverse magnetization $G(t) =< \mathcal{M}_x(t)\mathcal{M}_x >$, which can be also written as $G(t) = Tr\{\mathcal{M}_x(t)\mathcal{M}_x\} = Tr\{\mathcal{T}^* M_x \mathcal{T} M_x\}$ where $\mathcal{T} = e^{-i\mathcal{H}t/\hbar}$ is the time evolution operator, in agreement with the interaction representation, and $\mathcal{H}$ is the Hamiltonian describing the interactions of the nuclei with the surrounding particles. Before describing the effect of the rf pulse, the density matrix operator, which illustrates the statistical behavior of the spin ensemble, is derived

$$\rho_{eq} = \frac{\exp\left(-\frac{\mathcal{H}}{k_B T}\right)}{Tr\left\{\exp\left(-\frac{\mathcal{H}}{k_B T}\right)\right\}}. \tag{2.15}$$

In the high temperature limit, namely when $k_B T >> \hbar\omega_0$, the density matrix operator turns out to be:

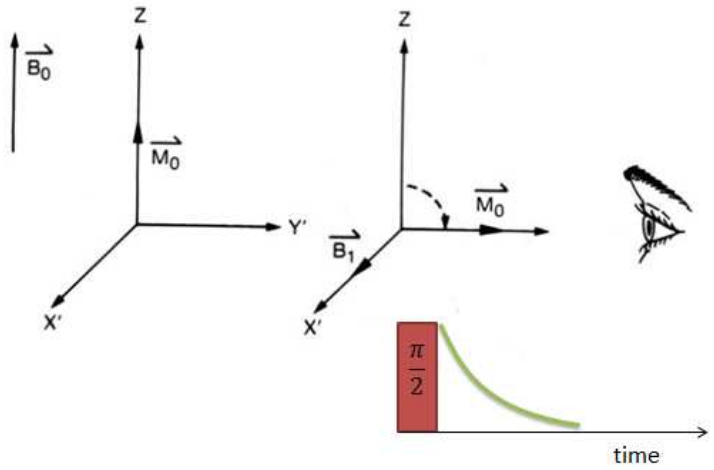

Figure 2.3: Starting from left, the magnetization is at the equilibrium condition (in a frame rotating with ω_L), i.e. the spin and the lattice temperatures are equalized. In the right frame, the application of an in-resonance 90° pulse has the effect of reversing the magnetization along the xy plane. Below this frame, a sketch of the NMR sequence representing the application of a square rf pulse. The Figure is adapted from Ref. [64].

$$\rho_{eq} \sim \frac{\left\{\mathbb{1} - \frac{\mathcal{H}}{kT}\right\}}{Tr\left\{\mathbb{1}\right\}} \tag{2.16}$$

where $\mathbb{1}$ is the identity matrix. If a rf pulse of amplitude H_1, tuned at the Larmor frequency ω_0, is applied for a duration τ, such that the two following conditions are fulfilled:

1. $\gamma H_1 \tau = \pi/2$;
2. The intensity of the rf H_1 field is smaller than the local magnetic field probed by the nuclei;
3. The dipolar interaction doesn't have the time to act while the pulse is on,

the longitudinal magnetization M_z will be flipped into the xy plane. In other words, one can describe such evolution, by applying the rotation operation $\mathcal{R} = e^{i\omega_0 I_z t}$ to the magnetization $\mathcal{R}^* M_z \mathcal{R} = M_x \cos(\omega_0 t) + M_y \sin(\omega_0 t)$. Immediately after the pulse, the statistical operator describing the nuclear spin system is given by:

$$\rho(\tau^+) = \mathbb{1} - \frac{\omega_0 V}{\gamma k T}[M_x \cos(\omega_0 \tau) + M_y \sin(\omega_0 \tau)]. \tag{2.17}$$

When the pulse is turned off, the nuclear magnetization will evolve under the effect of the interaction Hamiltonian $\mathcal{H}$ (see the following paragraph).

2.3 Dipolar nucleus-nucleus interaction

In solid state NMR, the dipole nucleus-nucleus interaction is one of the most relevant, and it is the main source of the broad linewidth and short T_2 relaxation. In fact, the bare nucleus would have a nearly Dirac delta NMR line yet,[3] in the realistic case of a nucleus embedded in matter, the line broadens due to the spread of the Larmor frequency, because of different interactions and/or distribution of interactions. The interaction hamiltonian can be specified as:

$$\mathcal{H} = \mathcal{H}_Z + \mathcal{H}_{n-n} + \mathcal{H}_{n-e} + \mathcal{H}_{EFG}, \tag{2.18}$$

where the different contributions are, the nuclear Zeeman interaction of the nuclear spin with the external magnetic field $\mathbf{H_0}$, the nuclear dipole-dipole interaction, the hyperfine nuclear-electron interaction, and finally the quadrupolar hamiltonian, due to the nuclear quadrupolar moment Q interaction with the electric field gradient (EFG). The last term is non-zero only for $I > 1/2$ spins. If the two first terms are taken into account (which is true for dipolar solids, but it might be a wrong assumption in case of a strong hyperfine field distribution), the hamiltonian turns out to be:

$$\mathcal{H} = -\gamma\hbar H_0 \sum_j I_z^j + \sum_{j<k} \frac{\hbar^2\gamma^2}{r_{jk}^3} \left[\mathbf{I}^j \cdot \mathbf{I}^k - 3\frac{(\mathbf{I}^j \cdot \mathbf{r}_{jk})(\mathbf{I}^k \cdot \mathbf{r}_{jk})}{r_{jk}^2} \right] \tag{2.19}$$

where the sums are performed on couples of nuclei (j and k) which are distant $\mathbf{r}_{jk}$. The dipolar term can be written as the sum of six contributions, as explained in Ref. [62]. In fact, if one calls θ_{jk} and ϕ_{jk} the angles formed by the field $\mathbf{H_0}$ and the $\mathbf{r}_{jk}$ vector, as illustrated in Fig. 2.4, the dipolar hamiltonian can be split in different terms

$$\mathcal{H}_{n-n} = \sum_{j<k} \frac{\hbar^2\gamma^2}{r_{jk}^3} [A_{jk} + B_{jk} + C_{jk} + D_{jk} + E_{jk} + F_{jk}], \tag{2.20}$$

[3] In the realistic case, the spontaneous emission is always present.

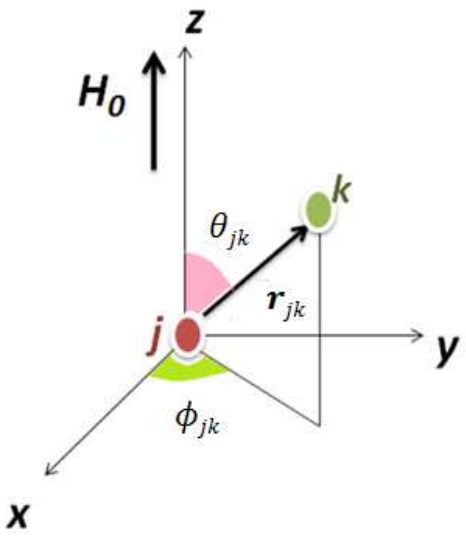

Figure 2.4: The j-*th* and k-*th* nuclei are represented as colored spheres, separared by $\mathbf{r}_{jk}$. The θ_{jk}, ϕ_{jk} angles are shown together with the magnetic field vector.

where

$$\begin{aligned} A_{jk} &= I_z^j I_z^k (1 - 3cos^2\theta_{jk}) \\ B_{jk} &= -\frac{1}{4}(1 - 3cos^2\theta_{jk})(I_+^j I_-^k + I_-^j I_+^k)^4 \\ C_{jk} &= -\frac{3}{2}\sin\theta_{jk}\cos\theta_{jk}(I_z^j I_+^k + I_z^j I_+^k)e^{-i\phi_{jk}} \\ D_{jk} &= C_{jk}^* \\ E_{jk} &= -\frac{3}{4}\sin^2\theta_{jk}e^{-2i\phi_{jk}} I_+^j I_+^k \\ F_{jk} &= E_{jk}^* = -\frac{3}{4}\sin^2\theta_{jk}e^{2i\phi_{jk}} I_-^j I_-^k. \end{aligned} \tag{2.21}$$

Each of these terms is responsible for a transition, in agreement with the selection rules listed below

$$\begin{aligned} A_{jk} &\rightarrow \Delta m_t = \Delta(m_j + m_k) = 0 \\ B_{jk} &\rightarrow \Delta m_t = 0 \\ C_{jk} &\rightarrow \Delta m_t = 1 \\ D_{jk} &\rightarrow \Delta m_t = -1 \\ E_{jk} &\rightarrow \Delta m_t = 2 \\ F_{jk} &\rightarrow \Delta m_t = -2 \end{aligned} \tag{2.22}$$

Since the dipolar interaction is usually of the order of few Gauss, while the Zeeman interaction is of the order of some Tesla, the former is usually a perturbation of the latter. Accordingly, the energy correction due to the dipolar interaction is given by first-order perturbation theory, which requires just the terms of the perturbation matrix that commute with the non-perturbed hamiltonian. The method of moments allows one to predict the NMR lineshape from first principles, without calculating the eigenstates of the total hamiltonian, which is sometimes a complex problem without an exact solution. Such theory shall be presented in Appendix B.

2.4 Electron-nucleus interaction

The third term of the Hamiltonian in equation (2.18) describes the nucleus-electron interaction. The hyperfine field is responsible for macroscopic effects, as the shift of the NMR line from the bare nucleus frequency, or the strong reduction of the electronic spin fluctuations, as observed in the spin-lattice relaxation rate (see Appendix A) [65]. In this section it is reported how the hyperfine interaction affects the Knight Shift, and how the hyperfine tensor is derived from the Knight Shift and Static Spin Susceptibility. The precise form of the hyperfine interaction is complicated for a general atom, but it can be worked out in detail for a single-electron atom interacting with a point nucleus. In the following, the problem will be treated with the purpose to show the basic mechanism of the interaction.

The hyperfine interaction couples the electronic to the nuclear magnetic moments and it is ascribed to two main contributions, the former being the **dipolar field**, namely the dipole-dipole interaction between the electronic $\mu_{\mathbf{e}} = -g\mu_B\mathbf{S}$ and nuclear $\mu_{\mathbf{N}} = \gamma\hbar\mathbf{I}$ magnetic moments, at a distance $\mathbf{r}$. In fact for two closely spaced dipoles, the potential energy is [66]:

$$E = \frac{\mu_{\mathbf{e}} \cdot \mu_{\mathbf{N}}}{r^3} - \frac{3(\mu_{\mathbf{e}} \cdot \mathbf{r})(\mu_{\mathbf{N}} \cdot \mathbf{r})}{r^5}. \tag{2.23}$$

The second contribution is called the **on-site** or **pseudo-dipolar hyperfine coupling** and it is related to the possibility of the electron sitting on the nuclear site, to polarize the nucleus itself, according to the following ideas:

1. If the wave function $\Psi(r)$ of the electron does not vanish at the nuclear position (s-states in atomic terminology), $\Psi(0) \neq 0$, one has a scalar term, which is called the **Fermi-contact interaction**. The energy cost of the

contact interaction is [67]

$$E_{Fermi} = -\mu_I \cdot \mu_e |\Psi(0)|^2 = \gamma g \hbar \mu_B \mathbf{I} \cdot \mathbf{S}$$

2. If the wave function of the electron has an angular dependence and vanishes at the nuclear position: $\Psi(0) = 0$ (e.g. a p-function), the interaction is proportional to $3\cos^2\theta - 1$, where θ is the angle formed by the magnetic field $\mathbf{H_0}$ with the orbital lobe function (Fig. 2.5).

In gases and liquids, only the isotropic part (1) is observable, since the rapid reorientation of the atoms or molecules averages the anisotropic contributions to zero. On the other hand, in the solid state, the site symmetry of the nuclear position is important. In fact in cubic symmetry sites, only the isotropic part is retained, but in the general case the interaction is a second rank tensor A_{hyp}. Such

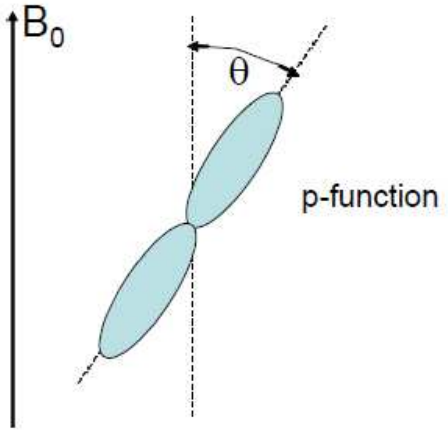

Figure 2.5: Sketch view of a p orbital, in a magnetic field.

a tensor is usually written in the principal axes system (x, y, z). In addition to the pseudo-dipolar, there is also the **transferred** hyperfine coupling, which couples electronic spins sitting on one site i, to nuclear spins sitting on a different site j. It is clear that to evaluate the complete hyperfine tensor from first principles one should have precise information about the orbitals involved, which also requires a non-negligible numerical effort. On the experimental side, NMR and SQUID magnetometry techniques help to overcome this problem. In fact the resonance frequency depends on the local field probed by the nucleus, which contains the hyperfine field itself:

$$\omega_{res} = \gamma_n < \mathbf{H_{local}}^z >= \gamma_n(\mathbf{H_0} + < \mathbf{h}^z >) = \gamma_n(\mathbf{H_0} + < A_{hyp}\mathbf{S}^z >) \qquad (2.24)$$

The Knight Shift is usually defined as:

$$K = \frac{\omega_{res} - \gamma_n \mathbf{H_0}}{\gamma_n \mathbf{H_0}} = \frac{< \mathbf{h}^z >}{\mathbf{H_0}} = \frac{A_{hyp} < \mathbf{S}^z >}{\mathbf{H_0}} \tag{2.25}$$

Since the molar static Spin Susceptibility is given by [67]

$$\chi_{mol} = g\mu_B N_A < \mathbf{S}^z > / \mathbf{H_0}, \tag{2.26}$$

it is straightforward to conclude that the hyperfine field is a proportionality constant between K and χ_{mol}:

$$K^{\alpha\beta}_{spin} = \frac{A^{\alpha\beta}_{hyp}}{g\mu_B N_A} \chi^{\alpha\beta}_{mol} \tag{2.27}$$

where $\alpha, \beta = x, y, z$. It is noticed that in the literature sometimes it is written:

$$K^{\alpha\alpha}_{spin} = A^{\alpha\alpha}_{hyp} \chi^{\alpha\alpha} \tag{2.28}$$

where all the factors are dimensionless. Nonetheless the hyperfine constant is often written in Oe/μ_B units, hence the origin of the confusion, because then χ should be expressed in μ_B/Oe, which are not standard units for χ. Then Johnston [15] derived more complete expressions to solve this inconsistency. The author of this thesis believes that is not necessary, provided that the electronic spin is taken as a dimensionless quantity. In fact, by referring to the considerations made in Appendix E, the equation (2.27) turns out dimensionally correct:

Dimension mismatch

$$K_{spin}[1] = \frac{A_{hyp}[Oe]}{gN_A[mol^{-1}]\mu_B[erg/G]} \chi[erg/G^2 mol] \tag{2.29}$$

From now on the hyperfine field will be expressed in $[Oe]$, or equivalently in $[G]$ units, which is particularly useful when calculating the Form Factor (see Appendix A).

2.5 Quadrupolar interaction

For nuclei with $I > 1/2$, the nuclear charge distribution does not have a spherical symmetry, hence a nuclear quadrupolar moment $eQ \neq 0$ arises. Such moment will interact with the electric field gradient (EFG), due to the charge distribution surrounding the nucleus, partially removing the degeneracy in the quantum number

m. When such interaction is so strong that it reaches the MHz range, the external magnetic field can be removed and the rf field can induce transitions directly between the eigenstates of the quadrupole Hamiltonian. The quantization axis will be given by the Z principal axis of the EFG tensor, of component V_{ZZ}, which is the direction of the largest electric field gradient. This is the basis of Nuclear Quadrupolar Resonance Spectroscopy (NQR). The quadrupolar hamiltonian is given by [68]:

$$\mathcal{H}_{\mathcal{Q}} = \sum_i \mathcal{H}_{\mathcal{Q}}{}^i = \sum_i \frac{e^2qQ}{4I(2I-1)} \left[3I_z^2 - I(I+1) + \frac{1}{2}\eta(I_+^2 - I_-^2) \right] \tag{2.30}$$

where $eq = V_{ZZ} = \partial^2 V/\partial z^2$ and V_{ij} are the EFG components in the principal axes of the reference frame, and $I_\pm$ is the common raising/lowering operator $I_\pm = I_x \pm iI_y$. The compounds investigated in this thesis have axial symmetry, with good approximation, namely the asymmetry parameter $\eta = |V_{XX} - V_{YY}|/V_{ZZ}$ is zero. Moreover, the probed nucleus (As) has a spin $I = 3/2$. Hence if one would like to perform NQR, he should then induce transitions between the hyperfine levels, where the energy correction is related to the quadrupolar frequency:

$$\nu_Q = \frac{3eV_{ZZ}Q}{2hI(2I-1)} \left(1 + \frac{\eta^2}{3} \right)^{1/2} \tag{2.31}$$

This quadrupolar frequency is so sensitive to the charge symmetry distribution around the nuclei that it can detect any lattice distortion/transition. In turn, the line first moment resulting from the quadrupolar interaction, is given by the following expression, at the first order:

$$\nu^{(1)}_{m\to m+1} = \nu_Q(2m-1)(3\cos^2\theta - 1 + \eta(\sin^2\theta)(\cos 2\phi))/4, \tag{2.32}$$

where the angle θ is formed between the magnetic field and the V_{ZZ} axis, while ϕ angle is formed between the xy projection of the magnetic field and the V_{XX} axis. At the second order, the central transition for a spin 3/2 will be corrected by:

$$\Delta^{(2)}_{1/2}\nu = -\nu_Q^2/16\nu_L(a - 3/4)(1 - \cos^2\theta)(9\cos^2\theta - 1) \tag{2.33}$$

with $a = I(I+1)$. It can be noticed that the first order correction for the transition $-1/2 \to 1/2$ is always null. Anyhow, the second order correction involves all the transitions and it is proportional to the second power of ν_Q.
The principal interactions and their action on the NMR line, are summarizes in Fig. 2.6.

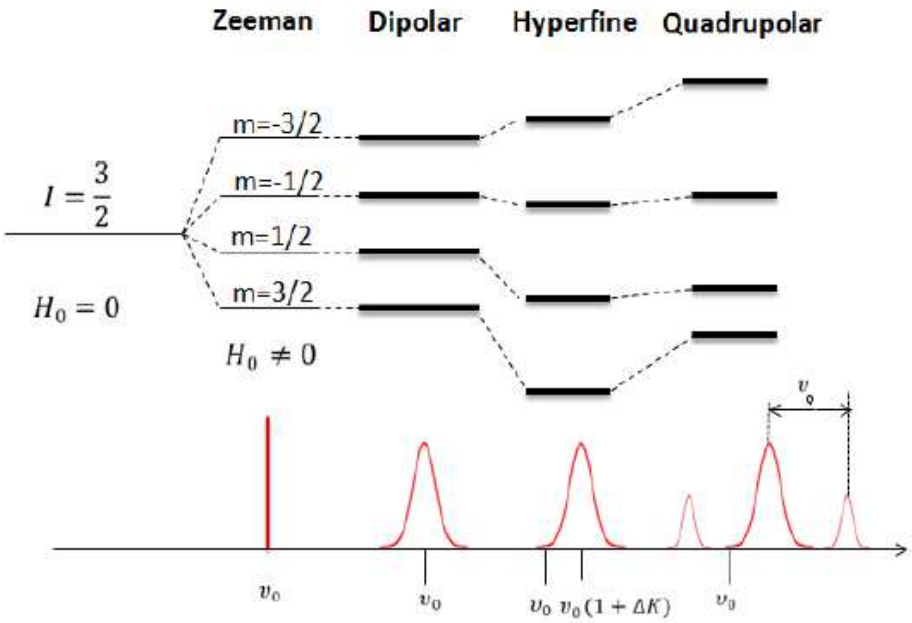

Figure 2.6: The nuclear levels evolution in presence of different interactions, and their effects on the spectrum, on a spin I=3/2 systems. In absence of magnetic field, the nuclear levels are degenerate. When a static field is applied, the Zeeman interaction removes the degeneracy, by creating equispaced levels, that give rise to a Dirac-delta like spectrum (red line in the bottom). When the dipolar interaction is taken into account, the line broadens. The hyperfine interactions shifts the levels, without affecting their width, and finally the quadrupolar interaction corrects the level spacing by generating three different lines, separated by ν_Q.

2.6 NMR in presence of a dynamic

In addition to the static interaction discussed above, NMR is able to provide many clues about the dynamical processes taking place into the system. Typically, NMR is sensitive to frequencies in the kHz-MHz range, but it can also push the limit to higher and slower frequencies. Whenever NMR is used as a tool to investigate some dynamical property, the following rule has to be remembered: *an NMR observable (i.e. linewidth, T_1 or T_2) is affected by the motion, when the characteristic frequencies of the dynamic match some specific time-scale, namely the Larmor frequency, in case of T_1, or the inverse of the pulse spacing, in case of the T_2.*[5] For instance, diffusive motion of the nuclei (or ions nearby), spin fluctuations, molecular motions, flux lines lattice motion in a superconductor (see Chapter 5), are examples of dynamics affecting the NMR variables. When the rate of the fluctuations of the local field, is comparable with the magnitude of the interaction which broadens the line, usually the dipolar field (a few Gauss or tenth of Gauss) the linewidth is affected. The motional effect of the line turns into a narrowing, that can be intuitively understood, by considering that the local field probed by the nucleus will be an average, over the time, of the longitudinal component of the local magnetic field $h_z(t)$. Since the average will be smaller than the instantaneous value of $h_z(t)$, the NMR line will be narrowed. In the following paragraph the description of the NMR line evolution in presence of a dynamic is reported.

2.6.1 Motional Narrowing of the line

If the time-dependent part of the hamiltonian is very small, it can be treated as a perturbation, $\mathcal{H}_P(t) = -\gamma\hbar\sum_i \mathbf{I}_i \cdot \mathbf{h}_i(t)$, where the fluctuating field acting on the i-th spin is smaller than the static field. The free induction signal, can be obtained by retaining, as shown before, just the secular part of the perturbation Hamiltonian, which is [68]

$$\mathcal{H}'_p = -\hbar\sum_i I_z^i \Delta\omega_i(t) \tag{2.34}$$

where $\Delta\omega_i(t)$ represents the fluctuations of the resonance frequency, of the i-th nucleus. Afterwards one has to find the correlation function of the longitudinal local field $g(\tau)$. In the rotating frame, the free induction decay amplitude $G'(t)$,

[5] This might be the dipolar field distribution, the flux line lattice distribution, etc...

is written as

$$G'(t) =< \exp\left(i\int_0^t \Delta\omega(t')dt'\right) > .$$

The symbol $<,>$ is the statistical average over the distribution probability $P(\omega,t)$. Indeed the fluctuations can be described by a probability distributions that, in case of independent motions, as in a random walk, can be assumed to be a stationary Gaussian, with a mean square amplitude $< \Delta\omega^2 >= M_2$:

$$P(\omega,t) = \frac{1}{\sqrt{2\pi M_2}} e^{\frac{-(\omega-\omega_0)^2}{2M_2}} \tag{2.35}$$

This is not the case of *sudden* jumps in the local field magnitude, but it is effective to describe slow molecular motions. By using the following equivalence [69]

$$< e^{-ix} >= \int P(x,t)e^{ix}dx = e^{-\frac{<x^2>}{2}} \tag{2.36}$$

and defining the *normalized correlation function* as $g(\tau) =< \Delta\omega(t+\tau)\Delta\omega(t) > / < \Delta\omega^2 >$, that is characterized by a correlation time τ_c:

$$\tau_c = \int_0^\infty g(\tau)d\tau, \tag{2.37}$$

representing a measure of the time after which the correlation starts to become negligible, one can finally write the free induction decay signal as:

$$G'(t) = G'(0)e^{-<\Delta\omega^2>\int_0^t (t-\tau)g(\tau)d\tau} \tag{2.38}$$

where T_2 is sometimes indicated as T_2'. From the last equation, some information can be obtained about the fast and slow motion case, without making **any assumption on the analytic form of** $g(\tau)$.

Slow Motion regime (s.m.r.)

In the slow motion limit, the correlation function decays so slowly that, over the measure time $t << \tau_c$, it can be approximated to $g(\tau) \approx g(0) \approx 1$ (Fig. 2.7). The FID signal becomes $G'(t) \approx G'(0)e^{\frac{-<\Delta\omega^2>t^2}{2}}$, namely it shows a Gaussian shape. Accordingly the NMR line is a Gaussian as well, with second moment $< \Delta\omega^2 >$.

Fast Motion regime (f.m.r.)

In the opposite case, after a time $t >> \tau_c$, the correlation function has already reached a value close to zero (Fig. 2.8). To calculate the FID expression, one can extend the integration upper limit to infinity and neglect τ with respect to t.

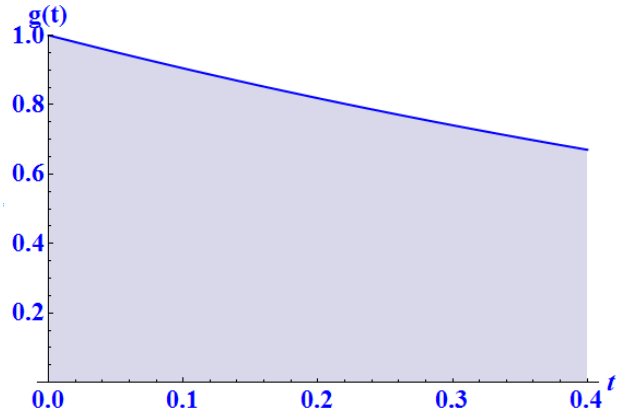

Figure 2.7: Sketch of a slowly decaying correlation function $g(t)$.

Equation (2.38) will then become:

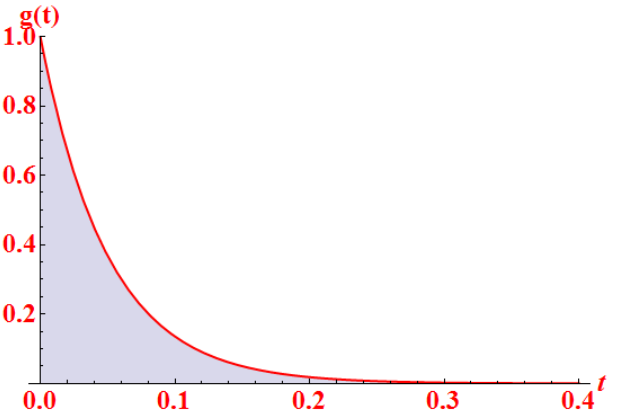

Figure 2.8: Sketch of the correlation function in case of fast motions.

$$\begin{aligned} G'(t) &= G'(0)e^{-<\Delta\omega^2>t\int_0^\infty g(\tau)d\tau} \\ &= G'(0)e^{-<\Delta\omega^2>t\tau_c} = G'(0)e^{\frac{-t}{T_2}} \end{aligned} \tag{2.39}$$

Since the FID signal is an exponential decay, the NMR line will be a Lorentzian: $f(\omega) = f(0)\frac{2T_2}{1+\omega^2T_2^2}$, and as a consequence of that, in correspondence to a transition from slow to fast motions, a change in the lineshape from Gaussian to Lorentian may be seen.
The last considerations suggest an "operative definition" for T_2, that is valid just in the fast motion regime,

$$\frac{1}{T_2} = M_2\tau_c = \int_0^\infty < \Delta\omega(t)\Delta\omega(t+\tau) > d\tau \tag{2.40}$$

If the fluctuation involves just the z axis of the local field $\Delta\omega(t) = \gamma h_z(t)$, one can write the correlation time as:

$$\frac{1}{T_2} = \gamma^2 \int_0^\infty < h_z(t)h_z(0) > dt = \gamma^2 J(\omega = 0) \tag{2.41}$$

where the last term is the spectral density of fluctuations, at zero frequency.
In case of an exponentially decaying correlation function, which is commonly used in case of Gaussian Markoffian processes, $g(\tau) = e^{-\frac{\tau}{\tau_c}}$, the free induction decay signal becomes:

$$G'(t) = G'(0)e^{-<\Delta\omega^2>\int_0^\infty (t-\tau)g(\tau)d\tau} = G'(0)e^{-<\Delta\omega^2>\tau_c^2\left\{e^{-t/\tau_c}-1+t/\tau_c\right\}}, \tag{2.42}$$

that nicely interpolates between the f.m.r and s.m.r (Fig. 2.9).

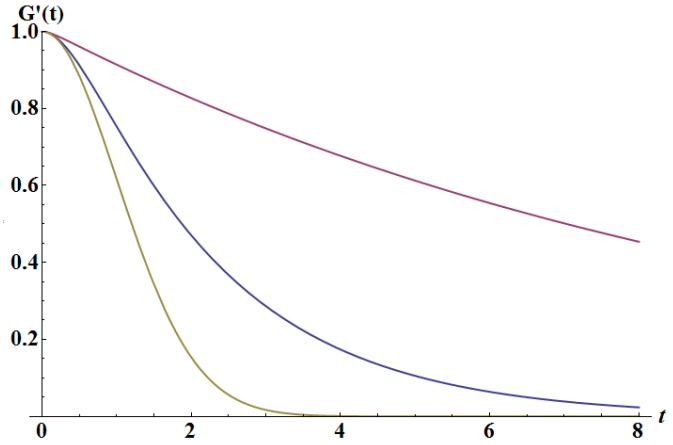

Figure 2.9: Sketch of the FID signal, according to Eq. (2.42), for different τ_c values. The long decaying purple solid curve corresponds to a very small correlation time, namely fast dynamics. The blue curve refers to an intermediate motion limit, while the yellow line is found when the correlation time becomes very long, namely slow dynamics.

2.7 Spin-Spin relaxation

T_2 has been introduced as the time over which the transverse nuclear magnetization decays by 1/e of its initial value, after a $\pi/2$ pulse. The decay can be induced by different mechanisms, that can be grouped into the *extrinsic* and *intrinsic* mechanisms. The first type is due to inhomogeneous distribution of resonance frequencies (as for instance in external inhomogeneous magnetic fields) and it is responsible of the so-called T_2^*. When T_2^* is particularly short, the measure of the

dephasing associated with the intrinsic mechanisms (normally dipole-dipole interaction), is quite challenging. To overcome this problem a spin echo sequence is usually employed. In the following, two of the most common methods to measure the "intrinsic" T_2 are discussed.

2.7.1 The Spin Echo

While liquid compounds usually have very narrow lines, the solid compounds are affected by **intrinsic** sources of line broadening, such as the distribution of hyperfine/dipolar fields. In metallic compounds with impurities this case is particularly common. In fact, magnetic, or also non magnetic, impurities can polarize the surrounding electronic environment, by giving rise to a staggered magnetization. As a consequence of that, the nuclei which are in different sites may experience a different local resonance frequency, which can be quite distant[6] from the Larmor frequency [70]. When the distribution of the local field/frequency is too much spread, the Free Induction Decay can be "too fast" to be seen. In NMR terminology it is said that the signal has a short T_2^*. A way to solve this problem was found by Hahn, [71]. Hahn was originally interested in measuring nuclear relaxation in liquid samples, by applying rf pulses. In the configuration used nowadays, a Hahn (or spin) echo is created after the application of a $\pi/2$ r.f. pulse, followed by a π pulse, after a time τ_{echo}. Such sequence produces an echo at $2\tau_{echo}$ (See Fig. 2.10) [63].

To understand the generation of the echo, one can imagine to apply, at $t = 0$, an in-resonance $\pi/2$ pulse, along the x' axis. Within the semi-classical picture of the magnetization, after the pulse, the magnetization vector will be flipped into the xy plane, along y' axis. At $t = 0^+$, owing to the local field distribution, some spins will probe a slightly larger field, thus precessing a little bit faster, and moving forwards in the rotating frame, while other nuclei that probe a smaller field, will precess a little bit slower, then moving backwards. Hahn's genial idea was to apply, at $t = \tau_{echo}$ a second pulse, double than the previous in duration, along y', the effect of which is to reverse every spin around the same axis. Now, if no time-dependent effects are acting, the same field distribution responsible for the spin dephasing, will also affect the spin signal in this second time window. As a consequence, at the time τ_{echo}, after the π pulse the spin will refocus around $+y'$, thus giving a non null NMR signal.
On the contrary, if a dynamic is playing a role, not all the spins will be refocused.

[6] Namely of the order of some Hz up to some tenths of kHz.

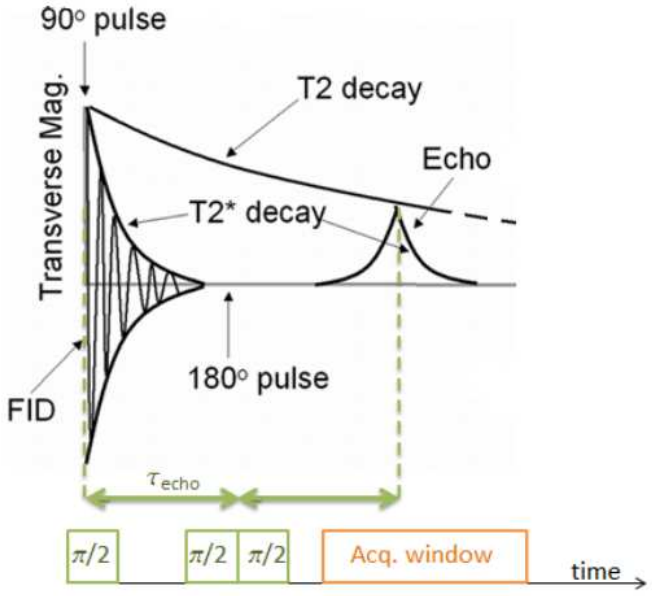

Figure 2.10: The figure represents the evolution of the transverse magnetization, after a r.f. pulse of $\pi/2$, followed by a π pulse. If the second pulse was not applied, the signal would decay by T_2^*. On the other hand, the effect of the second pulse is to refocus the spins, so that a second signal, called "echo" is formed. The amplitude of the echo will not be affected by the sources of field inhomogeneity, but it will evolve according to the intrinsic spin-spin relaxation time T_2.

Nevertheless the description of the spin echo $E(2\tau)$ can still be done according to the same idea presented above [69]:

$$E(2\tau) =< \exp(-i\int_0^{\tau}\omega(t)dt + i\int_{\tau}^{2\tau}\omega(t)dt) > \tag{2.43}$$

where the sign change in the second term is due to the fact that the π pulse will reverse the magnetization phase.
Takigawa and Saito [69] calculated the form of the Hahn echo, without making any assumption of the form of $g(\tau)$. They found that, when the dynamics is so slow that $\sqrt{<\Delta\omega^2>}\tau_c \gg 1$ or it is absent, the echo will be totally refocused

$$E(2\tau) \approx E(0). \tag{2.44}$$

However, in the opposite limit, namely $\sqrt{<\Delta\omega^2>\tau_c} \ll 1$, they showed that the echo has the same analytic form of the FID, $E(2\tau) = e^{-<\Delta\omega^2>\tau_c t}$. Finally if an exponentially decaying correlation function is assumed, the echo decay becomes:

$$E(2\tau) = E(0)\exp^{-<\Delta\omega^2>\tau_c[2t-\tau_c(1-\exp(-t/\tau_c))(3-\exp(-t/\tau_c))]}, \tag{2.45}$$

which still interpolates between the fast and slow limit. Further details about this expression will be provided in Chapter 6.

2.7.2 The CP Sequence

Every time there is an ongoing dynamic, the nucleus can change its precession frequency, for instance by diffusing to a point in the sample, where the static field assumes a different value, owing to some inhomogeneity in the sample or in the external magnetic field. Then the spin echo will decay because of an imperfect rephasing of the nuclear spins. One example of "imperfect rephasing" was brought by Slichter in the case of the spin diffusion into a field gradient $\frac{\partial H}{\partial z}$. In such a scenario, the transverse magnetization decay can be written as: [63]

$$M(2\tau) = M(0)\exp(-2\tau/T_2)\exp\left[-\left(\frac{\gamma\partial H}{\partial z}\right)^2\frac{2}{3}D\tau^3\right] \tag{2.46}$$

where D is the diffusion constant in the static field gradient. As it is clear from the this equation, the derivation of $1/T_2$ may be affected by the second exponential. Carr and Purcell (CP) invented a way for reducing the effect of the cubic term in τ, formulating a new clever sequence of pulses. The advantages of the CP sequence are the following:

- There is no need to wait for the T_1 recovery, after each echo (time saving), as the T_2 measure is made in a "single shot";
- It allows one to improve the signal-to-noise ratio by $\sqrt{N}$ (useful in case of weak signals), by summing up the echoes.[7]

The idea of the CP sequence is sketched below (see Fig. 2.11).

1. At t=0 a $\pi/2$ pulse at resonance, is applied along $+x$ axis, which leads the magnetization to reverse along the $+y$ axis.
2. After waiting for a time τ_{CP}, a second in-resonance π pulse is applied along $+x$ axis. The result of that is a precession of the spins along $+x$, and the growth of the magnetization along $-y$, giving a negative echo at time $2\tau_{CP}$.
3. Now, instead of waiting for the T_1 recovery, one just has to wait another τ_{CP}, and then apply a π pulse along $+x$, so that a second echo will be formed at $+y$.

[7] N is the scans number.

The final result is a train of echoes, formed every even multiple of τ_{CP}, whereas the pulse is applied every $(2n+1)\tau_{CP}$. After n cycles, the CP echo amplitude will be [63]

$$M(n2\tau) = M(0)\exp(-2n\tau_{CP}/T_2)\exp\left[-\left(\gamma n\tau_{CP}\frac{\partial H}{\partial z}\right)^2\frac{1}{3}D\tau_{CP}^2\right] \tag{2.47}$$

Finally, when τ_{CP} is chosen in such a way that the second term tends to 1, the normal exponential decay is restored. Basically, the best way to obtain the intrinsic T_2 is to repeat the CP sequence, by changing τ_{CP} every time, and taking the limit for $\tau_{CP} \to 0$.

CPMG sequence

Despite its utility, this sequence presents some drawbacks. In fact, if there is a slight error in the pulse width, the spins will not properly refocus and therefore, the more pulses, the more the accumulated (wrong) phase. Meiboom and Gill implemented the former sequence by a clever trick: if the π pulses are applied alternatively along $\pm x$ axis, the cumulative error is zero and the spins are refocused along $+y$, always generating a positive echo. More details about the so called $CPMG$ sequence can be found in [62, 63].

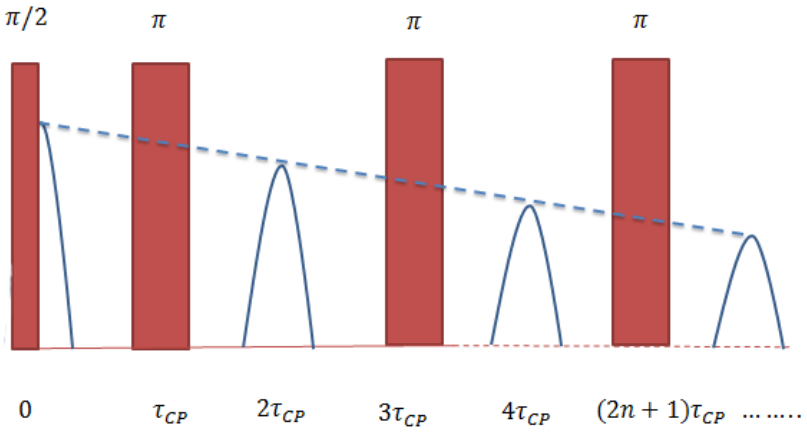

Figure 2.11: The idea of the CPMG sequence is sketched here. The red rectangle is the rf pulse the duration of which is either $\pi/2$ or π. The blue dome-like shape is the echo, while the blue-dotted line is the echo decay envelope profile.

2.8 Spin-Lattice relaxation

The spin-lattice relaxation time T_1 measures the recovery rate of the component of the nuclear magnetization along the direction of the external magnetic

field. T_1 yields information about the microscopic mechanisms responsible for energy exchange between nuclei and the elementary excitation of the lattice. It is customary to derive T_1 from quantum theory, namely one should consider the quantum states of the whole system and define the transition probabilities $W_{mm'}$ in terms of matrix elements of the interaction Hamiltonian, by using the Fermi Golden Rule [62].

$$W_{mm'} = \frac{2\pi}{\hbar} \sum_{ff'} P_f | < fm|\mathcal{H}'|f'm' > |^2 \delta(E_f + E_m - E_{f'} - E_{m'}) \tag{2.48}$$

where $|fm>$ and $|f'm'>$ are the initial and final state, respectively, $\mathcal{H}'$ is the perturbing hamiltonian and P_f is the probability of occupancy of the f state. This approach is usually applied for relaxation due to lattice vibrations.
From the former relation one can derive the following (more familiar) expression

$$W_{mm'} = \frac{1}{\hbar^2} \int e^{-i\omega_{mm'}\tau} < \mathcal{H}'_{mm'}(0)\mathcal{H}'_{mm'}(\tau) > d\tau \propto J(\omega) \tag{2.49}$$

where $J(\omega)$ is the spectral density of the fluctuating field.
Very often, when speaking of $1/T_1$ the terms "weak-collision" and "strong-collision" are encountered. The **weak-collision** limit is applicable when many fluctuating events are necessary to induce sizable relaxation. On the other hand, the **strong-collision** regime should be used when *each* fluctuation event it able to induce a sizable relaxation probability.
Some examples of mechanisms responsible for spin-lattice relaxation are the hyperfine interactions with the conduction electrons; lattice vibrations; quadrupolar interactions; vortex diffusion (in the superconducting state); quasi-particle scattering; fluctuating spin electrons/nuclei; and nuclear spin diffusion.

T_1 sequences

In order to measure T_1 one needs a special sequence. Any T_1 sequence is based on three steps: (1) the preparation of the initial magnetization, (2) the evolution of the magnetization and the (3) detection step. The last one can be a simple FID or a Echo (solid, Hahn, *CPMG*...), but what really distinguishes the different sequences is step (1). The more common methods are the inversion and saturation recovery sequences, usually employed when T_1 is shorter than 1 s. In the opposite limit, progressive saturation is helpful.
Hereafter the saturation recovery sequence is described, as it was the most frequently employed in the following experiments. The preparation step consists in

the application of a $\pi/2$ (in-resonance) pulse, which will tip the nuclear magnetization in the xy plane. After that, the system will be left to evolve under the effect of (nuclear) spin-lattice interactions, so that after τ, a component of $M_z(\tau)$ will be grown. To detected that signal, another $\pi/2$ pulse has to be applied, in order to turn the magnetization in the plane of the pick up coil. The name of the sequence comes from the fact that the first $\pi/2$ pulse will equalizes (i.e. saturate) the population of the Zeeman levels, leaving a zero magnetization along the z axis. The sequence is sketched in Fig. 2.12. In presence of large NMR spectra, the nuclear levels cannot be effectively saturated by a single $\pi/2$ pulse, rather a comb or train of pulses has to be applied [72]. This was not the case of the present study, since the pulse width allowed one to irradiated the whole line.

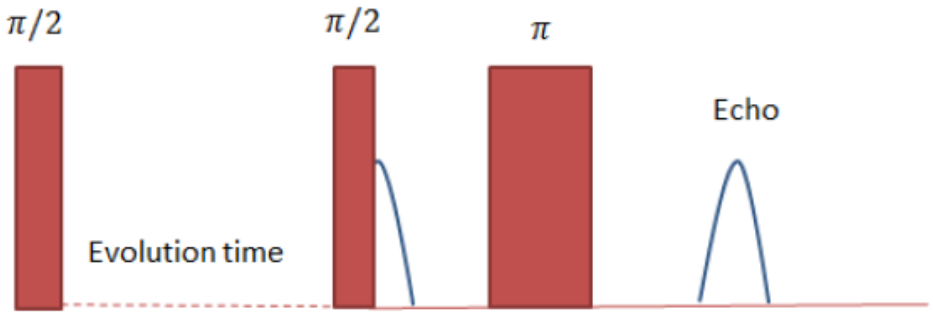

Figure 2.12: The figure represents the saturation recovery sequence. The pulses are the red rectangles, while the blue line is a sketch of the echo.

In any case, the recovery to equilibrium is determined by the transition probability, between the hyperfine levels associated with the time-dependent part of the hamiltonian. If one considers a system of N spins I, the evolution of the nuclear magnetization M_z is found once the $2I+1$ rate equations are solved:

$$\frac{dN_m}{dt} = \sum_{n \neq m} (N_n W_{nm} - N_m W_{mn}) \tag{2.50}$$

where N_n is the population of the $n-$th level. The solution of the former equation, for $I = 1/2$ can be worked out quite easily:

$$y(t) = \frac{M_z(\infty) - M_z(t)}{M_z(\infty)} = e^{-t/T_1} \tag{2.51}$$

where $1/T_1 = 2W_{\pm}$ and $M_z(\infty)$ is the equilibrium magnetization. In case of a

spin value I, the general solution is given by the sum:

$$y(t) = \sum_j c_j e^{-\alpha_j t/T_1} \tag{2.52}$$

where $1/T_1 = 2W_{\pm}^{I=1/2}$ and the coefficients depend on the spin value and on the relaxation mechanism (magnetic or quadrupolar).
A general definition of T_1, in presence of an oscillating transverse field $h_{x,y}(t)$ is commonly written as:

$$\frac{1}{T_1} = \frac{\gamma^2}{2} \int e^{i\omega_o t} < h_+(t)h_-(0) > dt \propto J(\omega_0) \tag{2.53}$$

where $h_\pm$ is related to the raising/lowering spin operator, and $J(\omega_0)$ is the Fourier Transform of the correlation function at the resonance frequency ω_0. This expression shows that $1/T_1$ is driven by the transverse components of the fluctuating field, and $1/T_1$ is proportional to the spectral density of the fluctuations, at the resonance frequency. So far the analytic form of the correlation function has not been specified, in order to keep the description as general as possible. In the next section, a famous case will be illustrated.

2.8.1 Bloembergen-Purcell-Pound (BPP) theory

In 1948, Bloembergen, Purcell, and Pound proposed a theory [73] to explain the relaxation rate taking place in a compound, affected by random motions, as in liquids. A simplified version of the discussion proposed in the original paper, will be reported without changing its physical meaning. This theory assumes that the autocorrelation function of the microscopic field fluctuations, causing the nuclear relaxation, is proportional to e^{-t/τ_c}. In fact, it can be shown that when the local field jumps randomly between two values $\pm h_0$, the correlation function of the transverse component of the local magnetic field will become $< h_+(t)h_-(0) >=< \Delta h_\perp^2 > e^{-t/\tau_c}$ [63]. The spin-lattice relaxation rate $1/T_1$ turns out:

$$\frac{1}{T_1} = \frac{\gamma^2}{2} < \Delta h_\perp^2 > \frac{2\tau_c}{1+\omega_0^2\tau_c^2} \tag{2.54}$$

In strong analogy to the case of the spin-spin relaxation, three significant dynamic regimes are found:

- In the fast motion regime, $\omega_0\tau_c \ll 1$, the denominator is ~ 1 and the relaxation rate becomes $\frac{1}{T_1} = \gamma^2 < \Delta h_\perp^2 > \tau_c$.

- In the slow motion regime, $\omega_0\tau_c \gg 1$, the unity at the denominator can be neglected, and then $\frac{1}{T_1} = \gamma^2 < \Delta h_\perp^2 > \frac{1}{\tau_c\omega_0^2}$.

- Remarkably, when $\omega_0\tau_c = 1$ the spin-lattice relaxation rate is extremely sensitive to the field fluctuations, and $1/T_1$ shows a peak sometimes referred as the BPP peak (Fig. 2.13).

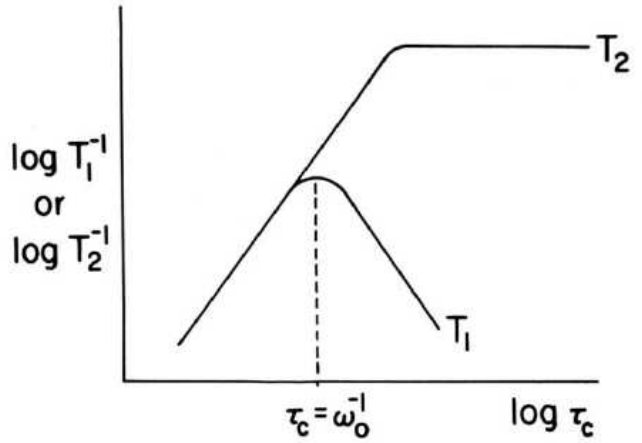

Figure 2.13: Dependence of the relaxation rates $1/T_1$ and $1/T_2$ on the correlation time τ_c. $1/T_2$ levels off in the rigid lattice limit, namely for long correlation times. The picture is adapted from Ref. [64].

The utility of the BPP theory will be clear after Chapters 4 and 5. The next sections will focus on the contributions that NMR can provide to study the superconducting state.

2.9 NMR as a probe of the superconducting state

NMR is an excellent technique to probe the superconducting properties of matter, because it is able to investigate the collective electronic behavior. Nonetheless, an NMR experiment in a superconductor can become tricky, in particular when the sample is a single crystal. In fact, the Meissner-Oschenfel effect [22] predicts that, below the critical temperature, any static magnetic field is shielded at the interior of the material, due to the screening supercurrents. The expulsion of the magnetic field takes place in the whole sample except from a small region of size

λ_L, which is related to the density of superconducting electrons n_s:[8]

$$\lambda_L^2 = \frac{mc^2}{4\pi n_s e^2} \tag{2.55}$$

and it's numerical value is typically in the range of $100 - 1000$ nm, depending on the material. In type-II superconductors, the sample volume accessible to NMR is wider, since the magnetic field will penetrate also in the interior of the superconductor, in form of tubes or filaments of section $\sim \pi\xi^2$, and then the field profile will decay, far from the core of the tube, as e^{-r/λ_L}, as recalled in Chapter 1.

The second technical problem is related to the penetration of the rf field. In fact, while above T_c the rf penetration is dominated by the skin effect [74]

$$\delta \sim \sqrt{\frac{\rho}{\omega\mu}} \tag{2.56}$$

where ρ is the resistivity and μ the magnetic permeability, below T_c the London and the Cambpell penetration depths are responsible for the signal intensity (see Appendix C). As a consequence of that, performing NMR in the superconducting state of a single crystal, on a non high sensitive nucleus may become challenging. One way to improve the signal-to-noise ratio is to increase the number of scans. However, when the spin-lattice relaxation rate is longer than 1 s, a single measurement may get extremely long. Regardless the long waiting times, NMR can still provide unique insights into the superconducting properties.

2.9.1 Yosida Theory

One of the consequences of the BCS microscopic theory of superconductivity is that the spin susceptibility of the conduction electrons will vanish exponentially, as the reduced temperature T/T_c, approaches zero [34, 75, 76]. This is true when the ground state of the superconductor is a singlet,[9] namely the Cooper pair is described by an eigenstate, whose total spin part has a zero eigenvalue. The spin state is reflected in the spin susceptibility, which can be measured by SQUID Magnetometry. Nonetheless SQUID is a macroscopic technique which actually measures an average over all the magnetic contributions, impurities included. Therefore, the paramagnetic contribution is totally screened by the Meissner ef-

[8] This results is found in the Ginzburg-Landau and in the London theory, as well.

[9] In addition to the singlet state superconductivity another state with $S = 1$, namely a triplet superconductivity, can be found.

fect. On the other hand, the first moment of the NMR line is sensitive to electronic spin susceptibility only. In fact, corresponding to each term of the susceptibility there exists a contribution to the Knight Shift. For example, for a transition metal material [77]:

$$K = K_P + K_{orb} = \alpha\chi_P + \beta\chi_{orb} \tag{2.57}$$

where the first term is the Pauli contribution, and the second term is the Van-Vleck orbital contribution, which is important to transition metal compounds with partly filled non-s bands. If one assumes, for simplicity, that the last contribution is temperature independent[10], what really determines the drop of the susceptibility down to T_c is the first term.[11] The spin susceptibility of a gas of non-interacting electron is usually written as [67, 74]:

$$\chi = -2\mu_B^2 \sum_k \frac{df}{dE_k} \tag{2.58}$$

where f is the Fermi-Dirac function of the excited states E_k, and μ_B the Bohr magneton. The sum can be replaced by an integral, by using the BCS energy density of states (see Fig. 2.14)

$$N_{BCS}(E) = N(0)\frac{|E|}{\sqrt{E^2 - \Delta^2}}, \tag{2.59}$$

in order to obtain

$$\chi = -4\mu_B^2 \int_\Delta^\infty N_{BCS}(E)(df/dE)dE. \tag{2.60}$$

The ratio between the susceptibility in the superconducting state, and in the normal state, directly allows one to extract the value of the superconducting gap Δ:

$$\frac{\chi_{SC}}{\chi_n}(T) = \int \frac{|E|}{\sqrt{E^2 - \Delta^2}}\frac{df}{dE}dE \tag{2.61}$$

Notice that the **q**-dependence of the gap, namely the presence of an anisotropy, is neglected, in this case.

[10] That is true for narrow-band materials.

[11] This is true for some elemental superconductors, and also some transition metal alloys.

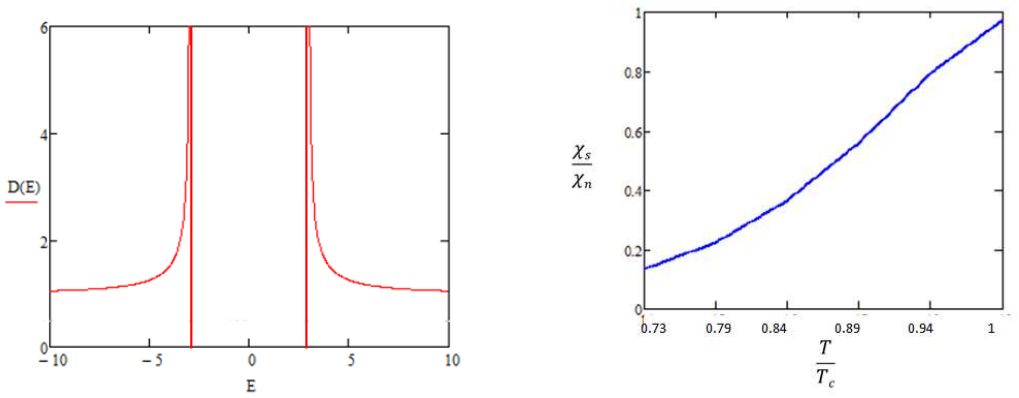

Figure 2.14: (left figure) A sketch of the density of state for an isotropic superconductor, according to BCS theory. The temperature dependence from the gap is not taken into account here. The opening of the gap results into a depletion of the energy levels. (right figure) A sketch of the susceptibility below T_c according to the Yosida theory, explained above.

2.9.2 Hebel-Slichter (HS) Peak

Another NMR quantity which is very sensitive to the opening of a spin gap in the DOS is the spin-lattice relaxation rate. The problem of accounting for the superconducting gap opening, in the spin-lattice relaxation time, was firstly undertaken by Hebel and Slichter [78, 79]. They were studying the NMR relaxation in superconducting Al, and assumed a nucleus-electron coupling of the form of the hyperfine contact interaction. Then, by using the perturbation theory, they evaluated the spin-lattice relaxation time, as the following:

$$\frac{1}{T_1} \sim \int_{\Delta}^{\infty} \frac{(EE' + \Delta^2)}{\sqrt{(E^2 - \Delta^2)(E'^2 - \Delta^2)}} f(E)(1 - f(E'))dE \tag{2.62}$$

where E is the energy of the initial state and $E' = E + \hbar\omega$ is the energy of the final state, while $\hbar\omega$ is the energy of the nuclear Zeeman level separation. When the difference in the energy between the initial and the final state is neglected, the former relation becomes:

$$\frac{1}{T_1} \sim \int_{\Delta}^{\infty} \frac{(E^2 + \Delta^2)}{(E^2 - \Delta^2)} \frac{1}{\cosh^2(E/2k_BT)} dE, \tag{2.63}$$

which turns into a logarithmic divergence at $E = \Delta$. Yet, in case of low temperature (namely $E \gg k_BT$) the expression is approximated to

$$\frac{1}{T_1} \sim Te^{-\Delta/k_BT}. \tag{2.64}$$

The exponential decay of $1/T_1$ was experimentally confirmed by Masuda and Redfield in superconducting Al, down to $T = 0.35$ K ($T_c = 1.2$ K) [80]. However, these authors found an inconsistency between the absolute value of their T_1, and the Hebel- Slichter's theory. In fact, a phenomenological broadening in the energy of the excited states, corresponding to a rectangle centered around $E' = E$ was initially taken into account in the HS theory. Afterwards Masuda and Redfield noticed that their data could be better fit by assuming that the gap itself exhibits a distribution of values. This suggested a natural explanation in term of the gap anisotropy. Indeed, in case of nodal gap, the spin lattice relaxation rate, in the limit of very low temperature may be a power law, $\frac{1}{T_1} \propto T^3$, while the Knight Shift is linear in T [81]. A detailed explanation of their results is beyond the aim of this work. A sketch view of a s-wave and d-wave gap is reported below.

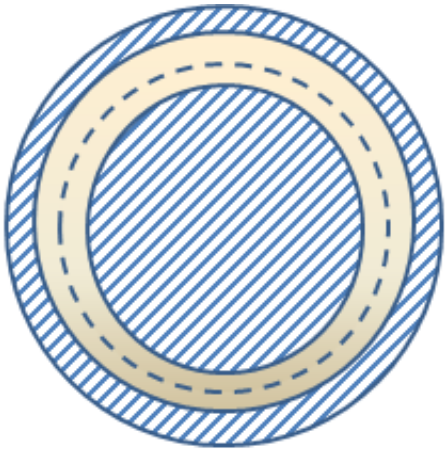

Figure 2.15: Sketch of a s-wave order parameter (pink zone). The Fermi surface is the inner blue dashed circle.

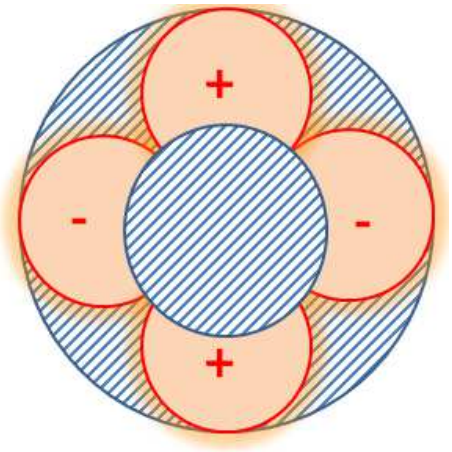

Figure 2.16: Sketch of a d-wave superconductor, where the value of the gap can assume both positive and negative values, but also zero values at certain wavevectors.

Before concluding this section it is stressed that in case of $s^{\pm}$-wave superconductor, no coherence peak is predicted. In fact the hole-band gap Δ_1 and
$s^{\pm}$-wave gap electron-band gap Δ_2 have opposite signs. As a consequence, the spin-lattice relaxation rate becomes:

$$\frac{1}{T_1} \sim \int_{\Delta}^{\infty} \frac{1}{\cosh^2(E/2k_BT)} dE. \tag{2.65}$$

Parker *et al.* [37] have shown that in $s^{\pm}$-wave superconductors the coherence peak

is not observed neither in the clean limit, as shown before, nor in case of impurity scattering, where a power-law behavior has been predicted.

2.9.3 Site-selective nuclear spin-lattice relaxation time

NMR is particularly useful in the mixed state of a type-II superconductor, as it provides two simultaneous information, namely the NMR spectrum reflects the magnetic field distribution, and T_1 probes electronic excitations. Given the one-to-one correspondence between the NMR line of a superconductor in the mixed phase, and the spatial arrangement of vortices, the NMR spectrum can access the vortex core or the intervortex position and, consequently, a frequency/site selective T_1 measurement can reveal the local density of states (LDOS). The great advantage of NMR with respect to other DOS-sensitive techniques, like STM, is that NMR probes bulk properties, free from surface problems [81]. The Bogoliubov-de Gennes theory for a $d_{x^2-y^2}$-wave pairing predicted that the temperature dependence of T_1^{-1} must be a power law, $\sim T^3$, for nuclear sites far from the center of the vortex core, as expected for a gap with a line (point) node. On the contrary, for positions close to the vortex core, a linear dependence on temperature is expected. The origin of this linear behavior is the presence of low-energy excitations, localized around the vortex core. These results are expected at low temperature, namely for $T/T_c < 0.1$.
The spacial distribution of T_1 has been extensively studied by several authors and has revealed a rich phenomenology, as Doppler shifted nodal quasiparticles states (Volovik effect), strong antiferromagnetic fluctuations in the vortex core and charge-induced vortex lattice instabilities [82–85]. Notice that the previous considerations do not take into account the dynamic of the vortex matter.

2.10 Conclusions

This Chapter sets the basis to understand the experimental results presented in the following chapters. The basic theory of NMR is reported, together with its capability of studying the spin correlations, and more generally the interactions among the nuclear spins themselves, and of the nuclei with the surrounding environment. NMR is also able to provide some insights into the superconducting state, as it can shed some light on the magnitude and the symmetry of the superconducting order parameter. Indeed the combination of spin-lattice relaxation rate, and Knight Shift is remarkably useful to probe the density of states and, in

particular cases, also the local DOS.
So far the vortex lattice dynamic has not been mentioned, as it will be the main subject of Chapters 5, 6 and 7. Moreover, Chapter 4 will present how NMR allows the study of spin fluctuations, emerging in the normal state of the $Ba(Fe_{1-x}Rh_x)_2As_2$ compounds.

Part II
Experimental results

Chapter 3

Observation of unconventional superconducting fluctuations by SQUID magnetometry

This Chapter addresses the fluctuating phenomena occurring above the transition temperature, due to the pre-formation of the Cooper pairs. The static spin susceptibility and macroscopic magnetization, as measured by Superconducting Quantum Interference Device (SQUID) can allow one to study this phenomenon, in single crystals of the $Ba(Fe_{1-x}Rh_x)_2As_2$ family, over different doping. In fact, a careful study of the static magnetization, shows that the temperature region just above T_c can host rather exotic effects.
Precursor diamagnetism was experimentally found in all the investigated specimens, with a quite intriguing phenomenology: while at high fields the precursor diamagnetism can be described in the framework of the Ginzburg-Landau theory (GL), at smaller fields the last theory cannot be invoked. In fact, in addition to the GL fluctuations, hereafter called "conventional", there are unconventional type of fluctuations, which are still matter of debate within the state-of-the-art research. The latter model has been developed nearly 10 years ago, and it has been successfully used to interpret the results found on the high-T_c cuprates [86]. According to this approach, the amplitude of the order parameter is supposed to remain fixed, while the phase is allowed to change from one region to the other of the specimen. These fluctuating regions are mesoscopic islands, the existence of which has been experimentally found by means of microscopic techniques.
In the following section, a quick overview of the Ginzburg-Landau (GL) theory, together with its main experimental predictions, is given. The pre-formation of

the Cooper pairs is explained in the limit of Gaussian approximation, and for long-wavelength limit of the order parameter.

3.1 The Ginzburg-Landau theory

The Ginzburg-Landau (GL) theory was formulated in the 50s to overcome some limits of the BCS theory, and regardless its phenomenological foundation, that made it initially the target of many criticisms, it allowed to predict several experimental evidences. Among the best achievements of the GL theory, the prediction of the existence of type-II superconductors is the most remarkable one. The theory comes from the intuition to extend the description of the second-order phase transitions to the superconducting one, in such a way that the order parameter turns out to be a complex wavefunction $\Psi(\mathbf{r})$,[1] describing the superconducting electrons

$$\psi(\mathbf{r}) = |\psi(\mathbf{r})|e^{i\theta(\mathbf{r})}. \tag{3.1}$$

Within the GL theory, the square modulus of the wavefunction, $|\psi(\mathbf{r})|^2$, is equal to $n_s(\mathbf{r})$, the superconducting electron density, at position $\mathbf{r}$. Moreover, the phase θ is related to the supercurrent $\mathbf{J}$ that flows through the material, below T_c, through:

$$\mathbf{J} = \frac{ie\hbar}{m}(\psi^*\nabla\psi - \psi\nabla\psi^*) = \frac{-2e\hbar}{m}|\Psi|^2\nabla\theta. \tag{3.2}$$

For temperature $T \to T_c$, the free energy density functional can be written in form of a power expansion of the order [22]

$$F_s(T,\psi) = F_n(T) + \alpha(T)\,|\psi|^2 + \frac{1}{2}\beta(T)\,|\psi|^4 + \frac{1}{2m^*}\left|\left(\mathbf{p} - e^*\frac{\mathbf{A}}{c}\right)\psi(\mathbf{r})\right|^2 \tag{3.3}$$

where and $m^* = 2m$ and $e^* = 2e$ are the effective mass and the charge of the Cooper pairs, and the indices n and s denote the normal and superconducting states, respectively.[2] The GL theory introduces two phenomenological parameters, α and β, and also assumes that the order parameter may change with the position. In absence of magnetic fields, namely $\mathbf{A} = 0$ and of a smooth order parameter, $\nabla\psi = 0$, the difference between the superconducting and normal free energy takes the form:

[1] This is not a trivial statement, since in other phase transitions, as in ferromagnets or paramagnets, the order parameter is a real quantity.

[2] When the GL theory was proposed (1952), the BCS theory was not yet developed, so there was not reason to speak of Cooper pairs.

$$F_s - F_n = \alpha(T)\,|\psi|^2 + \frac{1}{2}\beta(T)\,|\psi|^4 \tag{3.4}$$

Such a difference must be negative, in the superconducting state, and positive in the normal one. This condition is verified if

- $\alpha(T) > 0$, $\beta(T) > 0$ for $T > T_c$,
- $\alpha(T) < 0$, $\beta(T) > 0$ for $T < T_c$.

In the latter case $F_s - F_n$ will display a minimum, at a certain $|\psi|^2 = n_s > 0$ (see Fig 3.1). Within the Landau theory, one can assume that:

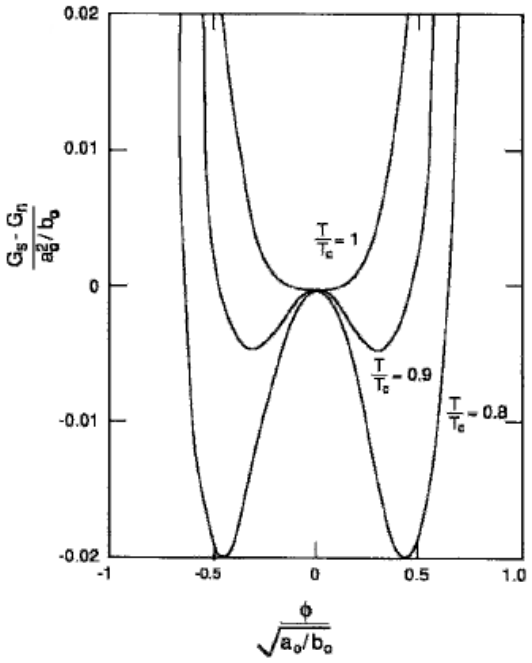

Figure 3.1: Dependence of the free energy difference, as a function of the normalized order parameter (see text above for explanation). The picture is adapted from Ref. [87].

$$\alpha(T) = \alpha_0(T - T_c) \text{ where } \alpha_0 > 0 \text{ and } \beta(T) = \beta_0 > 0.$$

By following the variational approach, the Copper pair concentration becomes:

$$\beta|\psi|^2\psi = -\alpha(T)\psi(\mathbf{r}) \Rightarrow |\psi|^2 = -\frac{\alpha(T)}{\beta} = |\psi(r \to \infty)|^2\,. \tag{3.5}$$

By substituting the former relation into Eq. (3.4), the difference in the free energy becomes $F_s - F_n = -\frac{\alpha^2(T)}{2\beta}$, and remembering that the superconducting

condensation energy is equal to $F_s - F_n = -\frac{H_c^2(T)}{8\pi}$, it is straightforward to get the temperature dependence of the critical field

$$H_c \propto (T_c - T), \text{ when } T \to T_c. \tag{3.6}$$

This expression can be particularly useful when the temperature dependence of some peculiar superconducting properties, such as the London penetration depth, are needed. Indeed, this turns out to be:

$$\lambda = \sqrt{\frac{m^* c^2 \beta_0}{4\pi e^{*2} |\alpha_0|}} \frac{1}{\sqrt{T_c - T}}, \text{ in the limit } T \to T_c. \tag{3.7}$$

The GL equations

In case of a non-null magnetic field, the variational condition will become:

$$\alpha\psi + \beta|\psi|^2\psi + \frac{1}{2m^*}(i\hbar\nabla + \frac{e^*}{c}\mathbf{A})^2\psi = 0, \tag{3.8}$$

where the moment operator $\mathbf{p}$ has been written in its explicit form. In the Landau Gauge, namely $\nabla \cdot \mathbf{A} = 0$, the former equation turns out [22]

$$-\alpha\psi - \beta|\psi|^2\psi + \frac{1}{2m^*}(\hbar^2\nabla^2\psi - e^{*2}\mathbf{A}^2\psi - 2i\hbar e^*\mathbf{A}\cdot\nabla\psi) = 0 \tag{3.9}$$

that is called the **first Ginzburg-Laundau equation**.
By recalling that $\mathbf{B} = \nabla \times \mathbf{A}$ and deriving with respect to $\mathbf{A}$:

$$\frac{c\nabla \times (\nabla \times \mathbf{A})}{4\pi} + \frac{ie^*\hbar}{2m^*}(\psi^*\nabla\psi - \psi\nabla\psi^*) + \frac{e^{*2}}{m^*c^2}\nabla|\psi|^2 = 0 \tag{3.10}$$

the **second Ginzburg-Landau equation** is obtained. The latter can be refined once the Ampére-Maxwell equation, $\nabla \times \mathbf{B} = \frac{4\pi\mathbf{J}}{c}$, is employed:

$$\mathbf{J} = -\frac{i\hbar e^*}{2m^*}(\psi^*\nabla\psi - \psi\nabla\psi^*) - \frac{e^{*2}}{m^*c^2}\nabla|\psi|^2. \tag{3.11}$$

Finally the GL equations constitute a set of two coupled differential equations, to be solved in the order parameter and the vector potential, in order to get complete information about the superconductor.

As stated before, a remarkable result of the GL theory is the prediction of the existence of two types of superconductors. A simple case shall be illustrated hereafter [22].
In case of a superconductor with a mono-dimensional spacial dependence, and

such that $\psi(x) \neq 0$, for $x > 0$, in absence of a magnetic field, the GL equation turns out to be

$$-\frac{\hbar^2}{2m^*}\frac{d^2\psi(x)}{dx^2} + \beta|\psi(x)|^2\psi(x) = -\alpha(T)\psi(x) \tag{3.12}$$

The former equation can be divided by $|\alpha(T)|$, in order to get the following

$$-\frac{\hbar^2}{2m^*}\frac{1}{|\alpha(T)|}\frac{d^2\psi}{dx^2} + \frac{|\psi|^2}{|\psi_\infty|^2}\psi(x) = \psi(x) \tag{3.13}$$

which has the solution:

$$\psi(x) = \psi(x \to \infty)\left[1 - e^{-\frac{x}{\xi}}\right] \tag{3.14}$$

where $\xi^2 = \frac{\hbar^2}{2m^*|\alpha(T)|}$ is the coherence length, which measures the spacial extension over which the Cooper pairs are correlated. Its temperature dependence, when $T \to T_c^+$, is given by

$$\xi \propto \frac{1}{\sqrt{T_c - T}} \tag{3.15}$$

Moreover, the ratio of λ and ξ, gives the so-called Ginzurg-Landau parameter

$$\kappa = \frac{\lambda(T)}{\xi(T)} = \frac{1}{\sqrt{2\pi}}\frac{m^*c}{e^*\hbar}\sqrt{\beta_0}, \tag{3.16}$$

Two types of superconductors

It can be shown that when $\kappa > \frac{1}{\sqrt{2}}$ the superconductor allows some magnetic flux to enter, partially violating the Meissner-Ochsenfeld effect, while for $\kappa < \frac{1}{\sqrt{2}}$ the superconductor expels all the flux inside it. The magnetization versus the magnetic field is sketched in Fig. 3.2. A. A. Abrikosov was the first to address the problem of the GL equations, in $\kappa > \frac{1}{\sqrt{2}}$ limit. He found that some magnetic flux can enter the superconductor, in form of filaments of fluxons, surrounded by supercurrents forming vortices [56], as explained in Chapter 1.

3.1.1 Anisotropic superconductors: the Lawrence-Doniach model

Lawrence and Doniach [22] in 1971 proposed a model to describe the properties of a layered superconductor, starting from the assumption that such material could be viewed as a stacked array of two-dimensional superconducting layers, coupled together by the Josephson tunneling between adjacent layers (Fig. 3.3). In any layer, the order parameter is a two-dimensional (2D) function $\psi_n(x, y)$, at which

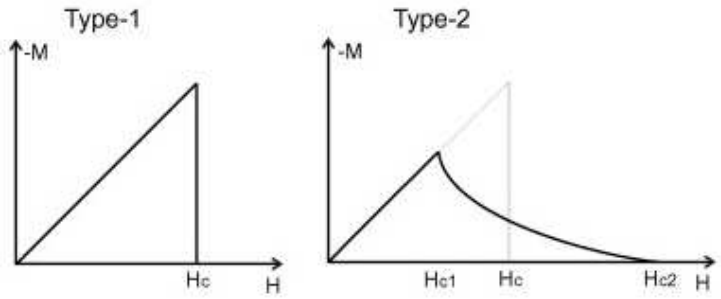

Figure 3.2: Sketch of the macroscopic magnetization versus the external field, for type-I and type-II superconductors. Type-I (left panel) exhibits perfect diamagnetism below the transition temperature, and it displays only one critical magnetic field H_c. Type-II (right panel) totally expels the magnetic flux below the lower critical field H_{c1}, while it partially expels it between H_{c1} and the upper critical field H_{c2}; all superconductors except elements are Type-II.

the authors associated, by omitting the vector potential, the following free energy functional:

$$F = \sum_n \int d\Sigma \left\{ \alpha |\psi_n|^2 + \frac{\beta}{2}|\psi_n|^4 + \frac{\hbar^2}{2m_{ab}} \left(|\frac{\partial \psi_n}{\partial x}|^2 + |\frac{\partial \psi_n}{\partial y}|^2 \right) + \frac{\hbar^2}{2m_c s^2}|\psi_n - \psi_{n-1}|^2 \right\}, \tag{3.17}$$

where the sum runs over the layers and the integral is made over the area of each layer. The reader may notice that here the electron mass is taken as a tensor of components:

$$\begin{pmatrix} m_{ab} & 0 & 0 \\ 0 & m_{ab} & 0 \\ 0 & 0 & m_c \end{pmatrix}$$

where the anisotropy in the ab plane is neglected. Also the z derivative has been replaced by its discrete version. Moreover, if the modulus of the order parameter is fixed across the planes, the last term of the equation can be written in a more familiar form, reminiscent of the Josephson coupling:

$$\frac{\hbar^2}{m_c s^2}|\psi_n|^2[1 - \cos(\theta_n - \theta_{n-1})]. \tag{3.18}$$

When the vector potential is restored, the variational approach is given by the derivative of the free energy density functional, with respect to ψ^*

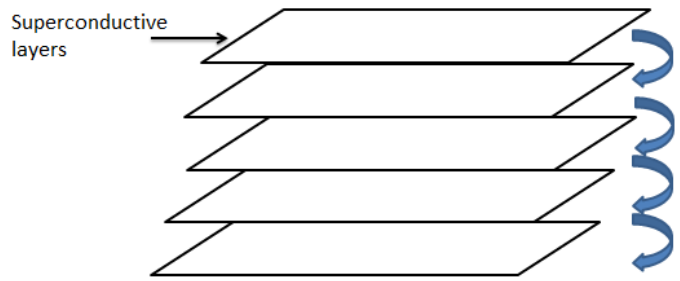

Figure 3.3: A sketch of a layered superconductor, where the blue arrows represent the inter-layer Josephson coupling.

$$\begin{aligned} 0 &= \alpha\psi_n + \beta|\psi_n|^2\psi_n - \frac{\hbar^2}{2m_{ab}}\left(\nabla - i\frac{e^*}{\hbar c}\mathbf{A}\right)^2\psi_n \\ &- \frac{\hbar^2}{2m_c s^2}(\psi_{n+1}e^{-2ieA_z s/\hbar c} - 2\psi_n - \psi_{n-1}e^{+2ieA_z s/\hbar c}) \end{aligned} \tag{3.19}$$

The GL theory can be extended to the anisotropic limit, for long wavelength fluctuations ($\mathbf{k}$=0), in which the variation along z is smooth enough so that $\frac{\psi_n - \psi_{n-1}}{s}$ can be replaced by $\frac{\partial\psi}{\partial z}$. The last equation can then be written as:

$$\alpha\psi + \beta|\psi|^2\psi - \frac{\hbar^2}{2}\left(\nabla - i\frac{e^*}{\hbar c}\mathbf{A}\right)\cdot\left(\frac{1}{\tilde{m}}\right)\cdot\left(\nabla - i\frac{e^*}{\hbar c}\mathbf{A}\right)\psi = 0 \tag{3.20}$$

The mass anitropy produces an anisotropic coherence length:

$$\xi_i^2(T) = \frac{\hbar^2}{2m_i|\alpha(T)|}, \tag{3.21}$$

and accordingly an anisotropic upper critical field (see Chapter 1). The degree of anisotropy is then quantified by the ratio:

$$\gamma = \left(\frac{m_c}{m_{ab}}\right)^{1/2} = \frac{\lambda_c}{\lambda_{ab}} = \frac{\xi_{ab}}{\xi_c}, \tag{3.22}$$

where λ_i describes the screening due to supercurrents flowing along the i-th axis.

3.1.2 The GL Superconducting Fluctuations

According to the Ginzburg-Landau (GL) theory, the complex order parameter $\psi(\mathbf{r}) = |\psi|e^{i\theta}$ has zero average value $< \psi(\mathbf{r}) >$ above the critical temperature T_c, while at thermal equilibrium the mean square value is $< |\psi(\mathbf{r})|^2 > \neq 0$. As a consequence, at $T > T_c$ there will be some islands, of the order of the correlation length ξ, where highly unstable Cooper pairs are formed. The lifetime of such pre-formed pairs is proportional to $\frac{\hbar}{k_B(T-T_c)}$ [22], as expected from the uncertainty principle.[3] The more direct way to derive the contribution of thermal fluctuations to the static magnetization is to start from the following

$$F = -k_B T \ln \mathcal{Z}, \tag{3.23}$$

where $\mathcal{Z}$ is the partition function. Then, to derive the fluctuation magnetization, namely the diamagnetic response due to the preformed Cooper pairs $M_{fl}(H,T)$, the derivative of F has to be taken

$$M_{fl}(H,T) = -\frac{1}{V}\frac{\partial F}{\partial H}. \tag{3.24}$$

In the Gaussian limit (i.e. neglecting the 4-th power of $|\psi_k|$), and for $\mathbf{A} = 0$ and $\mathbf{J} = 0$, the order parameter of the transition can be expanded in the Fourier sum:

$$\psi = \sum_k \psi_k e^{i\mathbf{k}\cdot\mathbf{r}}, \tag{3.25}$$

and accordingly the free energy becomes:

$$F_n = F_s + \sum_k \left(\alpha + \frac{\hbar^2}{2m^*}k^2\right)|\psi_k|^2 \tag{3.26}$$

Since the fluctuating variable is the *amplitude* of the order parameter, the statistic average of the square modulus has to be evaluated accordingly [22]

$$< |\psi_k|^2 >= \frac{\int |\psi_k|^2 e^{-F/k_B T} d|\psi_k|^2}{\int d|\psi_k|^2 e^{-F/k_B T}} = \frac{k_B T}{\alpha(1+\xi^2 k^2)} \tag{3.27}$$

The latter equation enters into the expression for the correlation function of the amplitude of the order parameter:

The correlation function

[3] In the estimation of the Cooper pairs lifetime, the GL energy has been approximated at the first order.

$$g(\mathbf{r}-\mathbf{r}') =< \psi(\mathbf{r})\psi(\mathbf{r}') >= \sum_k < |\psi_k|^2 > e^{i\mathbf{k}\cdot(\mathbf{r}-\mathbf{r}')}. \tag{3.28}$$

By calling $\mathbf{R} = \mathbf{r} - \mathbf{r}'$ and substituting equation (3.27) into the last one, and finally by transforming the sum into an integral, the correlation function turns out to be:

$$g(\mathbf{R}) = \frac{m^* k_B T}{2\pi\hbar^2}\frac{1}{R}e^{-\mathbf{R}/\xi}, \tag{3.29}$$

which shows the spacial extension of the fluctuations in $|\psi_k|$. In other words, the amplitude of the order parameter will have a fixed value within a correlation length $\sim \xi$. By approaching the critical temperature from above, the mesoscopic island will grow until the bulk superconductivity is reached. It can be argued that the transition to the bulk superconducting state is nothing but a percolation of the superconducting order parameter in the whole volume of the material (Fig. 3.4).

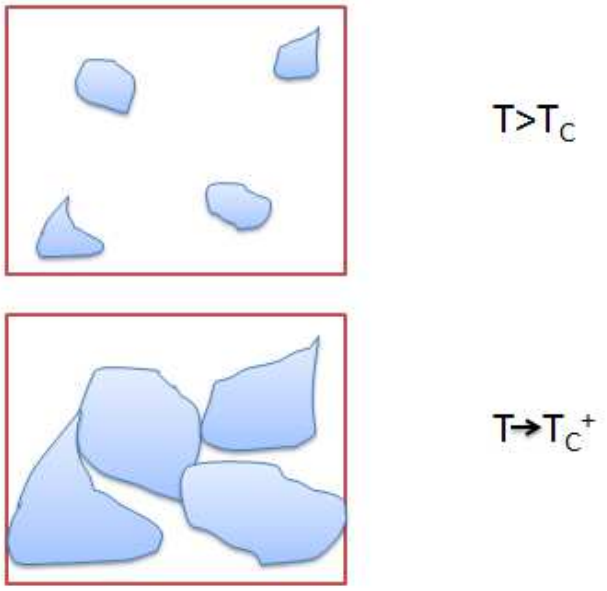

Figure 3.4: Sketch of the precursor islands (blue regions), through which the superconducting order parameter can percolate and induce the transition to the bulk superconducting state.

3.1.3 Scaling laws

Although the theory of the classical superconducting fluctuations can be exactly solved in the zero-dimensional case, where an analytic form of the spin suscepti-

bility can be given, in real samples it turns to be hardly suitable. Nonetheless, the general idea can be extended by treating a macroscopic sample as if it was made of small "droplets", of size $\mathcal{L}$. In such a case, Schmid [88] found for a bulk metallic sample, in the evanescent field limit $H \to 0$, a susceptibility divergence at T_c according to:

$$\chi \sim -10^{-7} \left(\frac{T_c}{T - T_c} \right)^{1/2}. \tag{3.30}$$

More generally, for evanescent fields, one finds a diamagnetic magnetization linear with the field H, and accordingly a susceptibility $\chi_{dia} \propto -\epsilon^{D/2-2}$, where $\epsilon = (T - T_c)/T_c$ is the reduced temperature, and D is the dimensionality.
In a more realistic case, when strong magnetic fields are applied, the previous approach does not apply anymore. The first theoretical effort to interpret the experimental results in the limit of finite fields was due to Prange, and it was based on the GL theory [89]. Prange predicted that the diamagnetic (or fluctuative) response could be written as:

$$\frac{M'}{\sqrt{H}T} = f_P(x), \tag{3.31}$$

where $f_P(x)$ is a function of $x = \frac{T-T_c}{2H} \frac{dH_{c2}}{dT}$ sketched in Fig. 3.5.

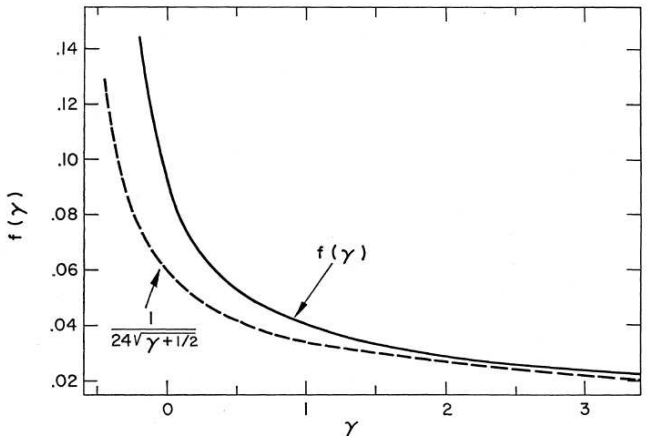

Figure 3.5: Sketch of the f_p originally calculated by Prange in reference [89], from which the sketch is taken.

Prange's law

In such a case, Prange [22, 90] predicted in 1970 that the fluctuating magnetization M_{fl} diverges as $(T - T_c)^{-1/2}$ and also that at $T_c(H = 0)$ there is a proportionality between M_{fl} and the field $H^{1/2}$. Later on these predictions were experimentally proven on In and Pb samples by Gollub *et al.* [91], and it was

found that the magnetic field has the effect to suppress the fluctuations, even more strongly than in the GL framework. In fact, on increasing the magnetic field above a characteristic value, the diamagnetic magnetization was found to decrease on increasing the field.
These "conventional" fluctuations have been experimentally found in metallic nanoparticles [92], as well as in optimally doped high-T_c cuprates: optimally doped $YBa_2Cu_3O_7$, for example, has been an excellent material to test the GL theory [93, 94]. The latter compounds are well described in a 3D XY universality class. In fact, the classical form of the GL free energy functional, has been effectively substituted by the Lawrence-Doniach (LD) $F[\psi]$ functional [95]. The high-T_c superconductors were indeed a fertile material for the study of the conventional superconducting fluctuations, because of their small coherence length ξ, reduced carrier density, strong anisotropy, and high transition temperature. Note that the Gaussian or, as called hereafter conventional fluctuations, as opposed to the unconventional ones, where originally well argumented by Aslamazov, Larkin, Maki and coworkers [96, 97].
Another hallmark of superconducting fluctuations is the presence of an upturn field, H_{up}. Since the size of fluctuating pairs $\xi(T)$ grows when the temperature approaches T_c, $|M_{fl}|$ is expected to show a progressive increase, on cooling. On the other hand, very high magnetic fields suppress the superconducting fluctuations. The combination of the two effects induces an upturn in the isothermal magnetization. The value of the upturn field H_{up} for layered superconductors, in the framework of the GL phenomenology, is approximately given by Φ_0/ξ^2. As a consequence of that, in high-T_c superconductors, the upturn can be detected only at very high fields, even for temperatures close enough to T_c.

The upturn field

3.2 Non GL fluctuations in the high-T_c superconductors

Contrary to the optimally doped cuprates, underdoped and overdoped materials show dramatic deviations from the conventional GL behavior [86]. Indeed, in correspondence with the upturn in $|M_{fl}|$ [86], the susceptibility χ_{dia} for $T \to T_c^+$ is anomalously large, and furthermore magnetic history dependence is detected. Sewer and Beck [98] tried to justify these anomalous value of χ_{dia} by taking into account the *phase fluctuations* of the order parameter, in the framework of a layered XY model which describes a liquid of vortices, that can be either

thermally excited or induced by the magnetic field. Such model was initially formulated to interpret the former experimental results in $YBa_2Cu_3O_{6+x}$ [99]. Afterwards, by following the inspiring idea of Sewer and Beck [98] and by taking into account terms in the free energy functional initially neglected, the model was extended [86, 100] and the upturn in $|M_{fl}|$ at low field was justified from a phenomenological point of view. The model assumes the occurrence, above T_c, of mesoscopic islands where $|\psi| \neq 0$, but with strong phase fluctuations which inhibit the long-range coherence, while ψ is fixed. Some authors claim that Nernst effect suggests that vortex excitation survive above T_c [101–103]. However such issue is still under discussion [104]. Moreover Scanning SQUID microscopy [105] in $La_{2-x}Sr_xCuO_4$ thin films has shown phase fluctuations above T_c, leading to local superconductivity.

As a result of the above discussion, one should finally remark that after the introduction of the phenomenological GL theory, many steps have been moved towards the comprehension of the superconducting fluctuations. There is plenty of experimental evidence of the occurrence of precursor diamagnetism in BCS superconductors [100] as well as high-T_c cuprates [86, 99, 102, 106]. Some of the techniques employed so far are Nuclear Magnetic Resonance (NMR) spectroscopy, Superconducting Quantum Interference Device (SQUID) magnetometry, [99, 107–109] torque magnetometry, [102, 103, 110] resistivity, [111] scanning SQUID microscopy, [105] Nernst effect [103] and infrared spectroscopy [112]. Moreover, very recent papers show a renewed interest in the fluctuating diamagnetism. Sarkar *et al.* [113] have shown that Banerjee and coauthor's phenomenological theory [114] has proven successful in describing the fluctuation diamagnetism of high-T_c superconductors, as a function of doping, temperature and field.

After these intense experimental investigations on the cuprates, it is conceivable to drive the attention towards the more recent iron-based superconductors. Pallecchi *et al.* [24] have shown that the 122 family seems to be the most promising for applications, as they are characterized by reduced thermal fluctuations, owing to a Ginzburg number of $\sim 1.5 \times 10^{-5}$. This means that a study of thermal fluctuations in 122 pnictides is quite challenging. The following paragraphs deal with high resolution magnetization of the $Ba(Fe_{1-x}Rh_x)_2As_2$ compounds, reporting the first study of precursor diamagnetism, systematically carried out in an iron-based superconductor, over a broad doping range. Before presenting the experimental results, some considerations on the phase fluctuation model are reported.

3.2.1 The Phase Fluctuation model

The Phase Fluctuation model is based on a 3D anisotropic layered XY mode functional $F[\theta]$, [95] where the only independent variable is the phase of the order parameter θ (London Approximation):

$$F[\theta] = \frac{1}{s}\sum_{l}\int\left\{J_{\parallel}\left(\nabla_{\parallel}\theta - \frac{2ie}{c\hbar}\mathbf{A}_{\parallel}\right)^{2} + J_{\perp}\left(1 - cos(\theta_{l+1} - \theta_{l})\right)\right\}d^{2}r \qquad (3.32)$$

being s the FeAs inter-layer distance, l the layer index, $J_{\parallel}$ and $J_{\perp}$ the in-plane and inter-plane couplings, and $\mathbf{A}$ the vector potential. In fact, in the theoretical framework introduced by Sewer and Beck, the amplitude of the order parameter $|\Psi|$ is supposed to be frozen, while the phase θ fluctuates among mesoscopic islands, preventing the formation of long-range superconductivity.
Sewer and Beck claimed that it is possible to model the critical behavior of 3D XY systems in terms of vortex excitations which, for topological reasons, have to form closed loops or continuous lines crossing the whole system. The loops are the 3D extension of the planar vortex-antivortex structure, whereas the lines rise from the presence of an external magnetic flux penetrating into the sample, likewise the Abrikosov vortices (Fig. 3.6). In the implementation due to Romanó

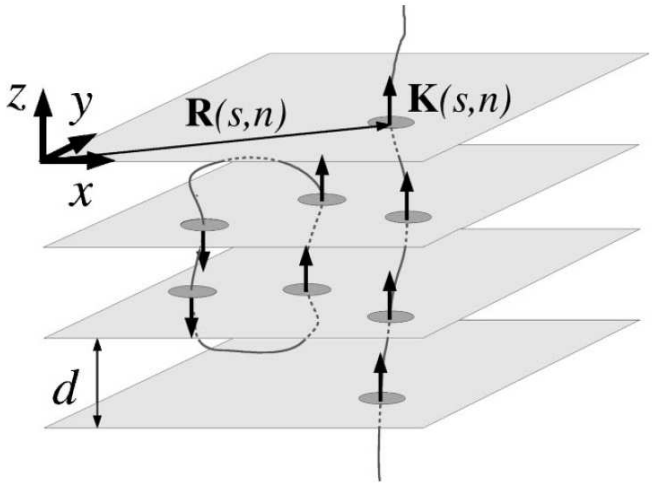

Figure 3.6: Sketch of a 3D thermally excited vortex loop (left) and of a field-induced vortex line (right), in a layered superconductor. The field induced vortices are equivalent to the traditional Abrikosov vortices, where the "pancake" pile up to form a single line of magnetic flux. Notice that d is the interlayer distance, while in the text it has been named s. The figure is adapted from Ref. [98].

et al. [100], the phase coherence occurs into "droplets" of size $\mathcal{L}$. Hence the

correlation function of the order parameter, namely the phase θ, is

$$g(\mathbf{r}) =< e^{i\theta(\mathbf{r})}e^{i\theta(\mathbf{0})} >\sim e^{-\mathbf{r}/\mathcal{L}}. \tag{3.33}$$

In such a scenario, the fluctuating susceptibility is evaluated by starting from the following relation:

$$\chi = \left\langle \frac{\partial^2 F_{LD}}{\partial H^2} \right\rangle^2 - \frac{1}{k_B T} \left\langle \left(\frac{\partial F_{LD}}{\partial H} \right)^2 \right\rangle + \frac{1}{k_B T} \left\langle \frac{\partial F_{LD}}{\partial H} \right\rangle^2 \tag{3.34}$$

where $<,>$ stands for the thermal average. In the gauge $A = -yH$, the susceptibility is given by:

$$\chi = \lim_{q\to 0} \frac{K(q)}{q^2}, \tag{3.35}$$

where $K(q)$ is made by the sum of three terms:

$$K(q) = \frac{J_\parallel}{d} \left(\frac{2\pi}{\Phi_0} \right)^2 \left[\frac{J_\parallel}{k_B T} (P(q) - Q(q)) - 1 \right]. \tag{3.36}$$

In the last equation $P(q)$ involves the current-current correlation function, $Q(q)$ comes from the third term of equation (3.34), and -1 is the diamagnetic response. By following Ref. [86] the response function turns out to be:

$$\begin{aligned} K(q) &= \frac{J_\parallel}{d} \left(\frac{2\pi}{\Phi_0} \right)^2 \left[\frac{2\pi J_\parallel}{q_v^2} (1+2n) - \delta \left(\frac{H}{H^*} \right)^2 - 1 \right] \\ &- \left[\frac{k_B T}{s\Phi_0^2} \frac{1}{1+2n} \frac{[1+\delta(H/H^*)^2]^2}{n_v} + \frac{s^2\gamma^2(1+n)}{1+2n} [1+\delta(H/H^*)^2] \right] q^2 \\ &+ \frac{47\mathcal{L}^2}{540} \frac{J_\parallel}{s} \left(\frac{2\pi}{\Phi_0} \right)^2 \delta (H/H^*)^2 q^2 \end{aligned} \tag{3.37}$$

where δ is equal to $\pi^2(J_\parallel/k_B T)$ and $H^* = \Phi_0/\mathcal{L}^2$ is a magnetic field that takes into account the dimension of the superconducting droplets. Beck and Sewer predicted the formation of thermally activated vortex loops n_{th}, and field induced vortex lines n_H, such that $n_v = n_{th} + n_H$. For small fields, the temperature dependence of the susceptibility is controlled by the vortex loops density [115]

Thermally activated and field induced vortices

$$n_{th} = n_0 e^{E_0/k_B T(1+\delta(h)^2)}, \tag{3.38}$$

where $h = H/H^*$ and n_0 is the density of thermal activated loops, in the limit of infinite temperatures. In the opposite limit, the field induced vortices are dominant, as their density n_H is linear in the field:

$$n_H = \frac{H}{\Phi_0} = \frac{H}{H^* \mathcal{L}^2} \tag{3.39}$$

Finally, n is the number of layers over which the vortices are correlated, which is a free parameter of the fit.

Owing to the presence of 2D weakly interacting vortices, the 2D XY model can be mapped into the 2D Coulomb gas. In such a case, each vortex can be associated to a charge $q_v = \sqrt{2\pi J_\parallel}$, and to an activation energy $E_0 = q_v^2 \ln(r/\xi_{ab})$. Moreover, a couple of vortex and antivortex has an energy:

2D Coulomb gas

$$E_{v-a} = q_i q_j \log |\frac{\mathbf{r_i} - \mathbf{r_j}}{a}|, \tag{3.40}$$

being a the intervortex spacing, $\mathbf{r_i}$ the $i-th$ vortex position, and q_i the vortex "charge". It is noticed, incidentally, that q takes the meaning of vorticity, within the 2D Coulomb gas

$$\oint d\theta(\mathbf{r}) = 2\pi q. \tag{3.41}$$

Nonetheless, in a 3D XY system, to avoid divergences of $K(q)/q$ in the long wavelength limit, it is necessary to renormalize both the former quantities:

$$q_v(H) = \sqrt{\frac{q_v^2(1+2n)}{1+\delta(h)^2}} \text{ and } E(H) = \frac{E_0}{1+\delta(h)^2} \tag{3.42}$$

Finally the diamagnetic susceptibility can be obtained:

$$\chi = -\frac{k_B T}{s\Phi_0^2}\frac{1}{1+2n}\frac{(1+\delta(h)^2)^2}{n_v} - \frac{s^2\gamma^2(1+n)}{1+2n}[1+\delta(h)^2] + \frac{47\mathcal{L}^2}{540}\frac{J_\parallel}{s}\left(\frac{2\pi}{\Psi_0}\right)^2 \delta(h)^2.$$

The main difference between the last model and the one presented in Ref. [98], consists in the presence of the factor $h = H/H^*$, and of a third positive term, which is responsible for the sign inversion of the susceptibility, corresponding to an upturn in the magnetization curves.

3.2.2 The phase-disordering scenario

The phase-disordering scenario is a three-dimensional version of the well-known two-dimensional Kosterlitz-Thouless (KT) transition. The latter describes a phase transition in the 2D XY model which occurs from bound vortex-antivortex pairs (Fig. 3.7), at low temperatures, to unpaired vortices and anti-vortices (liquid), occurring at the KT critical temperature. In correspondence to the dissociation of vortex couples, the superfluid density $n_s(T)$ exhibits a sudden jump. The phase disordering model is suitable to describe layered superconductors, which are not strictly 2D systems but quasi-2D, namely where there is a small (but non null) coupling $J_\perp$ among the layers.
If a superconductor is characterized by small regions (as compared to ξ) where the order parameter θ fluctuates, the energy cost of local variations in θ will be given by [103, 116]

$$\mathcal{E} = \frac{1}{2}\int dr^2 K_s(\nabla\theta)^2 \tag{3.43}$$

where the phase stiffness $K_s = 2n_s/4m^*$ is proportional to the superfluid electrons n_s. Moreover the former equation can be written in terms of the superfluid velocity $v_s = \frac{\hbar\nabla\theta}{2m^*}$ as:

$$\mathcal{E} = \frac{1}{2}m^* n_s(0)\int dr^2 v_s^2 \tag{3.44}$$

which takes the meaning of a kinetic energy.
In the Kosterlitz-Thouless problem, vortex-antivortex unbinding, occurring at the KT transition temperature T_{KT}, leads to a loss of long-range coherence in θ. More generally, the phase-disordering transition T_θ is proportional to the superfluid stiffness:

$$T_\theta = \frac{AK_s(T)}{k_B} \tag{3.45}$$

where the A parameter takes different values according to the dimensionality of the system [117]. Some authors claim the need to re-interpret the Uemura plot as initial evidence of the phase-disordering scenario [103]. Additionally, the renormalization group theory predicts the temperature for the "phase disordering" transition for quasi 2D systems [116]:

$$T_c = T_k + \left(\frac{\pi}{\ln(1/\sqrt{J_\perp/J})}\right)^2. \tag{3.46}$$

Summarizing, in the strict 2D case, a true phase transition is expected, whereas in the 3D case, no sudden jump in n_s is observed, while a crossover between 2D

and 3D behavior should occur.

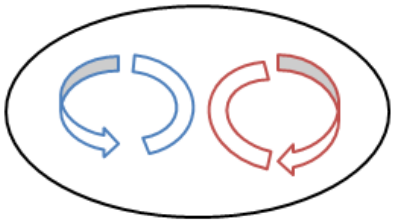

Figure 3.7: Sketch of a vortex-antivortex couple associated to an energy $\mathcal{E}$, and a charge q_v, according to the Coulomb 2D scenario.

3.3 SQUID Magnetometry of $Ba(Fe_{1-x}Rh_x)_2As_2$ single crystals

A. Experimentals

Magnetization measurements have been performed by Superconducting Quantum Interference Device (SQUID), in the Reciprocating Sample Operation (RSO) mode, which allows to get a better sensitivity (down to 10^{-8} emu).[4] Experiments have been carried out on three $Ba(Fe_{1-x}Rh_x)_2As_2$ single crystals, namely an underdoped sample, with x = 4.1% ($T_c(H_0 = 0) = 13.6$ K, with H_0 the magnetic field intensity), a nearly optimally doped sample, with x = 7% ($T_c(0) = 22$ K), and an overdoped sample, with x = 9.4% ($T_c(0) = 15.1$ K). All measurements were made in fields up to 7 T, parallel to the c axis. The critical temperature was estimated from the magnetization curves versus T at small fields (5 Oe), by extrapolating at $M = 0$ the linear behavior of M occurring below T_c, as measured in Zero Field Cooled (ZFC) (Fig. 3.8). A crucial issue that must be addressed, when approaching the anomalous precursor diamagnetism, is the exact determination of the critical temperature T_c. This indeed is a fundamental question, since the difference between the bulk transition temperature $T_c(H \to 0)$, and a possible distribution of local temperatures $T_c^{loc}(\mathbf{r})$ characterizing a diffuse transition, is a key-point for the interpretation of the fluctuating diamagnetism, as it will appear in the discussion of the experimental data. The narrow temperature range where χ shows a smooth increase, above T_c (Fig. 3.8), is supposed to be characterized

[4] See Appendix C for details about the experimental technique.

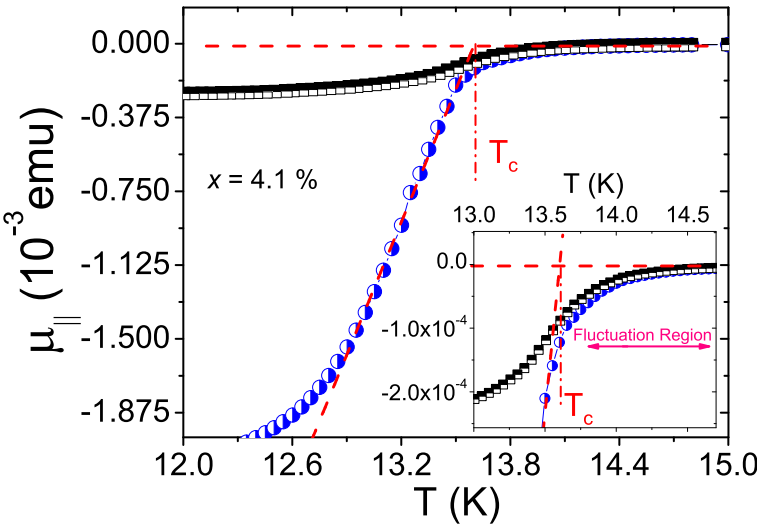

Figure 3.8: The longitudinal magnetic moment μ measured on the compound $x = 4.1\%$. The blue circles refer to the Zero-Field-Cooled data (ZFC) while the black squares refer to the Field-Cooled (FC) data. The dashed red horizontal line marks the Pauli-like trend, while the oblique line is a linear fit. The crossing point identifies the critical temperature T_c. The inset zooms around the critical temperature, to evidence the smoothing of the transition, which leads to precursor diamagnetism.

by Cooper pairs pre-formation, and in such a region, accurate isothermal magnetization measurements were carried out in ZFC, in steps of 2 Oe up to 1000 Oe. Magnetization was measured as a function of field (isotherm) and temperature. High resolution scans were performed for several isotherms in a narrow temperature region above T_c, generally in 0.03 K increments. Additional scans at a temperature well above T_c allowed the determination of the paramagnetic signal of the normal state, and background contributions from the sample holder. In fact, the measured magnetization M is a sum of the fluctuation magnetization M_{fl}, the normal state (mainly Pauli-like) M_P, and the sample holder M_{sh} contributions. Since the latter are nearly T-independent, in the limited temperature range just above T_c, the fluctuating magnetization was derived by the following subtraction:

Fluctuating magnetization

$$M_{fl}(T,H) = M(T,H) - (M_P + M_{sh}). \tag{3.47}$$

Other isothermal curves were measured also below T_c and well above T_c, for comparison. The isothermal curves show a clear upturn (Fig. 3.9) for all the samples, in the range of 10 - 30 Oe. Such a small field is not ascribable to conventional superconducting fluctuations, as it shall be explained hereafter.

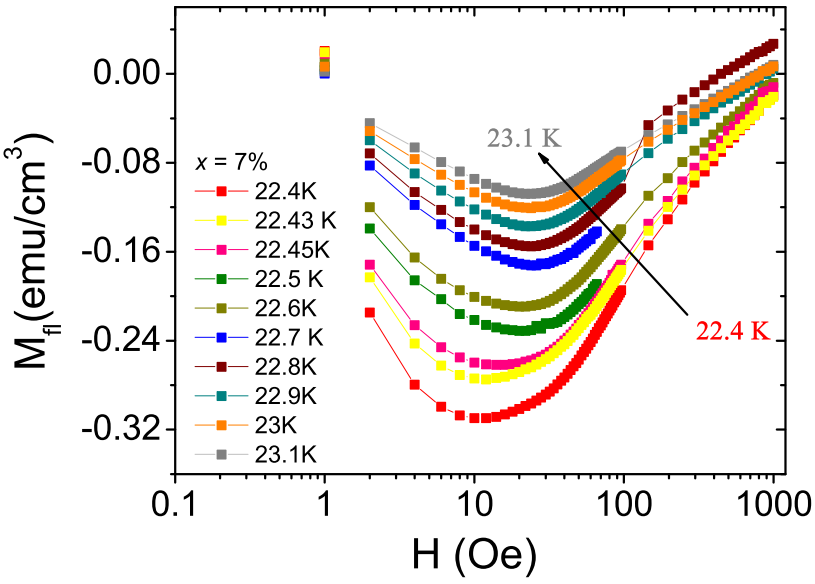

Figure 3.9: The fluctuating magnetization as obtained by equation (3.47), for x=7% compound, with $T_c(0) = 22$ K. The upturn, as well as its trend with temperature are clearly identified.

B. The Upturn field

The upturn field, observed in all the studied samples, shows a peculiar temperature dependence, namely it increases when the temperature increases, in contrast with H_{c1} field (Fig. 3.10). Moreover, the GL theory predicts that in case of zero-dimensionality systems, $H_{up} \sim \epsilon\Phi_0/\xi^2$. For $\xi \sim 20 - 30$ Å and $\epsilon \sim 0.02$, the upturn is expected to be in the range of 10 T, whereas the reported upturn field are four orders of magnitude smaller! Additionally, the value of the diamagnetic susceptibility is anomalously large, in the precursor region. These observations suggest that the origin of the present phenomenology cannot be ascribed to conventional GL fluctuations.

A tentative explanation may rely on the inhomogeneity of the sample, which is responsible for diffuse transition [118, 119]. In this respect, the behavior of the upturn field with the temperature is a crucial aspect for discriminating the presence of diffuse transition. In these compounds *the upturn field increases with the increase of the temperature*, although in a narrow temperature range above T_c (Fig. 3.10). At higher temperatures, the upturn field begins to decrease, suggesting a coexistence of non conventional superconducting fluctuations and diffuse transition, in the same sample (see Section C). Noticeable, ΔT_{fl}, defined as the range from T_c to the temperature where the upturn field begins to decrease,

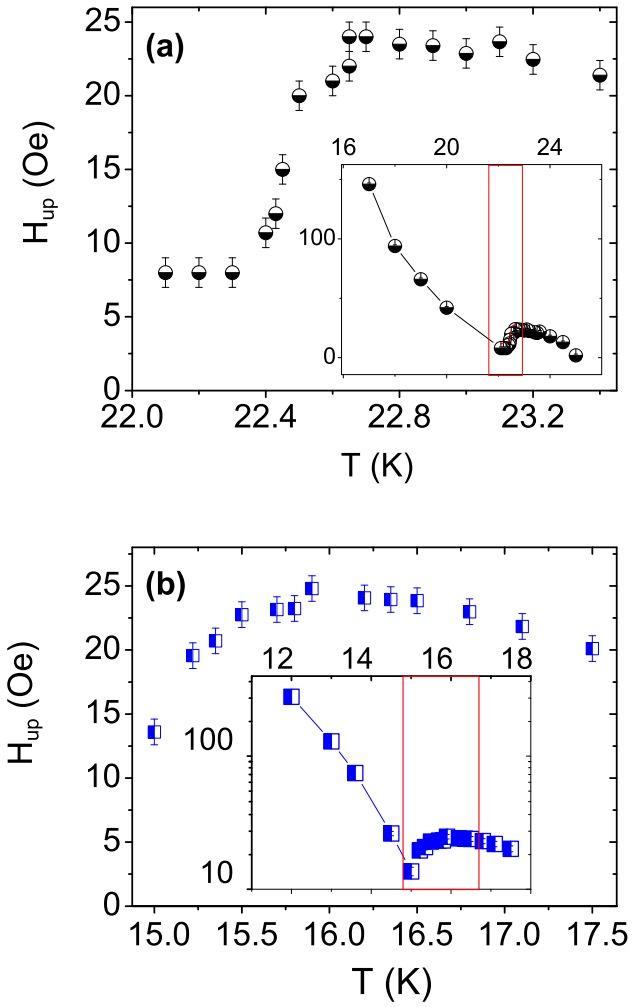

Figure 3.10: **(a)** The upturn field as a function of temperature for $x = 7\%$, derived by taking the derivative of M_{fl} with respect to the field. **(b)** The upturn field for $x = 9.4\%$, where the fluctuation region is wider. The insets show the profile of the upturn field over a large temperature range: below T_c the field shows the typical H_{c1} trend. Above T_c the upturn field increases, and then it decreases. The red lines show the temperature region which is zoomed in the main plot.

shows a consistent increase, when plotted as a function of the Rh content (Fig. 3.11), suggesting that the non-magnetic impurity may facilitate the formation of the superconducting pre-formed islands.[5] The latter result implies the following conclusions: (i) the anomalous superconducting fluctuations are not only present in the underdoped or overdoped regions, as found in cuprates, but also in the nearly optimally doped compounds; (ii) the extension of the fluctuation region increases when the doping concentration increases; (iii) no relationship can be established between the superconducting fluctuations and the pseudo-gap. In fact, the 122 iron-pnictides do not show any pseudo-gap feature and, in addition, the superconducting fluctuations seem more robust when the electronic concentration increases. Critical region

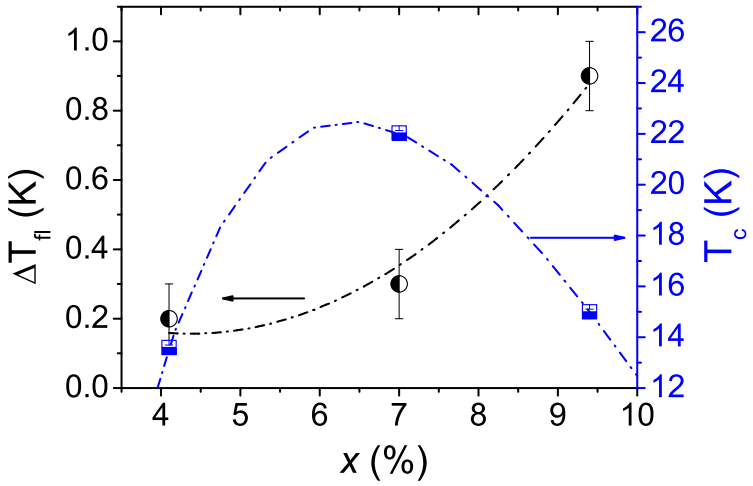

Figure 3.11: The plot shows the evolution of T_c (right axis) and ΔT_{fl} (left axis), as a function of Rh content, x. The dotted-dashed lines are guide for the eye: the blue line sketches the profile of the superconducting dome. ΔT_{fl} monotonically increases with the doping concentration.

C. Isothermal Magnetization

The analysis of these results initiates from the interpretative model based on a 3D XY liquid of vortices, as introduced by Sewer and Beck, and implemented later on by L. Romanó and coworkers [86, 100]. Here the amplitude of the order parameter $|\Psi|$ is supposed to be frozen at a non-zero value, while the phase θ fluctuates in time, preventing the formation of long-range superconductivity. Such

[5] Further experimental evidences are needed to explore such a claim.

model predicts the presence, above the bulk T_c, of superconducting "droplets", characterized by the formation of thermally activated vortex loops n_{th}, and field induced n_H vortex lines. For small fields, the temperature dependence of the susceptibility is controlled by the vortex loops density [115]

$$n_{th} = n_0 e^{-E_0(1+2n)/k_B T(1+\delta(h)^2)}, \tag{3.48}$$

where the energy activation depends on the number of layers n involved in the pancakes. The second derivative of the free energy with respect to H yields the field-dependent susceptibility, that is recalled below: [86]

$$\chi = -\frac{k_B T}{s\Phi_0^2}\frac{1}{1+2n}\frac{(1+\delta(h)^2)^2}{n_v} - \frac{s^2\gamma^2(1+n)}{1+2n}[1+\delta(h)^2] + \frac{47\mathcal{L}^2}{540}\frac{J_\parallel}{s}\left(\frac{2\pi}{\Phi_0}\right)^2\delta(h)^2 \tag{3.49}$$

where s is the interlayer distance and $\gamma = \xi_{ab}/\xi_c$ is the anisotropy ratio.
A first numerical integration of the last equation allows one to fit the experimental data. The results revealed the presence of an additional contribution, which is reasonably ascribed to the diffuse transition. In fact, the presence of regions where H_{up} decreases with increasing temperature, shows the fingerprint of a local distribution of $T_c(\mathbf{r})$. The latter contribution must be removed from the data, to correctly employ the discussed theoretical framework, that strictly refers to the case where only SF are present. For this reason, a curve $M_{fl}(T^*, H)$ was subtracted from the fluctuating magnetization, where T^* is found in the diffuse region, such that T^*= 23.1 K for x=7%, and 17.5 K for x=9.4%. Despite the heuristic nature of the approach, the result of the fit is very good (Fig. 3.12). Even though more accurate analysis is needed, this evidence suggests a simple approach to the problem of treating the coexistence of SF with a distribution of transition temperatures.

In the fitting procedure, the interlayer distance has been set s=6 Å according to the structural data [26],while the anisotropy ratio was taken $\gamma = 2 \div 3$ [21].

Fit results

This small anisotropy implies a large number of layers involved in the pancakes. Indeed, according to the best fitting of the isothermal magnetization curves, at temperatures T = 22.4 K for x=7% and 15.35 K for x=9.4%, the expression $E_0(1+2n)/k_BT$ is estimated about 96 in the former case, and 76 in the second one, corresponding respectively to $n \sim 11$ and $n \sim 9$. Hence, the activation energy in Eq. (3.48) turns out $E_0 \sim 2k_BT_c$ in the two cases, which is of the same order of magnitude usually estimated in YBCO ($E_0 \sim 10k_BT_c$). These values are confirmed also at other temperatures, suggesting that n is nearly temperature

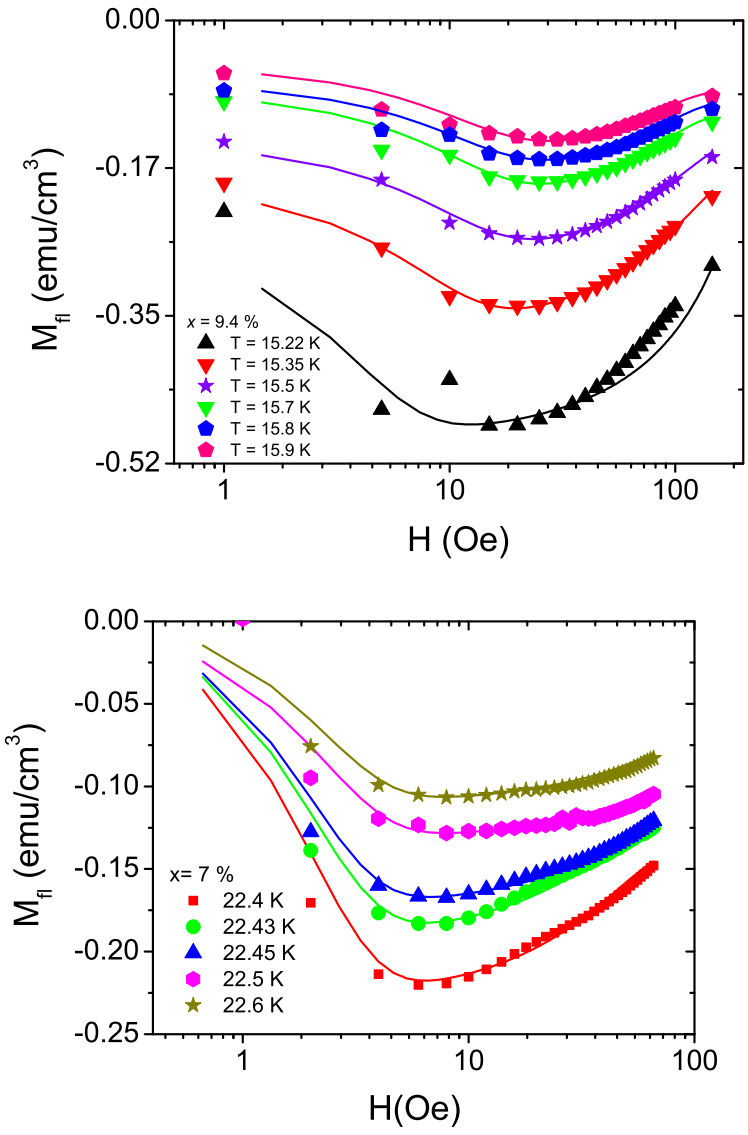

Figure 3.12: The fluctuating magnetization, as a function of the field, for sample $x = 9.4$ % (top panel), and $x = 7$ % (bottom panel). The curves have been corrected by the diffuse transition contribution, as explained in the text. The solid lines are the fit to the equation (3.49).

independent. By comparison, YBCO and Sm-based cuprates [106] have shown $n = 3$, as expected from their higher anisotropies.
In the numerical integration, also H^* and $J_\parallel$ are given as free parameters. From the characteristic field H^*, it is possible to estimate an order of magnitude of the average size $\mathcal{L}$ of the superconducting regions. In Tables 3.1 and 3.2 the significant fitting parameters, respectively for nearly optimally doped and overdoped compounds, are reported. The underdoped sample displayed the same phenomenology, however because of the poor quality of the data, a reliable fitting could be hardly achieved. Nevertheless, also in x=4.1%, the upturn field shows the same trend with the temperature.

Table 3.1: Fit results for sample x =7%. $\mathcal{N}$ represents the volumetric density of mesoscopic islands, of surface $\mathcal{L}^2$.

ϵ	$\mathcal{N} \times 10^{14}(\mathrm{cm}^{-3})$	$\mathcal{L}$ (nm)
0.0048	3.0234	580
0.0058	2.5426	574
0.0067	2.5176	550
0.0089	2.0198	530
0.01345	1.8153	510

From the fit the pre-exponential factor n_0 turns out to be 2.5×10^{19}, for $x = 7$ %, and 1.5×10^{20} for $x = 9.4$ % [120].

Table 3.2: Fit results for sample x =9.4%.

ϵ	$\mathcal{N} \times 10^{14}(\mathrm{cm}^{-3})$	$\mathcal{L}$ (nm)
0.01466	9.0625	480
0.023	1.2706	310
0.033	1.1784	270
0.0466	1.10283	260
0.0533	0.8610	260
0.06	0.7077	260

D. Restoring the Conventional Fluctuations

The results presented in the previous section show the occurrence of unconventional superconducting fluctuations, in the limit of small fields. On the contrary,

when a magnetic field above $\sim$ 4500 Oe is applied, a different phenomenology is found. The isothermal magnetization was measured at fixed field, in Field Cooled (FC). The diamagnetic magnetization was found by subtracting, from the raw data the high temperature (i.e. normal phase) contribution, the latter being estimated by a polynomial fit. Afterwards, the reduced magnetization $m_{red} = -\frac{M}{\sqrt{HT_c}}$, was studied as a function of the reduced temperature $\epsilon = (T - T_c)/T_c$. According to the GL theory, in the 3D anisotropic limit, the m_{red} curves should cross at $\epsilon = 0$ in correspondence to the value

$$m'_{red} = -\frac{M(T_c)}{\sqrt{HT_c}} = \frac{k_B}{\Phi^{3/2}} m_3(\infty)\gamma \tag{3.50}$$

where $m_3(\infty) = -0.323$ [121, 122]. Fig. 3.13 shows that the curves are nearly parallel below 4500 Oe, while above that threshold they begin to cross at about $\epsilon = 0$. Interestingly, the crossing point implies an anisotropy ratio of $\gamma = 2 \div 3$ (Fig. 3.13), in agreement with the values found in literature for these compounds [21, 26].

One might argue about the field dependence of the critical temperature T_c.

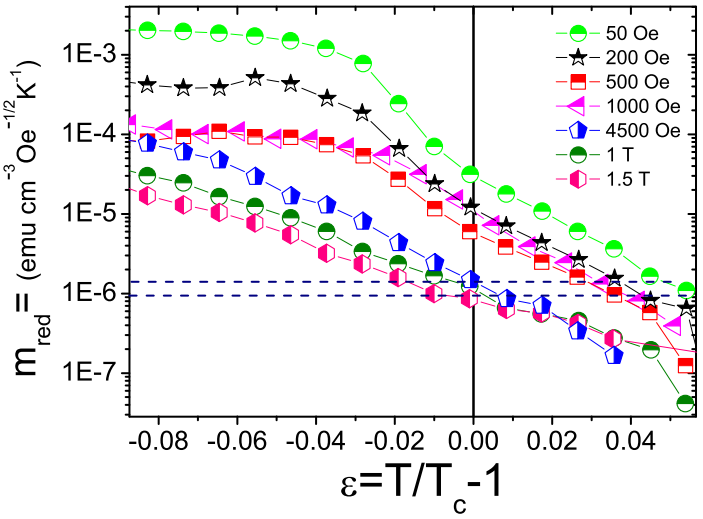

Figure 3.13: The reduced magnetization as a function of the reduced temperature ϵ is reproduced for fields below 2 T, for $x = 7\%$. Above $\sim$ 4500 Oe, the data cross at values included into the two dashed lines. Such values are in agreement with the GL theory for 3D XY systems, [121] when anisotropy ratio of $2 \div 3$ is assumed.

Indeed the former relation has been derived from Ref. [122]:

$$\frac{M_{fl}(T,H)}{\sqrt{H}} = -\frac{k_B T}{4\pi}\left(\frac{4\pi}{\Phi_0}\right)^{3/2}\sqrt{\frac{m_c(0)}{m_{ab}(0)}} \times \left(\frac{T-T_c(H=0)}{2H}|\partial H_{c2}/\partial T|_{Tc}\right). \tag{3.51}$$

For small fields H such that $T_c \sim T_c(0)$, the scaling function f, can be evaluated numerically: $f(0) \sim 0.09133$, and the former relation turns into equation (3.50). This suggests that one should be careful when applying the former scaling, in the high fields regime.

Prange regime

Furthermore, a study of the fluctuating magnetization, up to the maximum achievable field (7 T), can give insights into the occurrence of conventional fluctuations. Nevertheless one must be careful, since magnetic impurities are relevant at high fields. Indeed a ferromagnetic contribution was found and subtracted from each curve, eventually showing a non negligible diamagnetism, at high fields. Fig. 3.14 evidences the occurrence of a second strong diamagnetic contribution, which is precursor of the formation of a second upturn H_{up2}, at high fields as expected for the GL theory. The linear trend of M_{fl}, at high fields and for $T > T_c$ suggests that the Prange regime is fulfilled, namely $M_{fl} \sim H$ [122]. Note that Mosqueira

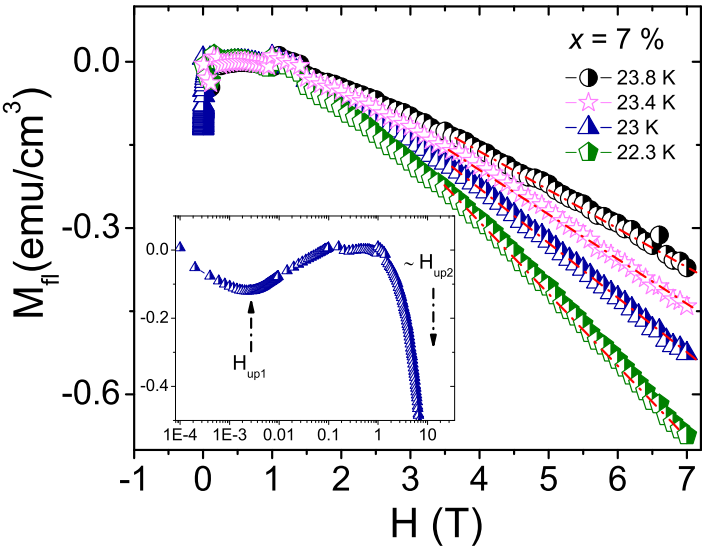

Figure 3.14: Field dependence of M_{fl} for $x = 7$ %: the strong diamagnetic contribution suggests the formation of a second upturn, at very high fields not achievable by the magnet. The first upturn has been added for comparison. The red solid curves are guides for the eye. The inset shows the first upturn field and the onset of the second one, that is marked by the second arrow.

et al. recently found classical GL fluctuations in $Ba_{1-x}K_xFe_2As_2$, [123] in agreement with a 3D anisotropic approach in the high field range. A recent Raman study on a sample of $Ca_4Al_2O_{5.7}Fe_2As_2$ showed an anomaly at 60 K $\sim 2\ T_c$, which has been ascribed to a strong coupling of the observed phonon mode with the superconducting order parameter fluctuations [124].
Finally, it should be remarked that the presence of both conventional and unconventional SF is not a totally unexpected result. In fact a similar phenomenology was observed by Prando *et al.* [125] in $SmFeAsO_{0.8}F_{0.2}$. However, while H_t is $\sim$ 4500 Oe in 122 iron-based superconductors, it turns into higher values ($H_t \sim 1.5$ T) in 1111 compounds.

E. Irreversibility and Relaxation

Another still debated issue concerning the cuprates, is the manifestation of an irreversibility effect in the isothermal magnetization, above T_c (Fig. 3.15) [126]. Such an effect, not predicted within the GL theory, is a clear indication that some magnetic flux enters into the sample. On the other hand, according to the superconducting island scenario, it is possible to ascribe irreversibility to the presence of vortices entering the superconducting "droplets". Remarkably, in Rh-doped Ba122 compounds, the FC and ZFC fluctuating magnetizations show very different absolute values, namely the ZFC magnetization turns out to be five time smaller than the FC one, at 16 Oe.
It is not clear whether the irreversibility is due to vortices entering the region of the sample characterized by a local distribution of T_c, or to field-induced vortices entering the metastable islands discussed in the text. In fact, even though the upturn field is increasing with the temperature, a simultaneous presence of diffuse transition with anomalous SF has been found. Noticeably, the reversibility is restored around 4000-5000 Oe, in good agreement with the field where the GL theory can be applied.

Finally, Fig. 3.16 shows another interesting result that is encountered just in the critical region: if the magnetization is measured at progressive time intervals (in ZFC) at 16 Oe,[6] a time-dependent phenomenon is observed, namely M relaxes to the FC value, in a long time scale (nearly 7 h). This relaxation mechanism cannot be directly related to the pre-formed Cooper pairs which are, by nature, fluctuating. Furthermore, magnetic relaxation above T_c might be confused with

Relaxation

[6] 16 Oe is the field of the maximum irreversibility.

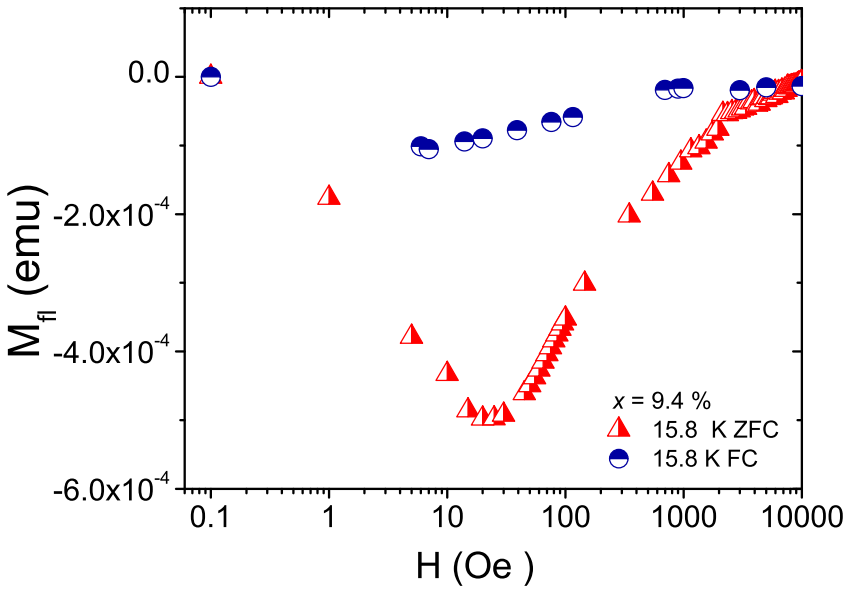

Figure 3.15: The plot shows a comparison between FC and ZFC magnetization, u just above T_c, in the fluctuation region, for sample $x = 9.4\%$. The evident difference among the two indicates the presence of a strong thermal history dependent effect.

magnetic impurities. Nevertheless, if this was the case, the region above the fluctuating phenomena should display the same trend. To work out the origin of this phenomenon, the relaxation has been compared in three different temperature regimes (Fig. 3.16). Remarkably, there is no relaxation in the normal state, while in the fluctuating phase and in the mixed phase, the effect is clearly observed. Indeed, this might be the proof that the precursor islands host persistent diamagnetism.

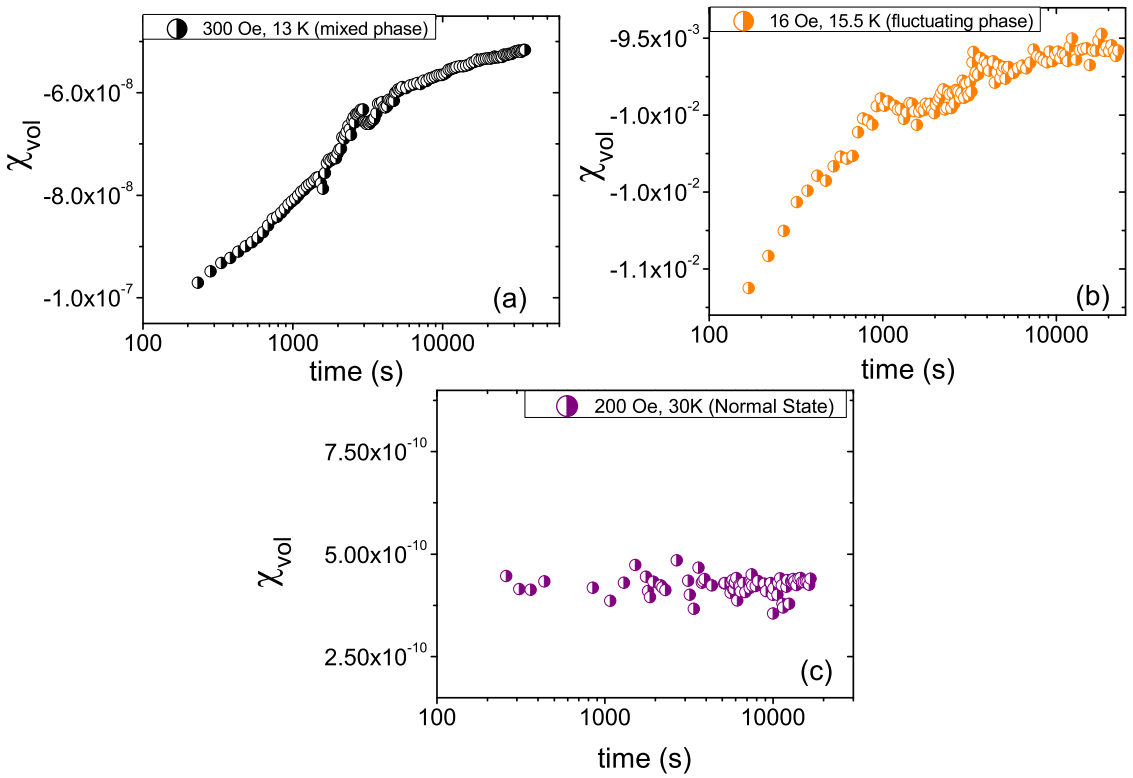

Figure 3.16: The relaxation of the magnetization for three different temperature regimes, namely the mixed phase **(a)** where the relaxation is ascribable to the Abrikosov vortex relaxation, the superconducting fluctuation **(b)** and the normal phase **(c)**.

3.4 Conclusions

The diamagnetic response of $Ba(Fe_{1-x}Rh_x)_2As_2$ crystals is studied by high resolution magnetization measurements, over a broad doping range. At low magnetic fields, namely $H < 4500$ Oe, the experimental findings cannot be described within the classical Ginzburg-Landau theory, and they seem to be consistent with the phase fluctuating scenario. In such framework, unconventional superconducting fluctuations are supposed to develop into precursor islands, where the amplitude of the order parameter is frozen, while the long-range phase coherence associated to the bulk superconducting state is prevented by strong fluctuations of the phase. At higher temperature, the effect of diffuse transition is likely responsible for the decrease of the upturn field. A first tentative to describe both phenomena has provided a good agreement with the theory of anomalous superconducting fluctuations.

On the other hand, when strong fields are applied, the GL theory is restored and the experimental findings agree with the 3D XY universality class. In fact,

the indication of a second upturn, together with the crossing of the reduced magnetization at T_c, are interpreted as the precursors of conventional fluctuations. Such dichotomy seems peculiar of the iron-based superconductors, since similar results were found also in a member of the 1111 family.

The phenomenology observed in these systems occurs in a narrow temperature region, which makes more difficult to study the effects accompanying the superconducting fluctuations, at variance of the more noticeably phenomena observed in the cuprates. Still, the experimental evidences displayed in this Chapter clearly support the presence of anomalous superconducting fluctuations, in the iron-based superconductors.

Chapter 4

Evidence of unconventional low-frequency dynamics in the normal phase of $Ba(Fe_{1-x}Rh_x)_2As_2$

It is widely believed that understanding the normal phase properties of the high temperature superconductors will also shed light onto the superconducting coupling mechanism. In the NMR study presented in this Chapter, a clear evidence for robust spin-fluctuations is deduced from the temperature dependence of $1/T_2$, the linewidth, and the spin-lattice relaxation rate in the normal state.

The motivation to study the spin-echo decay time T_2, lays on the fact that very few data reporting T_2 have been published so far, despite the large amount of Nuclear Magnetic Resonance studies on the iron-based superconductors. In fact, most of the NMR investigations have concentrated on the features emerging from the spin-lattice relaxation rate ($1/T_1$) measurements [37, 42, 43, 83, 127–129] and much attention has been paid to the intriguing issues of the superconducting coupling, the spin gap symmetry, and the nanoscopic competition/coexistence of superconductivity with magnetism [43,83,127,128]. However also $1/T_2$ is a useful tool to probe very low-frequency excitations [35, 130, 131].

This Chapter is organized as follows: at first the T_2 issue is introduced through a historical overview, and secondly a systematic study of ^{75}As NMR spin echo decay in $Ba(Fe_{1-x}Rh_x)_2As_2$ iron-based superconductors, is discussed. The spin echo shows a high temperature dominant Gaussian decay, which becomes exponential at low temperature. The exponential decay rate increases upon cooling already in

the normal phase, evidencing the onset of an unconventional very low-frequency activated dynamic, whose characteristic correlation time is derived together with the corresponding energy barrier. This dynamic persists across the whole phase diagram up to the overdoped compound, and it is less pronounced if the magnetic field is applied perpendicular to the FeAs layers. Moreover a similar dynamic affects $1/T_1$, as well as the linewidth. Toward the end of the Chapter, an interpretative framework based on domain walls motion, possibly involving nematic fluctuations will be discussed. Further considerations concerning an analogy with the spin/charge stripe order will be proposed.
Finally, the dependence of the Knight shift with the temperature, will be addressed, and it will reveal an "exotic" behavior, in the normal phase, that is currently under debate.

4.1 Spin-echo decay time as a probe of the spin fluctuations

The study of the spin excitations emerging in the normal phase of superconductors is of major importance to unravel the mechanisms driving the Cooper pair formation. Both in the cuprates and in the iron-pnictides, the presence of competing interactions gives rise to complex phase diagrams and to quasi-degenerate ground-states, which can cause unconventional dynamics at low energies.
Nuclear Magnetic Resonance has played a key role in the study of the low-frequency excitations, in the normal state both of high-T_c superconductors, and more recently of the iron-based superconductors. In particular, the issue of a dynamic effect emerging in the spin-echo decay time has been discussed in earlier times [132–135]. Several subjects were under discussion: firstly the indirect spin coupling was found as the main contribution to the dephasing of the NMR echo, while the dipole-dipole interaction was a negligible correction [136]. Secondly in some cuprates, like $YBa_2Cu_3O_{6.63}$ [134], the increase of the $1/T_2$ upon cooling revealed the growth of antiferromagnetic (AF) correlations, down to a temperature where the spin fluctuations probed by the $1/T_1$ seemed suppressed (Fig. 4.1). Indeed in the cuprates, one of the most significant achievements was the derivation of the staggered static spin susceptibility from ^{63}Cu(2) Gaussian echo decay rate $1/T_{2G}$ [134]. It was demonstrated by Pennington *et al.* [136],

Indirect spin coupling

that measurements of the nuclear transverse relaxation rate in high-T_c materials, provide important information concerning the static **q**-dependent spin suscepti-

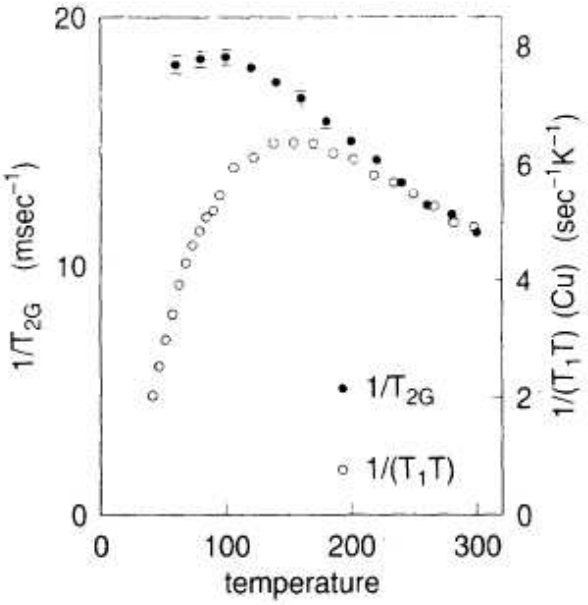

Figure 4.1: Temperature dependence of $1/T_{2G}$ (filled circles) and $1/(T_1T)$ (empty circles) of ^{63}Cu NMR on YBCO. The figure is adapted from Ref. [134]. The spin-spin relaxation rate keeps increasing, while the $1/(T_1T)$ (empty circles) drops down, because of the fundamental difference in the static and low-frequency susceptibility at the antiferromagnetic wavevector (π, pi).

bility, which is complementary to the information obtained from $1/T_1T$. They found that ^{63}Cu nuclear spins in $YBa_2Cu_3O_7$ are coupled via virtual electronic spin excitations, leading to a large enhancement of the transverse nuclear relaxation rate. Pennington and Slichter analyzed such indirect coupling in the light of the phenomenological model of antiferromagnetic spin correlations proposed by Millis, Monien, and Pines (MMP) [137]. Such an indirect coupling is well known in metals (as the Rudermann-Kittel-Kasuya-Yosida mechanism). MMP describe the spin dynamics of the CuO_2 planes with a spin susceptibility strongly peaked about the (Néel) antiferromagnetic wave vector. In essence, a nucleus $\mathbf{I_1}$, located at the origin, polarizes the electron spin at position $\mathbf{R_i}$, resulting into a spatially varying spin polarization:

$$< S^{\alpha}(\mathbf{R}_i) > \sim I_1^{\alpha} \sum_q e^{-iqR_i} \chi_q^{\alpha} A_q^{\alpha\alpha}, \tag{4.1}$$

where $\alpha = x, y, z$ are the components involved. Then the electron spin can polarize a second nuclear spin $\mathbf{I}_2$, resulting into a final indirect interaction among the two nuclei. By calculating the second moment (M_2) of the NMR spectrum,

in presence of that interaction, one finds [134]

$$2M_2 = \frac{1}{T_{2G}^2} = \frac{c}{8\hbar^2}\frac{1}{(\hbar\gamma_e)^4}\left[\sum_q |A_q^{zz}|^4\chi_q^2 - \left(\sum_q |A_q^{zz}|^2\chi_q\right)^2\right] \tag{4.2}$$

where A_q is the form factor (see Appendix A), χ_q is the wave-vector dependent spin-susceptibility, c is the abundance of the nuclear spin and z is the direction of the external magnetic field.

Later on, a similar compound was found to exhibit a bump in the echo decay rate of ^{89}Y nucleus [138]. Walstedt and Cheong [135] ascribed this feature to un-like nuclear dipolar interaction (Y-Cu) as a source of local field, and Cu spin-lattice relaxation as the source of field fluctuation. Remarkably, when the field was parallel to the c axis of the crystal, a peak in $1/T_2$ appeared (Fig. 4.2), just below the transition temperature T_c. Such a feature was associated with the freezing/melting of the vortex lattice. Additionally, an ^{17}O NMR study on the same

Controversial peaks in $1/T_2$.

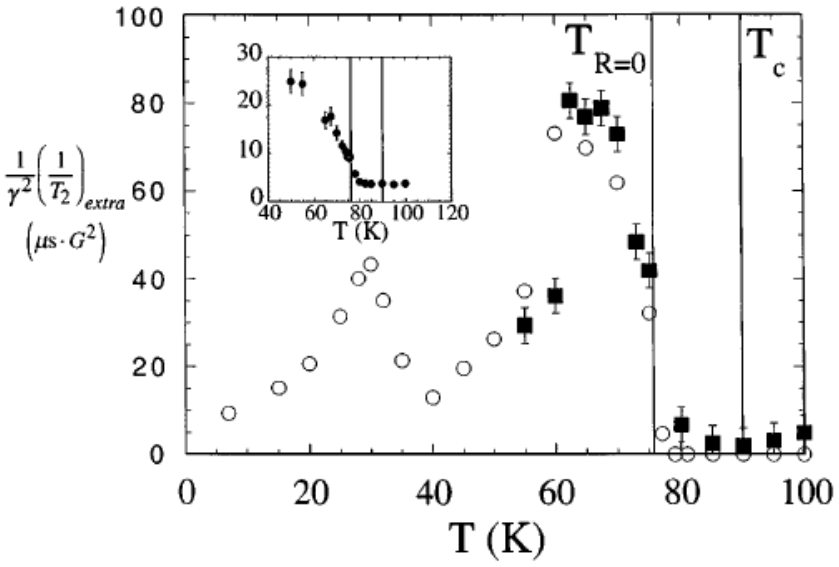

Figure 4.2: NMR echo decay rate for $YBa_2Cu_3O_7$, measured at 9 T, with the magnetic field oriented parallel to the c axis, for ^{17}O (open circles) and ^{89}Y (filled squares). Vertical lines label, for the applied field of 9 T, T_c (90 K) and $T_{R=0}$ (76 K), where resistance vanishes. Inset: ^{89}Y linewidth (square root of the second moment), in Gauss, vs T. The figure shows the presence of two peaks in the "extra" (namely exponential) relaxation rate, both below the superconducting transition. The Figure is adapted from Ref. [138].

compound evidenced a second peak, at a lower temperature. The second peak was not understood at that time [139]. Indeed, the same feature was observed

also in NQR experiments in $YBa_2Cu_3O_{7-x}$, thus ruling out the FLL hypothesis and suggesting other mechanisms involving charge fluctuations [138–140].
Noticeably, nuclei with a smaller hyperfine coupling show a different phenomenology of $1/T_2$. In fact ^{199}Hg NMR study of $HgBa_2CuO_{4+\delta}$ revealed that the echo decay could be fit by the product of a Gaussian and an exponential component [133, 141], the former being due to pseudo−dipolar interaction via the conduction electrons, while the latter was justified again in terms of vortex dynamics.
In addition to the phenomenology related to superconductivity and vortex lattice dynamics, the high-T_c superconductors, can shed light onto a totally different kind of problem. Indeed the precursor materials of cuprates are the prototypes of the two-dimensional Heisenberg antiferromagnets, which display magnetic frustration. In fact, other achievements of the T_2 study have been obtained from the investigation of spin fluctuations taking place in frustrated systems. Two-dimensional $S = 1/2$ Heisenberg antiferromagnets (2DQHAF), are characterized by strong quantum spin fluctuations because of (i) the reduced dimensionality of the interaction and (ii) the low spin value. In such systems, long range order would take place, in principle, only at zero temperature.[1] Moreover the presence of frustrated antiferromagnetic exchange interactions further enhances quantum fluctuations. This situation is described by the J_1-J_2 model on a square lattice, where the next-nearest-neighbor interaction J_2, acting along the diagonal of the square, competes with the nearest-neighbor interaction J_1, acting along the side of the square [142, 143]. On increasing J_2, one firstly expects a quantum phase transition from a Néel ordered phase to a nonmagnetic ground state, the nature of which is still a subject of debate, and then another transition to a collinear ground state. The collinear phase can be considered as formed by two interpenetrating sublattices with a reciprocal orientation of the Néel vectors, which can classically assume any orientation. In Li_2VOSiO_4 and Li_2VOGeO_4, μSR spectroscopy together with ^{7}Li NMR investigation, revealed the occurrence of very slow spin-fluctuations in $1/T_2$, which have been ascribed to domain walls motion associated with the two collinear phases, CAFI and CAFII (Fig. 4.3).

2DQHAF

Another vastly debated effect, that can be probed by means of $1/T_2$, is the spin/charge stripe ordering, mostly occurring in strongly correlated materials, such as transition metal oxides or organic conductors. Due to the strong interactions between electrons, charges are localized on different sites, leading to an ordered superlattice, which may assume different patterns, ranging from vertical

Spin/charge stripes

[1] More precisely, the magnetic order is prevented in low-dimensional systems by the Mermim-Wigner theorem. As a consequence of that, the magnetic order can occur if a dimensional crossover to 3D takes place.

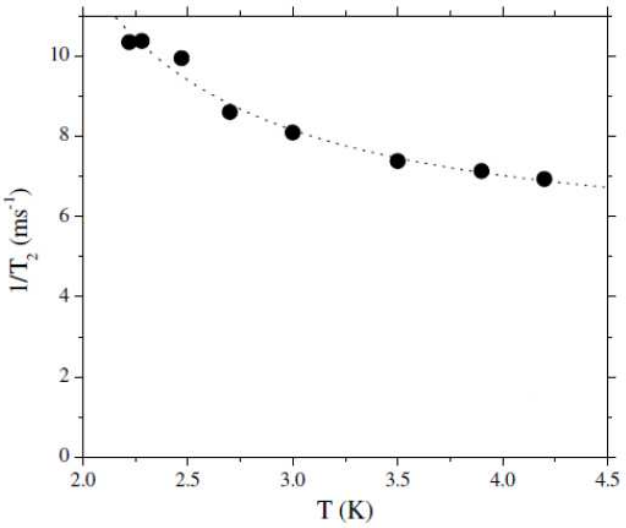

Figure 4.3: ^{7}Li NMR temperature dependence of $1/T_2$ in Li_2VOGeO_4 above T_N, for H =3.7 kG. The dotted line shows the best fit according to an activated temperature dependence of $1/T_2$, with an effective barrier of 3.5 K. The Figure is adapted from Ref. [143].

to horizontal stripes, or also checkerboard patterns. The charge order transition is accompanied by symmetry breaking, it may lead to ferroelectricity, and additionally it is often found in close proximity to superconductivity. NMR spectroscopy is a powerful tool to measure the charge re-arrangement, in particular via the study of the first moment of the line [144]. Very recently $1/T_2$ has provided some insights into this topic. In fact, Wu *et al.* [144] have found in YBCO, just below the temperature of the spin charge ordering, a strong increase of $1/T_2$(Fig. 4.4). That enhancement is accompanied, also in other systems, by a change in the analytic expression of the spin-echo decay, from Gaussian to exponential [145]. Wu *et al.* interpreted their result in term of antiferromagnetic spin-density-wave fluctuations, that are slow enough to appear frozen, on the timescale of a cyclotron orbit.

The iron -pnictides

After the discovery of iron-based superconductors, the scenario became more and more complex. T_2 was mainly studied via Hahn Echo (*HE*) and Carr-Purcell-Meiboom-Gill (*CPMG*) sequences (see Chapter 1). In essence, the optimally doped $Ba(Fe_{1-x}Co_x)_2As_2$ [35] and $Ba(Fe_{1-x}Rh_x)_2As_2$ [130] display a peak in $1/T_2$, below T_c, which was associated to the vortex dynamics (See Chapter 1). In spite of that, the behavior of $^{75}T_2$ in the normal phase of $Ba(Fe_{1-x}Rh_x)_2As_2$ superconductors is not completely understood [35, 130], and its absolute value is far from any theoretical expectation. In the following section the experimental results on $Ba(Fe_{1-x}Rh_x)_2As_2$ are presented.

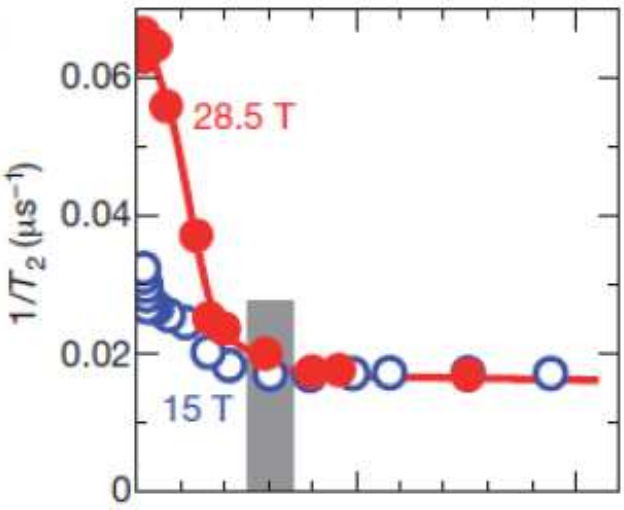

Figure 4.4: Increase in the ^{63}Cu $1/T_2$ on cooling below T_{charge} (grey rectangle), obtained from a fit of the echo decay with a stretched exponential. The $1/T_2$ is enhanced by the magnetic field. The Figure is adapted from Ref. [144].

4.2 Spin-spin relaxation rate study of the Ba($Fe_{1-x}Rh_x$)$_2As_2$ family

Three different single crystals belonging to the Rh-doped family Ba($Fe_{1-x}Rh_x$)$_2As_2$ have been investigated: an underdoped sample, with x = 4.1% ($T_c(0)$ = 13.6 K), a nearly optimally doped sample, with x = 6.8% ($T_c(0)$ = 22.4 K), and an overdoped sample, with x = 9.4% ($T_c(0)$ = 15.1 K). The critical temperature T_c of any sample was determined prior to the NMR experiment, via SQUID magnetometry, as described in Chapter 3. Subsequently, the samples were studied via ^{75}As NMR, at three different magnetic fields: 6.4, 9 and 11 T, with $\mathbf{H_0}$ parallel and perpendicular to the c axis. The spin-echo decay time was estimated by fitting the decay of the transverse nuclear magnetization, measured by a standard *HE* ($\pi/2-\tau-\pi$) and by a *CPMG* sequence ($\pi/2_x-\tau-\pi_y-\tau-\pi_y...$), by varying τ and extracting the intrinsic T_{2CPMG} for $\tau \to 0$ [146]. Firstly, the *HE* decay data are shown.

4.2.1 Hahn Echo decay

The high temperature decay rate revealed a non-negligible Redfield contribution, evidencing a linear dependence of T_2 on T_1 (Fig. 4.5). According to that, the raw data have to be corrected by the T_1 contribution to the dephasing of the nuclear

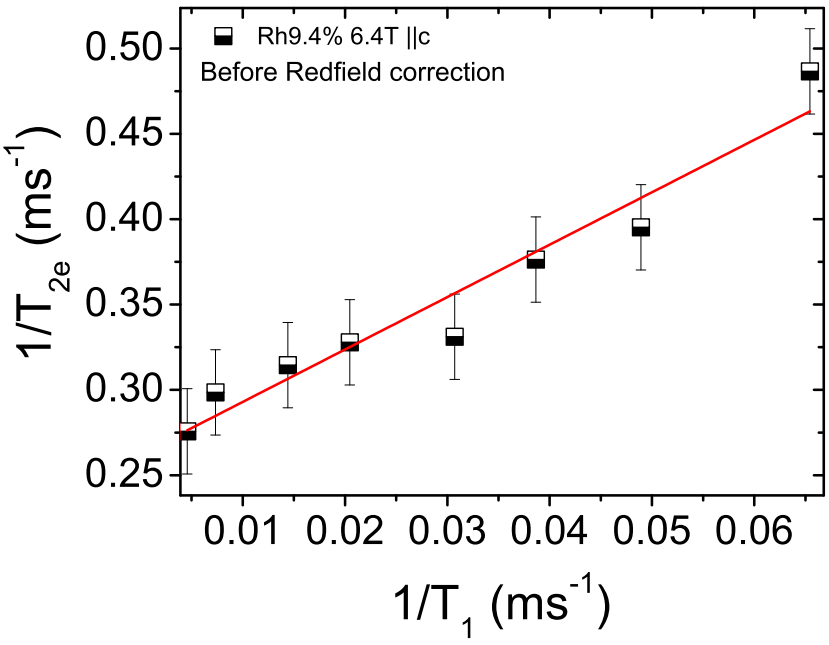

Figure 4.5: The $1/T_2$ versus $1/T_1$ measured in the normal phase, for $x = 9.4$ %, at 6.4 T $\parallel c$. T_2 is evaluated as the time when the (normalized) echo amplitude decays of $1/e$.

spin signal:

$$M_t(2\tau) = E(2\tau)\exp\left(-\frac{2\tau}{T_{1e}}\right), \tag{4.3}$$

which encloses the spin-lattice contribution to the echo decay. Walstedt *et al.* [135] calculated the expression of $\frac{1}{T_{1e}}$ when the spin-lattice relaxation rate shows anisotropy. According to these authors, the Redfield contribution becomes:

$$\frac{1}{T_{1e}^{\parallel c}} = \frac{3}{T_1^{\parallel c}} + \frac{1}{T_1^{\perp c}} \tag{4.4}$$

$$\frac{1}{T_{1e}^{\perp c}} = \frac{3}{T_1^{\perp c}} + \frac{1}{T_1^{\parallel c}}, \tag{4.5}$$

where the symbols $\parallel$ and $\perp$ refers to the external field. After that, the corrected data have been fit to the product of an exponential and a Gaussian decay (Fig. 4.6 inset):

$$E(2\tau)/E(0) = \exp(-2\tau/T_{2exp})\exp(-(2\tau)^2/2T_{2G}^2). \tag{4.6}$$

The two components evolve with the temperature in such a way that, in the high temperature regime, the Gaussian term is significantly larger than the exponential one, and both are weakly temperature dependent. This trend persists down

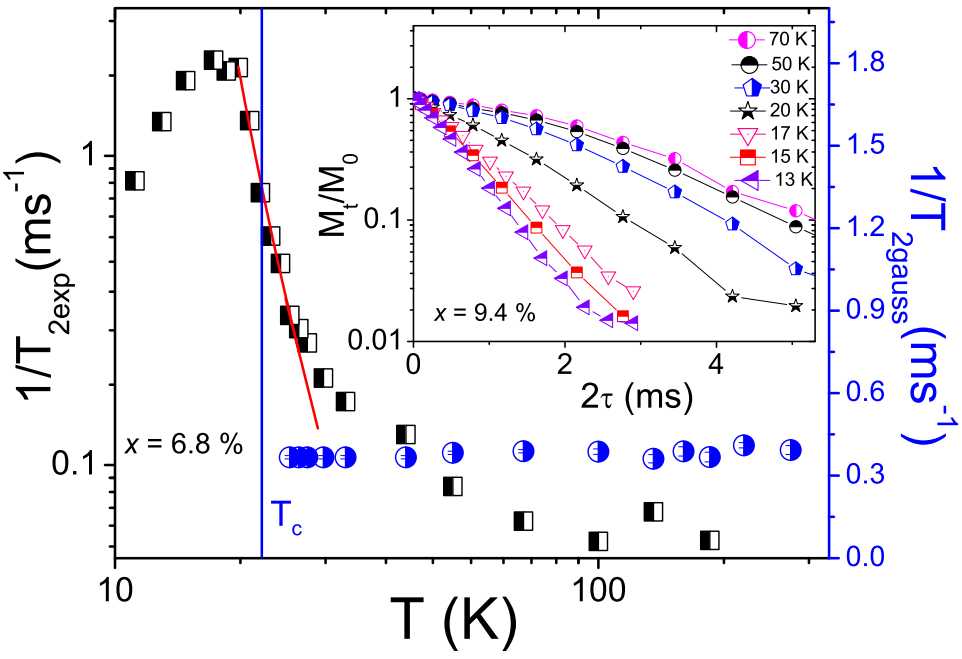

Figure 4.6: The exponential (black half filled squares) and Gaussian (blue half filled circles) $1/T_2$ measured by Hahn echo at 11 T $\parallel c$ of the x =6.8% sample. The red solid line shows the best fit to Eq. 5.12. (Inset) The spin-echo amplitude decay at different temperature , for $x = 9.4\%$, at $\mathbf{H_0} = 11$ T $\parallel c$ axis, corrected by the T_1 contribution.

to a temperature $T^* > T_c$, where the Gaussian contribution becomes negligible, while the exponential rate grows rapidly and becomes the main contribution to the echo decay (Figs. 4.6). The experimental values of T^* are 22 $\pm$2 K and 18$\pm$2 K for $x = 6.8\%$ and $x = 9.4\%$, respectively. Here the attention will be focused on the low temperature exponential component, while the high temperature constant behavior will been discussed in a following section. From Fig. 4.13 one notices that also $1/T_{2CPMG}$ is significantly reduced with respect to $1/T_{2exp}$ for $T < T^*$, and shows a less pronounced field and temperature dependence. *HE* and *CPMG* sequences are sensitive to fluctuations with a characteristic time scale $\tau_c \sim \tau$ and $\sim \tau_{CP}$, respectively. The difference between the magnitude of $1/T_{2CPMG}$ and $1/T_{exp}$ points out an upper and lower limit for the correlation time probed by ^{75}As nuclei. In fact, since a non-negligible effect is visible in both the sequences, one may argue that the correlation time of the fluctuations, τ_c, is between $\tau_{echo} \sim ms$ and $\tau_{CP} \sim \mu s$. More precisely, it can be observed, by the following T_1 analysis, that τ_c grows above the μs, below T^*.

Further insights into the low-frequency dynamics can be derived from the T-

dependence of the full width at half maximum (FWHM) of the central $1/2 \rightarrow -1/2$ NMR line, obtained from the Fourier transform of half of the echo (Fig. 4.7). Indeed the NMR spectrum displays an inhomogeneously broad lineshape,

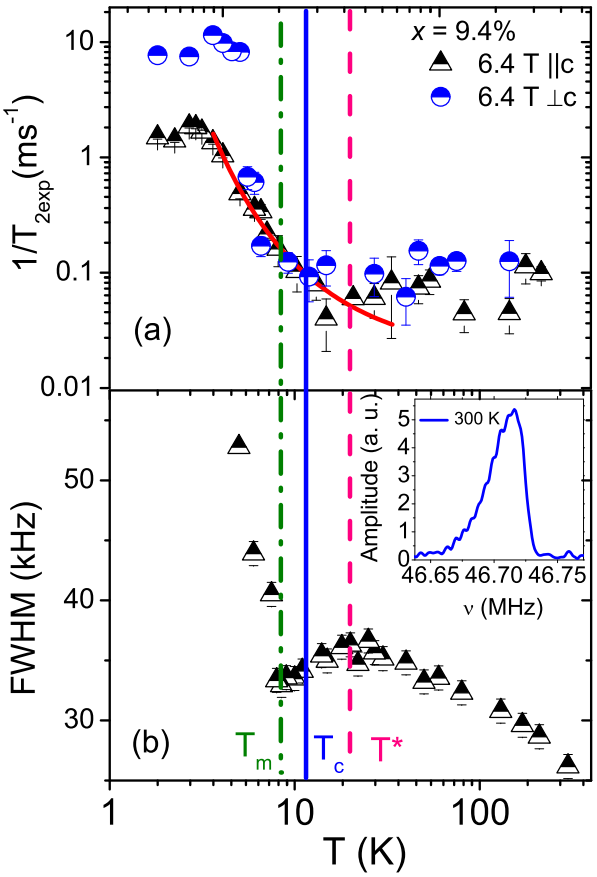

Figure 4.7: **(a)** $1/T_{2exp}$ measured at $H_0 = 6.4$ T $\parallel c$, for x =9.4%. The red solid line shows the best fit according to equation of fast motion (see text below). The blue circles show $1/T_{2exp}$ measured at $H_0 = 6.4$ T $\perp c$. **(b)** The T dependence of the FWHM of ^{75}As central line: the width increases with decreasing T down to T^* (red dashed line), where it begins to decrease. Finally the linewidth increases again at the vortex freezing temperature T_m (green dashed-dotted line). The blue line marks T_c at 6.4 T. The inset displays an example of the ^{75}As NMR spectrum, showing a clear asymmetry.

characterized by a low-frequency tail. A possible reason for that may rely on the mosaicity, namely the fact that such crystals may show some microscopic misalignment, within few degrees [147, 148].

The line becomes progressively broad and symmetric upon cooling. Surprisingly, at the same temperature where the echo decay becomes exponential, the linewidth

FWHM vs T

starts to decrease, suggesting the onset of low-frequency dynamics which can average-out the static frequency distribution probed by ^{75}As nuclei. Finally, at $T_m < T_c$, the line broadens again (Fig. 4.7), as expected when the solid/glassy

vortex phase sets in [35, 130, 149]. The increase of the linewidth upon cooling (in the high temperature range) may be due to a distribution of local hyperfine fields and/or quadrupolar frequencies around the Rh ions. A source of hyperfine fields distribution can be found in RKKY-like effects around each Rh ion, which would induce decaying alternated oscillations of the local paramagnetic susceptibility [70].

Being said that, there is an additional effect of the magnetic field amplitude on the spin-spin relaxation rate. Fig. 4.8 shows $1/T_{2exp}$ versus temperature, measured at two different fields. It turns out that the field intensity has the effect of enhancing the spin fluctuations, namely the slowing down of the fluctuations occurs at higher temperatures. By comparing the measurements performed on

Magnetic field effect

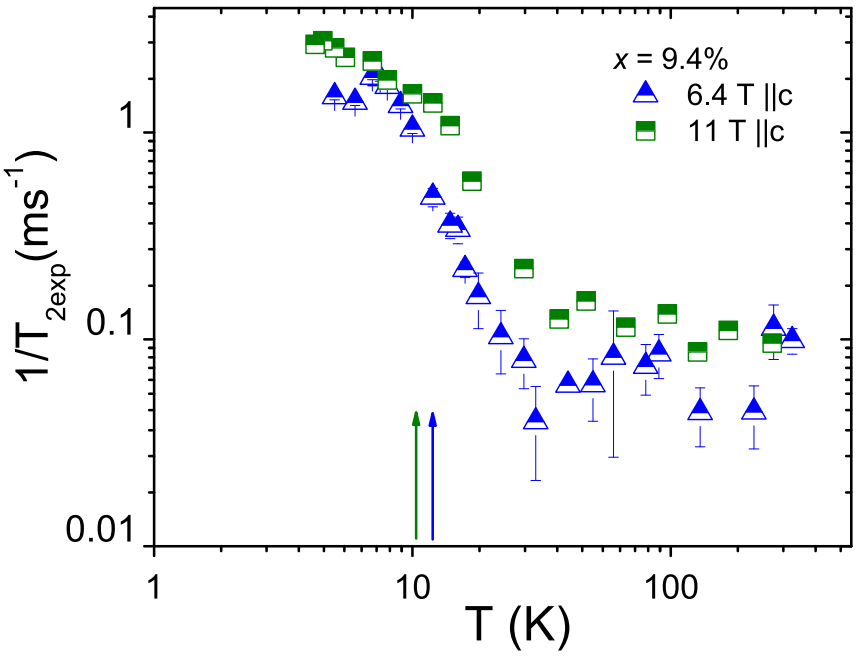

Figure 4.8: The exponential $1/T_2$ versus temperature is measured for x =9.4 %, with the field parallel to the c axis. The larger the field intensity, the higher the temperature when the dynamic starts to get slower (T*). The arrows mark T_c.

the three $Ba(Fe_{1-x}Rh_x)_2As_2$ crystals, for different magnetic field orientations (Fig. 4.7) and magnitudes (Figs. 4.7 and 4.13), one can conclude that the enhancement of $1/T_{2exp}$ has the following main features:

- the dynamic begins to slow-down above T_c;
- it is favored by the magnetic field;
- it is accentuated for in-plane fields;

- it persists across the whole phase diagram, up to the overdoped compound.

Fast motions

Further quantitative information on the correlation times describing the low-frequency activated dynamics, can be gained from the analysis of the spin-echo decay rate $1/T_{2exp}$. In fact, when the *HE* becomes exponential, $1/T_{2exp}$ can be fit by the *fast motions* expression [62, 69] (see Chapter 2)

$$\frac{1}{T_{2exp}} =^{75} \gamma^2 < h_{e\|}^2 > \tau_0 e^{U(H,x)/T} \tag{4.7}$$

where the energy barrier U is assumed to depend on the field intensity H_0 and on the Rh concentration x. The fit results, obtained by using the τ_0 value derived from $1/T_1$ (see section 4.3), are shown in Fig. 4.9. The reader may notice that U is field-independent, in the explored range, while it clearly depends on the electronic concentration, namely it decreases by increasing the Rh content. This trend indicates that the larger the electron doping, the faster the dynamics, which is in agreement with the expectations. In fact, when the compound lays into the underdoped region, a *static* antiferromagnetic order should set in [65]. Very recently a new NMR study, regarding the $Ba(Fe_{1-x}Co_x)_2As_2$ family [150], has shown a similar phenomenology both in the spin-lattice and spin-spin relaxation rates. The authors claim that their observations reveal the coexistence of frozen antiferromagnetic domains and superconductivity for $0.060 < x < 0.071$. The inhomogeneous glassy dynamics is argued to be an intrinsic response to the competition between superconductivity and antiferromagnetism.

4.2.2 The Gaussian contribution to T_2

Besides the exponential component of the spin-echo decay time, there is also a Gaussian contribution, which is weakly temperature dependent, and the value of which cannot be ascribed to the dipolar interaction among like As spins, since the experimental value of the T_{2G} is 3.6 times bigger than the theoretical prediction from the rigid lattice summations (0.7 ms) (see Appendix B). On the other hand Oh *et al.* in the ^{23}Na NMR investigation of $NaFe_{0.975}Co_{0.025}As_2$ found an experimental $T_2 = 0.34$ ms (at T_c) that is very close to the theoretical prediction (0.4 ms) [151]. Anyhow, the ^{75}As NMR study on the same compound still gives a much longer T_2, suggesting that the As nuclei interact via some kind of mechanism, which might be the exchange-narrowing one, debated in Chapter 1 [35]. On top of that, in $x = 7\%$ compound of $Ba(Fe_{1-x}Rh_x)_2As_2$ family, the spin-spin relaxation rate at low temperature agrees well with the Van-Vleck calculation [130].

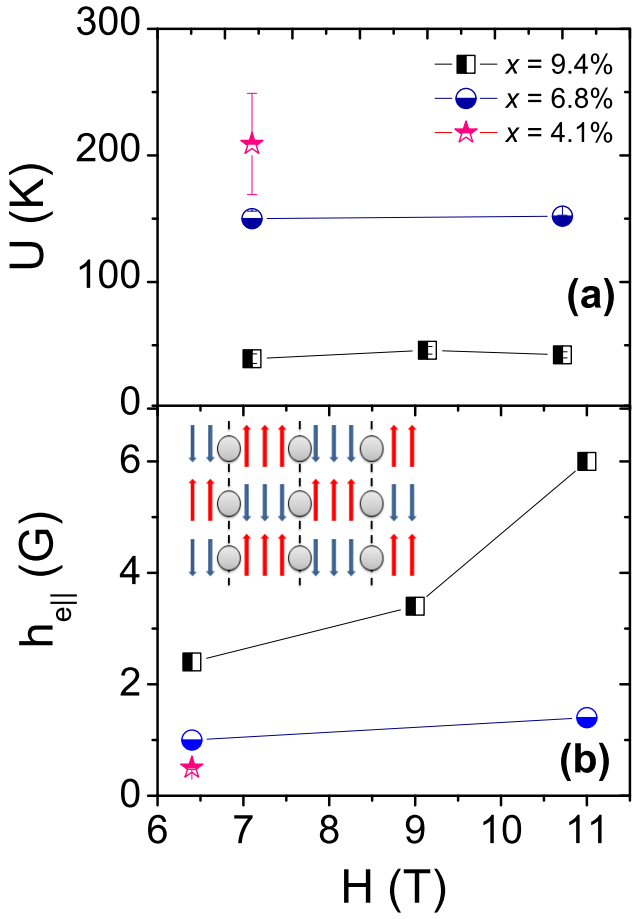

Figure 4.9: **(a)** The figure shows the energy barriers estimated from $1/T_{2exp}$ according to Eq. (4.7) at different doping. **(b)** The field dependence of the amplitude of the longitudinal field fluctuations is shown for different Rh concentration. A field and doping dependence is clearly visible for $x = 9.4\%$. The inset shows a sketch where columnar antiferromagnetic regions are separated by *antiphase* domain walls: the blue/red arrows stand respectively for the down/up spins, while the grey circles indicate the electronic charges which may favor the domain formation. Furthermore the fluctuating longitudinal local field $h_{e\|}$ shows a continuous increase with the applied field and the doping.

This was interpreted as the proof that the whole vortex excitations are frozen at low temperature and the only mechanism responsible for the spin-echo decay is the direct dipolar one (Fig. 4.10).

4.2.3 The *CPMG* sequence

T_2 becomes even longer when measured with the *CPMG* sequence. As recalled in Chapter 2, the *CPMG* sequence allows one to extract the intrinsic spin-spin

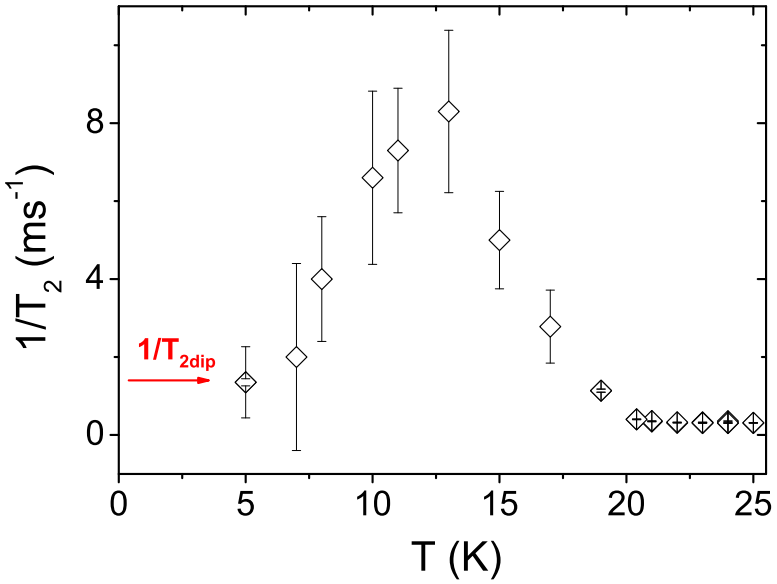

Figure 4.10: The figure shows the spin echo decay rate measured at 7 T $\parallel c$, for $x = 7\%$. The peak around 12 K has been ascribed to vortex lattice melting/freezing transition. The red arrow indicates the ab-initio value for $1/T_2$ given by the dipolar sums. T_c(7 T)$\sim$ 19 K.

relaxation time. In presence of a dynamic, the spin-spin relaxation time will depend on the τ_{CP} value, so a single *CPMG* sequence will not be very meaningful, and for this reason one should repeat the same sequence, by varying the τ_{CP}. An example is shown in Fig. 4.11. Afterwards, $1/T_{2CPMG}$ is extracted by an exponential fit of the echo decay. Remarkably, $1/T_{2CPMG}$ turns out to be linear with τ_{CP} (Fig. 4.12), instead of following a quadratic behavior, as expected in case of diffusive motion, taking place in a uniform gradient. A possible explanation is reported below.

It is recalled that the *HE* decay is well fit by the product of a Gaussian and exponential term, written here again, for the sake of clarity.

$$E(2\tau)/E(0) = \exp(-2\tau/T_{2exp})\exp(-(2\tau)^2/2T_{2G}^2). \tag{4.8}$$

After a generic τ, the echo will be reduced by:

$$\alpha = \exp(-2\tau/T_{2exp})\exp(-(2\tau)^2/2T_{2G}^2). \tag{4.9}$$

Accordingly, after the second π pulse, the echo amplitude will be:

$$E(2\tau) = E(0)\alpha^2. \tag{4.10}$$

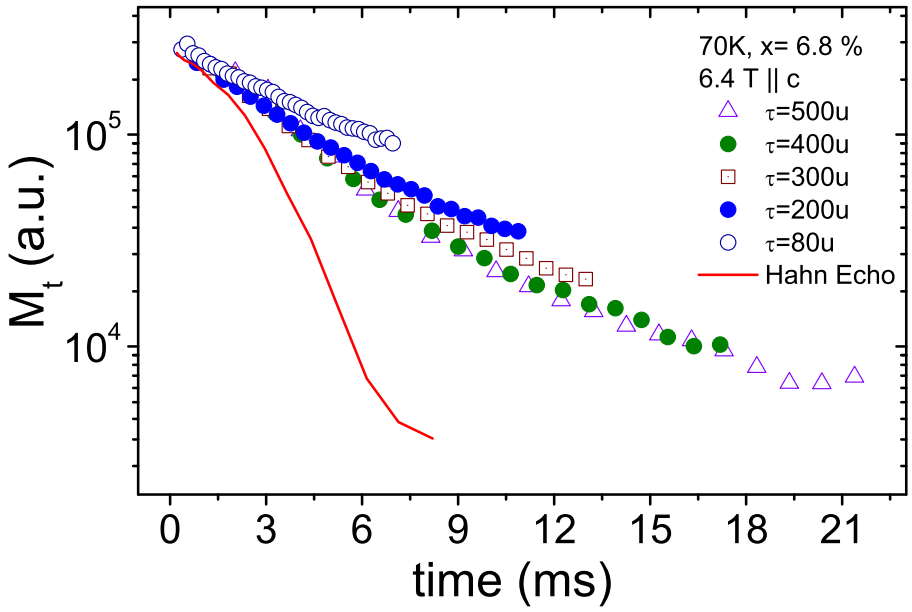

Figure 4.11: The decay of the transverse magnetization for Hahn Echo sequence (red solid curve) and CPMG at different τ_{CP}, for $x = 6.8\%$, at 6.4 T$\|$ c. This measurement was carried out in the normal state (70 K).

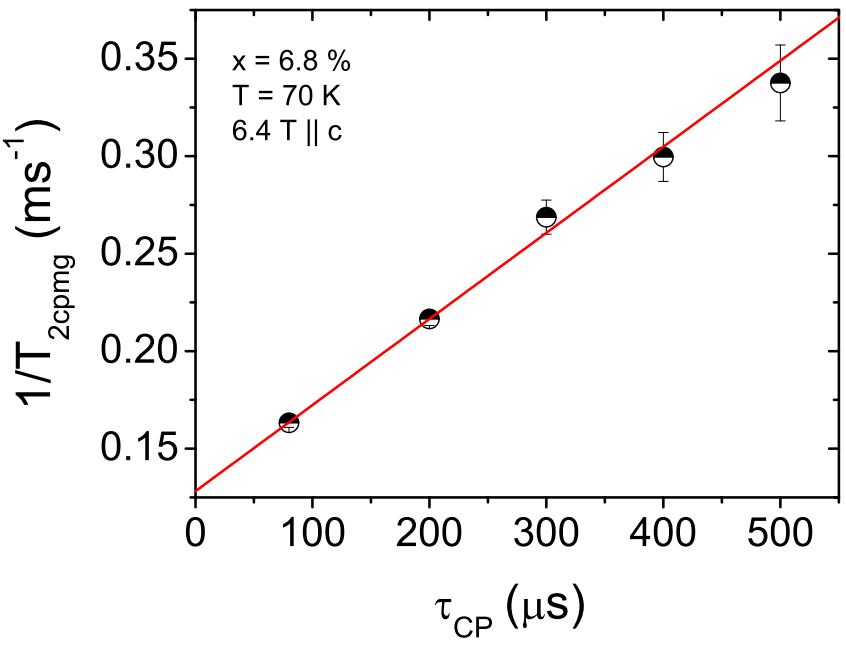

Figure 4.12: $1/T_{2cpmg}$ is plotted as a function of τ_{CP}. The measurement was carried out in the normal state (70 K) of $x = 6.8\%$, 6.4 T parallel c.

And finally, after the iteration of n pulses, one concludes that:

$$E(2\tau) = E(0)\alpha^n = \exp(-2n\tau/T_{2exp})\exp(-(2\tau)^2 n/2T_{2G}^2), \tag{4.11}$$

which can be written in a different form:

$$E(2\tau) = E(0)\exp\left(-\frac{2n\tau}{T_{2cpmg}}\right) \tag{4.12}$$

where the linear dependence of $1/T_{2cpmg}$ from τ is now straightforward:

$$\frac{1}{T_{2cpmg}} = \frac{\tau}{T_{2G}^2} + \frac{1}{T_{2exp}} \tag{4.13}$$

Notice that this argument is valid if the "Gaussian mechanism" (which is not longer visible via the *HE* sequence) is present as long as the *CPMG* sequence is performed.
If the results of two sequences are compared (Fig. 4.13), it appears that when the magnetic field is increased, the *HE* seems more sensitive to the slowing down of the dynamic, while the *CPMG* relaxation rate does not show any enhancement in the temperature range explored, as it remains weakly temperature dependent.

4.3 Spin-Lattice relaxation time T_1

The spin lattice relaxation rate $1/T_1$ was also measured over a broad range of temperatures, by a saturation recovery sequence. The raw data were fit according to the law for a magnetic relaxation mechanism, while irradiating the central transition $1/2 \rightarrow -1/2$ of a spin $I = 3/2$:

$$1 - m(t)/m_0 = 0.1e^{-t/T_1} + 0.9e^{-6t/T_1} \tag{4.14}$$

Noticeably, a bump in the spin-lattice relaxation rate was observed in the normal state, when $\mathbf{H_0} \perp$ c (Fig. 4.14) for x=9.4%. It is noticed that the correspondent $1/T_1T$ data for $\mathbf{H_0} \perp$ c, are quantitatively in agreement to those measured by Ning *et al.* [42], in $Ba(Fe_{1-x}Co_x)_2As_2$ crystals, for the same magnetic field orientation. The comparison of $1/T_1$ for the two crystal orientations suggests to fit the data measured for $\mathbf{H_0} \perp c$ with a Bloembergen-Purcell-Pound (*BPP*) law [62, 73], accounting for a low-frequency activated dynamic (Fig. 4.14), plus a power law trend T^α ($\alpha \rightarrow 1$), which characterizes these compounds when $\mathbf{H_0} \parallel$ c. More explicitly:

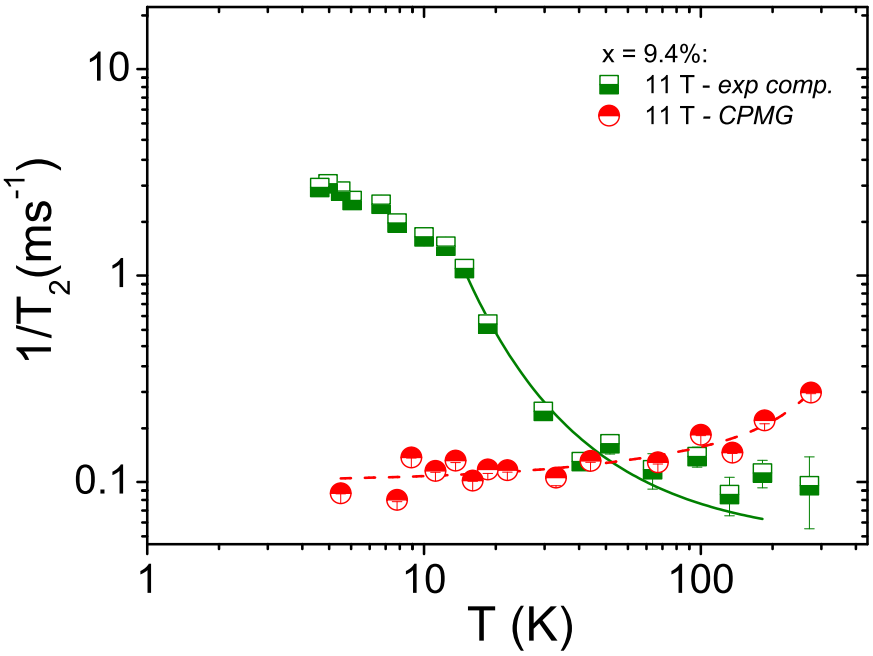

Figure 4.13: The green squares refer to the Hahn Echo $1/T_2$ while the red circles refer to the *CPMG* relaxation rate. Below $T_c \sim 11$ K, the curves deviate more than 1 order of magnitude from each other. The green solid curve is the best fit to the equation of fast motion, while the red dotted line is just a guide for the eye.

$$\frac{1}{T_{1\,\|ab}} = \gamma^2 h_\perp^2 \frac{\tau_c}{1+\omega_L^2\tau_c^2} + T^\alpha \tag{4.15}$$

$$\frac{1}{T_{1\,\|c}} = T^\alpha \tag{4.16}$$

where the first equation refers to the case where $\mathbf{H_0} \perp c$, while the second equation refers to $\mathbf{H_0} \parallel c$. By assuming an activated correlation time:

$$\tau_c(T,H) = \tau_0 e^{U/T}, \tag{4.17}$$

an energy barrier of $U = 50 \pm 5$ K, a correlation time at infinite temperature of $\tau_0 = 5.2 \times 10^{-10} s$, and the average fluctuating hyperfine field of $h_{e\perp} = 1.94 \pm 0.22$ G were found. Such parameters are comparable with the ones recently reported by Hammerath *et al.*, in underdoped $LaO_{1-x}F_xFeAs$ [47]. Two possible reasons for the anisotropy in $1/T_1$ should be considered:

- the role of the magnetic field in inhibiting the low-frequency fluctuations when $\mathbf{H_0} \parallel$ c;

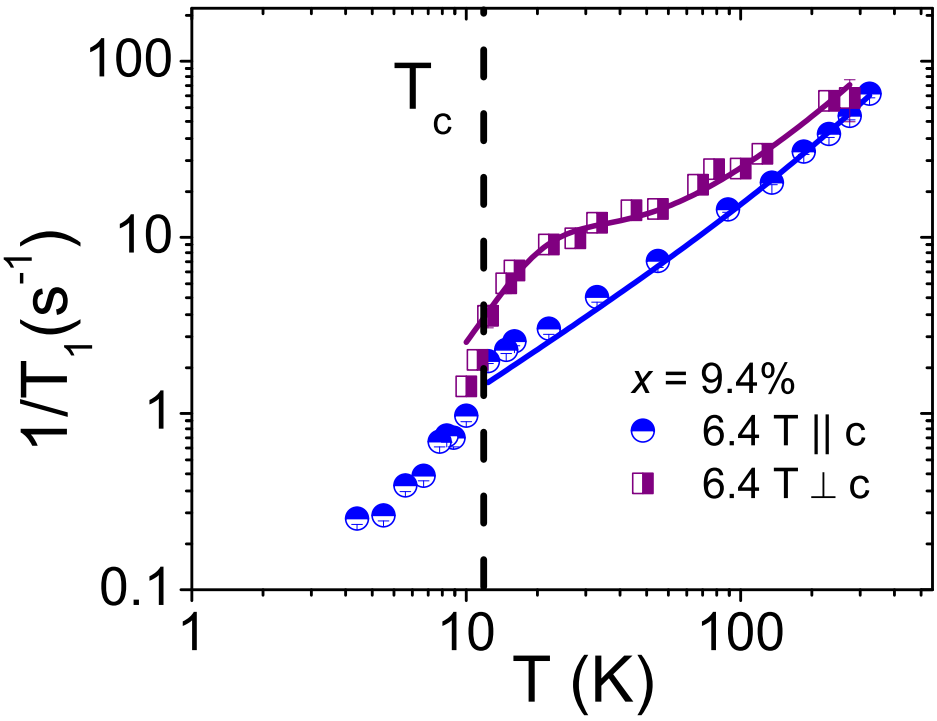

Figure 4.14: $1/T_1$ versus temperature measured at two orientations, for the $x = 9.4\%$. The solid lines are best fit to the equations above.

- the filter effect of the hyperfine form factor [65] (see Appendix A).

Given the behavior of $1/T_{2exp}$ for the different magnetic field orientations, the former framework appears more likely. Moreover Lester *et al.* provided clear experimental evidence for anisotropic spin excitation, through inelastic neutron scattering experiments [48].

4.4 Interpretative scenario

The low-frequency dynamics evidenced by $1/T_{2exp}$, by the linewidth and by the bump in $1/T_1$, cannot be ascribed to standard correlated electron spin fluctuations, which are of the order of the Heisenberg frequency, or to superconductive fluctuations, which typically occur at frequencies orders of magnitude larger than the frequency probed here. One should rather look for very low-frequency fluctuations, as the ones occurring close to a spin (or charge) freezing, or also taking place among quasi-degenerate ground-states. In this respect, one should consider that, owing to the geometry of the relevant exchange couplings, the magnetic properties of the iron pnictides have often been described within an effective J_1-J_2 model on

a square lattice [44]. The ground-state of that model is indeed characterized by two degenerate columnar antiferromagnetic ground-states corresponding to two nematic phases, with critical wavevectors $\mathbf{Q_c}(\pm\pi/a, 0)$ or $\mathbf{Q_c}(0, \pm\pi/a)$. Because the two states have the same energy, namely they are frustrated, slow quantum fluctuations may occur between these two states. In fact in vanadates, which can be considered the prototypes of that model, low-frequency fluctuations have been detected by μSR, above the magnetic ordering [143], in a temperature range where the electron spins are already correlated [142]. These dynamics can be associated with domain walls motion, separating correlated regions of the two nematic states. Such walls are intrinsic non-equilibrium structures, as they have an excess of free energy, that will induce their motion, in order to minimize their occupied area [49] (Figs. 4.9 and 4.15).

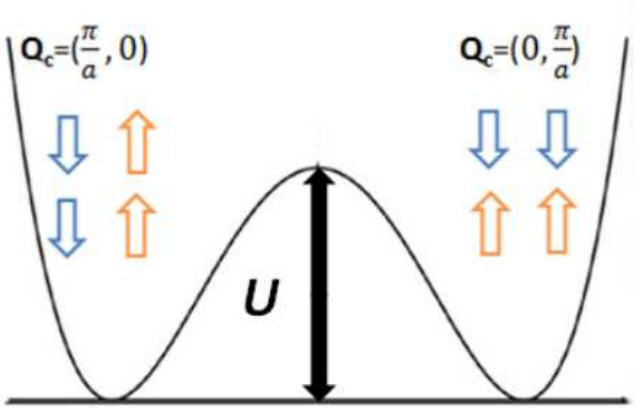

Figure 4.15: Sketch of the double potential well separating two collinear phases. The iron spins are represented together with the critical wavevector. The domain wall can develop among these two phases and can be put into motion.

A similar scenario has also been proposed in a recent study of the magnetic state of $CaFe_2As_2$ [131], where resistivity, magnetization and microscopic ^{75}As nuclear magnetic resonance measurements, in the antiferromagnetically ordered state, exhibit anomalous features that are consistent with the collective freezing of domain walls. Below a certain temperature, Xiao *et al.* [131] observed a peak in the resistivity and a downturn, plus a sharp increase in the bulk magnetization. ^{75}As NMR measurements reveal the presence of slow fluctuations of the hyperfine field. These features emerging both in the charge and in spin channels, are strongly field dependent and suggest the presence of filamentary superconductivity, nucleated at the antiphase domain walls.
Finally, an interesting analogy with the spin/charge stripe dynamics observed in

Spin/charge stripes

the cuprates, can be suggested. In fact, in Hg-based high-T_c superconductors, an enhancement in $1/T_2$ and $1/T_1$, with respect to the magnetic field has been observed. Also in this case, when $\mathbf{H_0} \parallel$ c, the spin fluctuations are reduced. Such an effect is reminiscent of the field-induced charge order, recently reported in underdoped $YBa_2Cu_3O_{6+x}$, where the blocking of the charge order occurs only if $\mathbf{H_0}$ is perpendicular to the highly conductive CuO_2 layers [144, 152]. In the light of these analogies, one could speculate that very low-frequency fluctuations associated with domain walls motion, involving charge stripes, are present both in the cuprates and in the iron-based superconductors. However, further experiments are required to support such a scenario.

4.5 Knight Shift in the normal state

As it has been shown in the previous paragraphs, the normal state of iron-pnictides reveals exotic and unconventional features. Another remarkable example, is the temperature behavior of the Knight Shift of 122 compounds. Indeed K(T) shows an activated behavior with the temperature, that is currently under discussion. Indeed, the experimental data shown in Fig. 4.16 on $x = 7$ %, can be fit to an equation:

$$K(T) = A + B\exp(-D/T),$$

yielding $A = 0.26$ %, $B = 0.071$ % and $D = 225 \pm 22$ K, in good agreement with the values found in Ref. [35]. The interpretation suggested here starts by considering the Van-Hove singularities occurring in the Density of States (DOS), which are evidenced by DFT calculations (Fig. 4.17). Such singularities can provide some insights into the anomalous temperature dependence of the spin susceptibility. In fact, by assuming a Pauli-like susceptibility for free electron spins [74, 153]:

$$\chi(T) = \mu_B^2 \int_0^\infty \left(-\frac{\partial f(E,T)}{\partial E}\right) D(E)dE \tag{4.18}$$

and inserting the DOS, calculated by the DFT theory, the spin susceptibility as a function of the temperature can be worked out, with one adjustable parameter, which is the Fermi level. As it is observed in Fig.4.18, the qualitative and quantitative results are fairly well reproduced, but only after adjusting "ad-hoc" the Fermi level.

Very Recently, Chaloupka and coworker [51] proposed a novel many-body approach to justify the quantum magnetism of the iron-pnictides (see Chapter

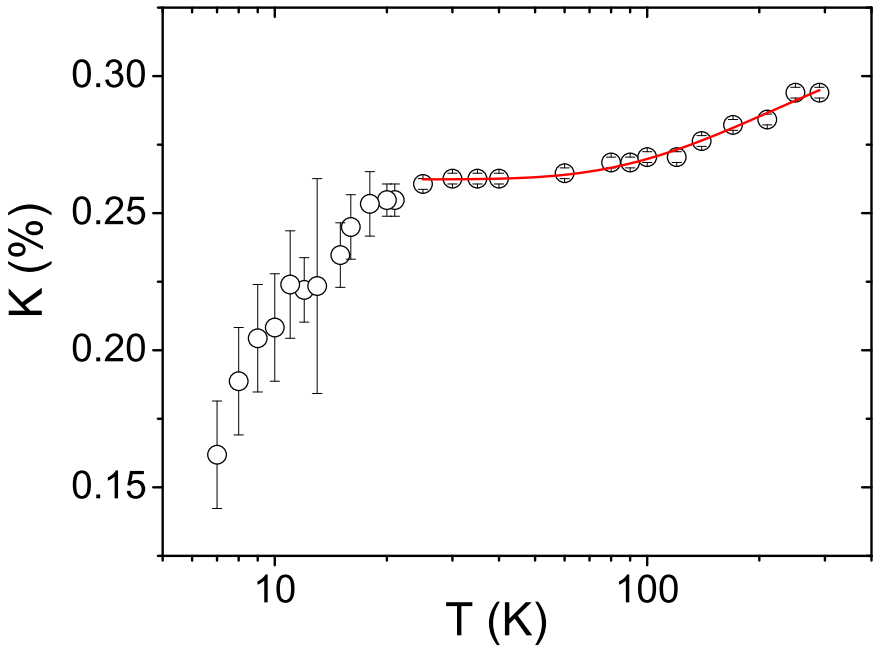

Figure 4.16: The figure shows the Knight Shift at 7 T $\parallel c$, for x=7%. The red line is the Arrhenius fit. $T_c \sim 19$ K.)

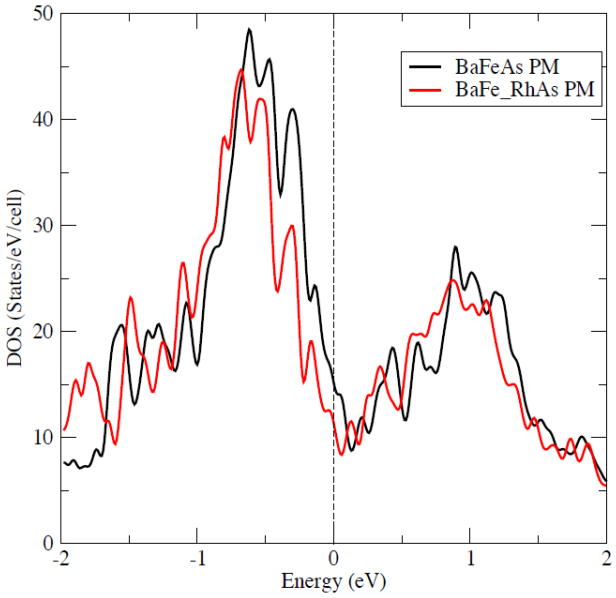

Figure 4.17: The DOS for the parent compound (black line) and the x=12.5% compond (red line), in the paramagnetic state, display Van-Hove singularities, around the Fermi level. The DFT analysis was done by G. Profeta (University of L'Aquila).

1 for details), invoking a dynamical mixing of quasi-degenerate states of Fe^{2+}, resulting into an effective local spin S_{eff}, that has a dependence on pressure

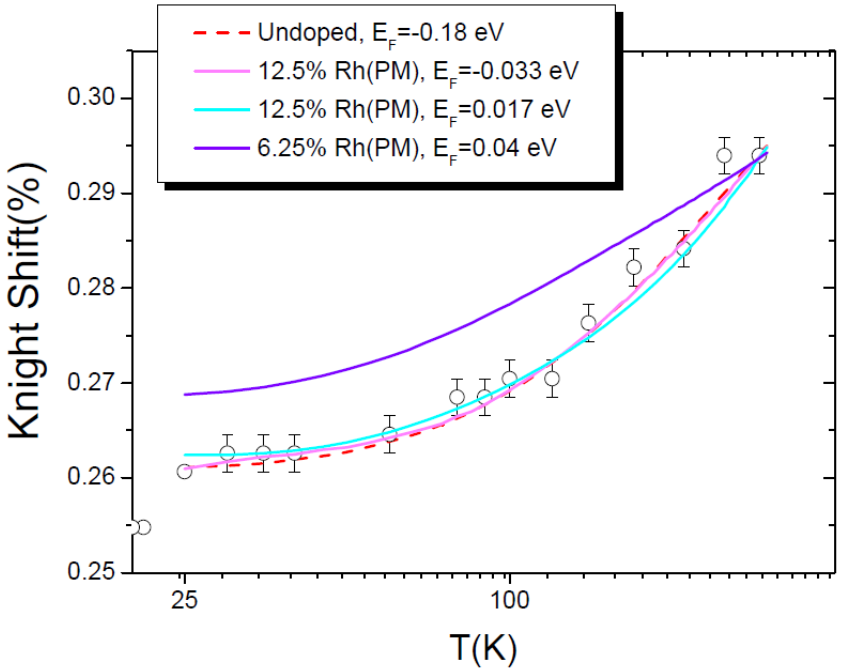

Figure 4.18: The Knight Shift as a function of the temperature (black circle) is compared with the simulations obtained by the DOS of a paramagnetic compound, for different doping concentrations, and in correspondence to different Fermi levels, which are free parameter.

(external or chemical) and temperature. They claim that singlet correlations inherent to the model may lead to an increase of the paramagnetic susceptibility upon warming. Considering the nonmagnetic phase, they found that the spin susceptibility turns into:

$$\chi(T) \sim \frac{1}{2T} \int \frac{N(\omega)}{\sinh^2(\omega/2T)} d\omega \tag{4.19}$$

where $N(\omega)$ is the density of states of magnetic excitations. The DOS is contributed mainly by the regions around the CAF critical wavevectors, hosting antiferromagnetic correlations. The resulting spin susceptibility is reported in Fig. 4.19. Finally, the temperature activated behavior of the knight shift is an implicit result of this model.

4.5.1 The Hyperfine coupling

The study of K(T), in the normal state, is remarkably useful also to derive the hyperfine field tensor. Indeed if the Knight Shift is plotted as a function of the

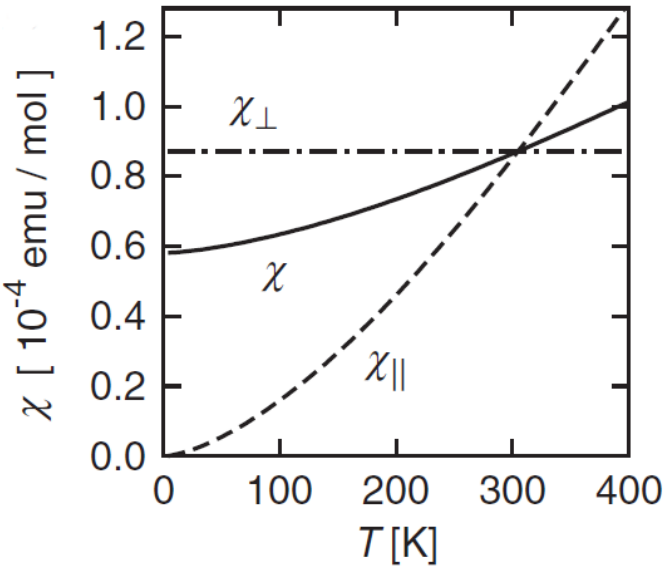

Figure 4.19: Temperature dependence of the uniform susceptibility, for parallel and perpendicular components to the local director of the stripe order [154]. The figure is adapted from Ref. [51].

Spin susceptibility (Fig. 4.20), with the temperature as an implicit parameter, one can observe a linear dependence. Here the zz component of the total hyperfine field is $A_{hyp}^{zz} = 43.99 \pm 6.25$ kG, which is reasonably close to the value found in literature: $A_{hyp}^{zz} = 18.8$ kOe/μ_B=37.6 kOe for the parent compound of $BaFe_2As_2$ [43] and 23 kOe/μ_B = 46 kOe for the parent compound of $CaFe_2As_2$ [131]. If the same calculation is repeated for $\mathbf{H_0} \in (a, b)$ plane (Fig. 4.21) one gets $A_{hyp}^{xx} = 102.7 \pm 6.25$ kG. The ratio $\frac{A_{hyp}^{xx}}{A_{hyp}^{zz}} = 2.33$ is larger than the literature value, i.e. 1.4, that can make wonder about the possible dependence of the hyperfine coupling on the temperature. This possibility has been discussed by some authors, but no detailed investigations have been done, so far. The Knight shift consists of the temperature dependent Spin Shift K_s, the temperature independent chemical K_{chem} and orbital K_{orb} shifts. In case of transition metals compounds, the angular orbital moment $\mathbf{L}$ is quenched (at the first order), then:

$$K(T) = K_{chem} + K_s(T).$$

Likewise, the susceptibility is the sum of the contributions from core diamagnetism, Van Vleck paramagnetism, and spin paramagnetism:

$$\chi(T) = \chi_{dia} + \chi_s(T).$$

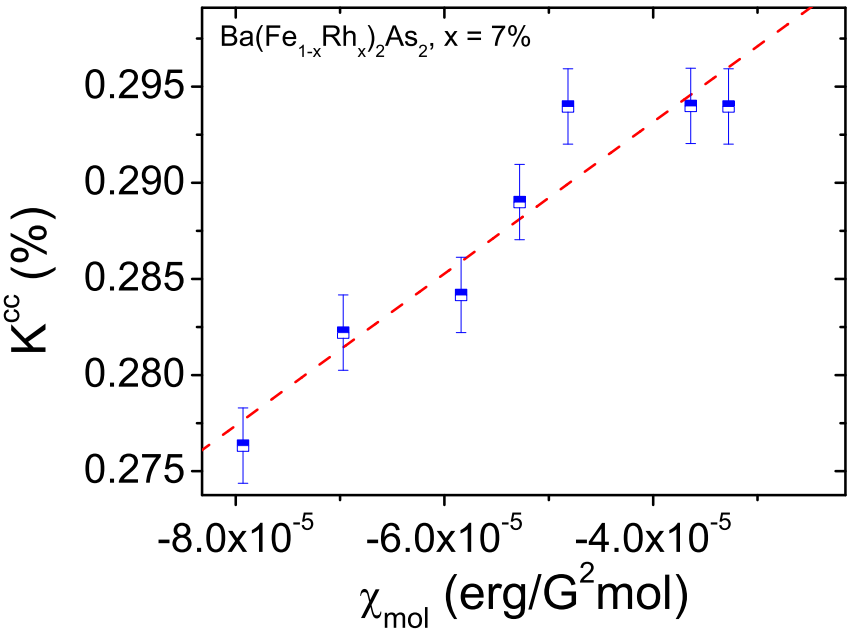

Figure 4.20: Knight Shift versus the Spin Susceptibility for x=7%, as measured by NMR and SQUID, respectively (at 7 T$\|$ c).

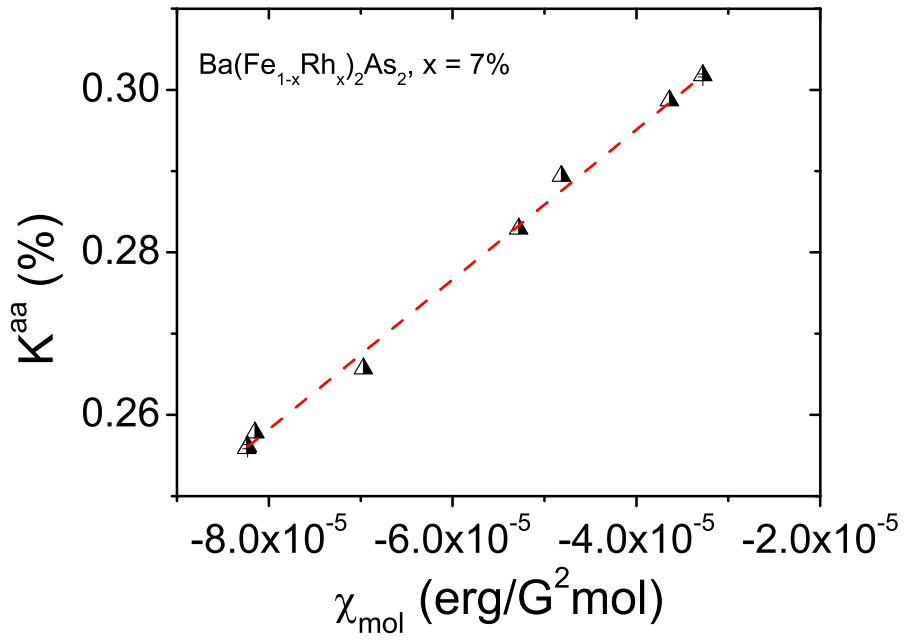

Figure 4.21: Knight Shift versus the Spin Susceptibility for x=7%, as measured by NMR and SQUID, respectively (at 7 T$\perp$ c).

In absence of a structural/magnetic phase transition, the hyperfine constants are supposed not to change with the temperature:

$$K^{aa}(T) = A^{aa}_{hyp}\chi(T) + K_{chem} + K_Q \quad (4.20)$$

$$K^{cc}(T) = A^{cc}_{hyp}\chi(T) + K_{chem}, \quad (4.21)$$

where K_Q is the quadrupolar contribution to the shift. For the central line, the quadrupolar frequency can be estimated to be $\nu_Q(100\ \mathrm{K}) \sim 1.5$ MHz, very close to the parent compound [155]. After some algebra, the previous system can be worked out

$$K^{aa}(T) = A^{aa}_{hyp}\frac{[K^{cc}(T) - K_{chem}]}{A^{cc}_{hyp}} + K_{chem} + K_Q = \alpha K^{cc}(T) + T.I., \qquad (4.22)$$

where $T.I.$ denotes the temperature independent terms.[2] By plotting $K^{aa}(T)$ versus $K^{cc}(T)$ the ratio $A^{aa}_{hyp}/A^{cc}_{hyp}$ is found. The results are shown in Fig. 4.22. The angular coefficient turns out to be $\alpha = 2.07 \pm 0.23$, in agreement with the

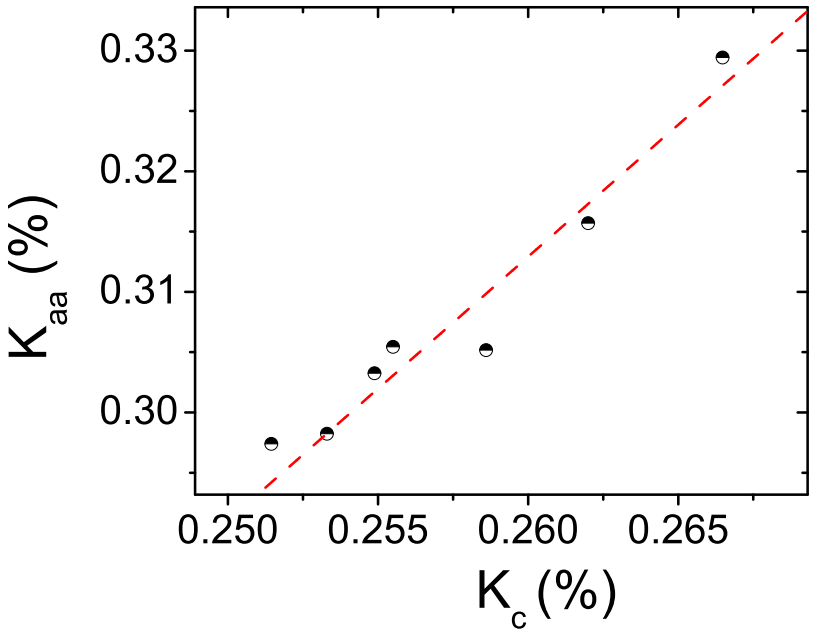

Figure 4.22: In-plane shift versus the out-of plane shift, for the x=9.4% compound measured at 6.4 T.

ratio found before. The hyperfine field tensor finally becomes:

$$A_{hyp} = \begin{bmatrix} 102.7 & 0 & 0 \\ 0 & 102.7 & 0 \\ 0 & 0 & 44.39 \end{bmatrix} kOe.$$

[2]The symbols (a, b, c) are used interchangeably with (x, y, z).

4.6 Conclusions

This Chapter presents a systematic study of the spin-echo decay rate in 122 iron-pnictides, over a broad doping range. A low-frequency spin dynamic is responsible for a bump in the spin-lattice relaxation time, as well as for an enhancement of the exponential component of the spin-echo decay rate. Such dynamics are common at all the doping concentrations, and get faster in the overdoped regime. One possible explanation is found in the onset of domain walls motion, possibly involving nematic fluctuations. The remarkable analogies with the cuprates indicate the need for a deeper investigation, also by other techniques. Moreover this phenomenology may shed some light into the hot topic of spin fluctuation-induced-superconductivity.

Moreover, the activated behavior of the Knight Shift with temperature is reported, and two interpretative scenarios are suggested. Such issue still represents a challenge for the NMR solid state community.

Finally, the study of the Knight shift versus the molar spin susceptibility allows one to derive the hyperfine field tensor.

Chapter 5

NMR and ac-susceptibility investigation of vortex dynamics in $Ba(Fe_{0.93}Rh_{0.07})_2As_2$ superconductor

In the first Chapter it has been shown that the iron-pnictide superconductors display promising qualities, regarding technological applications. Yet, once a current is injected, flux dynamics may lead to energy dissipation, which in turn prevents any efficient application. With regard to this, the pinning mechanism is very helpful to restore the resistanceless state [58]. Accordingly, the understanding of the pinning properties, such as J_c, the correlation times for the vortex motions τ_c, the pinning activation barrier U, their dependence on the magnetic field H and temperature T, has major relevance. When fields of some Tesla are applied, the time-scale of the vortex dynamics matches the nuclear magnetic resonance (NMR) and ac-susceptibility time-scales. As a consequence, these two experimental tools are excellent to study the pinning effect, and their joint employ provides complementary information on the vortex dynamics. In both cases the vortex lattice (VL) excitations are probed in the radio-frequency range but, while ac-susceptibility is sensitive to dissipative/dispersive mechanisms taking place at wave-vector $\mathbf{q} \rightarrow 0$, NMR is sensitive to the $\mathbf{q}$-integrated dynamics.
Besides the applications, the study of the vortex dynamics, in particular in low-dimensional systems, can reveal interesting scenarios. In fact, even in absence of an external current, the vortex lattice can experience a dynamic owed to thermal fluctuations. On the other hand, the presence of quenched disorder, such as crys-

tal defects, or atomic substitution, may hinder the motion and drive a crossover from a liquid vortex state to a vortex glassy state [58, 156–158], instead of the well ordered solid phase predicted by Abrikosov. In case of weakly anisotropic superconductors, such as the 122 family of iron-pnictides, the phase diagram is characterized, just below the upper critical field line, by a high mobility state of vortex lines [159]. The nature of such a motion is quite complex, since it involves the interplay among the pinning forces, the intervortex repulsion/attraction [58] and the thermal excitations. By taking advantage of the work carried out in cuprates, it is worth extending the investigation of the vortex lattice (VL) to the iron-based superconductors, bearing in mind the different structural and physical properties. In particular, the small anisotropy of the iron-based superconductors has the effect of reducing the extension of the liquid region, as the FLL becomes quite stiff.

This chapter deals with the NMR and ac-susceptibility results obtained on a nearly optimally doped (slightly overdoped) member of the $Ba(Fe_{1-x}Rh_x)_2As_2$ family, namely $x = 7$ %. Below the superconducting transition temperature T_c, when the magnetic field is applied along the c axis, a peak in $1/T_1$ and $1/T_2$ rates has been observed. Remarkably the peak in $1/T_1$ is totally suppressed when $\mathbf{H} \perp c$. The maxima in $1/T_1$ and $1/T_2$ have been ascribed to flux line lattice (FLL) motion, and the corresponding correlation times and pinning energy barriers have been derived on the basis of a phenomenological model. Further information on the flux lines motion was derived from the narrowing of the NMR linewidth below T_c, and it was found consistent with $1/T_2$ measurements, in the light of thermally activated vortex motion theory.
Further studies were performed, by employing higher fields (namely 11 and 15 T) at the Laboratoire National des Champs Magnétiques intenses (Grenoble). A complementary investigation was done by using ac-susceptibility, on the same single crystal. In this second step, the characteristic correlation times for the vortex dynamics have been derived. Upon cooling, the vortex dynamic displays a crossover consistent with a vortex glass transition. It shall be shown that the correlation times, in the fast motions regime, merge onto a universal curve which is fit by the Vogel-Fulcher law. Moreover, the pinning barrier shows a weak dependence on the magnetic field, which can be heuristically justified within a fragile glass scenario. In addition, the glass freezing temperatures obtained by the two techniques merge onto the de Almeida-Thouless line. Finally the phase diagram for the mixed phase has been drawn.

5.1 Introductory remarks

While Abrikosov predicted the formation of a well ordered arrangement of vortices, i. e. the flux lines lattice, in many cases experimental results evidenced that no order exists at large distances, while a short-range order survives. In such case, it is more appropriate to speak of a vortex glass state [58].

Thermal fluctuations

At finite temperature, the vortices can be thermally excited, and for evanescent external currents, they give rise to a flux creep motion, which is characterized by activated jumps from one pinned site to the other. In high-T_c superconductors, thermal depinning is observed in large intervals below the transition temperature. The term "giant flux creep" was introduced by Yeshurun and Malozemoff [160] to describe the phenomenon of very large creep rates characteristic of the oxide superconductors. The vortex creep leads to irreversible behaviors below the so-called irreversibility or depinning line.

Thermal depinning is enhanced by two factors [161]

- small coherence lengths ξ;
- large penetration depths λ;

In fact the depinning energy U, for small pinning centers, is written as

$$U = \frac{\Phi_0^2 c\xi}{32\pi^3\lambda^2},$$

where large penetration depths soften the FLL and decreases the pinning energy. Also the anisotropy ratio γ plays an important role in the pinning process. The 122 iron-based superconductors have very small coherence lengths, namely 1-3 nm, and quite large penetration depths, 100-300 nm, which lead to large κ. However the anisotropy is about $1 \div 3$. Moreover, G_i values [24] suggest that thermal fluctuations are limited to a narrow temperature range, hence any fluctuating phenomenon will be quite depressed, as compared to the high-T_c cuprates.

One of the main effects of thermal fluctuations is the smoothing of the quenched disorder potential producing the pinning. In fact, owing to thermal motion, the vortex core will probe the disorder potential, over an extended spatial region. As the amplitude of the thermal fluctuations increases beyond the extent of the vortex core, the vortex will experience an averaged disorder potential, and thereby the pinning will be reduced [58].

In weakly anisotropic systems, the flux line can be modeled as a 3D string, with

its own elastic energy. On the opposite limit, in strongly layered superconductors, Glazmann and Koshelev [162] showed that above $B_{cr} \sim \Phi_0^2/(\gamma s)^2$,[1] there is a dimensional crossover of the vortex lattice, between 2D and 3D. $Ba(Fe_{1-x}Rh_x)_2As_2$ compounds display a crossover field of 1.38 x 10^3 T, hence vortices have to be considered as 3D objects.

When vortices become so dense that their field profile overlaps (namely $H > 2H_{c1}$) and thermal fluctuations start to be less effective, the vortex matter eventually turns into a solid state. If no pinning is present, vortices form a well-ordered periodic structure, namely a lattice. However, the presence of quenched disorder may give rise to a low-temperature glassy state, where the long-range order is destroyed. Bitter pattern decorations and miscroscopic techniques have shown such disordered state [87, 163]. From the viewpoint of applications, the glass line determines the crossover below which the vortices can be pinned or supercurrent can still survive. In 2012 Ghorbani and coworkers [164] studied the vortex liquid-to-glass transition in $Ba_{0.72}K_{0.28}Fe_2As_2$, $Ba(Fe_{0.91}Co_{0.09})_2As_2$, and $Ba(Fe_{0.95}Ni_{0.05})_2As_2$ single crystals, by magnetoresistance measurements, and they found that non-magnetic K doping results in a high glass line close to the upper critical field line, while magnetic Ni and Co doping causes a low glass line which is far away from the same line. Magnetoresistance is indeed the easiest way to study the liquid-glassy transition. Usually in the vortex liquid, resistivity is described within a thermally assisted flux flow (TAFF) model [58]

Vortex glass

$$\rho(T, H) = \rho_n \exp(-U/k_B T) \tag{5.1}$$

where ρ_n is the normal state resistivity. The pinning barrier can be derived from the derivative $\frac{\partial \rho}{\partial(1/T)}$. The authors found a value of U equal to 192 K, 77 K, and 32 K for BaK-122, BaCo-122, and BaNi-122 single crystals respectively, suggesting that the non-magnetic impurity is more effective in the pinning process. Moreover the field dependence of the pinning barriers shows a crossover from single pinning to collective pinning (Fig. 5.1). Ghorbani *et al.*, and more recently Pervakov [165], employed the Vogel-Fulcher relation to interpret their resistivity data. Hereafter it will be shown that the same approach has been employed in this work, to describe the vortex correlation time, *independently from Ghorbani and Pervakov's results.*

Vortex liquid

[1] s is the interlayer distance.

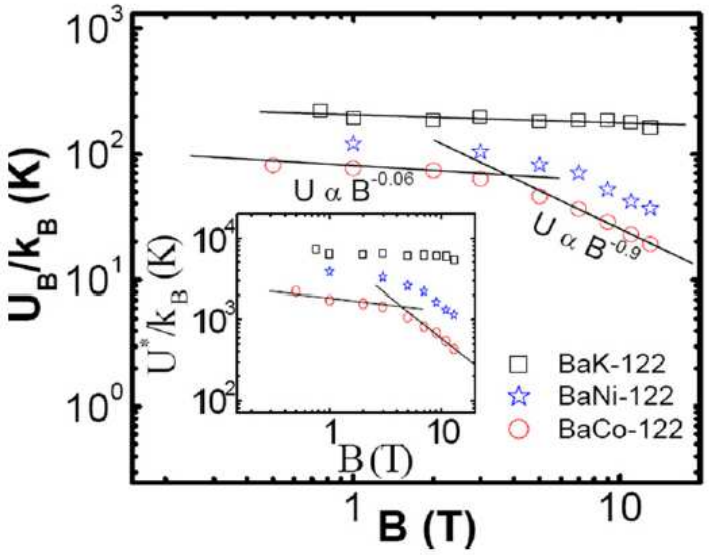

Figure 5.1: Magnetic field dependence of the pinning activation energy, for different compounds (see text). Notice that the K-doped compounds show weak field dependence, as expected from a single vortex mechanism, while in the other two compounds there is a crossover to a power-law. The inset refers to a fit based on the thermally activated flux flow (TAFF) model. Figure adapted from Ref. [164].

In addition to the macroscopic techniques, also the microscopic ones are employed to study the vortex state properties. Since the discovery of the iron-based superconductors [1] a systematic study of the vortex lattice was not possible until high quality single crystals were available [6].
In the past years a fruitful study performed on the cuprates [141,166,167] showed that the NMR linewidth and the spin-lattice relaxation times were effective markers of the vortex dynamics. Moreover, these two NMR observables provide complementary information, as the linewidth narrowing is sensitive to the magnetic field fluctuations along the direction of the external field, while the spin-lattice relaxation time is sensitive to the transverse field fluctuations.
Thanks to the study performed on the cuprates, it is now known that within anisotropic superconductors vortices can be considered as independent two-dimensional isles called "pancakes", which undergo diffusive thermal motions [22, 168]. Bearing this in mind, and looking at the structural similarities between cuprates and pnictides, some questions naturally rise: *is it possible to probe the thermal activated vortex dynamics in 122-pnictides by NMR, despite the narrow fluctuating range? What is the vortex structure in the new iron-based compounds? What is the nature of the frozen vortex state?* Motivations
In order to answer these questions, an NMR study of the superconducting state

of $Ba(Fe_{1-x}Rh_x)_2As_2$, with x$\sim$ 0.07, was performed. The spin-lattice ($1/T_1$) and spin-echo ($1/T_2$) relaxation rates of the ^{75}As nuclei, together with the Knight Shift and the NMR linewidth, at two different field intensities (7 T and 3 T) and orientations ($\mathbf{H} \parallel$ or $\perp c$) were initially measured.

The sample was grown by self-flux method according to the procedure reported in Ref. [26] and presented in Chapter 1. The sample looks like a flat 0.8 x 5 x 7 mm^3 parallelepiped shaped crystal, with the c axis along the shortest side. At $x = 7$ % both the structural and antiferromagnetic phase transitions are suppressed. To provide a first characterization of the crystal, the field cooled (FC) and zero field cooled (ZFC) magnetization were measured by means of a Quantum Design MPMS-XL7 Superconducting QUantum Interference Device (SQUID) magnetometer. The irreversibility line was estimated looking at the temperature where the ZFC curve departs from the FC one, as in Ref. [169], and it was found in agreement with the detuning of the NMR tank circuit [166] (Fig. 5.2).

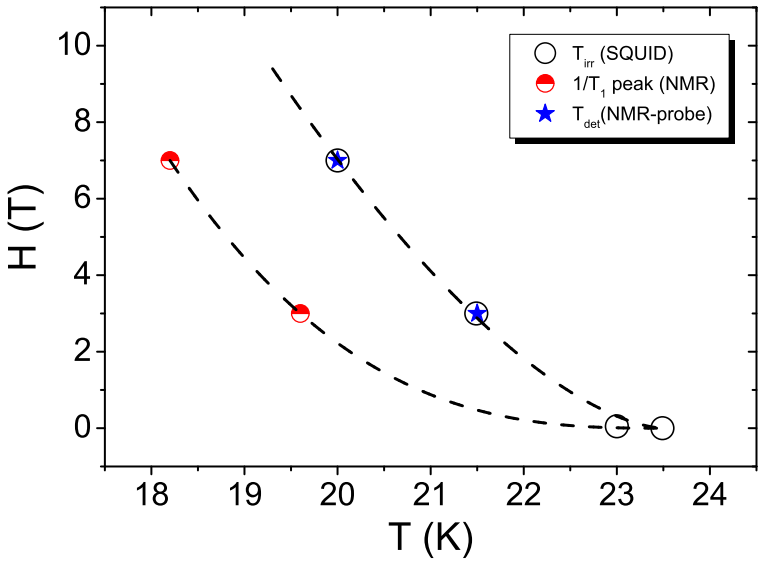

Figure 5.2: The irreversibility temperature measured with a DC SQUID magnetometer (open circle) is compared with that derived from the detuning of the NMR probe (blue stars). The red circles refer to the temperature of the peaks in $1/T_1$. The dotted lines are guides for the eye.

5.2 NMR Investigation of the vortex lattice

5.2.1 "Historical peaks" in $1/T_1$

The peaks emerging in $1/T_1$, and presented in the following sections are not a unique case in the study of the FLL via NMR. Indeed there are some widely agreed cases concerning the cuprates, as already mentioned. ^{89}Y NMR in YBCO, and ^{199}Hg NMR in $HgBaCuO_{4+\delta}$ (both oriented powders with $\mathbf{H} \parallel$ c) are reported here, for illustrative purposes (Fig. 5.3).

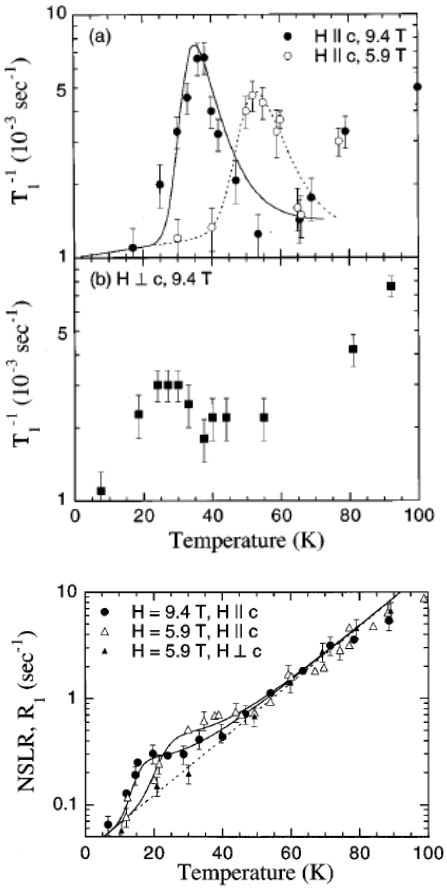

Figure 5.3: (Top panel) The spin-lattice relaxation rate, measured at different field intensities and orientations on Y. The Figure is adapted from Ref. [170]. (Bottom panel) Similar measurement on Hg nucleus. The Figure is adapted from Ref. [171].

In the previous picture a non-negligible dependence on the field orientation is reported.
More recently Laplace and coworkers found a similar peak in the superconducting

and normal phase of $Ba(Fe_{1-x}Co_x)_2As_2$ with x=6%, a sample which is expected to show the coexistence of superconductivity with magnetism [172]. The presence of the peak below T_c has been ascribed to the FLL dynamics.
Moreover, in 2009 Baek *et al.* [173] found a sharp peak in the $1/T_1$ just in the superconducting region of Ca122 compound. Such a feature disappeared in null field, and when strong fields ($H > 8$ T) were applied. Such behavior is still reminiscent of the cuprate superconductor, and this lead the authors to suggest a tentative interpretation related to FLL dynamics.
Hereafter the results on the Rh-doped Ba122 compounds are presented and discussed.

5.2.2 Spin-Lattice relaxation time

The NMR measurements were performed by using standard radiofrequency pulse sequences, as explained in Chapters 2 and 4. Initially, the spin-lattice relaxation time T_1 was measured by means of a saturating recovery pulse sequence, at two different magnetic fields $H = 7$ T and 3 T. The recovery of the nuclear magnetization $m(t)$ was fit to the relation [155, 174]:

$$1 - m(t)/m_0 = 0.1e^{-t/T_1} + 0.9e^{-6t/T_1} \tag{5.2}$$

expected for a nuclear spin $I = 3/2$, in case of magnetic relaxation (see Fig. 5.4). In the normal phase, $1/T_1T$ shows a temperature independent behavior, as expected for a weakly correlated metal (see the inset of Fig. 5.5).[2] In this case, scattering processes with the conduction electron spins can cause the nuclear spin to relax, as described by the Korringa process [63]:

$$\frac{1}{T_1T} = \frac{16\pi^3\hbar^3 k_B \gamma_e^2 \gamma_n^2}{9} < |u_k^2(0)| >_{Ef} N^2(Ef) \tag{5.3}$$

where $< |u_k^2(0)| >_{Ef}$ is the average over the Fermi surface of the periodic part of the Bloch orbital, which describes the quantistic state of the conduction electron.

Weakly interacting electrons

The former equation is reminiscent of the spin susceptibility, or analogously of the Knight Shift owed to contact interaction K_0:

$$\frac{1}{T_1} = \left(\frac{8\pi^2 k_B T}{h}\right)\left(\frac{\gamma_n}{\gamma_e}\right)^2 K_0 \tag{5.4}$$

[2] The x=7% sample displays a peculiar behavior in the spin-lattice relaxation rate, as compared to the others compounds of the same family (see next paragraphs and Chapter 4 for comparison).

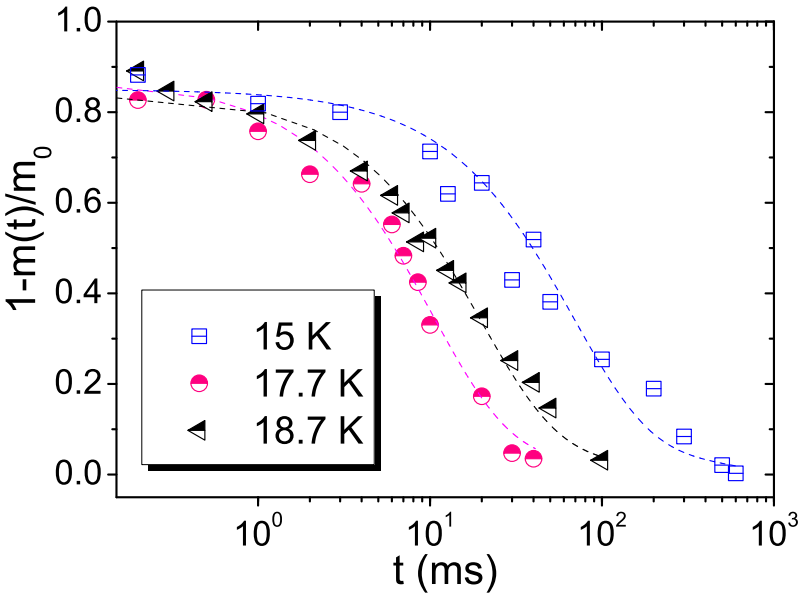

Figure 5.4: The recovery curves for three different temperatures are shown, for $x = 7\%$, at 7 T$\|$ c. The blue squares refers to the 15 K data, while the pink circles are taken at 17.7 K, in correspondence with the peak in $1/T_1$, and the black triangles refer to 18.7 K. The dotted colored lines are the best fits according to Eq. 5.2.

where K_0 is:

$$K_0 = \left(\frac{8\pi\chi_P}{3}\right) < |u_k^2(0)| >_{Ef} \Omega \tag{5.5}$$

where Ω is the unit cell volume and χ_P is Pauli susceptibility.
In short, Korringa's relation claims that $\frac{1}{T_1T}$ is a temperature independent quantity. Moreover, Korringa's ratio:

$$R_K = \frac{K_0^2 T_1 T}{S_n}, \tag{5.6}$$

where $S_n = \frac{\hbar}{4\pi k_B}(\gamma_e/\gamma_n)^2$ is supposed to be close to 1, in case of a non interacting electron gas (or Fermi liquid scenario). Deviations from $R_K = 1$ suggest that correlations effects among electrons can rise. For instance, when $R_K < 1$ it means that antiferromagnetic correlation can be found among the electrons. Ning *et al.* found $R_K = 0.85(10)$, in $Ba(Fe_{1-x}Co_x)_2As_2$ at $x = 26\%$ [15], suggesting that even the strongly overdoped compounds display antiferromagnetic correlations.
By decreasing the temperature below T_c, a well-defined peak in $1/T_1$ for $\mathbf{H} \parallel c$ has been found. The peak temperature decreases by increasing the magnetic field magnitude (see Fig. 5.5 (left panel)). Remarkably, when $\mathbf{H} \perp c$ the peak in $1/T_1$ disappears (see Fig. 5.5 (right panel)). At lower temperatures $1/T_1$ decreases

exponentially and it is only weakly dependent on the magnetic field orientation.

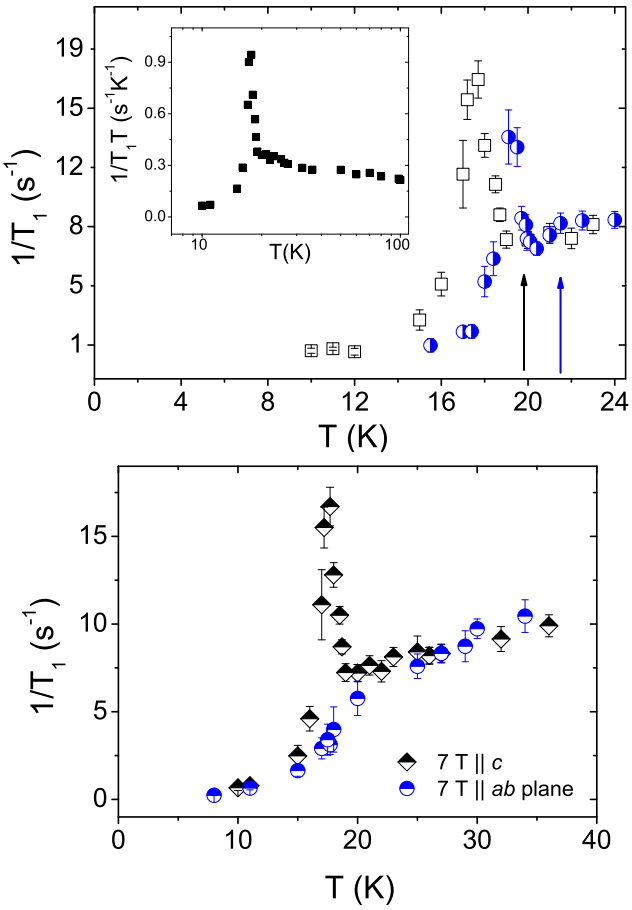

Figure 5.5: (Top panel) The spin-lattice relaxation rate, measured at 7 T (open squares) and 3 T (blue circles), for $\mathbf{H} \parallel c$. The inset shows the $1/T_1T$ data at 7 T, in a wider temperature range. The arrows show the temperature of the detuning of the NMR probe at the two fields: the blue arrow stands for 3 T and the black arrow for 7 T. (Bottom panel) The spin-lattice relaxation rate, measured at 7 T, in $\mathbf{H} \parallel c$ geometry (black diamonds) and $\mathbf{H} \perp c$ geometry (blue circles) is shown. A neat difference for the two field orientations is found in the 16-19 K range. Data, in $\mathbf{H} \perp c$ geometry, have been normalized by a value 1.55 to match $1/T_1$ for $\mathbf{H} \parallel c$, at T_c thus revealing an anisotropy of the spin fluctuations, as observed by Ref. [127].

As recalled above, in Co-optimally doped compound [175], no peak was observed in $1/T_1$, below T_c, except by Laplace *et al.* [172] in a 6% Co-doped $BaFe_2As_2$, and by Baek and coworkers in $CaFe_2As_2$ [173].
Such peak cannot be ascribed to the enhancement of the DOS, related to the opening of the superconducting spin gap (Hebel-Slichter peak [78]) since the majority

of the experimental and theoretical results point towards an extended $s^{\pm}$-wave pairing [32, 37, 176–178] where that feature is not expected. Furthermore the coherence peak predicts an activated behavior, well below T_c, namely $1/T_1 \sim e^{-\Delta/T}$ with Δ the amplitude of the superconducting gap. The fit to the data of Rh-doped x=7% compound gives $\Delta \simeq 200$ K which is too large as compared to the BCS theory, in the weak coupling limit, namely $\frac{2\Delta(0)}{k_B T_c} = 3.5$ (Fig. 5.6). Moreover ARPES and specific heat data report $\Delta(0) \sim 6$ meV (~ 70 K), in 122 compounds [177, 179]. Additionally, the suppression of the peak for $\mathbf{H} \perp c$ can hardly

Coherence peak?

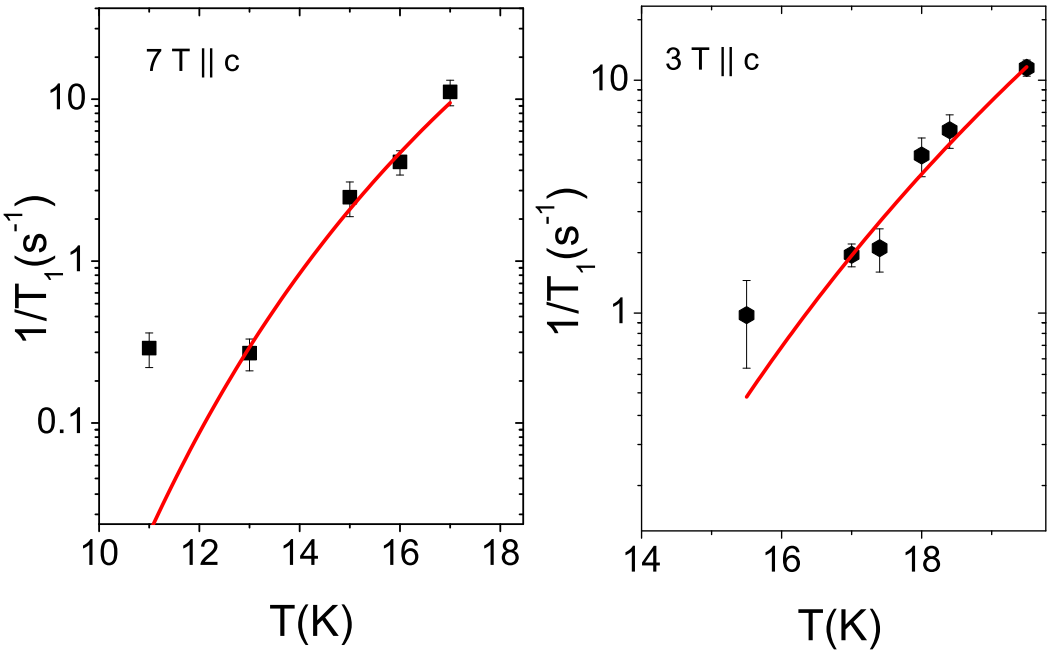

Figure 5.6: The spin-lattice relaxation rate a $T \ll T_c$. The red curves refer to the temperature activated fits, which are discussed in the text.

be reconciled with the small anisotropy of the electron spin susceptibility, hence the maximum in $1/T_1$ just below T_c cannot be associated with the electron spin dynamics. On the other hand, given the similarities with the behavior found in $HgBa_2CuO_{4+\delta}$ [171] and $YBa_2Cu_4O_8$ [170] cuprates, it is tempting to associate $1/T_1$ peak to the FLL dynamics.

In order to analyze the experimental results one can start from the basic modeling of FLL in strongly anisotropic superconductors [180]: the vortices enter the sample in form of quasi-two dimensional pancakes, lying in the FeAs planes. Ow-

FLL scenario

ing to thermal excitations the vortices randomly move out of their equilibrium positions. Such dynamics can be hindered by the action of pinning centers. Differently from cuprates, which exhibit a very high anisotropic ratio $\gamma = \xi_{ab}/\xi_c$, the Ba122 superconductors show $\gamma \sim 1 \div 3$, varying with temperature [21]. This suggests to describe the flux lines not as completely uncorrelated pancakes, but rather as a stack of correlated islands (see Fig. 5.7).[3] According to this physical

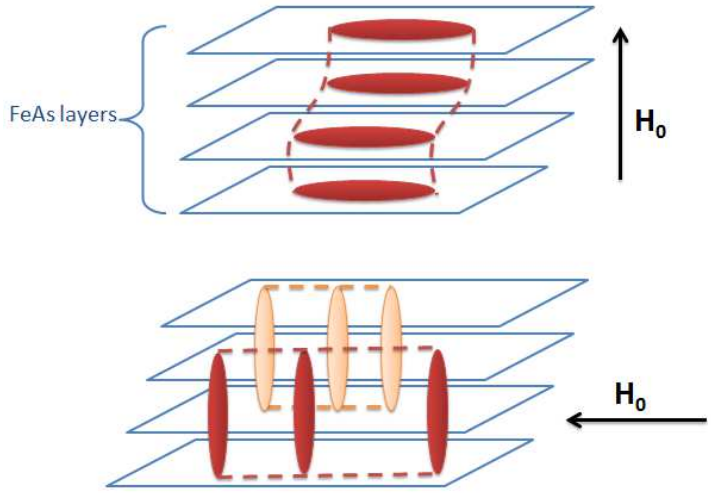

Figure 5.7: (Upper panel) A sketch of the vortex line made of a stacked of pancake vortices, in a layered iron-based superconductor. When the external field is perpendicular to the FeAs layers, the pancakes tend to line up with the field. Since these compounds are rather isotropic the interlayer Josephson coupling is not so small and the three dimensional appearance of the vortices is restored. (Bottom panel) When the field lays withing the *ab* plane, the vortices will tend to align along the field, to minimize their energy. However, the FeAs layers will act as intrinsic pinning centers. In this configuration, the thermal excitation of the vortex line is prevented.

picture, when $\mathbf{H} \perp c$, the flux lines are preferentially trapped between the planes and the FeAs plane boundaries act as pinning centers [58]. This intrinsic pinning hinders the dynamics and lead to the suppression of the $1/T_1$ peak.
In order to provide a quantitative description of this phenomenology, it can be firstly reminded that the spin-spin relaxation rate is written as

$$\frac{1}{T_1} = \frac{\gamma^2}{2} \int < h_\rho(t) h_\rho(0) > e^{-i\omega_L t} dt \tag{5.7}$$

with h_ρ is the magnetic field component perpendicular to $\mathbf{H}$. According to the last equation, $1/T_1$ probes the spectral density of the spin fluctuations, at the

[3] In fact $s = 6$ Å [5].

nuclear Larmor frequency $J(\omega_L)$. If the vortex fluctuations fulfill the following requisites:

- they are two-dimensional excitations;
- they take place in a spacial range smaller than the inter-vortex distance [181] $l_e = \sqrt{2/\sqrt{3}}\sqrt{\Phi_0/H}$ (for a triangular FLL);
- they move by Brownian motions [170, 171], described by a diffusive-like correlation function, $g_1(t) = \exp(-D_\perp q_\perp^2 t)$, $D_\perp$ being the diffusion constant of the motion taking place in the ab plane;

then $\tau_c(q_\perp) = 1/D_\perp q_\perp^2$ plays the role of a **q**-dependent correlation time, for the collective vortex motions. By summing over all collective in-plane excitations up to a cut off wave-vector $q_m = (1/l_e)(8\pi^3/3)^{1/4}$, Suh *et al.* [171] found the following spectral density

$$J(\omega_L) = \tau_m \ln\left[\frac{\tau_m^{-2} + \omega_L^2}{\omega_L^2}\right] \tag{5.8}$$

where the average correlation time is $\tau_m = 1/D_\perp q_m^2$. An activated correlation time $\tau_m(T) = \tau_0 \exp(U/T)$ was assumed, where U is an average pinning energy barrier and τ_0 refers to the correlation time, in the infinite temperature limit. The fit of the data according to this 2D vortex model is reported in Fig. 5.8.
Despite the quite good agreement with the data, one should wonder about the effect of the low anisotropy of 122 compounds, and how small γ affects the vortex structure and dynamics. If one considers the vortex line as a 3D string, and its excitations as generators of stationary waves oscillating in between the pinning centers, it can be introduced a modulation in the amplitude of the correlation function, characterized by a wavelength λ, which has an upper bound given by λ_c:

$$g_2(t) = \exp(-D_\perp q_\perp^2 t)\cos(z/\lambda)$$

By resuming the correlation function [170]

$$< h_\rho(0)h_\rho(t) > \;=\; \frac{\Phi_0^2 s^2}{4\pi\lambda_c^4} < u^2 > \frac{1}{\xi^2}\frac{1}{l_e^2\sqrt{3}} g_2(t) \tag{5.9}$$

and taking the root mean square amplitude of the vortex core fluctuations with respect to equilibrium position, for a 3D line [182, 183]

3D vortex line

$$< u^2 > \simeq \frac{\sqrt{2\pi\sqrt{3}}}{\Phi_0^2}\lambda_c\lambda_{ab} l_e k_B T$$

Eq. 5.9 can be written as:

$$< h_\rho(0)h_\rho(t) > \;=\; \sqrt{\frac{3}{8\pi}}\frac{s^2 k_B T}{l_e}\frac{\lambda_{ab}(T)}{\lambda_c^3(T)\xi^2(T)}g_2(t) \tag{5.10}$$

Taking the values for the London penetration depth reported in the literature [184], the coherence lengths derived from the H_{c2} measurements, and their temperature dependence according to the two-fluid model, a second fit was performed (Fig. 5.8 Table 5.1).

Table 5.1: Fit results for sample x =7%.

H (T)	U (K)	τ_0 (s)
7	322 ±66	5.7 $\pm 10^{-17}$
3	468 ±5	3.6 $\pm 10^{-14}$

Even though the activation energies are comparable with YBCO-124, [170] the extremely small τ_0 values indicate that the Arrhenius law is not the correct approach to describe the vortex motion, in 122 iron-based superconductors.

The magnetic field ripple

A stimulating comparison with the earlier study can be drawn, by deriving the root-mean-square amplitude of the transverse field fluctuations $\sqrt{< h_e^2 >}$ which represents the ripple of the magnetic field profile generated by the flux lines. In fact from Eqs. (5.7) and (5.10), $1/T_1$ can be written in a slight different form

$$1/T_1 = (\gamma^2/2) < h_e^2 > J(\omega_L),$$

from which $h_e \sim 30 - 40$ Gauss at 7 T and ~ 20 Gauss, at 3 T, are derived. Such values agree with the NMR full width at half maximum, measured below T_c, which gives the second moment of the FLL field distribution (see Paragraph 5.2).

To gain a better understanding of the ^{75}As spin-lattice relaxation rate results $1/T_1$, in the superconducting phase, further NMR experiments were done at higher magnetic fields, to analyze how the peaks in $1/T_1$ evolve with the magnetic field intensity. The ^{75}As NMR measurements were performed on the same single crystal at 11 and 15 T, at the LNCMI in Grenoble. Another experiment was carried out at 8.5 T in the NMR laboratory of Pavia University.[4] This time the

[4] T_1 was measured via the same sequence reported above.

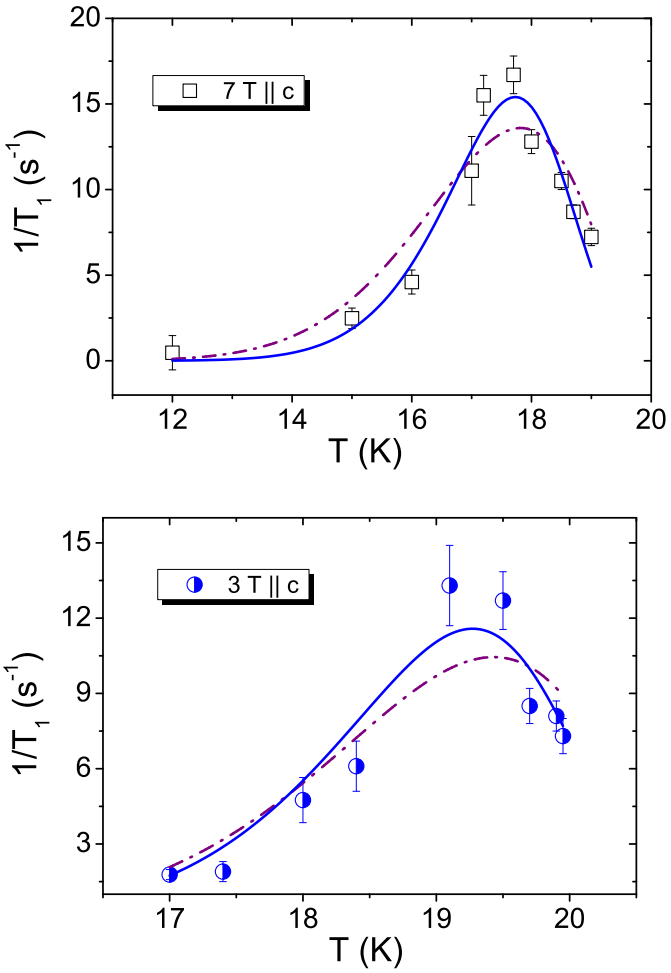

Figure 5.8: (Top figure) The spin-lattice relaxation rate at 7 T for $\parallel c$; (bottom figure) the spin-lattice relaxation rate at 3 T in the same geometry. The fitting curves are given by the 2D- uncorrelated pancakes model, deriving from the correlation function $g_1(t)$ (dash-dotted line) and the correlated vortices model, deriving from the 3D-correlated assumption, $g_2(t)$ (solid line). In both cases, the second model shows the best agreement with the experimental data.

recovery of nuclear magnetization $m(t)$ was fit to the stretched law:

$$1 - m(t) = 0.1 \exp(-t/T_1)^r + 0.9 \exp(-6t/T_1)^r \tag{5.11}$$

with $r \to 1$, as expected for the central transition of a nuclear spin $I = 3/2$. A deviation from $r = 1$ was found in the temperature region where the peak appears. In fact r turned out to be ~ 0.7, suggesting the occurrence of a (small) distribution of correlation times Fig. 5.9. The earlier data were then reanalyzed,

with the same stretched exponential. Again the fit shows peaks in $1/T_1$, visible

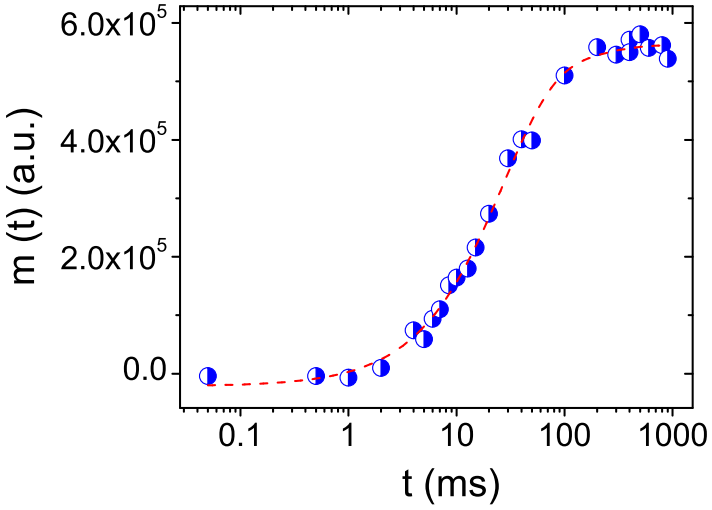

Figure 5.9: The raw saturation recovery data at 8.5 T ($\mathbf{H} \parallel c$) and 16.5 K. The dashed red line is the best fit according to the previous equation. From the best fit, the stretched exponent r is found to be $r = 0.93$.

solely in $\mathbf{H} \parallel c$ geometry. In addition the former case, now the contribution of the vortex dynamics to the spin-lattice relaxation rate $1/T_{1VL}$ was more correctly evaluated, by subtracting from the raw data the electronic contribution, estimated by extrapolating the data out of the peak region. This procedure is equivalent to subtract the data taken for $\mathbf{H} \perp c$, properly scaled by the hyperfine factors [130], since for that orientation the nuclear spin-lattice relaxation is only given by the electronic spin fluctuations (Fig. 5.5). Namely, one has

$$\frac{1}{T_1} = \frac{1}{T_{1VL}} + \frac{1}{T_{1el}}, \tag{5.12}$$

where the first term is the vortex-lattice contribution, whilst the latter is due to electronic spin fluctuations.

Fig. 5.10 shows the relaxation rate $1/T_1$ versus temperature, at all the applied fields. By increasing the field intensity, the peak in $1/T_1$ shifts towards lower temperatures and it is rapidly reduced above 7 T, so that only a small kink remains at 11 T and 15 T. The results of Fig. 5.10 show remarkable similarities with earlier studies on oriented powders of the cuprate $YBa_2Cu_4O_8$ (YBCO124) [141, 170]. The decrease of the peak amplitude is consistent with the drop of the magnetic field ripple due to the vortex penetration, as the magnetic field intensity increases. This is in fact a consequence of the reduction of l_e.

Below the temperature of the peak in $1/T_1$, a marked growth in the acoustic ringing was observed at all fields, mostly for $\mathbf{H} \parallel c$. This effect will be discussed in Chapter 7.

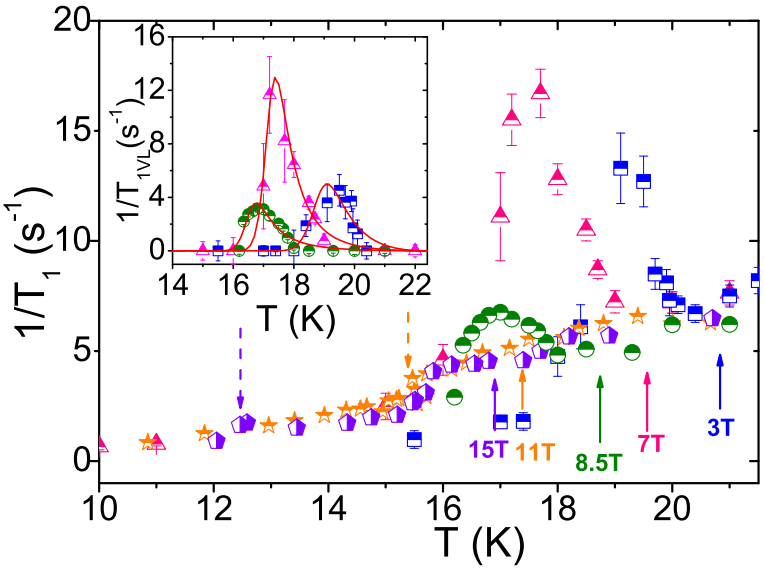

Figure 5.10: The spin-lattice relaxation rate at different magnetic field values: 3 T (blue squares), 7 T (pink triangles), 8.5 T (green circles), 11 T (yellow stars), and 15 T (purple pentagons), is reported. All data refer to $\mathbf{H} \parallel c$ orientation. The arrows show the temperature of the detuning of the NMR probe resonating circuit. The dashed arrows mark the position of the kink in the $1/T_1$, when the field reaches 11 T and 15 T. The inset shows the $1/T_{1VL}$ peak due to the VL dynamics, namely after the subtraction of the electronic contribution. The solid lines are guides for the eye.

To interpret the field dependence of the peak, it is noticed that there is a correspondence between $1/T_1$ and the $\mathbf{q}$-integrated correlation time τ_c',[5] by means of the equation:

$$\frac{1}{T_1} = \frac{(^{75}\gamma)^2}{2} \frac{\Phi_0^2 s^2}{4\pi\lambda_{ab}^4} < u^2 >_{3D} \frac{1}{\xi^2} \frac{1}{l_e^2\sqrt{3}} \tau_c' \ln\left[\frac{\tau_c'^{-2} + \omega_L^2}{\omega_L^2}\right], \tag{5.13}$$

has been numerically solved, keeping the correlation time τ_c', as a free parameter. This procedure is more reliable than the fit, because no multiple fitting parameters are involved, and the crossover between two dynamical regimes can be better evidenced. The result is visible in Fig. 5.11.

[5]From now on, the correlation time derived via NMR will be indicated with a "prime" symbol, in order to distinguish it from the same time obtained via ac-susceptibility.

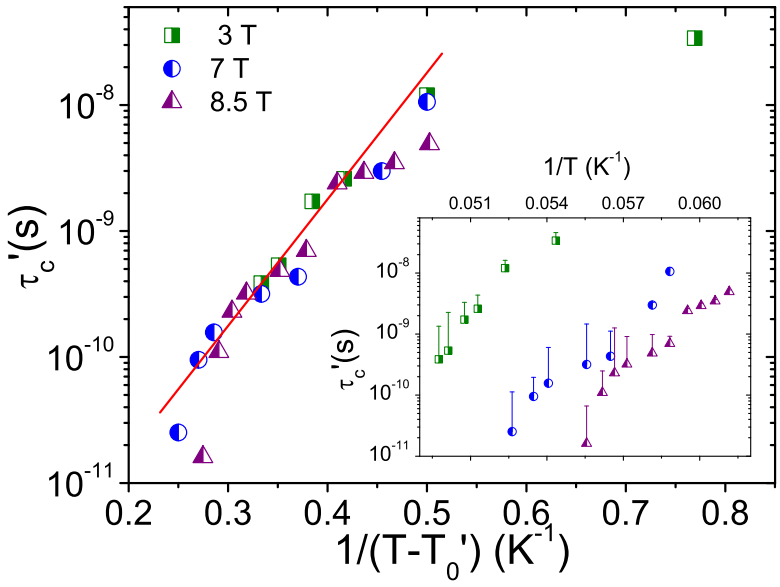

Figure 5.11: The **q**-integrated correlation time τ_c' of the vortex motions derived from $1/T_1$ is shown. The data are reported as a function of $1/(T-T_0')$, and they merge onto a universal curve that can be fit via the VF law (red line). The inset shows the correlation time calculated by Eq. (5.13), before correcting the temperature dependence.

One may wonder if the approach earlier employed is the best to describe T_1 in this weakly anisotropic system, as it starts from the assumption that the 3D vortex lines can be represented as stacks of 2D pancake vortices oscillating around their equilibrium positions. To check whether the dimensionality of the vortex plays a role in the description of the dynamics, a further analysis was done, by employing a relation where the correlation time has a 3D isotropic character [73], as assumed in the BPP theory, explained in Chapter 2. No significant difference in the qualitative behavior of τ_c' was observed. This result suggests that *the actual magnetic anisotropy of a superconductor, and then the topology of the vortex line, do not affect the local nature of the vortex line dynamic*. Further considerations on the temperature dependence of the correlation time will be done after the following section.

5.2.3 Spin-Spin relaxation rate in the superconducting phase

The transverse relaxation time T_2 was measured by recording the decay of the echo after a $\pi/2 - \tau - \pi$ pulse sequence, as a function of the delay τ. T_2 was initially defined as the time where the echo amplitude decreases by $1/e$.
In the normal phase, $1/T_2$ shows an activated temperature dependence which is

ascribed to the Redfield contribution, as discussed in Chapter 4. Below T_c, a remarkable increase in $1/T_2$ gives rise to a peak around 12-13 K, for $\mathbf{H} \parallel c$. Oh *et al.* found a similar behavior in their 7.4% Co-doped single crystal, where the peak was observed at 15 K [35]. Upon progressive cooling, the spin echo decay rate matches quite well the value derived by Van-Vleck lattice sums (see Appendix B), as it happens when all the spin dynamics freeze, and the only process giving rise to the echo decay is the nuclear dipole-dipole interaction. Furthermore, similarly to $1/T_1$, also $1/T_2$ peak gets significantly reduced for $\mathbf{H} \perp c$ (Fig. 5.12). Note

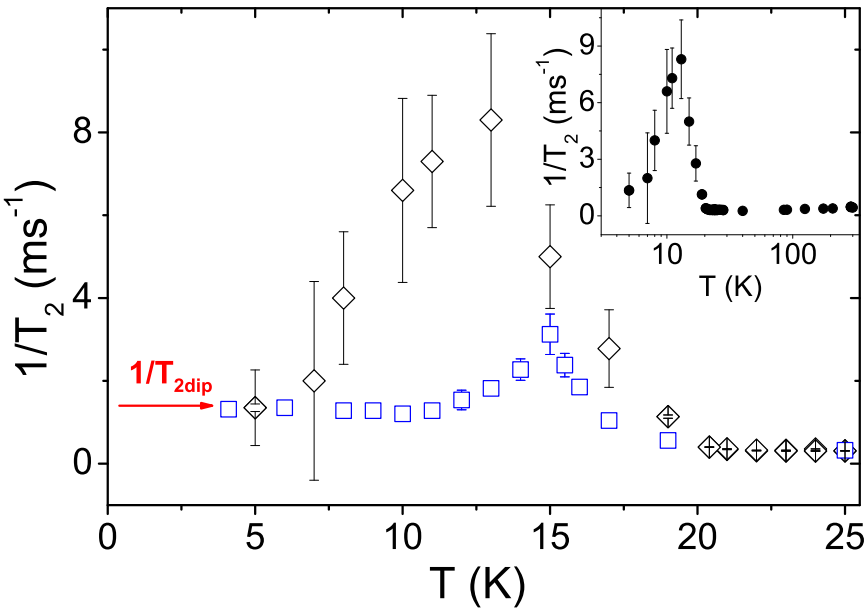

Figure 5.12: The spin echo decay rate measured at 7 T. A peak around 12 K is found for $\mathbf{H} \parallel c$ (black diamonds) while it strongly decreases, for $\mathbf{H} \perp c$ (blue squares), and shifts towards higher temperatures. The red arrow indicates the ab-initio value for $1/T_2$ given by the dipolar sums. The inset shows the spin echo decay rate for $\mathbf{H} \parallel c$ up to room temperature.

that when the vortices are strongly correlated along the c axes, the flux lines move rigidly and do not affect significantly the transverse field components, while they do change the longitudinal ones [182], hence the information derived from those two types of measurements can be complementary.

The analyze of the temperature dependence of $1/T_2$ has been inspired again by observation that the VL dynamics plays an important role, in affecting the NMR properties. One could begin from a relation similar to Eq. 5.9, nevertheless here, for the sake of simplicity, an exponential correlation function for the longitudinal

field fluctuations as been assumed

$$< h_l(0)h_l(t) >=< h_l^2 > e^{-t/\tau_L}, \tag{5.14}$$

where τ_L is the correlation time, for the longitudinal value of the field. Correspondingly, the decay of the echo amplitude can be written as a function of the delay τ between the $\pi/2$ and π pulses in the echo sequence as [69]

$$M(2\tau) = M_0 e^{-2\tau/T_{2dip}^2} \times M_2(2\tau) \tag{5.15}$$

$$M_2(2\tau) = e^{-\gamma^2 < h_l^2 > \tau_L^2 [2\tau/\tau_L + 4\exp(-2\tau/\tau_L) - \exp(-2\tau/\tau_L) - 3]} \tag{5.16}$$

where the first Gaussian term accounts for the nuclear dipole-dipole contribution, while the second term describes the low-frequency vortex motions. The fit to the former equations gives the temperature dependence of the longitudinal correlation time (Fig. 5.13). By decreasing the temperature, the FLL motion is supposed to go through different motional regimes. Above 11 K, where the peak in $1/T_1$ is observed, it is noticed that τ_L shows an activated behavior characterized by an activation barrier $U_L \simeq 50$ K much lower than the one derived from $1/T_1$ (see Fig 5.13). This observation will be clarified in the next section.

5.2.4 Linewidth

The NMR spectrum was determined by the Fourier transform of half of the ^{75}As echo signal, while below $T \simeq 13$ K, when the line became broader than 60 kHz, the spectrum was derived by sweeping the irradiation frequency. The full width at half maximum (FWHM) was determined by a Gaussian fit. In the normal state the linewidth increased on cooling, following a Curie-Weiss trend (Fig. 5.14), probably due to the presence of magnetic impurities (Rh ion). The impurities cause the appearance of a staggered magnetization and a broadening of the NMR line. On the other hand, the average magnetic field is only weakly affected, so we do not expect an extra-contribution to the shift [185]. After subtracting this impurity-dependent contribution $\Delta\nu_{NP}$, from the raw data, by using the relation

$$\Delta\nu(T) \simeq \sqrt{\Delta\nu(T)_{raw}^2 - \Delta\nu_{NP}^2} \tag{5.17}$$

an extra-broadening induced by the presence of the flux lines lattice appears (Fig. 5.14). The impurity-dependent contribution is well described by the Curie-Weiss

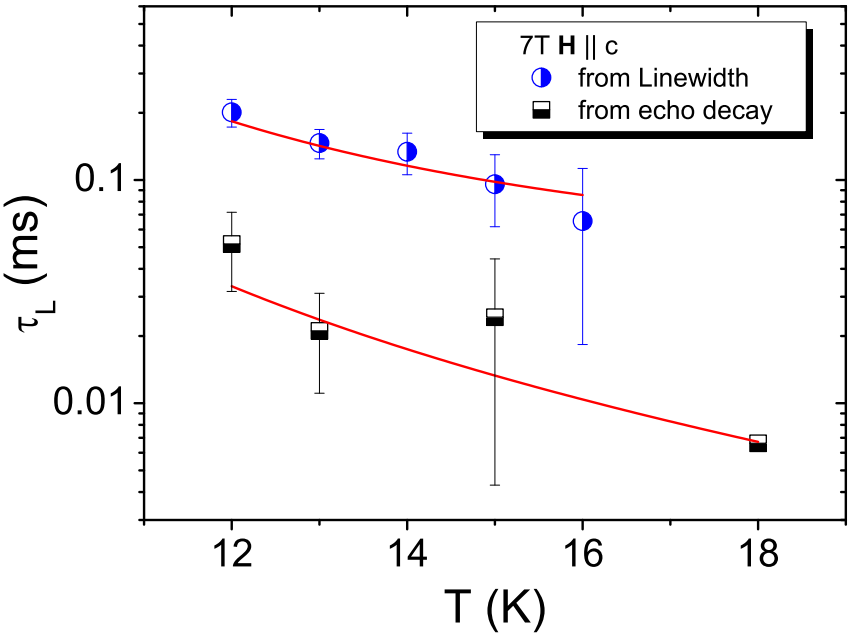

Figure 5.13: The temperature dependence of the correlation time τ_L derived from the echo decay time (black squares), as compared with the one derived by the linewidth analysis (blue circles) in the assumption of fast motions (see Eq. 5.19). The red curves are the fitting of the correlation time, according to an activated law.

relation, for both the sample orientations:

$$\Delta\nu_{NP}(T) = \frac{C}{T-\theta} + A \tag{5.18}$$

The fit gives $\theta = -60$ K, (for both the orientations) and, for the $\mathbf{H} \parallel c$, $C = 1319 \pm 118$ kHzK and $A = 20.8 \pm 1$ kHz, while for the perpendicular geometry the fit gives $C = 1264 \pm 50$ kHz K and $A = 23.4 \pm 0.1$ kHz.

In the superconducting region, when $\mathbf{H} \parallel c$, the vortex correlation time can be derived also from the linewidth data, by following the approach reported in Ref. [62]. Indeed, in the fast motions regime, namely $2\pi\overline{(\Delta\nu_R)^2}^{1/2}\tau_L << 1$, with $\overline{(\Delta\nu_R)^2}^{1/2}$ the square root of the rigid lattice second moment, the correlation time can be found by the following relation: Fast motion regime

$$\Delta\nu \simeq \tau_L \frac{\overline{(\Delta\nu_R)^2}}{2\pi}. \tag{5.19}$$

The temperature dependence of τ_L (Fig. 5.13) is then fit by an Arrhenius law. The pinning energy barrier is $U_L = 48 \pm 3$ K, consistent with the one derived

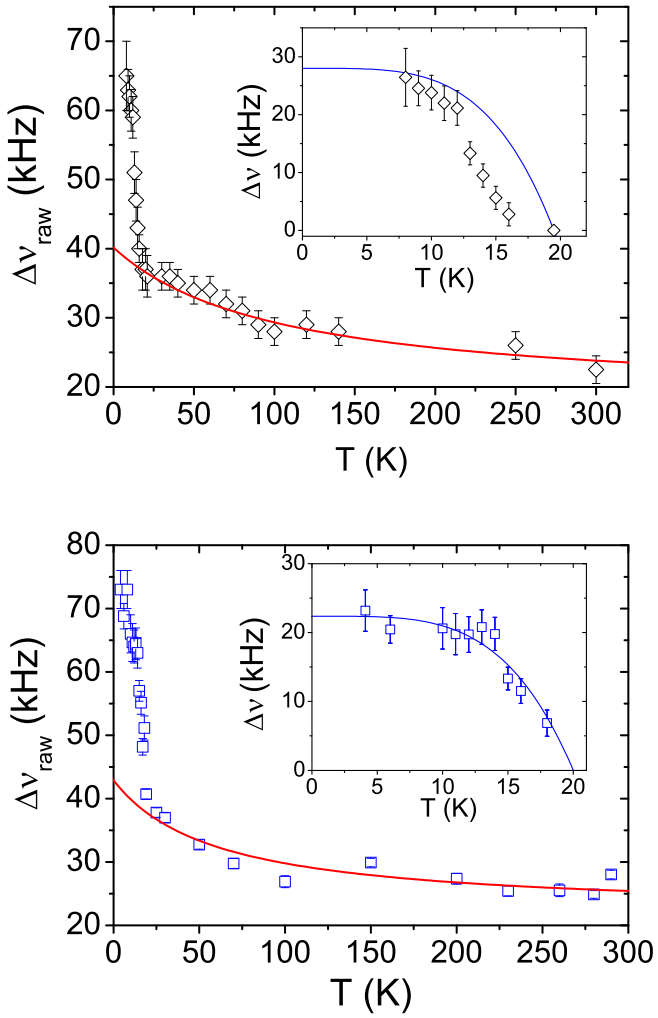

Figure 5.14: The two figures show the FWHM at 7 T, for $\mathbf{H} \parallel c$ (top) and $\mathbf{H} \perp c$ (bottom), with the Curie-Weiss fit curve (see Eq. 5.17). In the insets the raw data are subtracted from the impurity contribution and the extra-broadening effect due to the penetration of the FLL is analysed in terms of the London two-fluid model (blue line). For the longitudinal case one can observe a strong deviation, at high temperatures, just below T_c, which is hardly visible in the transverse case.

from the spin echo decay measurements. This is not surprising since both T_2 and $\Delta\nu$ probe the longitudinal component of the local field.

Additionally, a noticeable change in the line shape, from Lorentzian to Gaussian is observed upon cooling, as it is expected when the correlation time gets longer than few ms. The Gaussian lineshape, below T_c, indicates the presence of lattice distortions induced by randomly distributed pinning centers. In this scenario

one can only make a tentative estimate of the London penetration depth. These authors reported λ_{ab} values between 200 and 217 nm. On the other hand, by following Ref. [186]:

$$\lambda_{ab} = \sqrt{\frac{2.36\Phi_0\gamma\sqrt{k}}{\Delta\nu}} \tag{5.20}$$

where $\sqrt{k} = 0.04324$ depends on the lattice geometry and on the magnitude of the applied field, and taking $\Delta\nu(T \to 0) \simeq 30$ kHz, for $\mathbf{H} \parallel c$ a penetration depth of $\lambda_{ab}(0) \sim 226 \pm 9$ nm was found, in agreement with the former results, derived by transverse μSR, [187] transport [184] and the tunnel diode resonator measurements [188] on a similar 7.4% Co-doped $BaFe_2As_2$ single crystal.

5.3 Ac-susceptibility

In the present section, ac-susceptibility plays the role of a complementary technique to investigate the vortex lattice dynamics, since it detects a signal from the bulk, and just the $\mathbf{q} \to 0$ excitations are probed. Measurements of the real χ' and imaginary part χ'' of the ac-susceptibility are presented and discussed. Such measurements were carried out in Field Cooled (FC), by means of a Quantum Design MPMS-XL5 Squid ac-susceptometer, at the University of Parma. The sample was mounted on the experimental setup, with both the static H_{dc} and the oscillating H_{ac} fields laying in the crystallographic ab plane. The sample dimensions, compared to the ones of the experimental setup, allowed one to measure the spin susceptibility for the $\mathbf{H} \parallel ab$ geometry only.[6] During the experiment, the intensity of the oscillating magnetic field was kept constant at $H_{ac} = 1.5$ Oe, while the dc field intensity ranged from $H_{dc} = 500$ Oe to 4.8 T, so that the mixed phase regime could be explored. The ac field frequency range was $\nu = 37.5$-1488 Hz. Fig. 5.15 (top) shows the real χ' and imaginary χ'' part of the spin susceptibility.

From the real part the transition temperature can be evaluated, whereas the peak in χ'' provides information about the dissipative mechanisms occurring in the mixed phase. To gain insights into the VL dynamics, the maximum in χ'' has to be carefully analyzed. Just below the onset of superconductivity, evidenced in the χ' curve, a peak in χ'' appears (Fig. 5.15 (bottom)). The peak shifts towards high temperature, when increasing the frequency, thus excluding the occurrence of the Bean critical state [189]. In such a scenario, the peak in the imaginary part of the susceptibility is interpreted as the result of magnetic flux reaching

Bean critical state

[6] An explanation concerning the experimental techniques will be provided in appendix C.

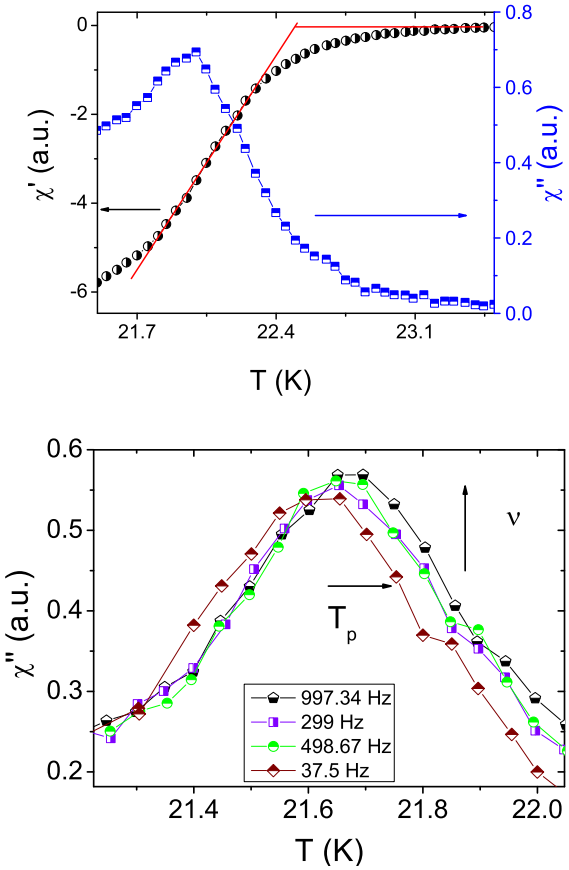

Figure 5.15: (Top panel) Temperature dependence of χ' (black circles), and χ'' (blue squares) measured at $H = 500$ Oe, and at $\nu = 37.5$ Hz. Below the transition temperature marked by the drop in χ', the peak in χ'' appears, pointing out that some dissipation mechanism plays role in the mixed phase. The red lines are fits to determine T_c. (Bottom panel) Frequency ν and temperature T dependence of χ'' peaks, measured at $H = 1$ T. The peak temperature T_p shifts towards high temperature when increasing ν.

the center of the specimen and giving a resultant magnetization M. This effect would be strongly dependent on the sample geometry and on the intensity of the applied field. Moreover, the peak temperature would not depend on the ac-frequency, at variance with the experimental findings. However, to definitely rule out the occurrence of Bean critical state, a further analysis should be carried out, by varying the intensity of the ac-field.

Cole-Cole plot

If the imaginary part of the spin susceptibility is plotted as a function of the real part, with the temperature as implicit parameter (see Fig. 5.16) the so-called

Cole−Cole plot is derived. The inset of the figure shows that the Cole−Cole plot lays on a circle, the center of which has a negative ordinate, pointing out that there is a likely distribution of correlation times τ_c, consistent with the NMR results [190].

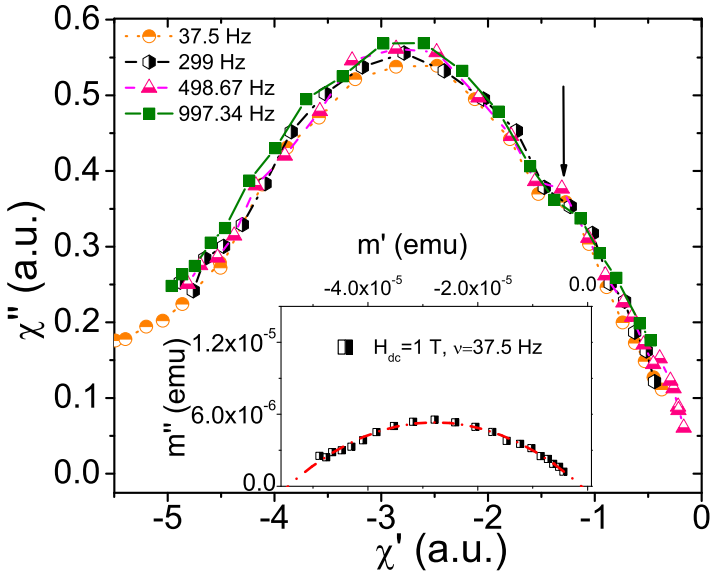

Figure 5.16: Cole-Cole plot, at $H = 1$ T, with the temperature as implicit parameter. The absolute value of χ'' increases slightly but systematically with increasing ν, as expected for a vortex glass phase [191]. The arrow shows a kink probably due to a residual inter-grain contribution [192]. The inset shows the Cole−Cole plot, and the dashed red line shows the fit (see text).

A possible interpretation relies on the following consideration: the peak in χ'' is dominated by the onset of irreversible behavior of the magnetization, occurring when the vortex lines are thermally excited across the pinning barriers [193]. This leads to a resonant absorption of energy for $2\pi\nu\tau_c \sim 1$, which is described by the Debye relation

Resonant absorption of energy

$$\chi'' \propto \frac{\omega\tau_c}{1+(\omega\tau_c)^2}, \tag{5.21}$$

Given the sharpness of the peaks in $\chi''(T)$, and the previous consideration on the Cole-Cole plot, a small distribution of correlation times may be assumed. Accordingly, τ_c shall be considered as an average value. Fig. 5.17 shows the temperature dependence of τ_c, and a crossover towards very slow motions (nearly 0.1 s) upon cooling. A fit of the correlation time data, to the Arrhenius law, as employed in cuprates [194] and in the $SmFeAsO_{0.8}F_{0.2}$ [125], non-physical values of τ_0 are found as previously found in the NMR data analysis.

When the data are plotted, the correlation times show the same slope (inset

Single-vortex dynamics

of Fig. 5.17), namely the pinning energy barrier does not depend on the field intensity. Now, if the data are properly scaled by a temperature $T_0(H)$, they merge onto a universal curve that can be fit by the Vogel-Fulcher (VF) law [195]:

$$\tau_c(T,H) = \tau_0 \exp\left[\frac{U_{eff}}{T - T_0(H)}\right] \tag{5.22}$$

The data display a nearly field-independent activation barrier ($U_{eff} = 120 \pm 20$ K), owing to a process of single vortex depinning, in contrast to the typical power low H^n [194], which evidences the occurrence of collective pinning phenomena (see next paragraph). Before presenting the phase diagram of the system, it

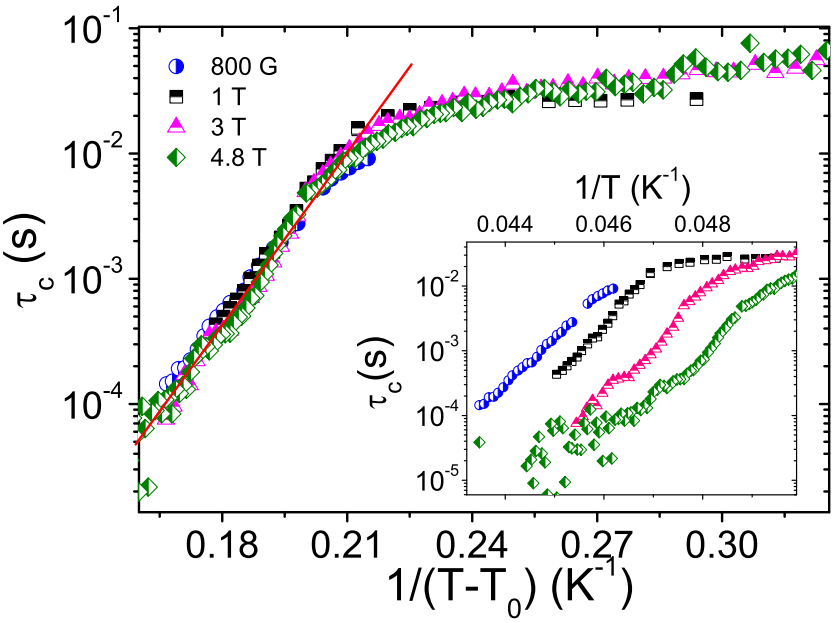

Figure 5.17: The correlation time for the $\mathbf{q} = 0$ motions derived from ac-susceptibility data, reported as a function of $1/(T - T_0)$. The data nicely merge onto a universal curve that obeys the VF law (red line). In the inset the τ_c is reported as a function of $1/T$. The dynamical crossover is clear.

is observed that the absolute value of the imaginary part of the susceptibility increases, while increasing the frequency ν. Moreover, the peak height of the Cole−Cole plot grows when increasing the ac-frequency, and so does the peak in the imaginary part of the spin susceptibility $\chi''(T)$. These findings are in agreement with the numerical simulations of Adesso *et al.*, based on the occurrence of a fragile vortex scenario, as well as with their experimental results on YBCO [191] and $LaFeAsO_{0.9}F_{0.08}$ [192]. In conclusion, it is pointed out that the same behavior has been recently observed in the optimally Cobalt doped Ba122 [196].

5.4 Phase diagram

Firstly it can be observed that the different absolute values of τ_c and τ_c' display a dispersive behavior in the vortex lattice excitations. Moreover, both τ_c and τ_c' data merge onto a universal trend, after being properly rescaled by T_0' (Fig. 5.11). The VF fit value (to the NMR data) of the pinning barrier is $U_{eff} \sim 200 \pm 20$ K, not far from the ac-susceptibility value, suggesting that the two techniques are indeed probing the same dynamic. Remarkably, the energy barriers U_{eff} are field independent both for NMR and ac-susceptibility. This result, together with the VF behavior, suggests the occurrence of a glass state that, by resorting to the "glass terminology" [197], can be named *fragile* glass. In fact, the field independence of U_{eff} can be justified by the following qualitative consideration: in case of weak pinning [19] and high magnetic fields, namely in case of a high vortex density, the pinning energy distribution can be characterized by close meta-stable minima, in the bottom of spatially extended and deeper energy minima, as in the fragile glass scenario [198, 199]. Hence, upon varying the magnetic field strength, the VL can be rearranged within those meta-stable minima without having to overcome the high energy barrier. Accordingly, the barrier will correspond to an average energy distribution $< U >$, determined solely by the quenched disorder, and not by the magnetic field. This idea is sketched in Fig. 5.18. When reporting T_0 and T_0' in the phase diagram, one finds a surprising result (see Fig. 5.19): the temperatures estimated by the two techniques merge onto the de Almeida-Thouless line [200]

$$H = H_0[1 - T_g(H)/T_g(0)]^{\gamma},$$

the exponent $\gamma \sim 1.5$ being in agreement with spin and superconductive glasses [201]. Moreover, both T_0 and T_0' lines intersect the $\mathbf{H} = 0$ axis at a temperature that is close to the zero field limit for the thermal "disruption" of a vortex line. By assuming that a vortex line is made by piling up many pancakes across the FeAs planes, Clem predicted that the thermal disruption of a vortex line would occur at the Kosterlitz-Thouless (KT) transition temperature [182]

$$T_{cr} = \frac{\Phi_0^2 d}{32\pi^2 k_B \lambda_{ab}(T)^2}, \tag{5.23}$$

where d is the FeAs layer thickness. The calculated value of T_{cr} for this compound is $\sim$ 17.5 K [202]. This observation agrees with the picture of vortices passing from a glass/solid phase to a liquid phase, namely a regime of poorly correlated vortices.

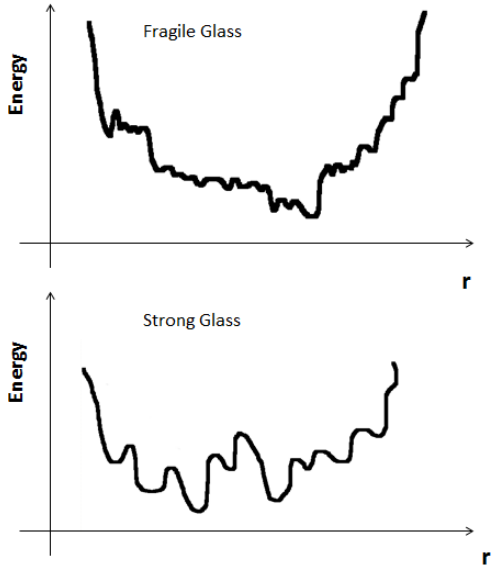

Figure 5.18: Sketch view of the pinning energy profile, as a function of the position, for two kind of glasses. In the top panel the fragile glass scenario is sketched: close metastable minima, nearly all equivalent, lay in the bottom of a deep energy minimum. In order to overcome the barrier, the vortex needs a thermal energy correspondent at least to the small wells. The bottom figure, on the contrary, shows the strong glass scenario. Here the mimima are spatially farther and deeper.

5.5 Conclusions

This Chapter presents a study of thermally activated vortex motion, by means of ^{75}As NMR spectroscopy, as well as ac-susceptibility.
Different frequency windows of the vortex motion are explored, by looking at different NMR quantities. In fact a feature in the spin-lattice relaxation time emerges when the vortex correlation rate is approximately in the MHz range. Moreover the $1/T_2$ maximum reveals, at a lower temperature, a longer correlation time, comparable to the interpulse spacing τ_{echo}, i.e. few ms. In the temperature window between those peaks, the motions are still effective and yield the motional narrowing of the NMR line. Indeed, in order to observe a line narrowing, the correlation times must be smaller than the inverse of the rigid lattice linewidth, namely $\tau_c \sim 10^{-4}$ s. Additionally, a remarkable anisotropic behavior has been observed.

Moreover, the joint employ of NMR and ac-susceptibility has revealed that the Arrhenius law is not effective to interpret the slowing-down of the vortex dynamics. Anyhow, the Vogel-Fulcher empirical law has shown to be more appropriate.

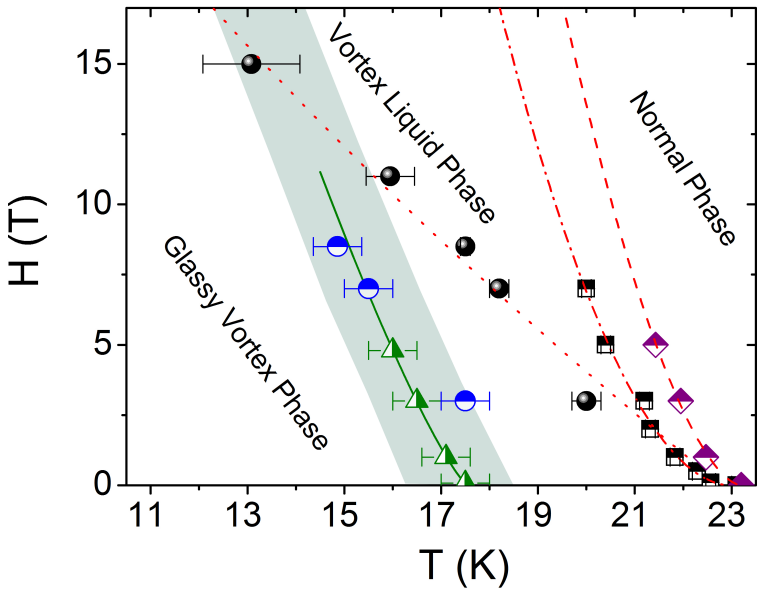

Figure 5.19: The phase diagram for the mixed phase of the $Ba(Fe_{0.93}Rh_{0.07})_2As_2$ compound. The purple diamonds show the upper critical field H_{c2} for $\mathbf{H} \parallel c$, while the squares mark the irreversibility temperature T_{irr}, for the static uniform susceptibility, which coincides with the detuning temperature of the NMR probe. The black circles mark the T_{peak} line for the NMR relaxation rate, namely the temperature of the peak in $1/T_1$. The green triangles represent T_0, while the blue half circles represent T_0'. The green solid line is the de Almeida-Thouless fit, while the other lines are guides for the eye. The blue-grey zone marks the thermal disruption of the vortices, and the crossover from slow dynamics (glassy state) to fast dynamics (liquid state).

Moreover, the Vogel-Fulcher temperatures merge on same curve, which is well fit to the de-Almeida Thouless line, with a power of 1.5, in agreement with a glass state. The presence of a correlation time distribution, together with the observation of the imaginary part of the spin susceptibility, and the comparison with the simulation carried out by Adesso and coworkers, show that the glass state is very likely to describe the vortex frozen state, in the Rh-doped Ba122 family.

Chapter 6

NMR study of current driven vortex dynamics

The last Chapter has shown how thermal excitations of the vortex matter affect the NMR properties, in the equilibrium state.[1] An additional source of motion is provided by the application of an external current. In such a case, a new scenario is established, as the Lorentz force induces a drift of vortices that, in turn, affects the local field dynamic. The study of the vortex dynamic under the action of an external current is particularly interesting in view of the applications. Indeed, when a superconductor is employed to generate high magnetic fields, one has to know J_0, which is responsible for the depairing, but more important is the depinning current $J_c < J_0$, which is able to generate a drift motion of the VL, and as a consequence, a non null resistance into the wire, which can eventually quench the magnet. In fact, the vortex motion will lead to slow changes in the trapped magnetic field and to measurable resistive voltages, which are detrimental for superconductivity. [2]

Besides the more widely employed magnetoresistance technique [19, 203], the response of a type-II superconductor, under the injection of a dc current, can be also investigated from a "microscopic viewpoint", by means of NMR. The first to employ NMR, with the aim of studying the vortex motion in the high-T_c superconductors, under non equilibrium condition was Carretta [204], after the inspiring experiment of Delrieu [205]. Carretta showed, via ^{89}Y NMR, that an applied Lorentz force induces a narrowing of the line in $YBa_2Cu_3O_{7-\delta}$, owing to

[1] The word "equilibrium" refers to the absence of an external current driving the VL. However the effect of the rf field still induces a perturbation, although weak.

[2] Note that type-II superconductors are more often employed, because of their high critical fields. For example V_3Si and Nb_3Sn have $H_{c2} \sim 10^5$ Oe.

a decrease in the effective correlation time of the vortex motion.

Some background about the dynamical properties of the FLL under J are first presented. Afterwards the experimental data obtained on $Ba(Fe_{1-x}Rh_x)_2As_2$ are shown and discussed.

6.1 Dynamical properties of the FLL

The study of the vortex phase, in presence of a driving current can be very interesting, not only form a technological viewpoint, but also in regards to fundamental aspects. According to the intensity of the external current, the following classification of the vortex motion can be done:

- Ideally **flux flow** occurs when there is no pinning, and the vortex motion can be explained in terms of a diffusion, in presence of some viscous damping, with a drag coefficient η. Since all real systems show pinning, the flux flow can be observed when the external current exceeds the depinning critical current J_c.
- **Flux creep** occurs when the motion is hindered by the presence of pinning centers which can trap the vortex, by modifying the free energy profile. The nature of the motion is not a drift but, as the name suggests, it is rather discontinuous ("hopping-like" dynamic).

In the former case, when a current density $\mathbf{J}$ is injected into a type-II superconductor, a Lorentz force acts on the vortices:[3]

$$\mathbf{F} = \mathbf{J} \times \frac{\Phi_0}{c}, \tag{6.1}$$

Flux flow

thus forcing them to flow with a velocity $\mathbf{v_L}$, that is perpendicular to the magnetic field, and generating an electric field:

$$\mathbf{E} = \mathbf{B} \times \frac{\mathbf{v_L}}{c} \tag{6.2}$$

Since $\mathbf{E}$ is parallel to the current $\mathbf{J}$, a non-zero resistance ρ_f will rise. The resistivity can be derived by equating the Lorentz force and the viscous force

$$\mathbf{J} \times \frac{\Phi_0}{c} = \eta \mathbf{v_L}, \tag{6.3}$$

[3]The following relations assumes a cubic shaped sample.

and recalling the Ohm law:

$$\rho_F = \frac{|\mathbf{E}|}{|\mathbf{J}|} = \frac{B\Phi_0}{c^2\eta}. \tag{6.4}$$

Bardeen and Stephen developed an intuitive model, experimentally verified by Kim and coworkers [206], to explicit the drag coefficient η. This model assumes that the dissipation takes place within the vortex core of radius ξ, according to ordinary dissipative processes [207].
If one takes the power dissipation:

$$W = -\mathbf{F} \cdot \mathbf{v_L} = \eta v_L^2 \tag{6.5}$$

and considers the Bardeen and Stephen's argument, one obtains:

$$W \sim \frac{v_L^2 \Phi_0^2}{2\pi\xi^2 c^2 \rho_n} \tag{6.6}$$

where a factor 2 has been accounted for the dissipation outside the core. Finally the resistivity becomes:

$$\rho_f = \frac{B\rho_n}{H_{c2}} \tag{6.7}$$

so the flow resistivity ρ_f is directly proportional to the field and it increases as much as the field approaches the upper critical field H_{c2}.

Flux creep

In the flux creep scenario, the vortex flow is prevented by the presence of pinning centers. Anderson and Kim noticed that when a driving current is taken into account, the energy profile changes in such a way that the jumps in the direction of the decreasing potential will be more likely than the opposite ones (Fig. 6.1). The creep-type motion of a vortex can be visualized as a thermal diffusion process in which different segments of the vortex move between metastable states. In absence of an external current, a vortex segment lowers its energy by finding the optimal low-energy state among its neighboring metastable states. Under the action of an applied current density $\mathbf{J}$, some other metastable states become more favorable and the vortex begins to move. The new optimal states are determined by the condition that the energy gain due to the driving Lorentz force is equal to the deformation plus the pinning energy of the vortex. Kim and Anderson assumed that the vortices move into bundles of average volume L^3. In order to move a bundle in the direction of the decreasing potential of a spacing equal to its size, there will be an energy cost $\mathcal{E}_f = fL^4$, while to move it to the opposite

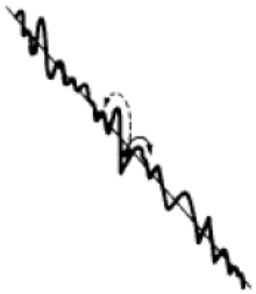

Figure 6.1: The potential energy profile as a function of the position, in case of a transport current. The downward jumps are more favored than the upward ones. The figure is adapted from Ref. [22].

direction $\mathcal{E}_b = -fL^4$, where f is the Lorentz force density. Then the net jump rate can be written as [22]:

$$\Omega = \omega_0 e^{-U_0/k_BT}(e^{\mathcal{E}_f/k_BT} - e^{-\mathcal{E}_f/k_BT}) = 2\omega_0 e^{-U_0/k_BT} \sinh\left(\frac{fL^4}{k_BT}\right) \tag{6.8}$$

where $\omega_0 L \sim 1 - 10^6$ cm/s. A rough estimate allows one to find the free energy U_0: $U_0 \sim H_c^2 L^3/(8\pi)$.[4] When $fL^4 \gg k_BT$, the former result can be approximated to:

$$\Omega \sim \omega_0 e^{(-U_0 + fL^4)/k_BT} \tag{6.9}$$

Linewidth study under the action of a current.

The previous model was successfully employed by P. Carretta [204] to interpret the motional narrowing of the ^{89}Y NMR spectrum. An YBCO sample, made of pressed powder, with $T_c = 90$ K, was injected by a dc current, up to 120 mA. The VL dynamic can affect the linewidth as reported in Fig. 6.2 (top). According to the vortex creep scenario, characterized by a hopping rate τ_c^{-1}, the linewidth is described by [204]

$$\frac{\delta\nu_0}{\delta\nu(I)} = \frac{\tau_{c0}}{\tau_c(I)} \sim \cosh(\mathcal{E}_f/k_BT). \tag{6.10}$$

In fact, while the resistivity measures the net jump rate, namely the difference between the jump rate in favor and against the Lorentz force, the nuclei probe, in an NMR experiment, the sum of the two processes. Hence the hyperbolic sine turns into the hyperbolic cosine showed in the equation above.
The author found a good agreement between the experimental data and the Kim-Anderson model, as the hyperbolic cosine was well reproduced (Fig. 6.2 (bottom)).

[4] p is usually much smaller than 1. See Ref. [22] for further explanations.

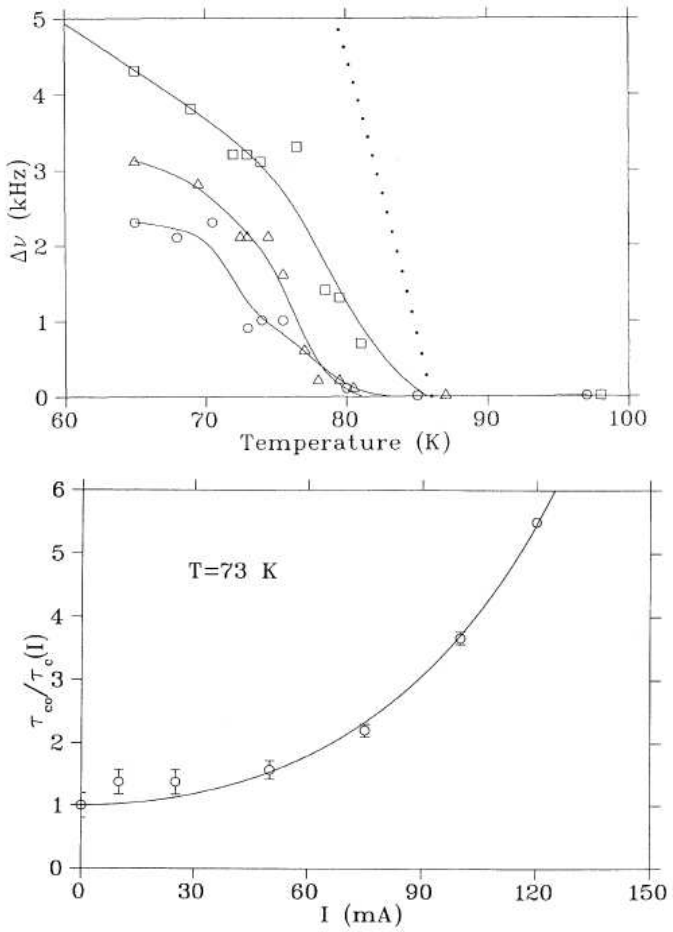

Figure 6.2: (Top panel) The NMR linewidth versus temperature at different current values. The normal phase linewidth has been subtracted, as shown in the next paragraphs. The applied currents were I =0 mA (squares), I = 50 mA (triangles) and I =120 mA (circles). (Bottom panel) Normalized correlation time as a function of the current. The solid line is a fit to equation (6.10). The figures are adapted from Ref. [204].

Few years later, Recchia *et al.* [208] studied the same material, in form of single crystal, via ^{63}Cu NMR, under the injection of a pulsed current. They performed spin-echo experiments, after injecting current pulses as large as 10 A/cm^2 (100 times larger than that used by Carretta). The NMR linewidth in the superconducting state, does not exceed the value measured in the normal state until the temperature reaches a value where the resistance vanishes. Moreover the linewidth was measured together with the resistance of the sample. The authors claimed that a vortex liquid state occurs between T_c and the temperature at

which the resistivity drops to zero. No effect on the spin-echo was observed. The sample resistance also served as an excellent sensor of the crystal temperature, as the measure was carried out at a fixed current. Their main results are shown in Fig. 6.3. By combining Einstein relation into the description of the vortex

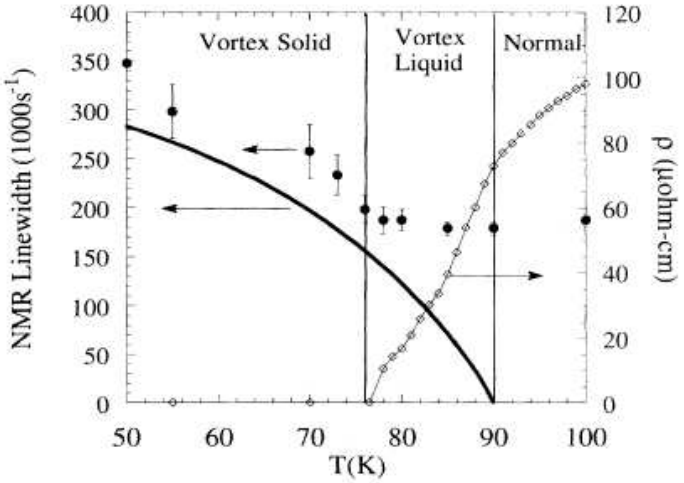

Figure 6.3: Resistivity and ^{63}Cu NMR linewidth versus temperature, YBCO crystal in a 9 T field applied parallel to the crystalline c axis. No broadening of the Cu line shape is seen down to temperatures below which the resistance becomes zero, suggesting the effect of motional narrowing. The figure is adapted from Ref. [208].

diffusion, Recchia *et al.* deduced that near 80 K, vortices diffuse at a distance larger than one lattice spacing, within a time of 10 μs. Moreover a vortex bundle of volume 2×10^{11} Å^3 was derived.

Motivations

The two last works have inspired the experiments presented in this chapter. As shown above, the VL motion can induce local field fluctuations, with a typical correlation time τ_c, defined here as the time in which the vortex bundle covers a distance of nearly an intervortex spacing l_e. Such fluctuating fields $h_i(t)$ are responsible for the motional narrowing effects observed by Carretta and Recchia. However, while the linewidth is sensitive just to the "fast motion limit", the spin echo decay time can give insights into a wider time range (typically μs - ms or shorter) [62]. Hereafter the spin-spin relaxation time T_2 will be studied, as a function of the current and temperature, in a $Ba(Fe_{1-x}Rh_x)_2As_2$ compound (x=6.8%).

6.2 Spin-echo decay under a Lorentz force: preliminary observations

Experimental setup

This experiment is basically very similar to a customary NMR experiment, as described in the previous chapters, with the further complication to inject a current through the sample, via two thin copper wires.[5] A static field of 6.4 T was applied parallel to the c axis. The wires were soldered to the sample surface, by means of a silver paste, and then connected to a current generator, that can provide currents larger than 1 A. The current density J injected into the sample is in the 0 - 4.5×10^3 A/cm^2 range, which is well below the depinning current measured in the Co-doped Ba122 family: $J_c \sim 10^5$ A/cm^2, at H =6.4 T and T =4.2 K [24]. The current was provided in form of pulses, by a switch box, triggered by the spectrometer, as in Fig. 6.4. The current pulse flows through the sample during the whole preparation and acquisition times, while it is injected into a resistance of 1 kΩ, during the "Last Delay" time (see Fig. 6.4). The duty cycle is approximately 1/60.

The reason to apply a pulse, instead of a continuous current, is to avoid sample

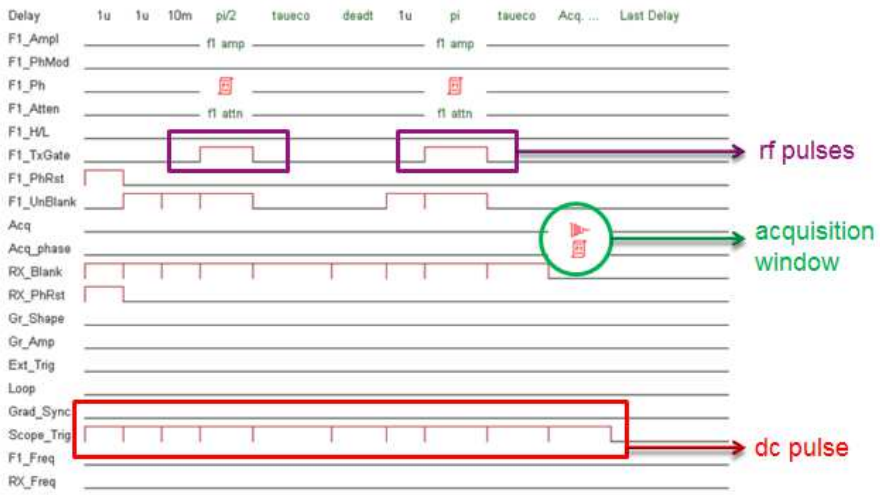

Figure 6.4: An example of the sequence employed in the experiment. The Hahn echo is built by the application of a $\pi/2$ pulse, followed by a π pulse (purple box). From the start of the sequence until the end of the acquisition the current pulse is switched on (red box).

heating, due to Joule effect. Particular attention has to be paid to such effect, as it is responsible for the increase of T_2, which can be easily mistaken with VL

[5] Wires of 0.19 mm diameter were employed.

dynamics, within the temperature range of $T_m - T_c$, i.e. the liquid vortex phase. Regardless the fact that above T_c no large current-induced effect has been observed on the echo-decay (Fig. 6.5 (bottom)), one should still be careful, below T_c. In fact:

- the echo intensity, at zero τ, is affected by the current intensity (not shown). Indeed the amplitude of the NMR signal is proportional to:

$$E_0 \propto \delta(T) H_0 / T \tag{6.11}$$

  where δ is the skin-depth.

- The spin echo decay becomes slower with the increase of the current intensity.

It is tentative to interpret the above phenomenology by stating that the sample heating is more effective below T_c, as the thermal capacity of the sample dramatically diminishes in the superconducting state. However the duty cycle may play an important role.
To check this hypothesis, the echo decay has been studied, while the sample was injected with 100 mA, and a comparison between a pulsed and a continuous current was carried out (Fig. 6.5 (top)). From the data it is clear that the smaller the duty cycle, the smaller the effect of the current on the echo decay. Moreover, deeper insights can be provided by the study of the echo intensity, at zero τ, as function of the current and temperature. Fig. 6.6 shows the temperature dependence of δ, which reflects the square root of the resistivity $\sqrt{\rho}$.

When a continuous current is injected, δ shifts towards lower temperature as the current intensity increases (Fig. 6.6 (top)). Moreover, the curves can be properly rescaled by a temperature correction (Fig. 6.6 (bottom)). On the other hand, when a pulsed current is applied, the experimental data overlap with the curve in absence of current.

As a consequence of the above discussion, it was deduced that the injection of a continuous current *does* heat the sample, therefore the following measurements are taken after injecting current pulses, ~ 10 ms long.

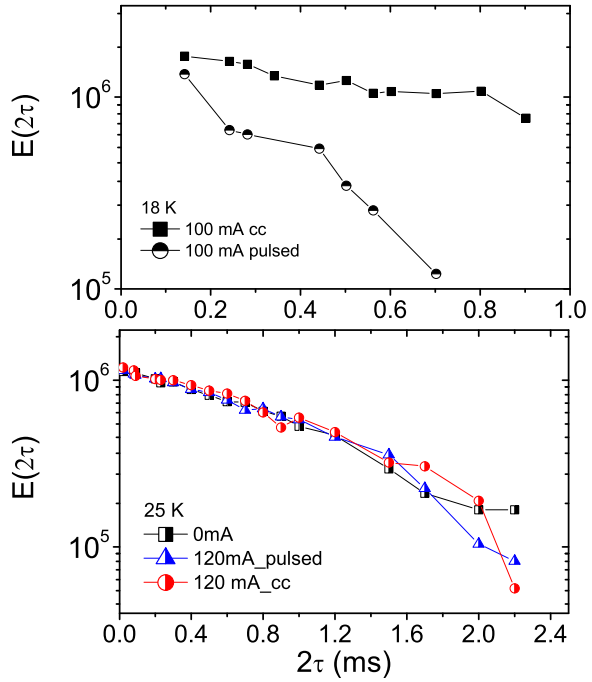

Figure 6.5: The top panel shows a comparison between the echo decay under the action of a pulsed current and of a continuous current, as described in the text above ($T_c \sim 19.5$ K). The bottom panel shows the echo decay in absence of a current, for 120 mA (pulsed and continuous), above T_c.

6.3 Spin-echo decay under a Lorentz force: experimental results and discussion

The spin echo decay was investigated as a function of the temperature and of the current intensity. T_2 was firstly derived as the time when the echo decays at 1/e. When the spin echo decay rate $1/T_2$ is plotted as a function of the current intensity, a dome-like shape develops with the temperature. The current at which $1/T_2$ shows its maximum progressively grows, as the temperature diminishes (Fig. 6.7). The increase in $1/T_2$ which appears at small current intensity, below 18 K, cannot be due to the Joule effect, as in such temperature range the opposite trend would be expected. More likely the dome-like shape of the spin-echo relaxation rate indicates that the current is affecting the motion of the VL, as discussed in the next paragraph.

What is the origin of such an effect?

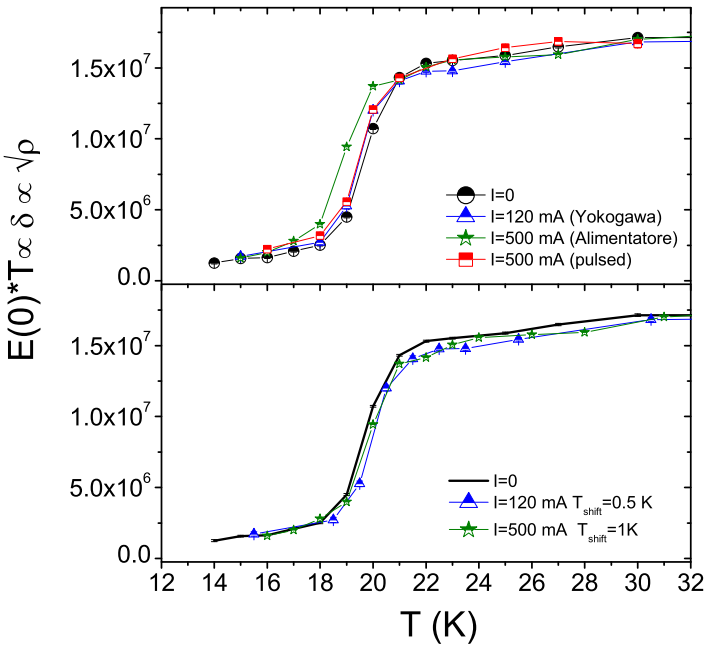

Figure 6.6: The top panel shows how the current affects the penetration depth. In the bottom panel the curve are scaled into the $I = 0$ data, by applying a shift of 0.5 and 1 K, for 120 mA and 500 mA, respectively.

T_2 decay requires that the nucleus probes a *longitudinal* magnetic field, which fluctuates in time [138]. As discussed in Chapter 4, such longitudinal field is hardly ascribed to direct dipolar interaction, but it is rather owed to indirect exchange mechanism. The source of dynamic likely originates, below T_c, by incoherent fluctuations, due to vortex diffusive motions.
It is recalled here that, in case of highly incoherent motions, as diffusive processes, it can be assumed that the longitudinal field (h_z) fluctuates in time, in such a way that the correlation function becomes:

$$< h_z(t)h_z(0) >=< h_0^2 > \exp(-t/\tau_c) \tag{6.12}$$

This leads to the following *general* expression for the echo decay [62, 134, 209]:

$$E(2\tau) = E(0)\exp^{-<M_2>\tau_c[2t-\tau_c(1-\exp(-t/\tau_c))(3-\exp(-t/\tau_c))]} \tag{6.13}$$

where M_2 is the second moment of the static field distribution, $M_2 =< \Delta\omega^2 >$, which is about the square of the linewidth,[6] in the rigid lattice limit. Nevertheless,

[6]Indeed M_2 coincides with the square of the linewidth just for a Gaussian line.

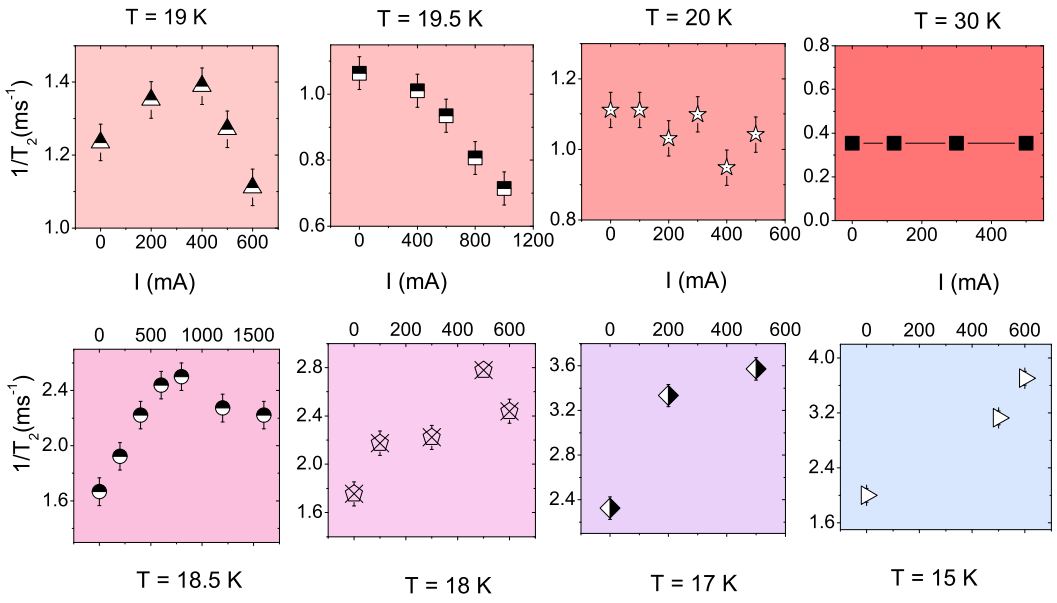

Figure 6.7: Progressive evolution of the spin echo decay rates, as a function of the current, from 30 K down to 15 K, with $T_c \sim 19.5$ K. Above the critical temperature no effect on the echo decay rate is visible, while below T_c a downturn behavior in $1/T_2$ versus I, emerges. An external magnetic field of 6.4 T was applied.

for each value of T_{2eff}, there correspond two values of τ_c which solve the former equation: the first one lays in the fast limit regime, and the second one lays in the slow limit regime, as also reported by Recchia and coworkers [209] (Fig. 6.8).

Indeed, for very long correlation times, T_{2eff} $(1/T_{2eff})$ becomes long (small), since field fluctuations should take place during the characteristic time of the echo experiment, in order to prevent the echo from refocusing perfectly. For very short correlation times, motional narrowing occurs, and again T_{2eff} $(1/T_{2eff})$ becomes long (short), as it occurs for the FID. Accordingly, for intermediate correlation times, where $1/\tau_c$ is of the order of Δ, T_{2eff} displays a minimum. The minimum (maximum) in T_{2eff} $(1/T_{2eff})$, is reminiscent of the well-known minimum in T_1, which occurs when a similarly fluctuation frequency matches the Larmor frequency [63].

In agreement with the above discussion, one would expect to observe a crossover similar to Fig. 6.8, once the effective correlation rate is plotted as a function of

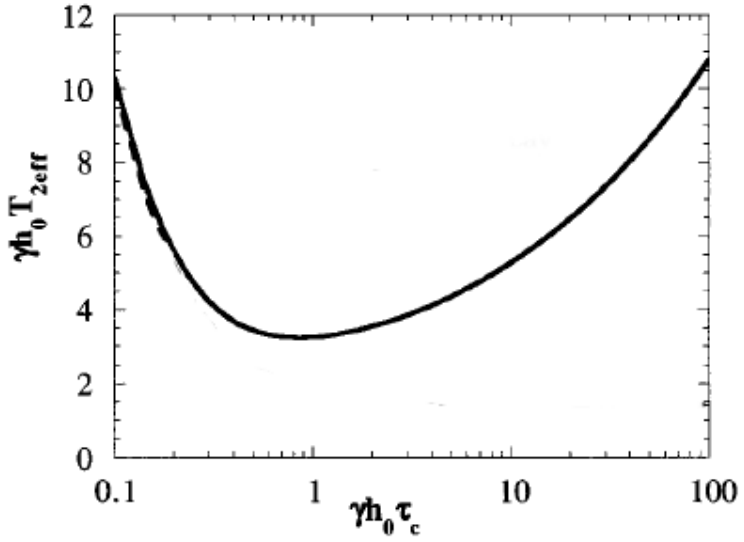

Figure 6.8: Effective transverse relaxation time, as derived from the Gaussian-approximation method described in Ref. [209], plotted as a function of the dimensionless parameter $\gamma h_0 \tau_c$. A crossover between long and short correlation time and it's effect on the echo decay time is observed for $\gamma h_0 \tau_c \sim 1$.

τ_c. In order to obtain τ_c, the equation reported in the Anderson-Kim theory has been employed

$$\tau_c(I) = \frac{\tau_0}{\cosh(\mathcal{W}I)} \tag{6.14}$$

where $\mathcal{W}$ takes into account the vortex correlation volume V and the hopping distance x_0:

$$\mathcal{W} = \frac{HVx_0}{\Sigma c k_B T} = \frac{Hx_0^2}{ck_B T} \tag{6.15}$$

where the lower limit for the hopping length, x_0, is the intervortex spacing, l_e. The former equation can be written again in a new form:

$$\tau_c(I,T) = \frac{\tau_0}{\cosh(\mathcal{U}I/T)} \tag{6.16}$$

where now $\mathcal{U}$ is naturally related to $\mathcal{W}$. In the last equation, the explicit dependence on the temperature and the current has been evidenced.
Note that τ_0 ($\sim 4.5\times10^{-3} ms$) has been derived by the condition for the maximum of $1/T_{2eff}$, namely $\Delta\tau_c \sim 1$, and it is fixed throughout the whole temperature range, while $\mathcal{U}$ is a free parameter, which varies within 1-10.
The result is shown in Fig. 6.9, where the effective $1/T_2$, namely the value taken at "1/e", is plotted as a function of the correlation time multiplied by the square

root of the second moment of the field distribution (Δ). Three temperature ranges

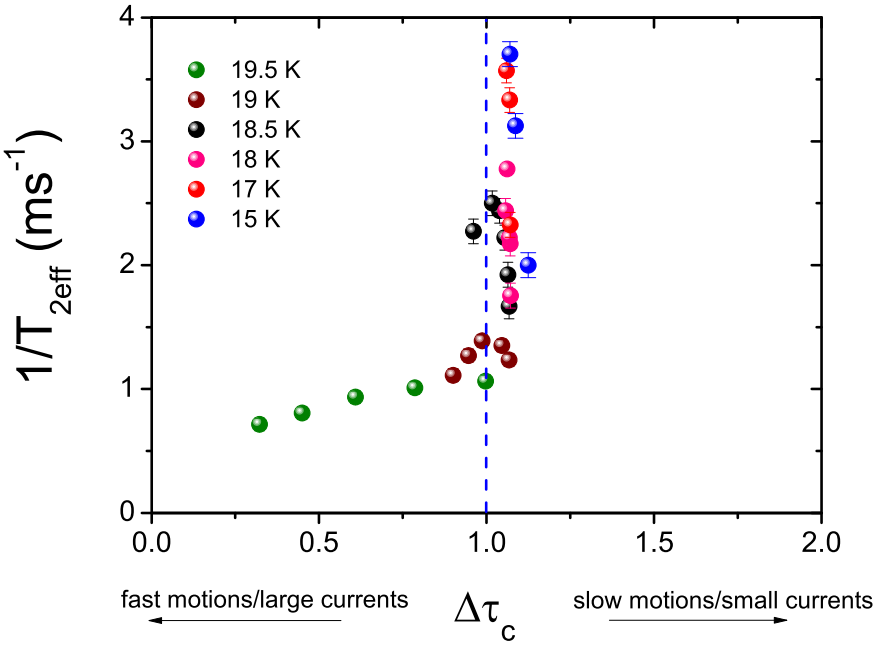

Figure 6.9: The effective spin echo decay rate as a function of the dimensionless parameter $\Delta\tau_c$, with the current as an implicit parameter. $1/T_{2eff}$ for different temperatures is displayed.

can be evidenced:

- At 19.5 K ($\rightarrow T_c^-$), the VL motion is fast, and it gets even faster upon increasing the current intensity (which, in turn, decreases τ_c);
- At 19 K and 18.5 K a dynamical crossover, from fast to slow motion, is well evidenced by the presence of the peak in $1/T_{2ff}$;
- Upon progressively decreasing the temperature down to 17 K and 15 K, the VL motion lays in the slow limit regime.

Therefore, the amplitude of the $1/T_{2ff}$ increases with the decrease of the temperature, because the second moment of the static field distribution behaves likewise. From the former results, one may deduce that the temperature and the current play a similar role in accelerating the VL dynamic, regardless the motion nature. In fact, in the absence of a current, the VL notion is purely thermally assisted, whereas, at a fixed temperature, the current increase enhances the correlation frequency.

Although the qualitative behavior of the data agrees with the expectations, further studies are required to provide more striking conclusions.

6.4 Conclusions

The present Chapter shows a study of the vortex lattice dynamics, driven by the injection of an external dc current, via the analysis of the spin echo decay time.
After addressing the issue of the Joule effect, which may cause a fake drop in the spin echo decay rate, the correlation time has been derived by the Anderson-Kim theory for collective flux-creep of vortex bundles, as it has been successfully employed in the high-T_c cuprates. T_{2eff} versus the adimensional parameter $\Delta\tau_c$ has been found in agreement with the general theory of the echo decay in the Gaussian approximation.
In addition to earlier studies, this analysis shows how temperature and current act simultaneously.
Further experimental and analytic efforts are envisaged to complete these results, and derive microscopic information about the quantities involved in the motion.

Chapter 7

Exotic Phenomena induced by Vortex Lattice

This Chapter presents novel approaches to study the thermal excitations of the vortex lattice, in absence of an external current. The first part of the Chapter deals with an anomalous acoustic ringing of the NMR coil, emerging below the transition temperature. Such an effect was initially very inconvenient, as it prevented low temperature measurements. At a deeper look, the phenomenon showed some systematic behaviors, that suggested an interpretation based on magneto-acoustic coupling between the vortex lattice and the superconducting sample.

The second part of the Chapter deals with a cantilever magnetometry experiment performed on a single grain of $NbSe_2$ superconductor. At first, the feasibility of Nuclear Magnetic Resonance Force Microscopy (NMRFM) is addressed, later on a study of field and temperature dependence of the cantilever energy dissipation and resonance frequency is analyzed and discussed.
The experimental results are interpreted in terms of the melting transition of the vortex lattice, and the pinning energy barriers are derived, together with the phase diagram of the superconducting particle.

In Chapter 5, the vortex melting/freezing phase transition has been experimentally observed, yet no so much mathematical formalism has been presented. Here some preliminary theoretical background is provided.

7.1 Vortex Melting transition

The study of vortex physics in type-II superconductors is extremely fascinating, as it touches on several phenomena, involving hydrodynamics, electromagnetism and quantum field theory. The interplay between thermal fluctuations, vortex repulsion/attraction and the role of quenched disorder contribute to create a puzzling scenario [58, 210]. Such a study is appealing not only form a fundamental viewpoint, both also in the light of the practical limitations related to the occurrence of a liquid vortex phase, where the dissipationless state, peculiar of superconductivity, vanishes.
The melting transition has been intensively studied during the last years, and many efforts from a theoretical [162, 182, 211] as well as experimental viewpoint have been carried out. In particular, the more widely employed techniques were resistivity, ac-susceptibility [194], ultrasound attenuation [212], mechanical measurements [163], STM [213], magnetic decoration, [214] SEM, [215] MFM, [216] NMR [35, 130, 141, 149, 167, 170, 205, 206, 208], μSR [217], and neutron scattering spectroscopy [218, 219].
Nevertheless all the above techniques need either big samples of at least a few mm^2 or cm^2 size, or small magnetic fields. However, the combination of small samples and fields in the Tesla range has not been often encountered. The B part of this Chapter suggests a new method to overcome this limit, while hereafter the attention will be focused on the mathematical formalism of the melting transition.

The derivation of the vortex line tension can be pursued by following Tinkham's argument [22], in case of non strongly interacting vortices. For $\kappa \gg 1$, a crude estimation of the core can be done, and it turns out that the vortex-line energy is written as the sum of the magnetic and kinetic energies (namely the term related to the currents):

$$\epsilon_1 = \frac{1}{8\pi} \int (h^2 + \lambda^2 |\nabla \times \mathbf{h}|) d^2 r \tag{7.1}$$

which can be reexpressed in the following form:

$$\epsilon_1 = \frac{H_c^2}{8\pi} 4\pi \xi^2 \ln \kappa. \tag{7.2}$$

In addition, the mutual vortex interaction has to be taken into account. In fact, between two flux lines oriented along the field direction (z) and with the same verse, there is a *repulsive* magnetic force $f_x = \frac{\Phi_0}{4\pi} \frac{\partial h_1(r_2)}{\partial x_2}$ where h_{1x} is the field

that flux line 1 induces on flux line 2. On the other hand, vortices on different planes feel an *attractive* force among each others, that induces the formation of 3D vortex lines (Fig. 7.1). If the vortices are periodically arranged, no net force will originate. On the contrary, if one vortex is displaced by δx with respect to the equilibrium position, a new force will appear [22]:

$$f_e = \frac{\Phi_0}{4\pi}\frac{\partial^2 h_1(r_2)}{\partial x_2^2}\delta x. \tag{7.3}$$

In presence of an array of vortices, a sum over all the neighbors must be per-

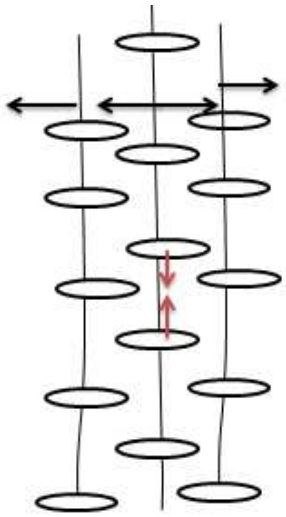

Figure 7.1: Sketch of three flux lines (black lines) and current vortices (black circles). The repulsive and attractive interactions are represented by arrows.

formed, in order to obtain the approximate total force (per unit length):

$$f_e \sim (\sqrt{3}\Phi_0/4\pi^2\lambda^2)H \sim H_{c1}H. \tag{7.4}$$

The elastic energy associated with f_e is finally:

$$\mathcal{E}_{el} = \frac{1}{2}f_e < u^2 > L_z$$

u being the displacement taking place in the plane perpendicular to z.
By summing over the elastic energy to the line tension, and minimizing the total energy with respect to L_z, it is found:

$$L_z \sim \sqrt{\Phi_0/H} \sim l_e.$$

Finally, by inserting the optimal L_z into the total energy expression, and invoking the energy equipartition theorem, the root mean square amplitude of the vortex fluctuation turns out to be:

$$< u^2 > \frac{\sim k_B T}{\sqrt{f_e \epsilon_1}}.$$

Now, the vortex melting transition can be explained by resuming the **Lindemann criterion**, which states that the melting occurs when $< u^2 >$ is a significant fraction c_L^2 of l_e^2.[1] Accordingly the temperature dependence of the melting field B_m is obtained [58]:

$$B_m \sim \frac{c_L^4 \Phi_0^5}{(k_B T)^2 \lambda_{ab} \gamma (\cos^2\theta + \gamma^2 \sin^2\theta)^{1/2}}, \tag{7.5}$$

where θ is the angle between the magnetic field and the ab plane. Strong anisotropy γ can suppress the melting field, giving rise to a broad liquid region, as reported in Fig. 7.2.

One might expect that the long-range order of the FLL would be broken in an abrupt way, as in a first order phase transition. On the other hand **the nature of the melting transition is not so clear to identify**, as sometimes it occurs so close to the H_{c2} line to be "hidden" in the superconducting transition itself. So the entropy reduction taking place at T_m, which is of the order of k_B per layer number is quite small, as compared to the entropy drop due to the superconducting transitions. That is why specific heat measurements are not suitable to observe this effect. On the other hand magnetic measurements are better candidates.

Part A:
Anomalous spurious ringing in the mixed phase of Rh-doped Ba122 compounds

The term "spurious ringing" refers to the mechanical vibration of a part of the NMR apparatus, usually the pick up coil, which turns into a fake NMR signal, 1-100 μs long, and may overlap to the real signal. This effect is sometimes called "the coil disease" [220], since it is so detrimental that it can prevent from collecting the FID or echo signal, especially when the T_2 is very short. In order

[1] Typically $c_L = 0.1 - 0.2$

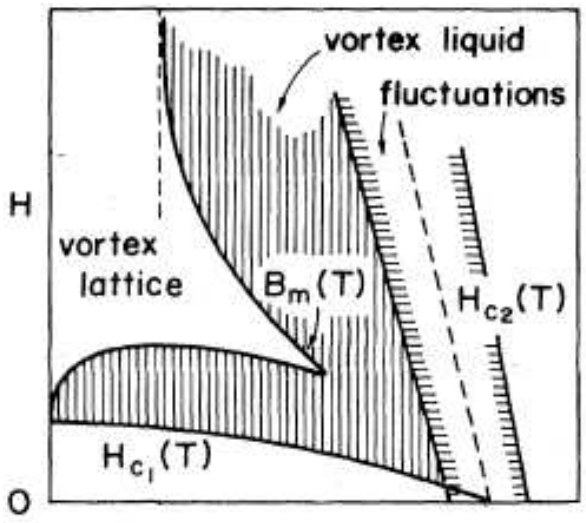

Figure 7.2: Phenomenological phase diagram for the strongly layered high-T_c superconductors. The part of the phase diagram occupied by the liquid phase is substantially larger than the case of more isotropic superconductors. The figure is adapted from Ref. [58] .

to get rid of this effect, some tricks are usually employed, as for instance making an irregular pick up **coil**, using a stiff copper wire, or coating the coil with epoxy. A further source of ringing comes from the **probe** body and walls. Finally, in case of metallic samples, also the **specimen** can generate ringing, the latter being the hardest to remove. In such a case, one may consider to work on a powder sample, instead of a single crystal, which has the additional benefit of increasing the surface/volume ratio and so the NMR signal intensity. Anyhow, when it is not possible to change the sample or the probe, the ringing may become so persisting, to stimulate new questions!

The "coil disease"

The source of ringing is often found in the electromagnetic generation of ultrasonic standing waves, in metals. When standing waves are generated in presence of a static magnetic field, the acoustic energy will be converted into magnetic energy, and then picked up by the NMR coil. This effect can be understood by recalling the *reciprocity theorem* of classical electrodynamics, that can be generalized in case of magnetic material. In particular, an effective analogy can be done by considering that in an ultrasound attenuation experiment, the interaction between the external acoustic wave and the static magnetic field will induce a vibration of the FLL that turns into an acoustic attenuation [221]. On the other hand, the coupling between the magnetic field and the thermally driven FLL dynamics, may give rise to an acoustic wave, as sketched in Fig.7.3.

An example of ringing observed in the $Ba(Fe_{1-x}Rh_x)_2As_2$ compounds is visible

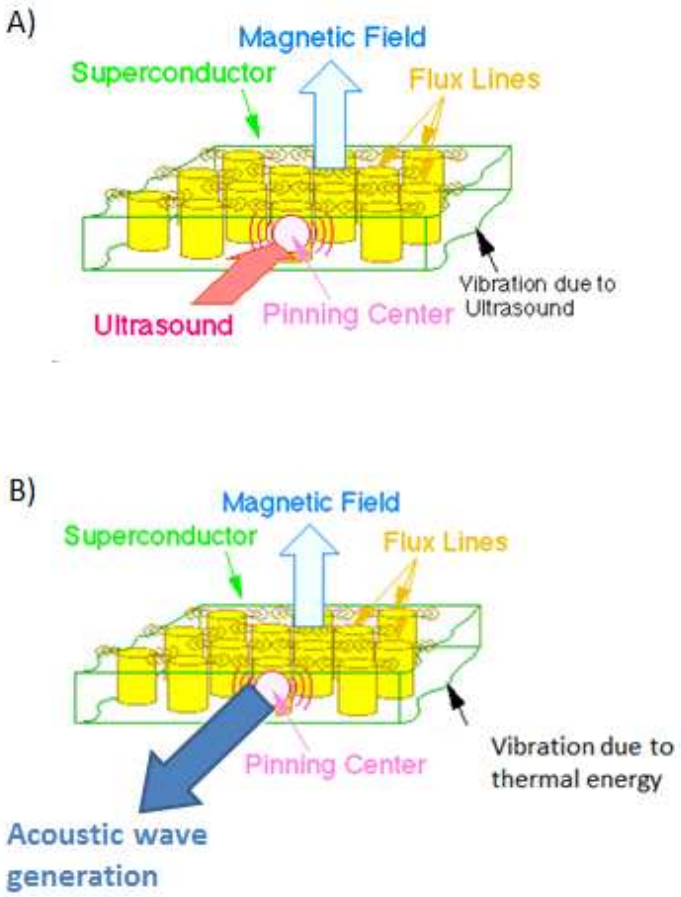

Figure 7.3: In picture A) the acoustic attenuation experiment is sketched: if flux lines are pinned, the flux line lattice is vibrated by the ultrasound propagating in the superconductor. The figure is adapted from the web (energy.eee.kagoshima−u.ac.jp). In picture B) the reverse mechanism is shown. Here the FLL dynamic is activated by thermal energy, and the motion by interacting with the external magnetic field, is able to generate an acoustic wave.

in Fig. 7.4.

7.2 Experimental results and interpretation

The phenomenology of the spurious ringing, as reported in Fig.7.4 can be summarized as follows:

- It is found in the nearly optimally doped compounds, namely $x = 7\%$ sample (and partially in the 6.8 %) at any magnetic field, i.e. from 3 up to 15 T;
- It appears just in the superconducting phase;

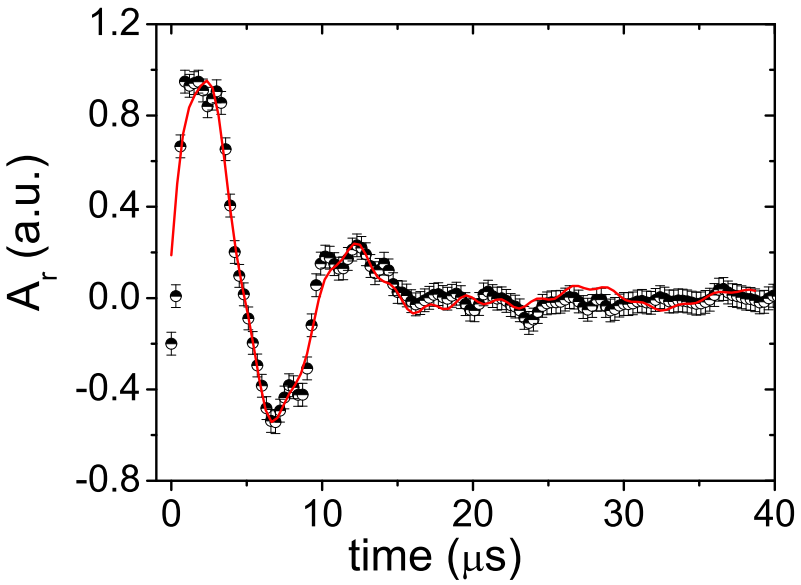

Figure 7.4: Example of the ringing signal (without the actual NMR signal) for x=7%, measured at 7 T $\parallel$ c, at 15 K (below T_c). The red solid curve is a tentative fit, with three resonance frequencies (see text below).

- Its amplitude increases with the magnetic field magnitude;
- It does not depend on the experimental apparatus employed: it was observed in Pavia, Grenoble, Northwestern University, and at NHMFL in Florida;
- It is enhanced when the field is perpendicular to the FeAs layers.

These evidences suggest that a tentative explanation of such an effect lays in a magneto-acoustic coupling between the vortex and the crystal lattices. In particular, when the vortex matter becomes glassy, the thermal excitation is too weak to overcome the pinning barrier, so the vortex elastic energy is transferred to the crystal lattice, causing a vibration. This would explain why the ringing is enhanced at low temperatures.
Fukushima *et al.* showed that the amplitude of the ringing signal induced in the coil is written as [220]:

$$A_r \sim H_1 \frac{H^2}{m v_s (1+\beta^2)} \tag{7.6}$$

where H_1 is the oscillating rf field at frequency ω, while m and v_s are the mass density and the acoustic shear velocity of the specimen. Moreover β is defined

as:

$$\beta = \frac{(q\delta)^2}{2} = \frac{\omega\rho(T)}{v_s^2\mu} \tag{7.7}$$

where the wave vector q is equal to ω/v_s, and ρ is the resistivity, which is related to δ, the penetration depth; finally μ is the magnetic permeability. From the previous equation β turns out to be a function of the temperature.
Two limit cases can be considered:

- In the solid vortex phase, $\rho \to 0$, then the amplitude of the spurious ringing can be approximately written as:

$$A_r \sim H_1 \frac{H^2}{mv_s} \tag{7.8}$$

Solid Phase

As a consequence of that, at low temperature, the quadratic relation $A_r \sim H^2$ should be satisfied. Remarkably, the ringing amplitude maximum, as measured on $Ba(Fe_{1-x}Rh_x)_2As_2$ in the time domain, agrees well with equation (7.8) (Fig. 7.5).

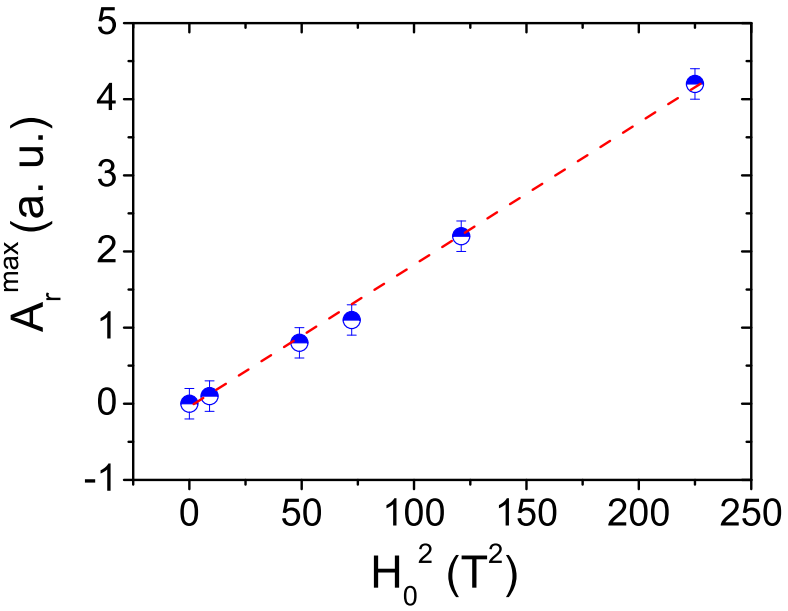

Figure 7.5: Maximum of the ringing amplitude, measured in the superconducting phase (about 10 K), below the temperature of the peak in $1/T_1$, as a function of the second power of the field. The linear behavior confirms the expectation of equation (7.8).

Moreover, the geometry of the sample is also relevant to the ringing forma-

tion. In fact, in a sample of size d, the resonance frequency is proportional to the sound velocity and inversely proportional to d. So, when the specimen is made of more than one crystal (as in a powder sample) a broadening of the resonance frequency can take place, and eventually the spectral density of the ringing becomes broader and flatter, leading to a less intense ringing. Another consideration relies on the coupling between the sample and the coil. It is sometimes useful to shield the sample with a metal cage or strip, like a copper tape, in order to get rid of the component of the electric field related to H_1, which in turn may give rise to the generation of acoustic waves. An attempt to isolate the sample with a copper tape was done, but the effect was negligible, thus suggesting that the physical origin of the ringing is magnetic and not electric (Fig. 7.6).

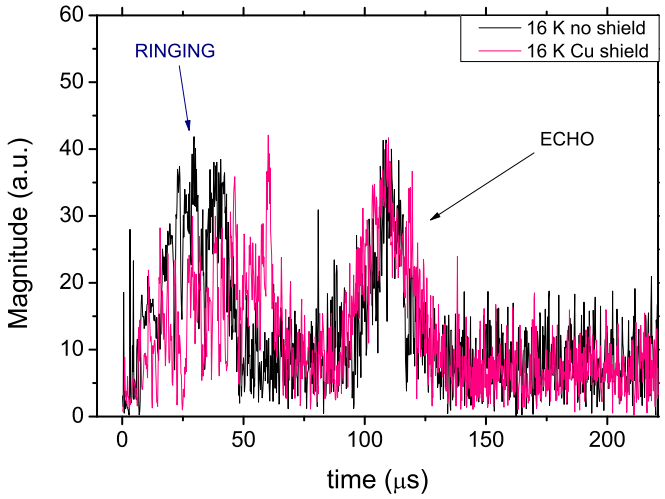

Figure 7.6: The echo with the ringing are displaced for x=6.8%, as they appear in an NMR experiment, at 16 K (below T_c) and 6.4 T, before and after the copper tape screening.

- When $T \to T_c^-$, the resistivity is non null, as vortices will move[2] by flux creep, and will dissipate energy. Since in the liquid phase the pinning mechanism is less effective, it is reasonable that the ringing magnitude will be strongly reduced. If the magnetic field is constant, the inverse of the maximum amplitude of the ringing signal versus temperature behaves like: Liquid Phase

$$\frac{1}{A_r}(T) = \frac{mv_s}{H_1 H}\left(1 + \frac{\rho^2}{d^2 v_s^2 \mu^2}\right) \tag{7.9}$$

[2]Usually ρ shows strong non-linear behavior with temperature.

Hence the temperature dependence of the ringing amplitude is mainly given by the resistivity term which, in the liquid phase, is strongly non linear and it usually follows an Arrhenius law:

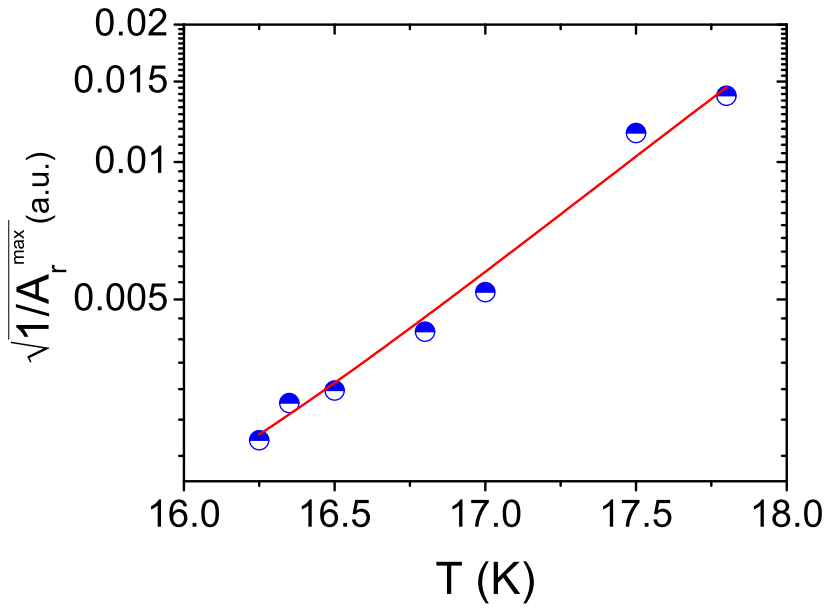

Figure 7.7: The square root of the inverse of the ringing amplitude is plotted as a function of the temperature, for $H = 8.5$ T $\parallel c$. The red curve is the best fit according to equation (7.10).

$$\log\left(\sqrt{\frac{1}{A_r}}\right) \sim \log \rho_0 - \frac{U}{T}. \tag{7.10}$$

From a fit to the previous equation (Fig. 7.7) the pinning activation energy becomes $U_p \sim 380 \pm 30$ K, which is of the same order of magnitude of the NMR measurements.

A further indication of the intrinsic relationship between vortex dynamics and the ringing effect is shown in the phase diagram (Fig. 7.8), from which it is clear that the ringing begins at a temperature above the liquid/solid crossover.

Ringing frequency

Before concluding this section some additional considerations concerning the natural frequency of the ringing are proposed. The fit in figure 7.4 is made by assuming three components in the ringing spectrum. This assumption has been verified in another experiment, carried out in Tallahasse, at 11 T on x=6.8%, where the Fourier transform of the ringing is characterized by three equidistant

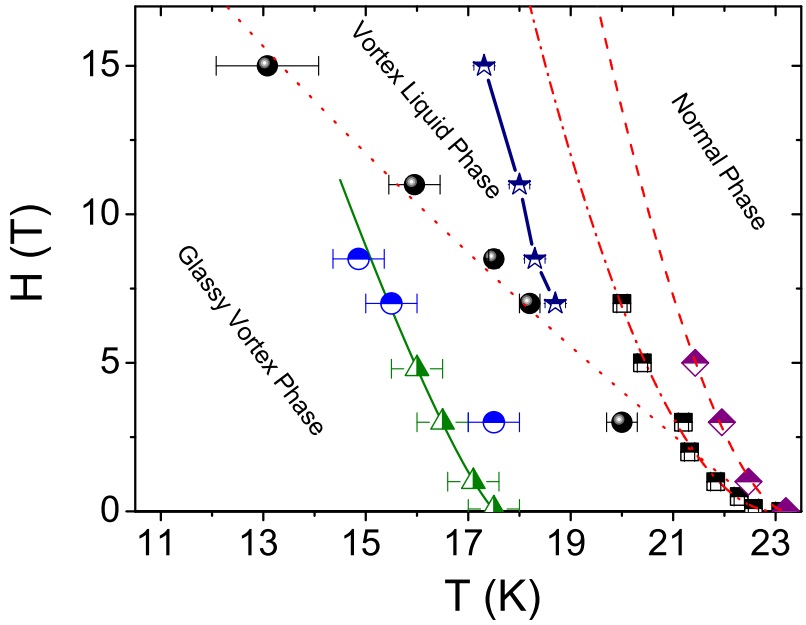

Figure 7.8: The phase diagram of Chapter 5, enriched with the blue stars data, showing the onset of the ringing effect, taking place in the liquid phase, where vortices are just a little correlated.

peaks (Fig. 7.9). These peaks are nearly 300 kHz far apart and their amplitude decreases with the increase of the frequency, but it does not depend on the temperature. If the origin of this resonance frequency is related to an optimal energy transfer from the vortex matter to the crystal, and consequently from the crystal to the coil, it is reasonable that when the pinning frequency matches the resonance energy of the coil, the ringing will be strongly enhanced. The subsequent decreasing maxima, in the Fourier transform of the spectra can be ascribed to harmonic resonances of the coil.

Finally, one may conclude that the study of the ringing can become a new methodology to explore the dynamical properties of FLL in type-II superconductors. However, in order to make other quantitative predictions some further analysis must be pursued, and the temperature/field dependence of the quality factor has to be taken into account.

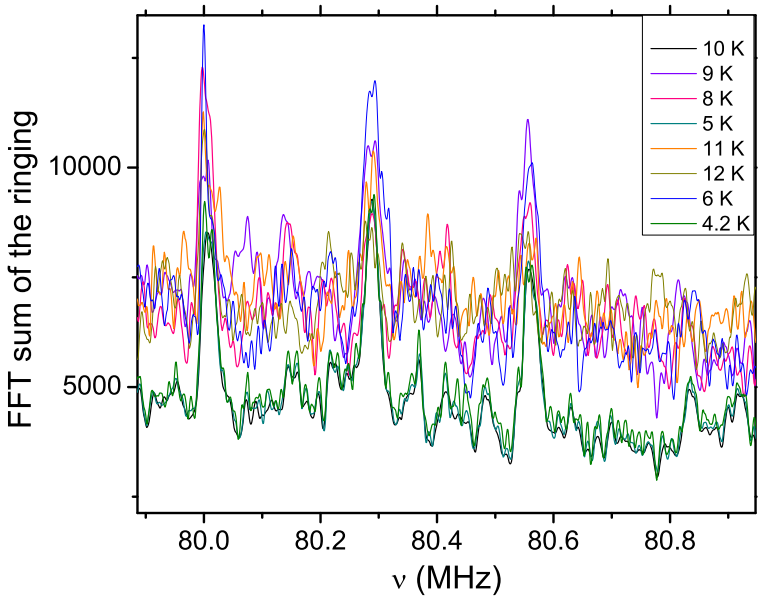

Figure 7.9: Field sweep of the ringing, as measured at 11 T $\parallel c$, on $x = 6.8$ % single crystal.

Part B:
Cantilever Magnetometry studies of $NbSe_2$ single grain

Dynamic cantilever magnetometry allows one to employ nm-μm size samples, and fields ranging from the mT up to $\sim$ 10 Tesla. Such a technique requires ultrasensitive cantilevers, the fabrication of which is rapidly improving [222]. Outstanding advances have been pushed forward through the results obtained by Wago *et al.* [223] and more recently, by the flourishing research activity based on the combination of AFM ultrasensitive cantilevers, and the achievements of ultralow temperatures [224–226]. While some recent papers address the problem of Ni nanotubes [227, 228], and semiconductor nanodevices [229, 230], a few studies drive the attention on superconducting particles [210, 231].
In this section, a well known type-II superconductor is investigated by cantilever magnetometry. $NbSe_2$ is chosen as it is a layered s-wave superconductor, with $T_c \sim 7.2$ K [232–234]. It also shows multiband superconductivity, with distinct small and large superconducting gaps on different sheets of the Fermi surface [235, 236]. Furthermore the vortex phase of niobium diselenide is known to show a plastic flow which dominates the dynamics [237].

Firstly an analytic expression for the vortex lattice magnetization is derived. Afterwards, the dynamical response of the flux lines lattice (FLL) is studied by measuring the cantilever energy dissipation and resonance frequency. In particular, the pinning energy barriers of the thermally activated creep motion are derived, and the mixed phase diagram of the material is drawn.

Before the realization of the cantilever magnetometry, an attempt to realize a Nuclear Magnetic Resonance Force Microscopy experiment was done. The basics of this fairly new technique are discussed below.

7.2.1 Principles of Nuclear Magnetic Resonance Force Microscopy (NMRFM)

NMRFM is a technique that aims at improving the detection sensitivity of inductive pick-up coils, usually employed in Magnetic Resonance Imaging (MRI), by mechanically detecting the magnetic forces produced by nuclear moments. In NMRFM, a soft cantilever is used to sense the magnetic forces arising between the nuclear spins in a sample and a nearby nanomagnet. This experiment can be carried out in two configurations:

- if the sample is placed on the cantilever, hanging above the nanowire+magnet, it is said to be in the "sample-on-cantilever configuration" (see Fig. 7.10);
- if the nanomagnet is fixed at the cantilever, the setup is called "tip-on-cantilever".

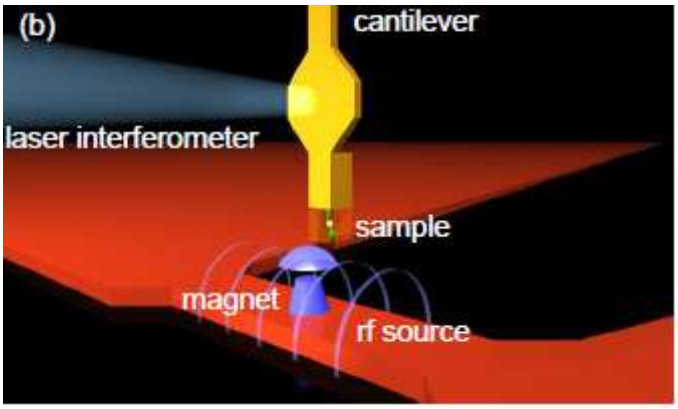

Figure 7.10: Schematics of an MRFM apparatus, in the sample-on-cantilever configuration. The figure is adapted from Ref [222].

A nanowire generates an oscillating rf field that, when tuned at resonance with the nuclear spins, can make them periodically flip, generating an oscillating ultra-small (attonewton) magnetic force on the cantilever. *In order to resonantly excite the cantilever, the nuclear spins must be inverted at the cantilever's mechanical resonance frequency.* The cantilever mechanical oscillations are then measured by an optical interferometer. The electronic signal produced by the optical detector is proportional both to the cantilever oscillation amplitude, and to the number of nuclear spins involved in the sample volume. As in a conventional MRI experiment, a field gradient is employed to get a spatial map of the nuclear spin density. In such a case the field gradient is generated by a nanomagnet, which is responsible for the high spacial resolution.
A noticeable example of this technique was realized by Degen *et al.* [238] on a sample of tobacco mosaic virus (TMV), less than 10 nm long. The probed nucleus was ^{1}H, which has the highest NMR sensitivity among all the nuclear species. The hydrogen spins are flipped at the cantilever frequency by means of the rf field, which is tuned at the Larmor frequency. This results in a periodic force that drives the mechanical resonance of the cantilever. Monitoring the cantilever oscillation amplitude, while mechanically scanning the magnetic tip with respect to the sample, allows the reconstruction of the proton density. In fact, the Larmor condition changes with the position, in such a way that:

$$\omega(\mathbf{r}) =^1 \gamma(H_0 + H_{tip}(\mathbf{r})), \tag{7.11}$$

where $\mathbf{r}$ is the position where the magnetic tip generates a field $H_{tip}(\mathbf{r})$.
Typical spin signal vibration amplitude is a fraction of an angstrom, which is smaller than the root mean square amplitude of cantilever thermal vibrations. A lock-in amplifier is employed so that the spin signal appears predominantly in the in-phase channel for on-resonance spins. Since the signal originates from the statistical (random) polarization of the spins, the sign of the detected signal can be either positive or negative and fluctuates during the course of the measurement, making conventional signal averaging ineffective. Degen *et al.* decided to detect the spin signal via its variance. To estimate the spin signal variance and to distinguish the spin signal from cantilever thermal vibrations, both the in-phase channel and the quadrature channel of the lock-in amplifier are digitized. These signals are then digitally filtered in software and the variances for the in-phase σ_i^2, and out-of-phase signal σ_q^2 are derived, and of course the cantilever thermal noise will contribute to the two channels, likewise. The spin signal variance is

thus estimated by the difference between the in-phase and quadrature variances:

$$\xi = \frac{k^2}{Q^2}(\sigma_i^2 - \sigma_q^2) \tag{7.12}$$

where k is the cantilever elastic constant, Q the cantilever quality factor, and ξ is called the "spin variance signal", or simply the "spin signal", that contains the physical information about the proton density distribution $\rho(\mathbf{r})$, and in turn allows one to build the three-dimensional image. Finally, since ξ is a convolution of $\rho(\mathbf{r})$ and the magnetic field distribution, the spin density map can be obtained after deconvolving the magnetic field profile. The advantages of this technique lay on the high resolution and on the record size of the device. In fact the smallest MRI sample can reach down to 3 μm, as the biggest limit is related to the fabrication of resonant coils. On the other hand mechanical, resonators can be fabricated with dimensions way smaller than a micron and, additionally, mechanical devices usually show resonant quality factors that surpass those of inductive circuits by orders of magnitude, resulting in a much lower baseline noise. In the next section the experimental results on the $NbSe_2$ grain are presented.

7.3 Experimental Results

The superconducting $NbSe_2$ powders were firstly characterized by SQUID magnetometry and by SEM microscopy. The static spin susceptibility showed $T_c(0) \sim$ 7.2 K, while the average grain size of the crystallites is 1.4 μm. A superconducting grain of surface 2x4 μm^2 was chosen with a glass needle using precision micromanipulators, combined with an optical microscope. The grain was attached to the cantilever tip, by using epoxy (Gatan G1), after coating the lever with a Si/Au bilayer, 5/10 nm thick (Fig. 7.11). Si was evaporated first, as an adhesive layer, Au afterwards, in order to shield unwanted electrostatic interactions between the cantilever and the surface. The single-crystal Si cantilever is 105 μm long, 4 μm wide, and 0.1 μm thick and includes a 18 μm long, 1 μm thick mass on its end. It has a small spring constant $k = 80$ μN/m, with low intrinsic dissipation, that is ideal for detecting small forces, down in the aN (attoNewton) range.
The motion of the lever was detected using laser light focused onto a 12 μm wide paddle, and using an optical fiber interferometer operating at a 1550 nm wavelength, with 20 nW of optical power incident. The sample with the cantilever and the chip with the magnetic tip were inserted into an ultra high vacuum (UHV) chamber at the bottom of a He3 continuous-flow cryostat, mechanically insulated

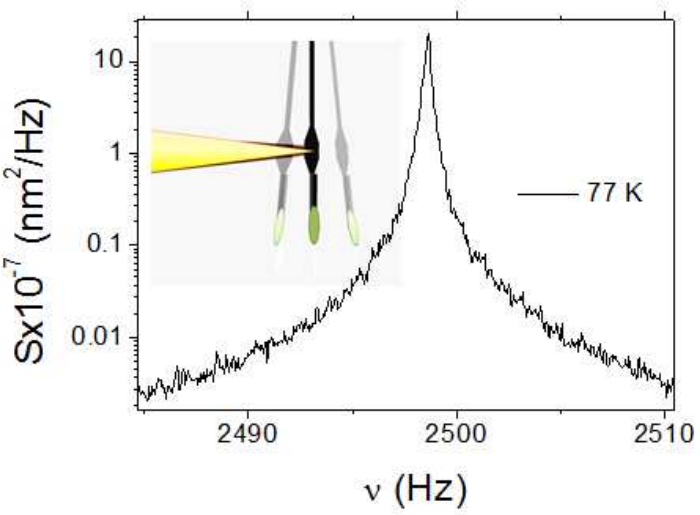

Figure 7.11: The sketch represents the sample-mounted-cantilever, oscillating in a static magnetic field $\mathbf{H_0}$, like a pendulum. The superconducting particle (green sphere) carries the magnetic moment μ, associated to the vortex lines lattice.

from the ground and equipped with a 6 T superconducting magnet, with the field applied along the cantilever axis.
After the sample preparation, a preliminary measure of the cantilever Q-factor was done, through the "ringdown" method, as described by Stipe *et al.* [239]. The cantilever is oscillated at its natural resonance frequency, with a root mean square amplitude of typically 10 to 20 nm, using a piezoelectric disk and a gain-controlled positive feedback loop. The drive circuit is then abruptly grounded and the cantilever rings down until thermal equilibrium is recovered. The same results were also obtained by measuring the spectral density of the cantilever's thermal motion and fitting the fundamental mode to a Lorentzian.
In the ringdown method, the cantilever displacement signal has been collected as a function of time. The power spectral density $S(\omega)$, i.e. the Fourier transform of the signal, has then been derived and fit to a dissipative harmonic oscillator model, with the Q-factor and the oscillation frequency ω as free parameters. Then the energy dissipation Γ was derived:

$$\Gamma = \frac{m\omega}{Q} \tag{7.13}$$

with m the motional mass, namely the sample mass plus the cantilever paddle.

The study of the cantilever mechanical response, as a function of the temperature, reveals a sudden increase in Γ, corresponding to a drop of the Q-factor,

close to T_c. Such an effect, reported in Fig. 7.12, has been observed earlier in other superconductors [163, 231, 240], and it has been interpreted as the sudden change of the sample magnetization, due to the Meissner-Ochsenfel effect. Furthermore, in type-II superconductors, the *incomplete* Meissner effect related to the FLL penetration, and the thermal fluctuations of the vortices competing with the pinning mechanism, can significantly affect the cantilever elastic response.

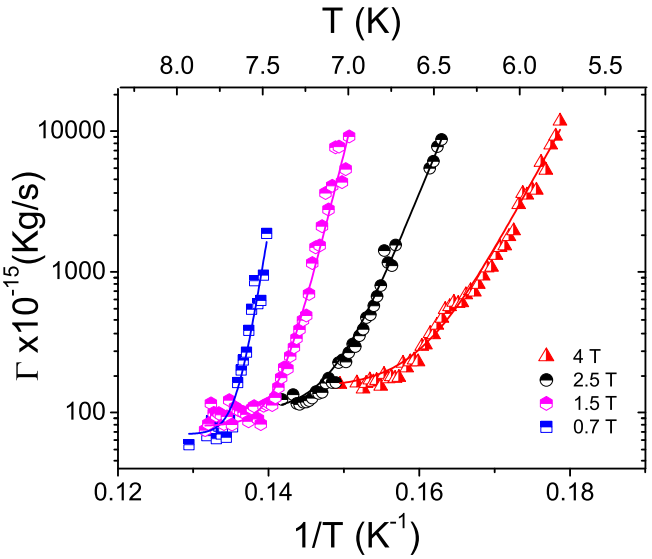

Figure 7.12: Temperature evolution of the cantilever energy dissipation, measured in field cooled, at different fields. The upturn of Γ marks the onset of the superconductivity transition. The solid curves are the fit discussed subsequently

Remarkably, at a temperature systematically *below* the drop in the Q-factor/increase in Γ, an abrupt increase in the cantilever resonance frequency ω has been observed (Fig. 7.13(a)). Moreover, a study of Γ as a function of H reveals a peak, denoting a phase transition, in the vortex matter (Fig. 7.13(b)), as shall be discussed subsequently.

Note that the sudden upturn of Γ hinders the performance of the NMRFM experiment, as in this condition the Q-factor becomes too small. Further consideration will be given towards the end of the chapter.

7.4 Vortex Lattice Magnetization

In the following, an analytic expression for the vortex lattice magnetization $\mathcal{M}$ as a function of the cantilever dissipation Γ, and resonance frequency ω is derived.

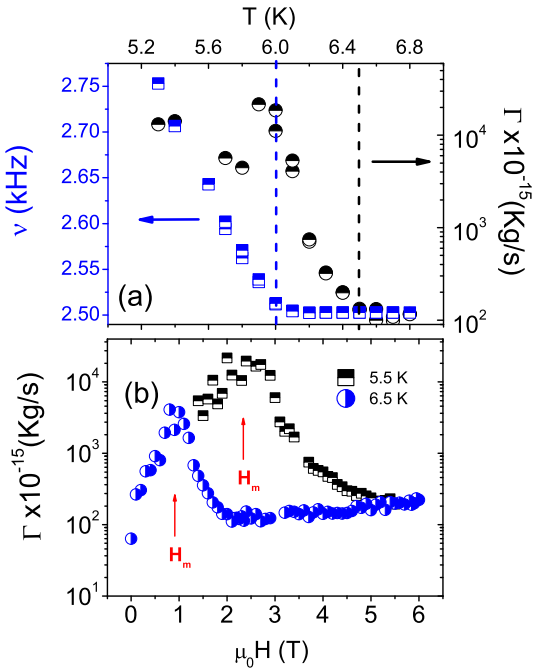

Figure 7.13: (a) Temperature evolution of the Q-factor (right axis) and fundamental mode frequency (left axis) of the sample-mounted cantilever, at 2 T. The increase of the cantilever natural frequency ν is found below the onset of the Q-drop, at each field. The dotted lines mark the Normal Phase (NP) from the Liquid Vortex Phase (LVP), and the Solid Vortex Phase (SVP). (b) Cantilever dissipation measured at 6.5 K (blue circles) and 5.5 K (black squares), by sweeping the field from 6 T to zero. Upon decreasing the magnetic field, the dissipation drops down, at the vortex freezing transition (red arrow).

Since the relaxation of the whole vortex lattice magnetization takes place over a timescale much longer than $1/\omega$ (typically few hours), it cannot give rise to the observed increase in Γ. Moreover the vortices are supposed to enter, when the cantilever is in the equilibrium position. The total energy of the sample-mounted cantilever, in the superconducting region, can be written as[3]

$$\mathcal{E} = \frac{1}{2}k(l_c\theta)^2 - V\mathcal{M}\cdot\mu_0\mathbf{H_0} \tag{7.14}$$

where l_c is the cantilever length, θ is the angle formed by the magnetic field direction and the cantilever axis, $\mu_0\mathbf{H_0}$ the external magnetic field, and V the sample volume. The scalar product in Eq. (7.14) gives a $\cos\theta$ factor, which is

[3]Form now on, all the equations will be written in I.S. units.

approximated up to the second order, for small angles:

$$\mathcal{E} \sim \frac{1}{2}k(l_c\theta)^2 - V\mathcal{M}\mu_0 H_0\left(1 - \frac{\theta^2}{2}\right) \tag{7.15}$$

The angular dependence of the energy gives rise to a torque force

$$\tau = -\frac{\partial \mathcal{E}}{\partial \theta} = -(kl_c^2 + V\mathcal{M}\mu_0 H_0)\theta \tag{7.16}$$

By recalling the equation of motion for the damped-forced harmonic oscillator [227]

$$m\frac{\partial^2 x(t)}{\partial t^2} + \Gamma\frac{\partial x(t)}{\partial t} = \frac{\tau}{l_c}, \tag{7.17}$$

being $x(t) \sim l_c\theta$ the tangential displacement, then:[4]

$$ml_c^2\frac{\partial^2\theta(t)}{\partial t^2} + \Gamma l_c^2\frac{\partial\theta(t)}{\partial t} + (kl_c^2 + V\mathcal{M}\mu_0 H_0)\theta(t) = 0. \tag{7.18}$$

By assuming the boundary condition $\theta(0) = 0$, the partial derivative equation has the following solution:

$$\theta(t) = ce^{-\alpha t}\sin(\omega t), \tag{7.19}$$

Indeed the system oscillates like an underdamped harmonic oscillator, where α is related to the dissipation:

$$\alpha = \frac{\Gamma}{2m}, \tag{7.20}$$

while the frequency ω:

$$\omega = \sqrt{-\frac{k}{m} + \frac{V\mathcal{M}\mu_0 H_0}{ml_c^2} - \frac{\Gamma^2}{4m^2}}. \tag{7.21}$$

By defining the natural oscillation frequency as $\omega_0 = \sqrt{k/m}$, it is possible to calculate the frequency shift (Fig. 7.14).

$$\Delta\omega = \sqrt{\frac{k}{m}}\left(\sqrt{1 - \frac{\Gamma^2}{4km} + \frac{V\mathcal{M}\mu_0 H_0}{kl_c^2}} - 1\right). \tag{7.22}$$

[4]If the vortices enter when the cantilever forms an angle $\theta_0 \neq 0$ with the field, the former solution can be easily modified, by adding a phase, which however does not affect the final result.

Since equation (7.21) shows a one-to-one correspondence between the sample magnetization and the measurable parameters (Γ, ω), the magnetization can be derived as

$$\mathcal{M}(\Gamma, \omega) = \frac{l_c^2}{V \mu_0 H} \left(m\omega^2 + k + \frac{\Gamma^2}{4m} \right). \tag{7.23}$$

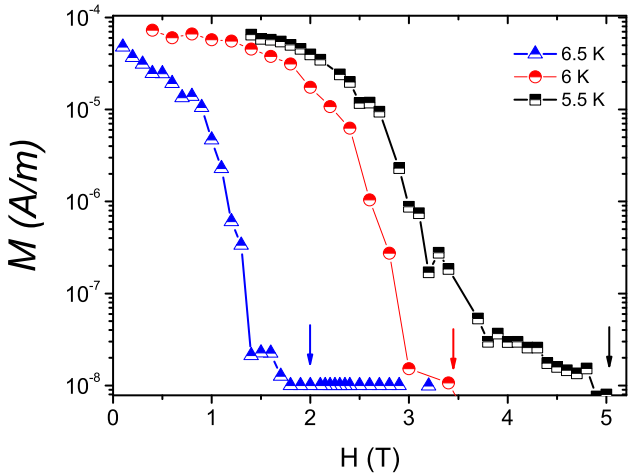

Figure 7.14: The magnetization as a function of the magnetic field, for three temperatures. The arrow marks the superconducting transition.

7.5 Vortex Freezing/Melting Transition

In addition to the above result, the study of Γ gives insights into the vortex lattice dynamics, as well. In fact, the upturn in cantilever dissipation, observed at T_c, can only occur through a non-conservative energy relaxation mechanism, such as spin relaxation or phonons escaping into the bulk, via the following relation:

$$\frac{d\mathcal{E}}{dt} = -\Gamma v^2 \tag{7.24}$$

where v is the cantilever velocity.

In the present case, the leading mechanism is ascribed to the flux-creep motion of vortices, hopping among metastable energy minima, generated by the pinning potential. In the former equation, $\Gamma(T, H)$ is taken as the sum of $\Gamma_c + \Gamma_v(T, H)$, i.e. intrinsic cantilever losses plus the vortex loss.

By drawing an analogy between Γ, and the imaginary part of the ac susceptibility, or the magnetoresistivity, which are all strictly related to the energy dissipation

induced by vortex motion, the data can be fit to the expression:

$$\Gamma(T,H) = \Gamma_c + \Gamma_0 e^{U(H)/T} \tag{7.25}$$

where U represents the pinning energy barrier of the thermally activated vortex motion. Fig. 7.15 shows that the thermally activated model fits the experimental data fairly nicely, supporting the initial assumption. Form the fit, the intrinsic cantilever dissipation turns out to be $\simeq 80 \times 10^{-15}$ kg/s, while $\Gamma_0 \simeq 10^{-35}$ kg/s. Moreover a study of the pinning energy barrier U as a function of the

activation barrier

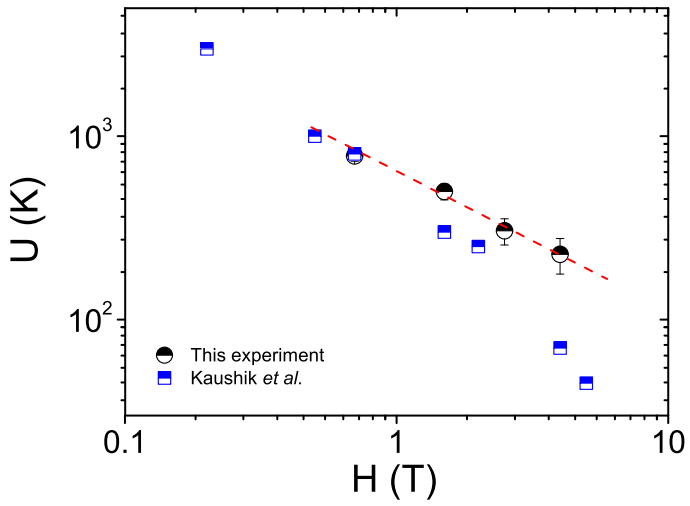

Figure 7.15: Energy barrier of the pinning as a function of the field, for $NbSe_2$ grain (black circles), as compared to the result presented in Ref. [242], on the same compound (blue triangles). The red dashed line is a guide for the eye.

magnetic field intensity is reported in Fig. 7.16. At first one notices a power-law behavior (red dotted line), as expected for a vortex bundle motion [22]. Indeed, a STM study on the same compound, shows the occurrence of a collective vortex bundle creep, taking place at 0.6 T, under the application of a strong current $J = 0.4J_c$ [241]. In the same panel, the pinning barriers are compared to Ref. [242], reporting a magnetoresistivity study on $NbSe_2$ (powder sample). The slight disagreement between the two data sets can be ascribed either to a powder effect, which in the transport measurements averages the activation barrier along the crystallographic directions, or to a little underestimation of Γ_c.

Furthermore, when the vortices enter into the solid phase, so that the hopping vortex correlation time becomes very long with respect to the cantilever natural oscillation frequency, one has to expect that (i) the small dissipation state is

vortex freezing

restored, and (ii) the sample-mounted cantilever becomes "stiffer". Fig. 7.13(a) shows a rise in ν, reflecting an increased stiffness of the cantilever, namely the presence of fixed vortex lines, while the Q-drop at T_c is associated to the entrance into the liquid phase.
Moreover, when Γ is plotted as a function of the magnetic field, a peak is observed and ascribed to the crossover from the liquid to the solid vortex phase (Fig. 7.13(b)). One may argue that such decrease of Γ at small field is not related to the freezing transition, but it is due to the diminished interaction of the field with the FLL. However, the peak moves towards higher fields, at lower temperatures, thus ruling out the former hypothesis.
An analogous phenomenology was found by Gammel *et al.*, [163] using mechanical measurements on high temperature superconductors single crystals, with a surface of about 1 mm^2, 0.1 mm thick, and containing many twins.
However note that here **the sample dimension is pushed to the limit of few μm, and a wider field range is explored**.

7.6 Phase diagram

Finally, a phase diagram of the mixed state of the $NbSe_2$ particle can be drawn (Fig. 7.16). In fact, the Γ onset overlaps with the H_{c2} data, measured by the SQUID magnetometer. Furthermore, the so called "Q-drop offset", namely the deviation from the normal state, well overlaps with the increase of the frequency response of the cantilever. The diagram allows one to identify the vortex liquid phase and the transition to the solid phase.

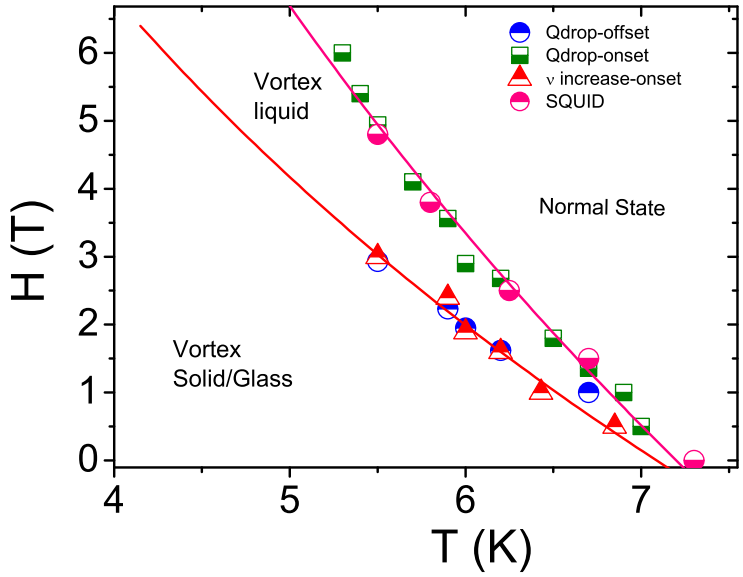

Figure 7.16: The phase diagram of $NbSe_2$ grain: the H_{c2} line is derived from the Q-drop onset (green squares) and the SQUID measurement (not shown). The Q-drop offset (blue circles) and the frequency increase (red triangle) mark the melting transition, as discussed in the text.

7.7 Conclusions

The last Chapter of this thesis deals with some novel approaches to study the vortex melting/freezing transition. The first method focuses on the persistent acoustic ringing affecting the NMR coil, below T_c. Such phenomenology has been analyzed in terms of magneto-acoustic coupling between the vortex lattice and the crystal itself.

The second part of the Chapter shows a cantilever magnetometry experiment, on a $NbSe_2$ single grain, carried out in the sample-on-cantilever geometry. The solution of the equation of motion results in an analytic expression for the vortex state magnetization, which depends on the measured parameters, Γ and ω. The temperature and field dependence of the cantilever energy dissipation and oscillation frequency reveals the energy barrier of the pinning mechanism, as a function of the field. Such results show that the ultrasensitive cantilever magnetometry is effective to derive the dissipation properties of the vortex lattice in micrometer and submicrometer size samples, and that its results are directly comparable with macroscopic techniques.

Moreover, the present discussion points out that in the liquid vortex phase the feasibility of an MRFM experiment becomes extremely challenging, as a result of the thermally activated depinning motions. However, the solid vortex phase the MRFM experiment may be a good candidate for such a study.

Conclusions and future perspectives

This thesis has addressed different issues regarding the $Ba(Fe_{1-x}Rh_x)_2As_2$ family of iron-pnictide superconductors, paying particular attention to the dissipative and fluctuative phenomena, occurring both below and above the transition temperature T_c. The mixed phase of these compounds, grown in form of single crystals, is characterized by a very rich phenomenology, despite the rather narrow fluctuating temperature region, which makes them good candidates for technological applications.
Among the various experimental techniques presented in such a study, nuclear magnetic resonance spectroscopy has been the most widely employed. In addition, SQUID magnetometry, ac-susceptibility and cantilever magnetometry have been used either to support the NMR results, or to study a new phenomenology.

The experimental part of this dissertation begins with a detailed study of static spin susceptibility, over a broad range of electron doping. The results provide a clear evidence for the occurrence of low-fields unconventional superconducting fluctuations, as well as Ginzburg-Landau fluctuations at intermediate and high fields, in a narrow temperature range, above the transition temperature. The experimental data have been supported by a theoretical analysis, which has earlier proven to be remarkably successful in interpreting similar phenomenology, occurring in the high-T_c superconductors. To the best of the author's knowledge, this is the first detailed study of static spin susceptibility, above the transition temperature, in 122 iron-pnictides, over a broad range of physical parameters. Furthermore, given the renewed interest in the superconducting fluctuations, and the great attention paid to the iron-pnictides, it is believed that these results may

open a fruitful discussion in the field and also stimulate new experiments, in other families of iron-based superconductors.

As far as the normal phase of the $Ba(Fe_{1-x}Rh_x)_2As_2$ family is concerned, a deep study of ^{75}As NMR spin-echo decay rate $1/T_2$ has been carried out, over a broad range of electron doping, magnetic fields and with different rf pulse sequences. The experimental results suggest the onset of an unconventional low-frequency dynamics, occurring in the normal state, below a characteristic temperature T^*. In particular it has been found that (i) the dynamic is favored by the magnetic field; (ii) it is accentuated for field in-plane; and (iii) it persists across the phase diagram. Moreover, the same dynamic is also observed in the spin-lattice relaxation rate $1/T_1$, in a quantitatively consistent manner. These observations have been discussed in the light of nematic fluctuations involving domain walls motion, and have been also suggested interesting analogies with the cuprates. New measurements at high fields would be desirable to discriminate between the nematic or stripe-like dynamics. A recent paper [150], has presented NMR results on the $Ba(Fe_{1-x}Co_x)_2As_2$ family, which support the interpretative framework proposed in Chapter 4.

When the temperature is lowered below T_c, a noticeable phenomenology related to the Abrikosov vortex lines motion has been observed. Ac-susceptibility and NMR spectroscopy have been employed as comparative techniques, to gain some insights into the temperature and field dependence of the vortices correlation time. Such an analysis has evidenced a dynamical cross-over from a liquid vortex state, to a glassy vortex state. This work also shows that the Arrhenius law, usually employed to describe the vortex dynamics in high-T_c superconductors, has to be abandoned in 122 iron-pnictides, in favor of the Vogel - Fulcher law. Still in contrast to the previous materials, the vortex pinning mechanism in $Ba(Fe_{1-x}Rh_x)_2As_2$ 122 pnictides seems to be fairly individual, rather than collective, over a broad field range. A fairly rich phase diagram characterizing the vortex state has been drawn.

In addition to the equilibrium phase diagram, another - more complex - scenario concerning the vortex dynamics can be pictured, as an external dc current is injected into the sample. NMR can still provide deep insights into the issue, given its microscopic character, through the study of the spin - spin decay time. Moreover, a detailed study of J_c in the $Ba(Fe_{1-x}Rh_x)_2As_2$ family is till lacking,

and it would be beneficial to inspect more deeply into the current driven vortex dynamics.

Finally, the concluding chapter introduces some novel approaches to investigate the melting transition occurring in the vortex matter of two type-II superconductors: (i) the analysis of the acoustic ringing emerging from the NMR coil, below the critical temperature, and (ii) the study of the energy dissipation and resonance frequency of the sample-mounted cantilever, in an ultrasensitive cantilever magnetometry investigation. Even though such observations still need theoretical and experimental confirmations, they may become new methodologies to inspect the fascinating world of the Abrikosov lattice dynamics.

Part III
Appendices

Appendix A: The form factor

This appendix reports a step by step calculation, of the form factor of the local magnetic field probed by the nucleus, in a spin-lattice relaxation rate $1/T_1$ experiment. In general, this quantity is related to the **q**-averaged low-energy dynamical electron-spin susceptibility, and it can shed some light on the spin fluctuations issue. In order to understand this relationship the general expression for the spin-lattice relaxation rate is recalled: [63]

$$\frac{1}{T_1} = \frac{\gamma_n^2}{2} \int e^{i\omega_L t} \{< h_x(t)h_x(0) > + < h_y(t)h_y(0) >\} \, dt \tag{7.26}$$

where (x, y, z) are the coordinate of a system oriented according to the external magnetic field $\mathbf{H_0}$, i.e. $\mathbf{H_0} = H_0\mathbf{z}$. The local field at the nuclear site $\mathbf{h}(t)$ is given by:

$$\mathbf{h}(t) = \sum_i \tilde{A}_{hyp_i} \cdot \mathbf{S}_i \tag{7.27}$$

$\tilde{A}_{hyp}$ is the hyperfine tensor, which couples the nuclear spins to the electronic spins $\mathbf{S}_i$, and the sum runs over the i-th electronic ion sites. The FeAs magnetic cell will be taken as the model to develop this calculation. In such a case every As nucleus is coordinated with four Fe ions.
As it will be shown shortly, it is very useful to introduce the collective spin components

$$\mathbf{S}_i(t) = \frac{1}{\sqrt{N}} \sum_{\mathbf{q}\in BZ} e^{i\mathbf{q}\cdot\mathbf{r}_i} \mathbf{S}_\mathbf{q}(t), \tag{7.28}$$

where the sum runs over the wave vectors of the first Brillouin zone, and $\mathbf{r}_i$ is the ion position. Moreover, the α-th component of the local field can be written as:

$$h_\alpha(t) = \frac{1}{\sqrt{N}} \sum_{\mathbf{q}\in BZ} \sum_{i=1}^{4} \sum_{\beta=x,y,z} A^{\alpha\beta}_{hyp_i} S^{\beta}_{\mathbf{q}}(t) e^{i\mathbf{q}\cdot\mathbf{r}_i}. \tag{7.29}$$

Assuming to deal with a Heisenberg system, $S^{\beta}_{\mathbf{q}}(t)$ will not depend on the β component, so the former equation can be written in an equivalent form

$$h_\alpha(t) = \frac{1}{\sqrt{N}} \sum_{\mathbf{q}\in BZ} \sum_{i=1}^{4} \left(\sum_{\beta=x,y,z} \tilde{A}^{\alpha\beta}_{hyp_i} \right) S^{\beta}_{\mathbf{q}}(t) e^{i\mathbf{q}\cdot\mathbf{r}_i}. \tag{7.30}$$

The **correlation function** of the local field $< h_\alpha(t) h_\alpha(0) >$ turns out to be:

$$< h_\alpha(t) h_\alpha(0) >= \frac{1}{N} \sum_{\mathbf{q}\mathbf{q}'\in BZ} \left(\sum_{i=1}^{4} \sum_{\beta=x,y,z} A^{\alpha\beta}_{hyp_i} e^{i\mathbf{q}\cdot\mathbf{r}_i} \right) \left(\sum_{j=1}^{4} \sum_{\beta=x,y,z} A^{\alpha\beta'}_{hyp_j} e^{i\mathbf{q}'\cdot\mathbf{r}_j} \right) < S^{\beta}_{\mathbf{q}}(t) S^{\beta'}_{\mathbf{q}'}(0) > \tag{7.31}$$

A further substitution can be made

$$A^{\alpha\beta}_{hyp\mathbf{q}} = \sum_{i=1,4} e^{i\mathbf{q}\cdot\mathbf{r}_i} A^{\alpha\beta}_{hyp_i}. \tag{7.32}$$

Moreover, since the following properties are holding [243]

1. $\sum_{qq'} < S_{\mathbf{q}}(t) S_{\mathbf{q}'}(0) >= \sum_q < S_{\mathbf{q}}(t) S_{-\mathbf{q}}(0) >$ given the translation symmetry of the $q-$space;
2. $S(-\mathbf{q}, 0) = S(\mathbf{q}, 0)^*$;

the **dynamical structure factor** is naturally introduced

$$S^{\alpha\alpha}(\mathbf{q}, \omega_L) = \int e^{i\omega_L t} < S^{\alpha}_{\mathbf{q}}(t) S^{\alpha}_{-\mathbf{q}}(0) > dt \tag{7.33}$$

It is recalled that the dynamical structure factor is related to the imaginary part of the Spin Susceptibility, via the **Dissipation-Fluctuation Theorem**, which in low frequency limit reads

$$S^{\alpha\alpha}(\mathbf{q}, \omega) = \frac{2k_B T}{\omega} \chi''(\mathbf{q}, \omega) \tag{7.34}$$

Now, the analytic expression of $1/T_1$ can be written in a more compact form:

$$\frac{1}{T_1} = \frac{\gamma_n^2}{2N} \sum_{\mathbf{q}\in BZ} (|\sum_{\beta=x,y,z} A^{x\beta}_{\mathbf{q}}|^2 + |\sum_{\beta=x,y,z} A^{y\beta}_{\mathbf{q}}|^2) S^{\alpha\alpha}(\mathbf{q}, \omega_L) \tag{7.35}$$

The term in brackets is called **Form Factor**. Because the correlation function of the local field for orthogonal direction is zero, namely $< S_{\mathbf{q}}(t)^{\alpha} S_{-\mathbf{q}}(0)^{\beta} > \neq 0 \Longleftrightarrow \alpha = \beta$, it can be concluded that:

$$|\sum_{\beta=x,y,z} A_{\mathbf{q}}^{x\beta}|^2 = \sum_{\beta=x,y,z} |A_{\mathbf{q}}^{x\beta}|^2 \tag{7.36}$$

As a consequence of that, the form factor is given by the sum of six squared moduli. The two following geometries will be considered:

1. $\mathbf{H_0} \parallel c$ axis;
2. $\mathbf{H_0} \in (a, b)$ plane;

To go further into the calculation the coordinates of Fe ions, and As are needed. Recalling the crystalline structure of the $Ba(Fe_{1-x}Rh_x)_2As_2$compounds [26], it is known that the As nucleus sits at the apex of a tetrahedron the basis of which is formed by four Fe ions, and it is rotated of $\pi/4$ rads with respect to the unit cell (Fig. 7.17). Nonetheless it's more effective to orient the axes like the magnetic

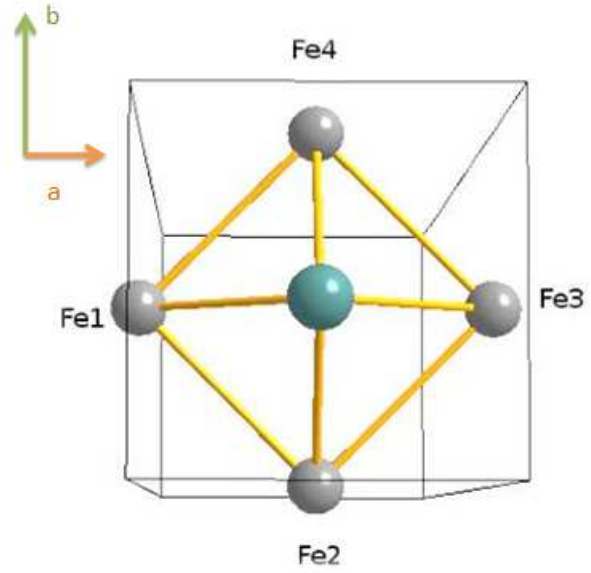

Figure 7.17: Sketch view of the FeAs tetrahedron, seen through the c direction. Fe ions are depicted as grey spheres, while As nucleus is the blue sphere, in the middle.

cell (Fig. 7.18), so from now on the origin of the axes sits at the As site, and it is rotated of $\pi/4$, with respect to the crystal unit cell. Since the magnetic cell has the same symmetry of the crystal cell, the Fe coordinates are written accordingly

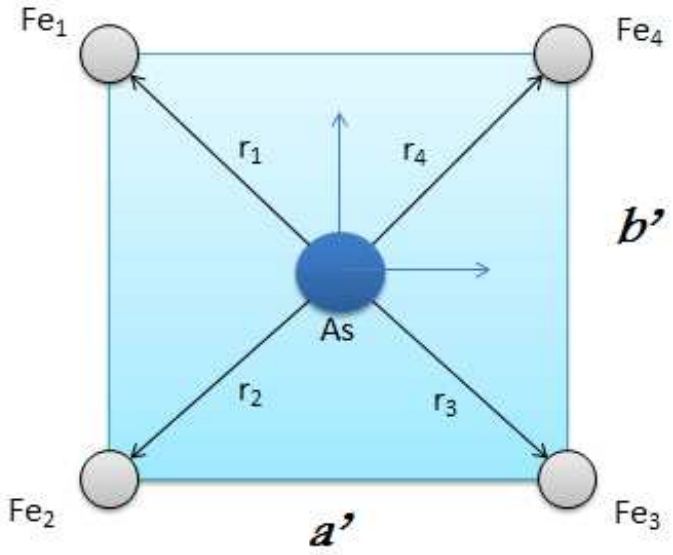

Figure 7.18: Sketch view of the magnetic cell.

$$\begin{aligned} Fe_1 \quad & (-a'/2, a'/2, -h) \\ Fe_2 \quad & (-a'/2, -a'/2, -h) \\ Fe_3 \quad & (a'/2, -a'/2, -h) \\ Fe_4 \quad & (a'/2, a'/2, -h) \\ As \quad & (0, 0, 0) \end{aligned} \tag{7.37}$$

where $a' = a\sqrt{2}/2$ is the magnetic cell parameter, $a = b = 3.6925$ Å is the unit cell parameter in the tetragonal symmetry, and $h = 1.36$ Å is the distance of the As ion as respect to the Fe plane.
Now the form factor for the x component becomes:

$$\begin{aligned} |A^x_{\mathbf{q}}|^2 &= |\sum_i A^{xx}_i e^{i\mathbf{q}\cdot\mathbf{r_i}}|^2 + |\sum_i A^{xy}_i e^{i\mathbf{q}\cdot\mathbf{r_i}}|^2 + |\sum_i A^{xz}_i e^{i\mathbf{q}\cdot\mathbf{r_i}}|^2 = \\ &= (A^{xx}_1 e^{i\mathbf{q}\cdot\mathbf{r_1}} + A^{xx}_2 e^{i\mathbf{q}\cdot\mathbf{r_2}} + A^{xx}_3 e^{i\mathbf{q}\cdot\mathbf{r_3}} + A^{xx}_4 e^{i\mathbf{q}\cdot\mathbf{r_4}})(c.c.) + \\ &+ \text{"xy" terms} \\ &+ \text{"xz" terms} \end{aligned} \tag{7.38}$$

where "c.c." means complex conjugate. After some algebra, it is found

$$\begin{aligned} |A^x_{\mathbf{q}}|^2 &= E^2 + 2((A_xB_x + C_xD_x)\cos(q_yb') + (A_xD_x + B_xC_x)\cos(q_xa') \\ &+ A_xC_x\cos(-q_xa' + q_ya') + B_xD_x\cos(q_xa' + q_ya')) \\ &+ \text{"xy" terms} \\ &+ \text{"xz" terms} \end{aligned} \tag{7.39}$$

where $A_x = A^{xx}_1$, $B_x = A^{xx}_2$, $C_x = A^{xx}_3$, $D_x = A^{xx}_4$ and $E = A^2_x + B^2_x + C^2_x + D^2_x$. The complete Form Factor is given by the sum $|A^x_{\mathbf{q}}|^2 + |A^y_{\mathbf{q}}|^2$, where the same procedure applies for the y components.

The Hyperfine tensor: dipolar coupling

The second rank tensor of the hyperfine interaction is a key ingredient of this calculus. The latter is usually given by the dipolar interaction A_{dip} between the nucleus and the electron plus the transferred interaction A_t, as described in Chapter 2. The former, in cgs units,[5] reads:

$$A^i_{dip} = g\mu_B \begin{bmatrix} \frac{3x_i^2 - r_i^2}{r_i^5} & \frac{3x_iy_i}{r_i^5} & \frac{3x_iz_i}{r_i^5} \\ \frac{3x_iy_i}{r_i^5} & \frac{3y_i^2 - r_i^2}{r_i^5} & \frac{3y_iz_i}{r_i^5} \\ \frac{3x_iz_i}{r_i^5} & \frac{3y_iz_i}{r_i^5} & \frac{3z_i^2 - r_i^2}{r_i^5} \end{bmatrix}$$

where $g \sim 2$, μ_B is the Bohr magneton and $\mathbf{r_i} = (x_i, y_i, z_i)$ is the vector connecting the i-th electron to the nuclear site. The dipolar tensor of the four Fe sites fulfills the symmetry properties listed below:

$$A^{dip}_1 = \begin{bmatrix} A_{xx} & -A_{xy} & A_{xz} \\ -A_{xy} & A_{yy} & -A_{yz} \\ A_{xz} & -A_{yz} & A_{zz} \end{bmatrix}$$

$$A^{dip}_2 = \begin{bmatrix} A_{xx} & A_{xy} & A_{xz} \\ A_{xy} & A_{yy} & A_{yz} \\ A_{xz} & A_{yz} & A_{zz} \end{bmatrix}$$

$$A^{dip}_3 = \begin{bmatrix} A_{xx} & -A_{xy} & -A_{xz} \\ -A_{xy} & A_{yy} & A_{yz} \\ -A_{xz} & A_{yz} & A_{zz} \end{bmatrix}$$

[5] $\frac{\mu_0}{4\pi} = 1$.

$$A_4^{dip} = \begin{bmatrix} A_{xx} & A_{xy} & -A_{xz} \\ A_{xy} & A_{yy} & -A_{yz} \\ -A_{xz} & -A_{yz} & A_{zz} \end{bmatrix}$$

The Hyperfine tensor: transferred coupling

To evaluate the hyperfine transferred coefficients, it should be considered both the contribution of the s-wave orbitals, which provides a scalar term, plus the $l \neq 0$ orbitals, which has a complicated angular dependence. A trick to overcome this problem is to recall that the Knight Shift and the spin susceptibility are related to the hyperfine constant via the equation (see Chapters 2 and 4)

$$K_{\alpha\alpha}(T) = \frac{A_{\alpha\alpha}}{gN_A\mu_B}\chi_{\alpha\alpha}(T) \tag{7.40}$$

So that $A^t_{\alpha\alpha} = A_{\alpha\alpha} - A^{dip}_{\alpha\alpha}$, being N_A the Avogadro number. If the transferred term is equal for each Fe ion, namely $A^t_{\alpha\alpha i} = (A_{\alpha\alpha} - 4A^{dip}_{\alpha\alpha i})/4$, it can be finally written

$$A_t = \begin{bmatrix} 25.6 & 0 & 0 \\ 0 & 25.6 & 0 \\ 0 & 0 & 11.3 \end{bmatrix} kOe$$

When the external field is parallel to the crystallographic c axis, the coordinate system can be mapped onto one another so that $(x, y, z) \rightarrow (a, b, c)$. All the excitation at wavevectors on the border of the Brillouin zone will be strongly reduced by the form factor, which however is not null at this border.

$\mathbf{H_0} \parallel c$

On the other hand, when the magnetic field lays in the (a, b) plane, the coordinates can be replaced with the following: $z \rightarrow a$, $x \rightarrow b$, $y \rightarrow c$. This is just one of the possible choices since all the other combinations are equivalent, provided that $z \in (a, b)$ plane, owing to the cylindrical symmetry of the hyperfine tensor. The results are compared in 7.19.

$\mathbf{H_0} \in (a, b)$

The second Form Factor is flatter, however its value at the critical wavevector for the antiferromagnetic (nematic or CAF) excitations, namely $\mathbf{Q_c}(0, \pm\pi/a)$ or $\mathbf{Q_c}(\pm\pi/a, 0)$ is about twice the value of the other orientation, a more effective filter effect of the spin fluctuations can be done by the form factor, when the field lays along the c axis. This however is not enough to explain the anisotropy if the peak observed in $1/T_1$, above the critical temperature (Chapter 4), and a different explanation involving spin fluctuation dispersion may be rather invoked. Before concluding the appendix it is shown what is the effect of the dipolar

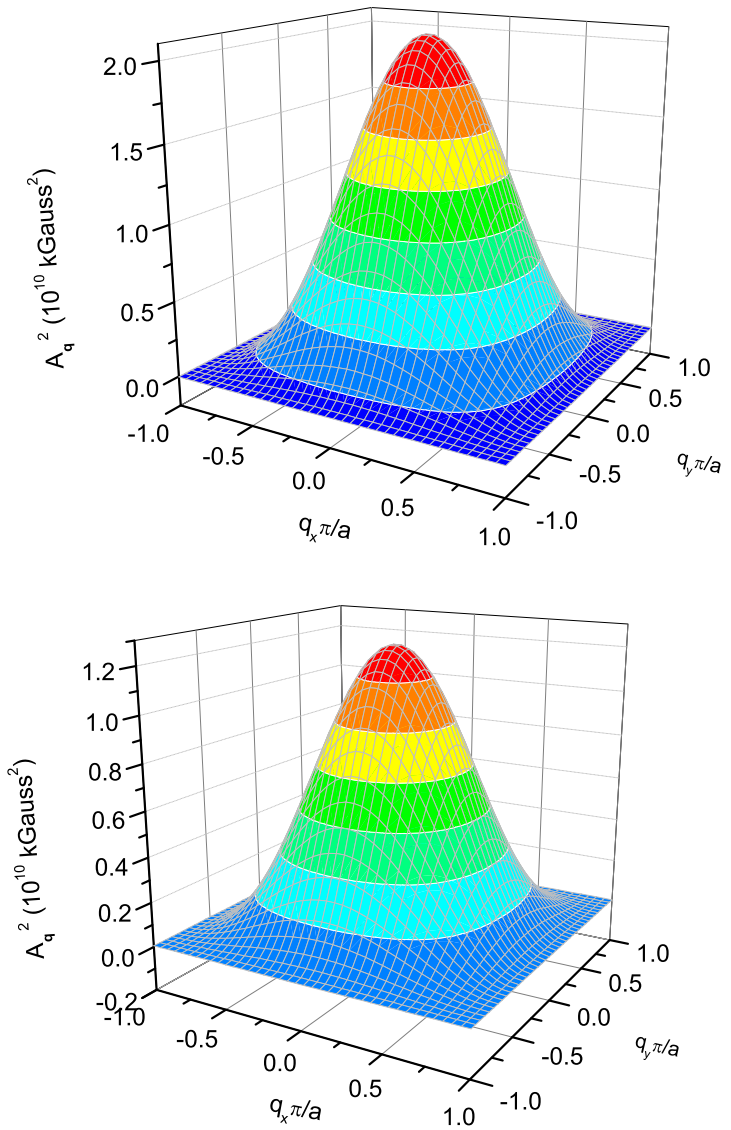

Figure 7.19: The Form Factor of As nucleus coordinated with four Fe ions, for a magnetic field applied along the c axis (top figure), and within the (a, b) plane (bottom figure).

coupling to the Form Factor. In fact, without the dipolar term, the Hyperfine tensor is diagonal. The results show that, for both the orientations of the sample, a null form factor at the critical wave vectors $(0, \pm\pi)$, $(\pm\pi, 0)$ rises, thus leading to a null relaxation rate, which is not physically correct. So, even though the dipolar field is smaller than the transferred one, it should not be omitted.

Appendix B:
Methods of moments

The Method of moments allows to predict the NMR linewidth due to dipolar interaction among nuclei, from first principles, with no need to estimate the eigenstates of the total hamiltonian. This appendix deals with the calculation of the second and fourth moments of *like nuclei*, namely in the assumption that just one nuclear species is present. However, when unlike spins are also present, a similar reasoning can be followed [62].
The Free Induction Decay (FID) signal is described by the *correlation function* of the transverse magnetization $\mathcal{M}_{\S}(t)$, which depends on the time:

$$G(t) = \cos(\omega_0 t) < \mathcal{M}_x(t)\mathcal{M}_x(0) > \tag{7.41}$$

where the symbol $<,>$ refers to the statistic average over the quantum operator $\mathcal{M}_{\S}$. In the rotating reference frame (at the Larmor frequency ω_0), the signal will drop off the cosine factor. Moreover, the temporal evolution of $\mathcal{M}_{\S}$ operator, implies to resume the *interaction representation* [244]:

$$\mathcal{M}_x(t) = e^{i\mathcal{H}_0 t/\hbar}\mathcal{M}_x e^{-i\mathcal{H}_0 t/\hbar} \tag{7.42}$$

From the complete hamiltonian presented in Chapter 2, just the terms that commute with the Zeeman interaction are retained, namely A_{jk} and B_{jk}, and the deriving $\mathcal{H}'_{n-n}$ is called the "truncated" dipolar interaction:

$$\begin{aligned} G(t) &= Tr\left\{e^{-i\omega_0 I_z t}e^{iH'_{n-n}t/\hbar}\mathcal{M}_x e^{+i\omega_0 I_z t}e^{-i\mathcal{H}'_{n-n}t/\hbar}\mathcal{M}_x\right\} \\ &= Tr\left\{e^{i\mathcal{H}'_{n-n}t/\hbar}\mathcal{M}_x^{-i\mathcal{H}'_{n-n}t/\hbar}e^{i\omega_0 I_z t}\mathcal{M}_x e^{i\omega_0 I z t}\right\} \end{aligned}$$

By recalling that $e^{i\omega_0 I_z t} = \mathcal{R}_{\ddagger}$ is the rotation operator around the z axis of an angle $\omega_0 t$, it can be written ${\mathcal{R}_{\ddagger}}^* \mathcal{M}_{\S} R_z$ as $\mathcal{M}_x cos(\omega_0 t) + M_y sin(\omega_0 t)$. The correlation function becomes:

$$G(t) = Tr\left\{e^{i{\mathcal{H}'}_{n-n}t/\hbar}\mathcal{M}_x^{-i{\mathcal{H}'}_{n-n}t/\hbar}(\mathcal{M}_x\cos(\omega_0 t) + \mathcal{M}_y\sin(\omega_0 t))\right\} \tag{7.43}$$

Finally,

$$G(t) = \cos(\omega_0 t)Tr\{e^{i{\mathcal{H}'}_{n-n}t/\hbar}\mathcal{M}_x^{-i{\mathcal{H}'}_{n-n}t/\hbar}\mathcal{M}_x\} + \sin(\omega_0 t)Tr\{e^{i{\mathcal{H}'}_{n-n}t/\hbar}\mathcal{M}_x^{-i{\mathcal{H}'}_{n-n}t/\hbar}\mathcal{M}_y\}$$

the second term of the sum gives the mixed correlation of $\mathcal{M}_x$ and $\mathcal{M}_y$ which can be proved to be zero.
In passing, it can be defined $G(t) = G'(t)\cos(\omega_0 t)$ as the correlation function seen in the laboratory frame, and viceversa $G'(t)$ as the auto-correlation function, seen in the rotating frame. Now the relation between the correlation function and the NMR spectrum $f(\omega)$ is

$$f(\omega) = K\int_0^\infty G(t)\cos(\omega t)dt.$$

and conversely,

$$G(t) = \frac{2}{K\pi}\int_0^\infty f(\omega)\cos(\omega t)d\omega \tag{7.44}$$

K being the normalization constant.
If the variable ω is replaced by $u = \omega - \omega_0$ and $h(u) = f(\omega_0 + u)$ is written instead:

$$\begin{aligned} G'(t)\cos(\omega_0 t) &= \frac{2}{\pi K}\int_{-\omega_0}^\infty f(\omega_0 + u)\cos((\omega_0 + u)t)du \\ &= \frac{2}{\pi K}\left(\cos(\omega_0 t)\int_{-\infty}^\infty h(u)\cos(ut)du - \sin(\omega_0 t)\int_{-\infty}^\infty h(u)sin(ut)du\right) \end{aligned}$$

$h(u)$ is an even function, so the last term will drop off. Eventually

$$G'(t) = \frac{2}{\pi K}\int_{-\infty}^\infty h(u)\cos(ut)du, \tag{7.45}$$

the extension of integral lower limit to infinity is allowed, in case of narrow lines. Finally, the **moment** of the function $h(u)$ centered at zero (Van Vleck treatment)

is written as [62]

$$M_n = \int_{-\infty}^{\infty} h(u) u^n du. \tag{7.46}$$

Since $h(u)$ is an even function, only the even moments survive:

$$M_{2n} = (-1)^n \frac{\pi K}{2} \frac{d^{2n} G'(t=0)}{dt^{2n}} \tag{7.47}$$

To find the n−th moment, $G'(t)$ can be expanded:

$$G'(t) = \sum_k M_k \frac{t^k}{k!} \tag{7.48}$$

where M_k stands for the k-th moment of the NMR spectrum. Moreover by expliciting equation 7.45, it is written

$$\frac{d^n G_d(t=0)}{dt^n} = \left(\frac{i}{\hbar}\right)^n Tr\left\{{H'}_{n-n}, [{H'}_{n-n}, [....[{H'}_{n-n}, \mathcal{M}_x]]]\mathcal{M}_x\right\} \tag{7.49}$$

where it can be shown that the n-times commutator is equal to $[.., ..]^n$.
Finally it is easy to show that the expressions for the second and fourth moments become:

$$M_2 = -\frac{1}{\hbar^2} \frac{Tr\left\{[{H'}_{n-n}, \mathcal{M}_x]^2\right\}}{Tr\left\{I_x^2\right\}} \tag{7.50}$$

$$M_4 = \frac{1}{\hbar^4} \frac{Tr\left\{[{H'}_{n-n}, [{H'}_{n-n}, \mathcal{M}_x]]^2\right\}}{Tr\left\{I_x^2\right\}} \tag{7.51}$$

After expliciting the commutator $[{H'}_{n-n}, \mathcal{M}_x]$, the most important result of this appendix is written:

$$M_2 = \frac{\gamma^4 \hbar^2}{3} I(I+1) \sum_k \frac{3}{2} \frac{1 - 3\cos^2(\theta_{j,k})}{r_{j,k}^3} \tag{7.52}$$

The fourth moment can be calculated analogously. Moreover, a Gaussian line shape, namely a FID $G'(t) = G'(0) e^{-M_2 t^2/2}$, has to fulfill the property

$$\frac{M_4}{M_2^2} = 3 \tag{7.53}$$

In such a case the NMR line has the form:

$$f(\omega) = \frac{1}{\Delta\sqrt{2\pi}} e^{-(\omega-\omega_0)^2/(2\Delta^2)} \tag{7.54}$$

where the second moment Δ^2 is related to the FWHM by the following:

$$\text{FWHM} = 2\Delta\sqrt{2log(2)} = 2.36\Delta. \tag{7.55}$$

On the other hand, when the line is a Lorentian, no second or higher order moment can be defined.

This calculation is not just useful to obtain the linewidth of the NMR line, but also to predict the magnitude of the spin-spin relaxation time, if the dipole interaction is the only mechanism responsible for the signal dephasing.
A C++ program has been implemented to calculate the second moment of As nucleus, in case of dipolar interaction. A value of $T_2 = 0.7$ ms, for $\mathbf{H} \parallel c$ axis, and 0.64 ms for $\mathbf{H} \perp c$, are found. Such results are in agreement with Ref. [52]. Nevertheless, the experimental value of the T_2 is 3.6 times bigger than the theoretical prediction from the rigid lattice summations [130, 245]. However the previous calculation does not take into account K. Kambe *et al.*'s argument for the second moment of the central line of a $I > 1$ spin [246]. Additionally, if one neglects the flip-flop terms in the interaction Hamiltonian, assuming that the dipolar contribution to the line linewidth may be much smaller than the xy components of the indirect coupling, thus inhibiting the spin-flip process [134], one finds $T_2 = 1.36$ ms, which is nearly two times bigger than the former estimation, but still too far from the experimental value (~ 2.5 ms).

Appendix C: Magnetic Susceptibility

Among all the materials present on Earth, none of them is "non-magnetic". These words mean that any material has a magnetic response, called magnetic susceptibility χ, to a magnetic field, either static or time-dependent. The operative definition of such a quantity originates from the constitutive equation of magnetism, where the magnetic induction is written as [247]

$$\mathbf{B} = \mathbf{H} + 4\pi\mathbf{M} \tag{7.56}$$

being $\mathbf{H}$ the magnetic field and $\mathbf{M}$ the magnetization, namely the magnetic moment per unit volume, and $\mathbf{B}$ the magnetic induction. In the linear response theory, the susceptibility can be written as the ratio:

$$\chi = \frac{M}{H}, \tag{7.57}$$

hence the previous equation becomes:

$$\mathbf{B} = \mathbf{H}(1 + 4\pi\chi). \tag{7.58}$$

When the magnetic field is not homogeneous, the sample will probe a force $\mathbf{F} = \mathbf{M} \times \nabla\mathbf{H}$, that is attractive in case of paramagnetic and ferromagnetic samples, while it is repulsive in case of diamagnetic samples. This is the starting point for the so-called "Force Methods"[6], employed to measure the magnetization.

[6]Such as Gouy and Faraday methods.

In an anisotropic system, the previous definition has to be extended appropriately:

$$\mathbf{M} = \chi \cdot \mathbf{H} \tag{7.59}$$

where the susceptibility is a tensor of rank two. In magnetism, it is customary to classify materials according to the sign and value of the spin susceptibility. Diamagnetism is fundamental of all chemical compounds, since it is generated[7] by electrons moving in a closed orbit around the nucleus. The spin susceptibility in such a case is negative and typically small, namely $\chi \sim -10^{-6}$ to -10^{-7} erg/G g.
On the other hand, a paramagnetic material, at room temperature, has a susceptibility of the order of 10^{-4} to 10^{-6} emu/g, with a positive value. For the sake of completeness, it is recalled that the Curie law describes the temperature dependence of the susceptibility in a paramagnet:

$$\chi = \frac{Ng^2\mu_B^2 S(S+1)}{3k_B T} \tag{7.60}$$

where g is the Landé factor, μ_B the Bohr magneton, S the spin value and k_B the Boltzmann constant.
When a magnetic interaction acts among neighboring spins, the susceptibility can be modified into the Curie-Weiss law:

$$\chi = \frac{Ng^2\mu_B^2 S(S+1)}{3k_B(T-\theta)}. \tag{7.61}$$

The experimental techniques which allow to measure the spin susceptibility are usually classified in terms of the main physical principle on which they are based, for example there are:

- Force methods: when a magnetic specimen is placed into an inhomogeneous magnetic field, a displacement force is exerted on the sample. Such force is proportional to the sample magnetization;
- Inductive Methods: this technique probes the change in the magnetic flux density that results when a sample is placed into a pick up coil.

This appendix focuses mainly on the second method. When the magnetic moment changes in time, a magnetic flux Φ variation will be detected by the coil $\mathcal{L}$, inductively couple to it via $\Phi = \mathcal{L}i$. Eventually, an e.m.f. will result in the

SQUID-susceptometer

[7]Note that this is not the only source of diamagnetism, but it is common to all materials.

detection coil

$$V = \mathcal{L}\frac{di}{dt} = \frac{\mu N^2 A}{L}\frac{di}{dt} \tag{7.62}$$

being $\mu = 1 + 4\pi\chi$ the magnetic permeability of the medium, N the number of turns of wire, A the cross-sectional area and L the wire length.

Superconducting QUantum Interference Device (SQUID) magnetometer has been invented in the early 60s, after the development of the BCS theory of superconductivity, the GL theory and most important, the discovery of the flux quantization in a superconducting ring. A SQUID is formed by one superconducting ring which has a weak link. Via the inductance coupling to a pick up coil, this device is able to amplify very small changes in magnetic flux, (even in presence of large static fields) into a large electrical signal. The experimental setup requires the sample to be inserted into a second order gradiometer, which is inductively coupled to the SQUID ring. The signal is given by either a permanent magnetic moment or a field induced magnetization.

A **gradiometer** is obtained by replacing the single loop by two or more loops (four in the used system) arranged so that no net flux is coupled with the application of a uniform magnetic field, namely the gradiometer is able to collect the flux variations deriving only from the sample magnetic moment. A second order gradiometer is used to cancel out both the uniform field and the first order derivative, leaving the flux proportional to the second order derivative of the flux generated by the sample magnetic moment.

The sample is placed in the middle of a plastic straw, which is moved into the gradiometer (see Fig. 7.20), by means of a stepper-motor. As the sample moves through the detection coil, the magnetic moment induces a current. Since the detection coil, the wires and the SQUID form a superconducting closed loop, any flux change will be detected by the loop and converted (by the SQUID) in a voltage signal. The gradiometer is designed with a superconducting wire that is wound counterclockwise at the extremes and clockwise at the center, in order to subtract the background unbalanced signal. The standard transport configuration can measure a magnetic moment down to 10^{-5} emu, while the Reciprocating Sample Operation (RSO) goes down to 10^{-8} emu. In the MPMS Quantum Design system used in this thesis, the sample space is a 9 mm diameter tube, that is kept in a static helium gas atmosphere. The sample is inserted from above by opening an airlock valve, which puts the sample space into contact with a chamber, that can be purged and pumped with helium gas (coming from the magnet boil-off). The lower part of the sample chamber is lined with copper, to provide thermal uniformity to the sample space. The temperature is then measured with

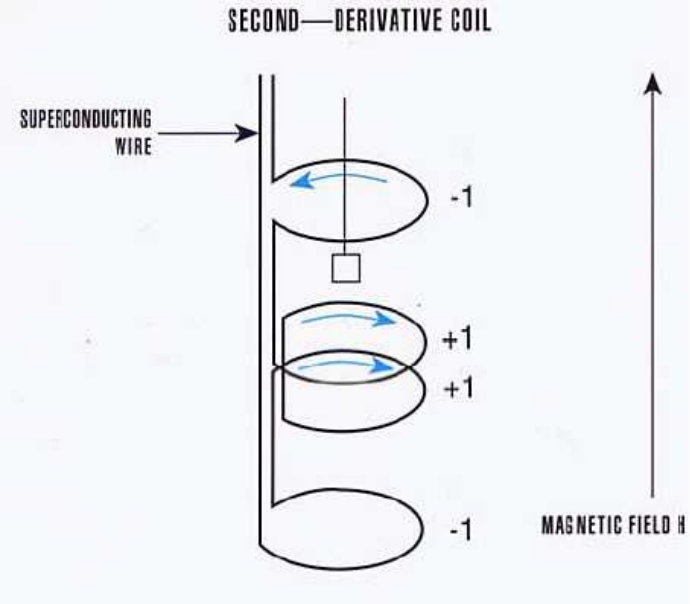

Figure 7.20: Sketch view of the second order gradiometer employed to pick up the signal, in the MPMS SQUID. The gradiometer is put out of the sample chamber and it is immersed into liquid helium. The figure is adapted from Ref. [248].

two sensors.

The field is generated by a superconducting magnet (Max. field 7 T) which is kept in persistent mode (see next Appendix). A sketch view of the superconductor can be seen in Fig. 7.21. The field can be changed in oscillating or no-overshoot mode. In the former case, the wanted field is achieved after an oscillation around the desired values, in order to get rid of pinned flux that can cause a residual field inside the magnet. In the latter case, the magnet ramps up to the desired value, by slowing down at the end of the ramp, to avoid over-shooting. The magnetization measurements are usually carried out in zero-field-cooled (ZFC) or field cooled (FC) mode. ZFC is done by cooling the sample to the lowest measurement temperature in H=0. Later on, a magnetic field is applied, and the magnetic moment is measured as a function of temperature. The FC mode can be done by collecting data while warming the sample, after a cooling process done with H$\neq$ 0, or while cooling in field.

The actual magnetic moment measurement is performed by a fit or integration of the Voltage versus position (Fig. 7.22), by assuming that the magnetic behavior of the sample can be approximated to a point-source magnetic dipole moving through a second order gradiometer. As a consequence of that, when a big sample is measured, sample centering and moment measuring can be rather difficult. One way to perform the measurements is to simply integrate the Volt-

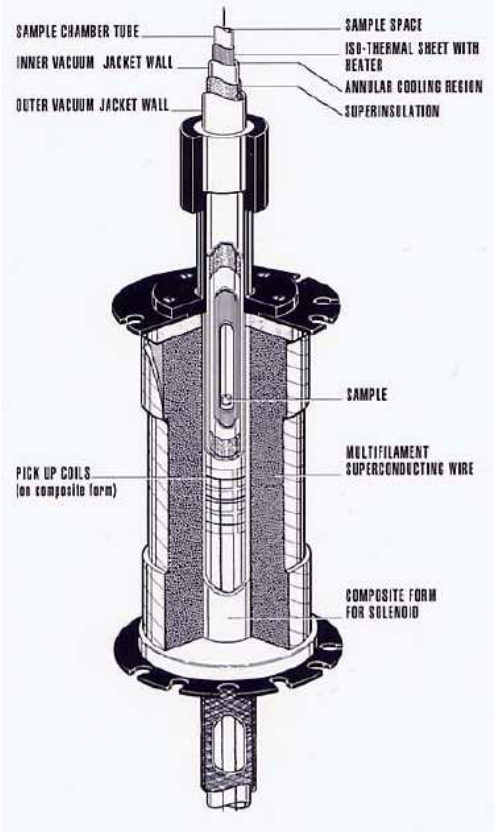

Figure 7.21: Sketch view of a section of the magnet with the sample space. The figure is adapted from Ref. [248].

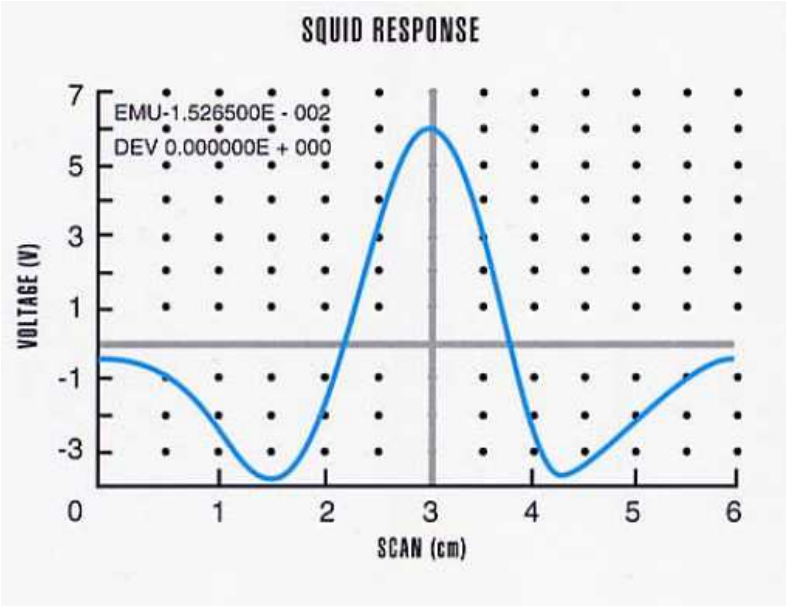

Figure 7.22: Voltage versus the sample position, after a scan of the sample in the gradiometer. The figure is adapted from Ref. [248].

age versus position curve (full scan method). The second way is to fit the data with a theoretical curve (linear regression method) as explained above, provided that the sample has not moved along its centered position. The third way (iterative regression) takes into account possible movements of the sample and sample holder, via inserting other parameters into the fit.

ac-susceptibility

In an ac-susceptometer,[8] an oscillating ac magnetic field is applied to the sample, in addition to the static field:

$$H(t) = H_0 + H_1 \cos(\omega t) \tag{7.63}$$

where ω is the oscillation frequency. The resulting magnetization is written as:

$$M(t) = M_0 + M_1 \cos(\omega t + \phi) \tag{7.64}$$

where the additional phase ϕ describes the retarded response of the magnetization. The previous equation can be reformulated in such a way that the in-phase and out-of-phase components can be evidenced:

$$M(t) = \chi_0 H_0 + \chi' H_1 \cos(\omega t) + \chi'' H_1 \sin(\omega t) \tag{7.65}$$

where the static components is trivially defined as

$$\chi_0 = \frac{M_0}{H_0}, \tag{7.66}$$

while the in-phase response is

$$\chi' = \frac{M_1 \cos\phi}{H_1} \tag{7.67}$$

and the out-of-phase is

$$\chi'' = \frac{M_1 \sin\phi}{H_1}. \tag{7.68}$$

The used setup allowed to measure only the longitudinal moment, since the pickup coils are parallel to the static magnetic field. The measurement is carried out by the same methods described above.
ac-superconductivity is a standard tool for determining the physics of superconductors, in particular for measuring critical temperatures. Indeed, in the fully

[8] The model employed in this thesis is MPMS XL.

superconductive state, $\chi' = -4\pi$, while χ'' describes a dissipative behavior.
The ac field penetration depth is a relevant issue, as the intensity of the NMR signal, as well as the ac-susceptibilty signal, will depend on the amount of rf penetrating into the surface of the sample. Cambpell and Brandt answered this question, giving a very simple equation. If one supposes to have a slab sample with the field applied parallel to the surface, H_1 will take the following profile [211,249]:

Cambpell length

$$H_1 = H_s e^{r/\lambda} \text{ where the penetration depth } \lambda = \sqrt{\lambda_L^2 + \lambda_c^2}, \tag{7.69}$$

being the first the London or GL penetration depth, while the second the Cambpell length:

$$\lambda_c^2 = c_{ii}/\alpha_L, \tag{7.70}$$

where $ii = 11$ (compression modulus) or 44 (tilt modulus), according to the way vortices enter the specimen, namely if the field is applied parallel to the surface or perpendicular to it. Yet when $H_0 > 2H_{c1}$ the two moduli nearly coincides. Moreover α_L is the Labusch parameter that quantifies the FLL rigidity, such that the softer the FLL, the deeper the flux line enters the sample.

Appendix D: NMR equipment

To begin this appendix, the *tank circuit*, namely the RLC circuit that is usually handmade, is presented. That indeed is the place where the rf signal is either transmitted and received, in a pulse NMR experiment. The circuit is made of an inductance where the sample is inserted, so that the coil (usually copper-made) has to optimize the filling factor, by miming the sample dimension as much as possible, but at the same time it is made of a number of turns, such that the associated inductance L must guarantee a big quality factor:

$$Q = \omega L/R \tag{7.71}$$

being R the resistance associated to all the circuital elements. The pick up coil is sometimes immersed in a bi-component epoxy resin, which allows to get mechanic stability and to minimize the annoying spurious ringing effect that can emerge from the coil ring-down.
The maximum power transmittance to the sample is provided by the impedance matching (namely 50 Ω) at the Larmor frequency. The tuning and matching procedure is made by a set of variable capacitors, that can be put either in series or parallel to the coil, and also within the tank circuit (*cold-tuned*) or as a part of the transmission line (*warmed-tuned*). The latter induces rf losses, on the coax, of the sensitivity of the probe, and a smaller quality factor Q. On the other hand, the cold-tuned scheme is likely to turn into capacitor breakdown when helium is used as exchange gas [250]. High quality factors are clearly useful to have a better transmittance of the power, but on the other hand the circuit becomes extremely sensitive to the magnetic sample behavior. For example, a superconducting sample may affect the circuit inductance so much, that the resonance shifts towards

too high frequency, out of the Larmor frequency range.
When a sample of susceptibility χ is inserted in a pick up coil of inductance L_0, the total inductance will change to $L=L_0[1+4\pi q\chi(\omega)]$, where q takes into account the filling factor[9]. The result will be a change in the imaginary (i.e. inductive) as well as real (i.e. resistive) part of L:

$$\begin{aligned} Z &= iL_0\omega[1+4\pi\chi'(\omega)+i4\pi\chi''(\omega)]+R_0 = \\ &= iL_0\omega[1+4\pi\chi'(\omega)]-L_0\omega 4\pi\chi''(\omega)+R_0 \end{aligned} \tag{7.72}$$

hence the variation of the resistive part is equal to

$$\frac{\Delta R}{R_0} = -\frac{L_0\omega}{R_0}4\pi\chi''(\omega) = 4\pi\chi''(\omega)Q,$$

being Q of the order of 50-100, for handmade coils for rf applications).

Since the energy stored in an inductance of volume V is $E=\frac{1}{8\pi}H_1^2V$, also in absence of nuclei, then the average power stored in the inductance and dissipated by the nuclei is given by

$$\begin{aligned} \bar{P} &= \frac{1}{2}I_0^2\Delta R = \frac{1}{2}I_0^2L_0\omega 4\pi\chi''(\omega) = \\ &\quad -\frac{1}{2}\omega H_1^2V\chi''(\omega) \end{aligned} \tag{7.73}$$

where the last equation has a minus sign, because the energy is transferred from the circuit to the nuclei. In Continuous Wave (CW) NMR experiment, the detected signal is directly proportional to the absorbed power, and then to χ''.
As the transmitted power is received, the sample "responds" by inducing a time-varying magnetization, which is responsible for the e.m.f. generated in the same pick up coil. A rf duplexer is then needed in order to decouple the in coming signal (transmission), to the out-going signal (receiver). The duplexer is usually done by a solid state device made of crossed diodes. This device is also called *directional coupler* and it works in such a way that during the high power rf transmission, there is an open circuit after the probe/tank circuit, allowing all rf power to go into the probe and tank circuit. When the pulses are complete,

[9]The filling factor is given by the ratio between the volume occupied by the sample and the coil volume.

during the receiving mode, there is an open circuit before the probe/tank circuit, allowing all of the induced e.m.f. to go only into the pre-amplifier and receiver end of the spectrometer.
The e.m.f. induced signal is then ready to be pre-amplified, received, and analyzed by the spectrometer and the user. The real heart of the NMR experiment is the spectrometer. The author used two kind of spectrometers. The spectrometer hardware used at Northwestern University and NHMFL, MAGRes2000, comes with a user interface program called MAGRes2000 commercially made by Arneil Reyes at the NHMFL. The spectrometer used at Pavia University is a commercial Fourier transform NMR spectrometer, Apollo Tecmag. The common building blocks of an NMR spectrometer are sketched in the following (see Fig. 7.23).

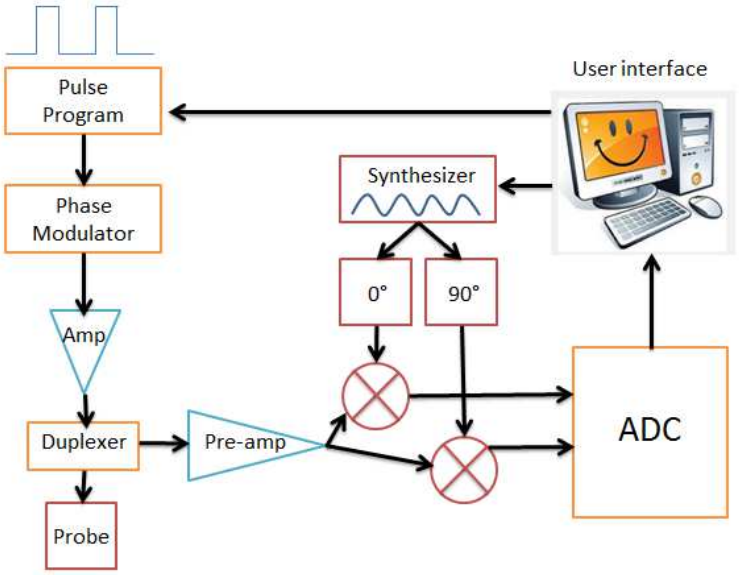

Figure 7.23: Sketch view of an NMR spectrometer.

The core of the NMR spectrometer is the pulse generation, namely the synthesizer generates a reference wave $\cos(\omega_{rf}t)$, the frequency of which can be chosen by the user via a software interface, that is cut into pulses of a particular shape.[10] The modular mixes the signal to four possible carriers with a phase difference of 0°, 90°, 180°, 270°, from the reference. Particular phase cycling sequences are employed as an additional way to get rid of the spurious ringing. The (de-phased) signal is then amplified (up to several kV) and send it to the duplexer which opens the path to the pre-amplifier. The signal generates and oscillating magnetic field, whose amplitude is usually small (1 - 100 Oe). Afterwards the new signal (coming

[10]The rectangular is the most commonly employed.

from the sample) will pass to the duplexer, which now will open the transmission line and will close the pre-amplifier path. Indeed the signal is very small (μV) and it has to be amplified. Later on the signal will be mixed with two reference signals: and in-phase $\cos(\omega_{rf}t + \beta)$ and and out-of-phase $\sin(\omega_{rf}t + \beta)$ signal. From the mixing, the dissipative and dispersive parts will be extracted and then converted by a 2 channel analog to digital converter. The voltage measurement is sampled at a frequency which is the inverse of the time resolution of the experiment (dwell time), and then it is digitalized.

Magnets

Magnets are the very basic "ingredients" needed to perform NMR. In case of electromagnets, magnetic fields up to nearly 2 T can be produced if the core of ferromagnetic material, such as soft iron, is placed inside the coil. Indeed the ferromagnetic core increases the magnetic field to thousands of times the strength of the field of the coil alone, due to the high magnetic permeability μ of the ferromagnetic material. To prevent damages generated by heat, a water-based cooling systems is usually employed. However, for this work, superconducting magnets are more useful. These are typically made of many fine filaments of a niobium-titanium (NbTi) alloy embedded in a copper matrix. Although most magnets are wound with multi filamentary niobium-titanium conductors, some are constructed with multi filamentary, niobium-tin (Nb_3Sn) conductors and some with single filaments of niobium-titanium. Single filament NbTi magnets are preferred where the stability of the magnetic field over a long period of time is essential, as in nuclear magnetic resonance measurements. Persistent switches are provided on many magnets to increase their stability over long periods of time, or to reduce the rate of helium boil-off associated with continually supplying current to the magnet. A persistent switch is comprised of a short section of superconducting wire, connected across the input terminals of a magnet, and an integral heater used to drive the wire into the resistive, normal state. When the heater is turned on and the wire is resistive, a voltage can be established across the terminals of the magnet and the magnet can be energized. Once energized, the heater is turned off, the wire becomes superconducting and further changes in the magnet current cannot be made. In this persistent mode of operation, the external power supply can be turned off to reduce the heat input to the helium bath and the current will continue to circulate through the magnet and the persistent switch. Superconducting magnets can provide a limited (although high) magnetic field, usually not higher than $\sim$ 20 T, due to flux creep. When higher fields are needed, resistive Bitter magnets are usually employed. These magnets require high quan-

tity of coolant (usually water), so they have to be built in large scales facilities. Since 2011 the National High Magnetic Field Laboratory in Tallahassee houses the world's strongest resistive magnet. This system has a maximum field strength of 36.2 T, and consists of hundreds of separate Bitter plates. The system consumes 19.6 megawatts of electric power and requires about 139 liters of water pumped through it per second, for cooling. The strongest continuous magnetic field, 45 T, was produced by a device consisting of a Bitter magnet inside a superconducting magnet, hence it's name: "hybrid". More information can be found on Ref. [251].

When using superconducting magnets as well as superconducting sample, the cryogenics is an important part. For the most of this work, magnets cooled in a liquid helium 4 bath, surrounded by a liquid nitrogen jacket isolated from the outside via a vacuum chamber, have been employed. Moreover, the sample has to be cooled down with liquid helium as well. A dynamic flux cryostat was commonly used, where the liquid helium is transferred from the dewar to the cryostat, via a transfer line, under continuous pumping. Another possibility (static flux cryostat) needs the sample to be inserted into an evacuated sample space, that is put into contact with the helium bath, via helium gas flow. This second method is usually needed when the "tuning" and "matching" capacitors are close to the sample space and not outside, in order to prevent arching between the ceramic capacitors or the coil and the capacitors.

Cryogenics

Appendix E:
The Unit Systems in Magnetism

To conclude the results of this research activity, it is recalled that all the physical quantities in thesis thesis are written in the Gaussian unit system, or the CGS EMU system, both of which are CGS subsystems.[11] In fact there is a kind of discomfort in the solid state physics community about the unit systems used in magnetism, which sometimes turns into a real confusion when trying to compare the theoretical expression with the experimental results. The origin of the misunderstanding comes from the fact that the designation "*emu*" (for the magnetic moment) is not a real unit. In fact in the CGS system, it should rather be said that the unit of the magnetic moment is the erg/G. Because of this reason, this short appendix aims to clarify the dimensions and the employed units.

The merit to create a new unit system, after the well known SI, is ascribed to H. Hertz [252], who combined the electrostatic and electromagnetic CGS units into a single system, which is called the **Gaussian system of units**. The two former systems depended on whether the law of force for electric charge or for electric currents were taken as fundamental, and they where just related by the c constant. Nonetheless, even if the three systems (namely CGS ESU, EMU and Gaussian) are different it can be said that from a numerical point of view the Gaussian units coincides with the EMU (i.e. no conversion factors are involved), as far as the magnetic quantities are concerned, whereas it coincides with the ESU system as far as the electric quantities are concerned. Furthermore it is noted that both the subsystems have assumed that the electric permittivity ϵ_0 and magnetic permeability μ_0 are equal to 1. As an example the **Bohr magneton**, is $\mu_B =$

[11] The exceptions have been declared by the author.

$\frac{e\hbar}{2m_e} = 2.78027710^{-10}\ esu$ in CGS ESU, instead of $\mu_B = \frac{e\hbar}{2m_e c} = 9.27400910^{-21}$ emu in CGS EMU.

At the beginning of the XX century the Gaussian system was so vastly employed that many physicists like A.H. Lorentz, M. Planck, A. Einstein, A. Millikan, N. Bohr, A. Sommerfeld, W. Pauli, L. de Broglie, E. Schrodinger, M. Born, W. Heisenberg, P.A.M. Dirac and others, used it in their theories. The particular benefit of the system came from the discovery that, in the Gaussian units, the magnetic and the electric fields have the same dimensions and units. [253] More recently, in 2006, the **Bureau International des Poids et Measures** (BIPM) mentioned that there is a scientific advantage of "*the use of CGS Gaussian units in electromagnetic theory applied to quantum electrodynamics and relativity*". Despite its undeniable benefits, the author believes that the use of the *emu* units produces too much misunderstanding. For this reason the following table displays the magnetic quantities, used in the present work, with the actual units employed.

Quantity	**Symbol**	**EMU/Gaussian**	**SI**
Magnetic Field	$\mathbf{H}$	Oe	A/m
Magnetic Induction	$\mathbf{B}$	G	T
Flux of Magnetic Induction	Φ	Gcm^2	Wb
Magnetic Moment	μ	erg/G	Am^2
Magnetization	$\mathbf{M}$	erg/Gcm^3	A/m
Volume Susceptibility	χ_{vol}	1	1
Molar Susceptibility	χ_{mol}	erg/G^2mol	$A/(m \cdot mol)$
Hyperfine field	A_{hyp}	Oe	T
Electronic Spin	S	$dimensionless$	$dimensionless$

The volume Spin Susceptibility is dimensionless, in fact the magnetic constitutive equation reads: $\mathbf{B} = \mathbf{H} + 4\pi\mathbf{M} = \mu\mathbf{H}$ with $\mu = 1 + 4\pi\chi$, [153] where $\mathbf{M} = \chi\mathbf{H}$ defines the dimensionless magnetic susceptibility χ. In fact, in the linear response regime one can write

$$\chi = \frac{\mu}{HV}\frac{[erg]}{[G^2cm^3]}$$

this unit is correct, but additionally, by recalling that the integral of the magnetic energy density $\int H^2dr^3[G^2cm^3]$ has the dimension of an energy $[erg]$, by defini-

tion, hence $\chi = [G^2cm^3][G^2cm^3] = 1$. Sometimes the Susceptibility is written in emu/cm^3, where the label "emu" now refers to "susceptibility emu", which in EMU system is equivalent to cm^3. On the other hand, the molar Spin Susceptibility is not dimensionless. The decision to write also the hyperfine field and electronic spin unit aims at getting rid of some confusion that rises in the NMR community, when trying to extract the actual value of hyperfine field A_{hyp} from the Knight Shift and Spin Susceptibility, as it was presented in Chapter 4.

Bibliography

[1] Y. Kamihara, T. Watanabe, M. Hirano, and H. Hosono, J. Am. Chem. Soc. **130**, 3296 (2008).

[2] Y. Hirata, K. M. Kojima, M. Ishikado, S. Uchida, A. Iyo, H. Eisaki and S. Tajima, Phys. Rev. B **85**, 054501 (2012).

[3] H. Takahashi. K. Igawa, K. Arii, Y. Kamihara, M. Hirano, H. Hosono, Nature **453**, 376 (2008).

[4] Z.-A. Ren, W. Lu, J. Yang, W. Yi, X.-L. Shen, Z.-C. Li, G.-C. Che, X.-L. Dong, L.-L. Sun, F. Zhou, and Z.-X. Zhao, Chin. Phys. Lett. **25**, 2215 (2008).

[5] M. Rotter, M. Tegel, D. Johrendt, I. Schellenberg, W.Hermes, and R. Pottgen, Phys. Rev. B **78**, 020503(R) (2008).

[6] P. C. Canfield and S. L. Bud'ko, Annu. Rev. Condens. Matter Phys. **1**, 27-50 (2010).

[7] A. S. Sefat, R. Jin, M. A. McGuire, B. C. Sales, D. J. Singh, D. Mandrus, Phys. Rev. Lett. **101**, 117004 (2008).

[8] X. C. Wang, Q. Liu, Y. Lv, W. Gao, L. X. Yang, R. C. Yu, F. Y. Li, and C. Jin, Solid. State. Comm. **148**, 538 (2008).

[9] S.-H. Baek, H.-J. Grafe, F. Hammerath, M. Fuchs, C. Rudisch, L. Harnagea, S. Aswartham, S. Wurmehl, J. van den Brink and B. Büchner, EuroPhys. Jour. B **85**, 159 (2012).

[10] K.-W. Yeh, T.-W. Huang, Y. lin Huang, T.-K. Chen, F.-C. Hsu, P. M.Wu, Y.-C. Lee, Y.-Y. Chu, C.-L. Chen, J.-Y. Luo, D.-C. Yan, and M.-K. Wu, Europhys. Lett. **84**, 37002 (2008).

[11] K. Kudo, K. Iba, M. Takasuga, Y. Kitahama, J.-i. Matsumura, M. Danura, Y. Nogami, M. Nohara, Scientific Reports **3**, 1478 (2013).

[12] N. Katayama, K. Kudo, S. Onari, T. Mizukami, K. Sugawara, Y. Sugiyama, Y. Kitahama, K. Iba, K. Fujimura, N. Nishimoto, M. Nohara, H. Sawa, J. Phys. Soc. Jpn. **82** 123702 (2013).

[13] K. Ishida, Y. Nakai and H. Hosono, J. Phys. Soc. Jpn. **78**, 062001 (2009).

[14] R. H. Liu, T Wu, G. Wu, H. Chen, X. F. Wang, Y. L. Xie, J. J. Ying, Y. J. Yan, Q. J. Li, B. C. Shi, W. S. Chu, Z. Y. Wu, and X. H. Chen, Nature **459**, 64 (2009).

[15] D. C. Johnston, J. Adv. Phys. **59**, 803-1061 (2010).

[16] S. Thirupathaiah, D. V. Evtushinsky, J. Maletz, V. B. Zabolotnyy, A. A. Kordyuk, T. K. Kim, S. Wurmehl, M. Roslova, I. Morozov, B. Büchner, and S. V. Borisenko, Phys. Rev. B **86**, 214508 (2012).

[17] M. Monni, F. Bernardini, G. Profeta, A. Sanna, S. Sharma, J. K. Dewhurst, C. Bersier, A. Continenza, E. K. U. Gross, and S. Massidda, Phys. Rev. B **81**, 104503 (2010) and quotation therein.

[18] I. I. Mazin, D. J. Singh, M. D. Johannes, and M. H. Du, Phys. Rev. Lett. **101**, 057003 (2008).

[19] A. Gurevich Rep. Prog. Phys. **74**, 124501 (2011).

[20] N. R. Werthamer, E. Helfand, and P. C. Hohenberg, Phys. Rev. **147**, 295 (1966).

[21] N. Ni, M. E. Tillman, J.-Q. Yan, A. Kracher, S. T. Hannahs, S. L. Bu'ko, and P. C. Canfield, Phys. Rev. B **78**, 214515 (2008).

[22] M. Tinkham, *Introduction to Superconductivity*, Second Edition, Dover (1996).

[23] J. D. Weiss, C. Tarantini, J. Jiang, F. Kametani, A. A. Polyanskii, D. C. Larbalestier and E. E. Hellstrom, Nature Mat. **11**, 682 (2012).

[24] I. Pallecchi, M. Tropeano, G. Lamura, M. Pani, M. Palombo, A. Palenzona, M. Putti, Physica C **482**, 68 (2012).

[25] P. C. Canfield, S. L. Bud'ko, N. Ni, J. Q. Yan, and A. Kracher, arXiv:0904.3134 (unpublished).

[26] N. Ni, A. Thaler, A. Kracher, J. Q. Yan, S. L. Bud'ko, and P. C. Canfield, Phys. Rev. B **80**, 024511 (2009).

[27] P. Carretta, R. De Renzi, G. Prando, S. Sanna, http://arxiv.org/abs/1307.8283 (2013).

[28] R.S. Gonnelli, M. Tortello, D. Daghero, P. Pecchio, S. Galasso, V.A. Stepanov, Z. Bukowski, N. D. Zhigadlo, J. Karpinski, K. Iida, and B. Holzapfel, http://arxiv.org/abs/1301.3782v1 (2013).

[29] D. J. Singh, Phys. Rev. B **78**, 094511 (2008).

[30] C. Fang, H. Yao, W.-F. Tsai, J. Hu, and S. A. Kivelson, Phys. Rev. B **77**, 224509 (2008).

[31] C. Liu, T. Kondo, R. M. Fernandes, A. D. Palczewski, E. D. Mun, N. Ni , A. N. Thaler, A. Bostwick, E. Rotenberg, J. Schmalian, S. L. Bud'ko, P. C. Canfield and A. Kaminski, Nature Physics **6**, 419 (2010).

[32] H. Ding, P. Richard, K. Nakayama, K. Sugawara, T. Arakane, Y. Sekiba, A. Takayama, S. Souma, T. Sato, T. Takahashi, Z. Wang, X. Dai, Z. Fang, G. F. Chen, J. L. Luo and N. L. Wang, Europhys. Lett. **83**, 47001 (2008).

[33] Y.-Y. Tai, J.-X. Zhu, M. J. Graf and C. S. Ting, Europhys. Lett. **103**, 67001 (2013).

[34] K. Yosida, Phys. Rev. **110**, 769 (1958).

[35] S. Oh, A. M. Mounce, S. Mukhopadhyay, W. P. Halperin, A. B. Vorontsov, S. L. Bud'ko, P. C. Canfield, Y. Furukawa, A. P. Reyes, and P. L. Kuhns, Phys. Rev. B **83**, 214501 (2011).

[36] Y. Nakai, K. Ishida, Y. Kamihara, M. Hirano, and H. Hosono, J. Phys. Soc. Jpn. **77**, 073701 (2008).

[37] D. Parker, O. V. Dolgov, M. M. Korshunov, A. A. Golubov, and I. I. Mazin, Phys. Rev. B **78**, 134524 (2008).

[38] O. V. Dolgov, A. A. Golubov, and D Parker, New Journal of Physics **11**, 075012 (2009).

[39] Y. Nakai, S. Kitagawa, K. Ishida, Y. Kamihara, M. Hirano and H. Hosono, Phys. Rev. B **79**, 212506 (2009).

[40] T. Oka, Z. Li, S. Kawasaki, G. F. Chen, N. L. Wang, and G.-g. Zheng, Phys. Rev. Lett. **108**, 047001 (2012).

[41] Y. Nakai, S. Kitagawa, T. Iye, K. Ishida, Phys. Rev. B **85**, 134408 (2012).

[42] F. L. Ning, K. Ahilan, T. Imai, A. S. Sefat, M. A. McGuire, B. C. Sales, D. Mandrus, P. Cheng, B. Shen, and H.-H. Wen, Phys. Rev. Lett. **104**, 037001 (2010).

[43] K. Kitagawa, N. Katayama, K. Ohgushi, M. Yoshida and M. Takigawa, J. Phys. Soc. Jpn **77**, 114709 (2008).

[44] Q. Si and E. Abrahams, Phys. Rev. Lett. **101**, 076401 (2008).

[45] I. I. Mazin, M. D. Johannes, L. Boeri, K. Koepernik, D. J. Singh, Phys. Rev. B **78**, 085104 (2008).

[46] Y. Nakai, T. Iye, S. Kitagawa, K. Ishida, S. Kasahara, T. Shibauchi, Y. Matsuda, H. Ikeda, and T. Terashima, Phys. Rev. B **87**, 174507 (2013).

[47] F. Hammerath, U. Gräfe, H. Kühne, P. L. Kuhns, A. P. Reyes, G. Lang, S. Wurmehl, B. Büchner, P. Carretta, and H.-J. Grafe, Phys. Rev. B **88**, 104503 (2013).

[48] C. Lester, Jiun-Haw Chu, J. G. Analytis, T. G. Perring, I. R. Fisher, and S. M. Hayden, Phys. Rev. B. **81**, 064505 (2010).

[49] P. Chandra, P. Coleman, and A. I. Larkin, Phys. Rev. Lett. **64**, 88 (1990).

[50] C. L. Henley, Phys. Rev. Lett. **62**, 2056 (1989).

[51] J. Chaloupka and G. Khaliullin, Phys. Rev. Lett. **110**, 207205 (2013).

[52] S. Mukhopadhyay, S. Oh, A. M.Mounce, M. Lee, W. P. Halperin, N. Ni, S. L. Bud'ko, P.C. Canfield, A. P. Reyes and P. L. Kuhns, New Jour. of Phys. **11**, 055002 (2009).

[53] Y. He and C. M. Varma, Phys. Rev. B **85**, 155102 (2012).

[54] A.M. Mounce, Sangwon Oh, Jeongseop A. Lee, W.P. Halperin, A. P. Reyes, P. L. Kuhns, M. K. Chan, C. Dorow, L. Ji, D. Xia, X. Zhao, and M. Greven, Phys. Rev. Lett. **111**, 187003 (2013).

[55] A. Kreisel, Y. Wang, T. A. Maier, P. J. Hirschfeld, and D. J. Scalapino, Phys. Rev. B **88**, 094522 (2013).

[56] A. A. Abrikosov Soviet Phys. JETP **5**, 1174 (1957).

[57] N. V. Zavaritskii, Dokl. Akademii Nauk SSSR **78**, 665 (1951).

[58] G. Blatter, M. Y. Feigel'man, Y. B. Geshkenbein, A. I. Larkin, V. M. Vinokur, Rev. Mod. Phys. **66**, 1125 (1994).

[59] J. R. Clem, J. Low. Temp. Phys. **18**, 427 (1975).

[60] Z. Hao and J. R. Clem, Phys. Rev. B **43**, 7622 (1991).

[61] V. F. Mitrovic, E. E. Sigmund, M. Eschrig, H. N.Bachman, W. H. Halperin, A. P. Reyes, P. Kuhns and W. G. Moulon, Nature **413**, 501-504 (2001).

[62] A. Abragam, *Principles of Nuclear Magnetism* (Oxford University Press), New York (1961).

[63] C. P. Slichter, *Principles of Magnetic Resonance*, Third Enlarged and Updated Edition, Springer Series In Solid-State Sciences 1, Heidelberg (1996).

[64] T. L. James, *Biophysics Textbook Online* (1998).

[65] A. Smerald and N. Shannon, Phys. Rev. B **84**, 184437 (2011).

[66] S. Blundell, *Magnetism in Condensed Matter*, Oxford Master Series in Condensed matter physics, New York (2012).

[67] C. Kittel, *Introduction to Solid State Physics*, Eight Edition, John Wiley and Sons, Inc. (2005).

[68] P. Carretta and A. Lascialfari, *NMR-MRI, μSR and Mössbauer Spectroscopies in Molecular Magnets*, Springer-Verlag Italia, Milano (2007).

[69] M. Takigawa and G. Saito, J. Phys. Soc. Jpn. **55**, 1233 (1986).

[70] H. Alloul, J. Bobroff, M. Gabay and P. J. Hirschfeld, Rev. Mod. Phys. **81**, 45 (2009).

[71] E. L. Hahn, Phys. Rev **50**, 580 (1950).

[72] E. Fukushima and S. B. W. Roeder, *Experimental Pulse NMR, A Nuts and Bolts Approach*. Reading, MA: Addison-Wesley, (1981).

[73] N. Bloembergen, E. M. Purcell, and R. V. Pound, Phys. Rev. **73**, 679 (1948).

[74] G. Grosso and G. Pastori Parravicini, *Solid State Physics*, Academic Press, San Diego (2003).

[75] J. Bardeen, L. N. Cooper, and J. R. Schrieffer, Phys. Rev. **108**, 1175, (1957).

[76] A. M. Clogston, A. C. Gossard, V. Jaccarino, and Y. Yafet, Rev. Mod. Phys. **36**, 170 (1964).

[77] D. E. MacLaughlin, *Magnetic resonance in the superconducting state, in Solid State Physics* (H. Ehrenreich, F. Seitz, and D. Turnbull, eds.), vol. 31, New York: Academic Press (1976).

[78] L. C. Hebel and C. P. Slichter, Phys. Rev. **113**, 1504 (1959).

[79] P. Phillis, *Advances Solid State Physics*, Cambridge University Press (2012).

[80] Y. Masuda and A. G. Redfield, Phys. Rev. **125**, 159, (1962).

[81] R. P. Huebener, N. Schopohl and G. E. Volovik, *Vortices in Unconventional Superconductors and Superfluids*, Springer Series in Solid State Sciencs, Heidelberg (2002).

[82] V. F. Mitrovic, E. E. Sigmund, M. Eschrig, H. N. Bachman, W. P. Halperin, A. P. Reyes, P. Kuhns, and W. G. Moulton, Nature **413**, 501-504 (2001).

[83] S. Oh, A. M. Mounce, W. P. Halperin, C. L. Zhang, P. Dai, A. P. Reyes, and P. L. Kuhns, Phys. Rev. B **85**, 174508 (2012).

[84] A. M. Mounce, S. Oh, W. P. Halperin, Frontiers of Physics **6**, 450 (2011).

[85] A. M. Mounce, S. Oh, S. Mukhopadhyay, W. P. Halperin, A. P. Reyes, P. L. Kuhns, K. Fujita, M. Ishikado and S. Uchida, Nature Phys. **7**, 125 (2011).

[86] A. Lascialfari, A. Rigamonti, L. Romanó, P. Tedesco and D. Embriaco, Phys. Rev. B **65**, 144523 (2002).

[87] C. P. Poole Jr., H. A. Farach, R. J. Creswick and R. Prozorov, *Superconductivity*, Elsevier, Second Edition (2009).

[88] A. Schmid, Phys. Rev. **180**, 527 (1969).

[89] R. E. Prange, Phys. Rev. B **1**, 2349 (1969).

[90] A. I. Larkin and A. A. Varlamov, *Theory of Fluctuations in Superconductors*, Clarendon Press, Oxford (2005).

[91] J. P. Gollub, M. R. Beasley, R. Callarotti and M. Tinkham, Phys. Rev. B **7**, 3039 (1973).

[92] E. Bernardi, A. Lascialfari, A. Rigamonti, L. Romanó, V. Iannotti, G. Ausanio and C. Luponio, Phys. Rev. B **74**, 134509 (2006).

[93] S. Kamal, D. A. Bonn, Nigel Goldenfeld, P. J. Hirschfeld, Ruixing Liang, and W. N. Hardy, Phys. Rev. Lett. **73**, 1845 (1994).

[94] U. Welp, S. Fleshier, W. K. Kwok, R. A. Klemm, V. M. Vinokur, J. Downey, B. Veal, and G. W. Crabtree, Phys. Rev. Lett. **67**, 3180 (1991).

[95] C. Baraduc, A. Budzin, J. Y. Henry, J. P. Brison, and L. Puech, Physica C **248**, 138 (1995).

[96] L. G. Aslamazov, A. I. Larkin, Soviet Solid State **10**, 875 (1968); Phys. Letters **26A**, 238 (1968).

[97] K. Maki, Progr. Theor. Phys. (Kyoto) **39**, 897 (1968); **40**, 193 (1968).

[98] A. Sewer and H. Beck, Phys. Rev. B **64**, 014510 (2001).

[99] P. Carretta, A. Lascialfari, A. Rigamonti, A. Rosso, and A. Varlamov, Phys. Rev. B **61**, 12420 (2000).

[100] L. Romanó, A. Lascialfari, A. Rigamonti and I. Zucca, Phys. Rev. Lett. **94**, 247001 (2005).

[101] Z. A. Xu, N. P. Ong, Y. Wang, T. Kakeshita, and S. Uchida, Nature (London) **406**, 486 (2000).

[102] L. Li, Y. Wang, S. Komiya, S. Ono, Y. Ando, G. D. Gu, and N. P . Ong, Phys. Rev. B **81**, 054510(R) (2010).

[103] Y. Wang, L. Li and N. P. Ong., Phys. Rev. B **73**, 024510 (2006).

[104] Olivier Cyr-Choinié r, R. Daou, Francis Laliberté, David LeBoeuf, Nicolas Doiron-Leyraud, J. Chang, J.-Q. Yan, J.-G. Cheng, J.-S. Zhou, J. B. Goodenough, S. Pyon, T. Takayama, H. Takagi, Y. Tanaka and Louis Taillefer1, Nature Lett. **458**, 743 (2009).

[105] I. Iguchi, T. Yamaguchi, and A. Sugimoto, Nature (London) **412**, 420 (2001).

[106] E. Bernardi, A. Lascialfari, A. Rigamonti, L. Romanó, M. Scavini and C. Oliva, Phys. Rev. B **81**, 064502 (2010).

[107] A. Lascialfari, A. Rigamonti, E. Bernardi, M. Corti, A. Gauzzi and J. C. Villegier, Phys. Rev. B **80**, 104505 (2009).

[108] M. Randeira and A. A. Varlamov, Phys. Rev. B **50**, 10401(R) (1994).

[109] A. Rigamonti, A. Lascialfari, L. Romanó A. Varlamov, and I. Zucca, Journal of Superconductivity **896**, 1107 (2005).

[110] L. Li, Yayu Wang, N. P. Ong, Phys. Rev. B **87**, 056502 (2013).

[111] D. S. Fisher, M. P. A. Fisher and D. A. Huse, Phys. Rev. B **43**, 130 (1991).

[112] A. Dubroka, M. Rössle, K.W. Kim, V. K. Malik, D. Munzar, D. N. Basov, A. A. Schafgans, S. J. Moon, C. T. Lin, D. Haug, V. Hinkov, B. Keimer, Th. Wolf, J. G. Storey, J. L. Tallon, and C. Bernhard, Phys. Rev. Lett. **106**, 047006 (2011).

[113] K. Sarkar, S. Banerjee, S. Mukerjee, T. V. Ramakrishnan, arxiv.org/abs/1309.3776v1 (2013).

[114] S. Banerjee, T. V. Ramakrishnan, and C. Dasgupta, Phys. Rev. B **83**, 024510 (2011).

[115] A. Lascialfari, A. Rigamonti, L. Romanó, A. A. Varlamov and I. Zucca, Phys. Rev. B **68**, 100505(R) (2003).

[116] S. Hikami and T. Tsuneto, PTP **63**, 387 (1980).

[117] P. A. Lee, N. Nagaosa, X-G. Wen, Rev. Mod. Phys. **78**, 17 (2006).

[118] L. Romanó, Int. J. Mod. Phys. B **17**, 423 (2003).

[119] L. Cabo, F. Soto, M. Ruibal, J. Mosqueira, and F. Vidal, Phys. Rev. B **73**, 184520 (2006).

[120] The pre-exponential factor n_0 is equal to 2.5×10^{19}, for x = 7%, and 1.5×10^{20} for x = 9.4 %. For the previous calculation it has been used $n = 19$ correlated layers and the interlayer distance has been set $s = 6 \times 10^{-8}$ cm.

[121] A. Junod, J.-Y. Genoud, G. Triscone and T. Schneider, Physica C **294**, 115 (1998).

[122] M. A. Hubbard, M. B. Salamon and B. W. Veal, Physica C **259**, 309 (1996). T. Schneider and H. Keller, Physica C **207**, 366 (1993).

[123] J. Mosqueira, J. D. Dancausa, F. Vidal, S. Salem-Sugui Jr., A. D. Alvarenga, H.-Q. Luo, Z.-S. Wang, and H.-H. Wen, Phys. Rev. B **83**, 094519 (2011).

[124] P. Kumar, A. Bera, D. V. S. Muthu, P. M. Shirage, A. Iyo, A. K. Sood, Appl. Phys. Lett. **100**, 222602 (2012).

[125] G. Prando, A. Lascialfari, A. Rigamonti, L. Romanó, S. Sanna, M. Putti, and M. Tropeano, Phys. Rev. B **84**, 064507 (2011).

[126] E. Bernardi, PhD thesis, University of Pavia (2005).

[127] K. Kitagawa, Y. Nakai, T. Iye, K. Ishida, Y. Kamihara, M. Hirano and H. Hosono, Phys. Rev. B **81**, 212502 (2010).

[128] M. Fu, D. A. Torchetti, T. Imai, F. L. Ning, J.-Q. Yan, and A. S. Sefat, Phys. Rev. Lett. **109**, 247001 (2012).

[129] D. A. Torchetti, M. Fu, D. C. Christensen, K. J. Nelson, T. Imai, H. C. Lei, and C. Petrovic, Phys. Rev. B **83**, 104508 (2011).

[130] L. Bossoni, P. Carretta, A. Thaler and P. C. Canfield, Phys. Rev. B **85**, 104525 (2012).

[131] H. Xiao, T. Hu, A. P. Dioguardi, N. Roberts-Warren, A. C. Shockley, J. Crocker, D. M. Nisson, Z. Viskadourakis, Xianyang Tee, I. Radulov, C. C. Almasan, N. J. Curro, and C. Panagopoulos, Phys. Rev B. **85**, 024530 (2012).

[132] A. Reyes, X. P. Tang, H. N. Bachman, and W. P. Halperin, J. A. Martindale and P. C. Hammel, Phys. Rev. B (R) **55**, 737 (1997).

[133] B. J. Suh. PhD thesis, Iowa State University (1995).

[134] M. Takigawa, Phys. Rev. B **49**, 4158 (1994).

[135] R. E. Walstedt and S.-W. Cheong, Phys. Rev. B **51**, 3163 (1995).

[136] C. H. Pennington and C. P. Slichter, Phys. Rev. Lett. **66**, 381 (1991).

[137] A. J. Millis, H. Monien and D. Pines, Phys. Rev. B **42**, 167 (1990).

[138] C. H. Recchia, J. A. Martindale, C. H. Pennington, W. L. Hults and J. L. Smith, Phys. Rev. Lett. **78**, 3543 (1997).

[139] A. V. Bondar et al., JETP Lett. **50**, 146 (1989). K. Kumagai et al., J. Phys. Soc. Jpn. **59**, 2336 (1990). Y. Itoh et al., *ibid.* **59**, 3463 (1990).

[140] S. Krämer and M. Mehring, Phys. Rev. Lett. **83**, 396 (1999).

[141] A. Rigamonti, F. Borsa, P.Carretta, Rep. Prog. Phys. **61**, 1367-1439 (1998).

[142] L. Bossoni, P. Carretta, R. Nath, M. Moscardini, M. Baenitz, and C. Geibel, Phys. Rev. B **83**, 014412 (2011).

[143] P. Carretta, R. Melzi, N. Papinutto and P. Millet, Phys. Rev. Lett. **88**, 047601 (2002).

[144] T. Wu, H. Mayaffre, S. Krämer, M. Horvatić, C. Berthier, W. N. Hardy, R. Liang, D. A. Bonn and M.-H. Julien, Nature **477**, 191 (2011). J. M. Tranquada, B. J. Sternlieb, J. D. Axe, Y. Nakamura, and S. Uchida, Nature **375**, 561 (1995).

[145] N. J. Curro, C. Milling, J. Haase, and C. P. Slichter, Phys. Rev. B **62**, 3473 (2000).

[146] L. Bossoni, P. Carretta, W. P. Halperin, S. Oh, A. Reyes, P. Kuhns, and P. C. Canfield, Phys. Rev. B **88**, 100503 (R) (2013).

[147] H.-J. Grafe, private communication.

[148] J. E. Hamann-Borrero, M. Philipp, O. Kataeva, M. v. Zimmermann, J. Geck, R. Klingeler, A. Vasiliev, L. Bezmaternykh, B. Büchner, and C. Hess, Phys. Rev. B **82**, 094411 (2010).

[149] L. Bossoni, P. Carretta, M. Horvatić, M. Corti, A. Thaler and P. C. Canfield, Europhys. Lett. **102**, 17005 (2013).

[150] A. P. Dioguardi, J. Crocker, A. C. Shockley, C. H. Lin, K. R. Shirer, D. M. Nisson, M. Lawson, N. apRoberts-Warren, P. C. Canfield, S. L. Bud'ko, S. Ran, and N. J. Curro, Phys. Rev. Lett. **111**, 207201 (2013).

[151] S. Oh, A. M. Mounce, J. A. Lee, W. P. Halperin, C. L Zhang, S. Carr and P. Dai, Phys. Rev. B **87**, 174517 (2013) and S. Oh. Private communication.

[152] T. Wu, H. Mayaffre, S. Kraemer, M. Horvatić, C. Berthier, C.T. Lin, D. Haug, T. Loew, V. Hinkov, B. Keimer, M.-H. Julien, Nature Communications **4**, 2113 (2013).

[153] A. Rigamonti and P. Carretta, *Structure of Matter: An Introductory Course with Problems and Solutions*, 2nd edition, Springer-Verlag Italia, Milano (2009).

[154] A. Laüchli, F. Mila, and K. Penc, Phys. Rev. Lett. **97**, 087205 (2006).

[155] H. Fukazawa, K. Hirayama, K. Kondo, T. Yamazaki, Y. Kohori, N. Takeshita, K. Miyazawa, H. Kito, H. Eisaki, A. Iyo, J. Phys. Soc. Jpn. **77**, 105004 (2008).

[156] D. A. Huse, M. P. A. Fisher and D. S. Fisher, Nature **358**, 553 (1992).

[157] M. P. A. Fisher, Phys. Rev. Lett. **62**, 1415 (1989).

[158] M. C. Marchetti and D. R. Nelson, Phys. Rev. B **59**, 13642 (1999).

[159] E. Zeldov, *100 Years of Superconductivity*, H. Rogalla and P. H. Kes Editors, CRC Press, Boca Raton, FL (2012).

[160] Y. Yeshurun, A. P. and Malozemoff, Phys. Rev. Lett. **60**, 2202 (1988).

[161] E. H. Brandt, Rep. Prog. Phys **58**, 1465 (1995).

[162] L. I. Glazman and A. E. Koshelev, Phys. Rev. B **43**, 2835 (1991).

[163] P. L. Gammel, L. F. Schneemeyer, J. V. Waszczak, and D. J. Bishop, Phys. Rev. Lett. **61**, 1666 (1988).

[164] S. R. Ghorbani, X. L. Wang, M. Shabazi, S. X. Dou, K. Y. Choi, and C. T. Lin, Appl. Phys. Lett. **100**, 072603 (2012).

[165] K. Pervakov, private communication.

[166] P. Carretta, Phys. Rev. B(R) **45**, 5760 (1992).

[167] P. Carretta, Phys. Rev. B **48**, 528 (1993).

[168] P. W. Anderson and Y. B. Kim, Rev. Mod. Phys. **36**, 39 (1964).

[169] A. Lascialfari, A. Rigamonti, E. Bernardi, M. Corti, A. Gauzzi and J. C. Villigier, Phys. Rev. B **80**, 104505 (2009).

[170] M. Corti, J. Suh, F. Tabak, A. Rigamonti, F. Borsa, M. Xu, B. Dabrowski, Phys. Rev. B **54**, 9469 (1996).

[171] B. J. Suh, F. Borsa, J. Sok, D. R. Torgeson, M. Corti, A. Rigamonti, and Q. Xiong, Phys. Rev. Lett. **76**, 1928 (1996).

[172] Y. Laplace J. Bobroff, F. Rullier-Albenque, D. Colson, and A. Forget, Phys. Rev. B **80**, 140501(R) (2009).

[173] S.-H. Baek, H. Lee, S. E. Brown, N. J. Curro, E. D. Bauer, F. Ronning, T. Park, and J. D. Thompson, Phys. Rev. Lett. **102**, 227601 (2009).

[174] W. W. Simmons, W. J. O'Sullivan and W. A. Robinson, Phys. Rev. **127**, 1168 (1962).

[175] F. Ning, K. Ahailan, T. Imai, A. S. Sefat, R. Jin, M. A. McGuire, B. C. Sales, and D. Mandrus, Jour. Phys. Soc. of Jpn. **77**, 103705 (2008).

[176] P. Szabo, Z. Pribulova, G. Pristas, S. L. Bud'ko, P. C. Canfield, and P. Samuely, Phys. Rev. B **79**, 012503 (2009).

[177] G. Mu, H. Luo, Z. Wang, L. Shan, C. Ren, and H. H. Wen, Phys. Rev. B **79**, 174501 (2009).

[178] K. Terashima, Y. Sekiba, J. H. Bowen, K. Nakayama, T. Kawahara, T. Sato, P. Richard, Y.-M. Xu, L. J. Li, G. H. Cao, Z.-A. Xu, H. Ding, and T. Takahashi, Proc. Natl. Acad. Sci. USA **106**, 7330 (2009).

[179] K. Nakayama, T. Sato, P. Richard, Y.-M. Xu, Y. Sekiba1, S. Souma, G. F. Chen, J. L. Luo, N. L. Wang, H. Ding and T. Takahashi, EuroPhys. Lett. **85** 67002 (2009).

[180] E. H. Brandt, Physica B **169**, 91-98 (1991).

[181] M. Cyrot and D. Pavuna, *Introduction to Superconductivity and High-Tc materials*, World Scientific Publishing, Singapore (1995).

[182] J. R. Clem, Phys. Rev. B **43**, 7837 (1991).

[183] H. E. Brandt, Physica C **195**, 1 (1992).

[184] M. A. Tanatar, N. Ni, C. Martin, R. T. Gordon, H. Kim,V. G. Kogan, G. D. Samolyuk, S. L. Bud'ko, P. C. Canfield, and R. Prozorov, Phys. Rev. B **79**, 94507 (2009).

[185] H. Alloul, J. Bobroff, and M. Gabay and P. J. Hirschfeld, Rev. Mod. Phys. **81**, 45 (2009).

[186] E. H. Brandt, Phys. Rev. B(R) **37**, 2349 (1988).

[187] T. J. Williams, A. A. Aczel, E. Baggio-Saitovitch, S. L. Bud'ko, P. C. Canfield, J. P. Carlo, T. Goko, H. Kageyama, A. Kitada, J. Munevar, N. Ni, S. R. Saha, K. Kirschenbaum, J. Paglione, D. R. Sanchez-Candela, Y. J. Uemura and G. M. Luke, Phys. Rev. B **82**, 094512 (2010).

[188] R. T. Gordon, N. Ni, C . Martin, M. A. Tanatar, M.D. Vannette, H. Kim, G. D. Samolyuk, J. Schmalian, S. Nandi, A. Kreyssig, A. I. Goldman, J. Q. Yan, S. L. Budko, P. C. Canfield, and R. Prozorov, Phys. Rev. Lett. **102**, 127004 (2009).

[189] C. P. Bean, Phys. Rev. Lett. **8**, 250 (1962).

[190] E. R. Mognaschi and A. Rigamonti, Phys. Rev. B **14**, 2005 (1976).

[191] M. G. Adesso, M. Polichetti and S. Pace, Physica C **401**, 196 (2004).

[192] M. Polichetti, M. G. Adesso, D. Zola, J. Luo, G. F. Chen, Z. Li, N. L. Wang, C. Noce and S. Pace, Phys. Rev. B **78**, 224523 (2008).

[193] A. P. Malozemoff, T. K. Worthingtin, Y. Yeshurun, F. Holtzberg and P- H. Kes, Phys. Rev. B(R) **38**, 7203 (1988).

[194] T. M. Palstra, B. Batlogg, R. B. van Dover, L. F. Schneemeyer and J. V. Waszczak, Phys. Rev. B **41**, 6621 (1990).

[195] F. Rao, A. Cristanti and F. Rotort, Europhys. Lett. **62**, 869 (2003).

[196] G. Prando, M. Abdel-Hafiez, S. Aswartham, A.U.B. Wolter, S. Wurmehl and B. Büchner, Journ. Phys.: Cond. Matt. **25**, 505701 (2013).

[197] F. Varnik and K. Binder, Journ. of Chem. Physics **117**, 6336 (2002).

[198] P. G. Debenedetti and F. H. Stillinger, Nature **410**, 259 (2001).

[199] C. A. Angell, Insulating and semiconducting glasses, Series on Directions in Condensed Matter Physics, P. Boolchand, 17, World Scientific Publishing, Singapore (2000).

[200] J. R. L. de Almeida and D. J. Thouless, J. Phys. A **11**, 983 (1978).

[201] K. A. Müller, M. Takashige and J. G. Bednorz, Phys. Rev. Lett. **58**, 1143 (1987).

[202] For the estimate of T_{KT}, the used numerical values are the plane thickness $d = 2.1$ Å, and the bulk penetration depth $\lambda_{ab} = 240$ nm. Notice that T_{KT} takes into account the T-dependence of λ_{ab}, according to the two-fluid model.

[203] D. S. Inosov, J. T. Park, P. Bourges, D. L. Sun, Y. Sidis, A. Schneidewind, K. Hradil, D. Haug, C. T. Lin, B. Keimer and V. Hinkov, Nature **6**, 178 (2010).

[204] P. Carretta, Phys. Rev. B **48**, 528 (1993).

[205] J−M Delrieu, J. Phys. F. **893** (1993).

[206] Y. B. Kim, C. F. Hempstead, and A. R. Strnad, Phys. Rev. Lett. **12**, 145 (1964).

[207] J. Bardeen and M. J. Stephen, Phys. Rev. **140**, 1197 (1965).

[208] C. H. Recchia, C. H. Pennington, H. Hauglin, and G. P. Lafyatis, Phys. Rev. B **52**, 9746 (1995).

[209] C. H. Recchia, K. Gorny, and C. H. Pennington, Phys. Rev. B **54**, 4207 (1996).

[210] J. Jang, D. G. Ferguson, V. Vakaryuk, R. Budakian, S. B. Chung, P. M. Goldbart and Y. Maeno, Science **331**, 186 (2011).

[211] E H Brandt, Rep. Prog. Phys. **58** 1465 (1995).

[212] J. Pankert, Physica C **168**, 335 (1990).

[213] H. F. Hess, R. B. Robinson, and J. V. Waszczak, Phys. Rev. Lett. **64**, 22 (1990).

[214] U. Essmann and H. Trauble, Physics Letters, **24A**, 526 (1967).

[215] L. Ya. Vinnikov et al., Phys. Rev. B **67**, 092512 (2003).

[216] A. Moser et al., Phys. Rev. Lett. **74**, 10, (1995).

[217] S. L. Lee, P. Zimmermann, H. Keller, M. Warden, I. M. Savic, R. Schauwecker, D. Zech, R. Cubitt, E. M. Forgan, P. H. Kes, T. W. Li, A. A. Menovsky, and Z. Tarnawski, Phys. Rev. Lett. **71**, 3862 (1993). T. Blasius, Ch. Niedermayer, J. Tallon, D. Pooke, A. Golnik, and C. Bernhard, Phys. Rev. Lett. **82**, 4926 (1999). J. E. Sonier, J. Brewer, and R. Kiefl, Rev. Mod. Phys. **72**, 769 (2000).

[218] B. Keimer, I. Aksay, F. Dogan, R. W. Erwin, J. W. Lynn, and M. Sarikaya, Science **262**, 83 (1993).

[219] J. W. Lynn, N. Rosov, T. Grigereit, H. Zhang, and T. W. Clinton, Phys. Rev. Lett. **72**, 3413 (1994).

[220] E. Fukushima and S. B. W. Roeder, Journ. of Magn. Res. **33**, 199 (1979).

[221] J. Pankert, G. Marbach, A. Comberg, P. Lemmens, P. Fröning and S. Ewert, Phys. Rev. Lett. **65**, 3052 (1990).

[222] M. Poggio and C. L. Degen Nanotechnology **21**, 342001 (2010).

[223] K Wago, O. Züger, R. Kendrick, C. S. Yannoni and D. Rugar, J. Vac. Sci. Technol. B **14**, 1197 (1996).

[224] H. J. Mamin, R. Budakian, B. W. Chui and D. Rugar, Phys. Rev. Lett. **91**, 207604 (2003).

[225] M. Poggio, C. L. Degen, C. T. Rettner, H. J. Mamin and D. Rugar, Appl. Phys. Lett. **90**, 263111 (2007).

[226] A. Vinante, G. Wijts, O. Usenko, L. Schinkelshoek, T.H. Oosterkamp,Nature Communications **2**, 572 (2011). G.J. Verbiest, T. H. Oosterkamp, M.J.Rost, Ultramicroscopy **135**, 113 (2013). T.H. Oosterkamp, M. Poggio, C.L. Degen, H.J. Mamin, D. Rugar Appl. Phys. Lett. **96**, 083107 (2010).

[227] D. P. Weber, D. Rüffer, A. Buchter, F. Xue, E. Russo-Averchi, R. Huber, P. Berberich, J. Arbiol, A. Fontcuberta i Morral, D. Grundler, and M. Poggio Nano Lett. **12**, 6139 (2012).

[228] A. Buchter, J. Nagel, D. Rüffer, F. Xue, D. P. Weber, O. F. Kieler, T. Weimann, J. Kohlmann, A. B. Zorin, E. Russo-Averchi, R. Huber, P. Berberich, A. Fontcuberta i Morral, M. Kemmler, R. Kleiner, D. Koelle, D. Grundler, and M. Poggio, Phys. Rev. Lett. **111**, 067202 (2013).

[229] P. Peddibhotla, F. Xue, H. I. T. Hauge, S. Assali, E. P. A. M. Bakkers, M. Poggio, Nature Phys. **9**, 631 (2013).

[230] A. V. Kuhlmann, J. Houel, A. Ludwig, L. Greuter, D. Reuter, A. D. Wieck, M. Poggio, and R. J. Warburton, Nature Phys. **9**, 570 (2013).

[231] S. Rast, U. Gysin, P. Ruff, Ch. Gerber, E. Meyer and D. W. Lee, Nanotechnology **17**, 189 (2006).

[232] P. Garoche, J. J. Veyssié, P. Manuel and P. Molinié, Solid State Comm. **19**, 455 (1976).

[233] H. A. Leupold, F. Rothwarf, J. J. Winter, J. T. Breslin, R. L. Ross and T. R. AuCoin, Journ. of Appl. Phys. **45**, 5399 (1974).

[234] S.S. Banerjee, N.G. Patil, K. Ghosh, Subir Saha, G.I. Menon, S. Ramakrishnan, A.K. Grover, P.K. Mishra, T.V. Chandrasekhar Rao, G. Ravikumar, V.C. Sahni , C.V. Tomy, G. Balakrishnan, D. Mck Paul, S. Bhattacharya, Physica B **315**, 237-238 (1997).

[235] E. Boaknin, M. A. Tanatar, J. Paglione, D. Hawthorn, F. Ronning, R.W. Hill, M. Sutherland, L. Taillefer, J. Sonier, S. M. Hayden, and J.W. Brill, Phys. Rev. Lett. **90**, 117003 (2003).

[236] J. D. Fletcher, A. Carrington, P. Diener, P. Rodiere, J. P. Brison, R. Prozorov, T. Olheiser and R. W. Giannetta, Phys. Rev. Lett. **98**, 057003 (2007).

[237] S. Bhattacharya and M. J. Higgins, Phys. Rev. Lett. **70**, 2617 (1993).

[238] C. L. Degen, M. Poggio, H. J. Mamin, C. T. Rettner, and D. Rugar, PNAS **106**, 1313 (2008).

[239] B. C. Stipe, H. J. Mamin, T. D. Stowe, T.W. Kenny, and D. Rugar, Phys. Rev. Lett. **87**, 096801 (2001).

[240] M. Kisiel, E. Gnecco, U. Gysin, L. Marot, S. Rast and E. Meyer, Nat. Mat. **10**, 119 (2011).

[241] A. M. Troyanovski, J. Aarts, and P. H. Kes, Nature **399**, 665 (1999).

[242] S. D. Kaushik, V. Braccini and S. Patkaniki, Pramana, Jour. of Phys. **71**, 1335 (2008).

[243] R. M. White, *Quantum Theory of Magnetism*, McGraw-Hill (1970).

[244] J. J. Sakurai and J. J. Napolitano, *Modern Quantum Mechanics*, Addison-Wesley, (2011).

[245] J. H. Van Vleck Phys. Rev. **74**, 1168 (1948).

[246] K. Kambe and J. F. Ollom, J. Phys. Soc. Jpn **11**, 50 (1956).

[247] *Magnetochemistry - Advances in Theory and Experimentation*, Stephen J. Lippard and Charles J. O'Connor, Progress in Inorganic Chemistry, Volume **29**, 203 (2007).

[248] M. McElfresh, *Fundamentals of Magnetism and Magnetic Measurements*, Purdue University (1994).

[249] A. M. Campbell, J. Phys. C **2**, 1492 (1969); *ibid.* **4**, 3186 (1971).

[250] A. P. Reyes, H. N. Bachman and W. P. Halperin, Rev. Sci. Instrum. **68**, 2132 (1997).

[251] http://www.magnet.fsu.edu.

[252] H. Hertz, *Ueber die Einwirkung einer geradlinigen electrischen Schwingung auf eine benachbarte Strombahn*, Annalen der Physik, vol.270, no.5, pp.155-170 (1888). H. Hertz, *Ueber die Ausbreitungsgeschwindigkeit der electrodynamischen Wirkungen*, Annalen der Physik, Vol.270, no.7, pp.551-569 (1888).

[253] R. E. Peierls, *The laws of nature*, London: George Allen and Unwin (1955).

Acknowledgments

Se sono giunta alla fine di questo lavoro di tesi, e di questo progetto di Dottorato, lo devo ad alcune persone speciali che mi hanno accompagnato, sostenuto e guidato con perseveranza e pazienza. Se ogni percorso di crescita comporta il superamento di sfide e l'accettazione della sconfitta, penso di essere cresciuta quanto basta. Il risultato finale tuttavia, non sta a me giudicarlo.
Voglio esprimere la mia gratitudine verso il Prof. Carretta, che in questi anni é stato sia una figura di riferimento professionale, che un sostegno in alcuni momenti di mancanza di motivazione e fiducia.

I proff. A. Lascialfari, L. Romanó e A. Rigamonti sono stati una preziosa risorsa di crescita e confronto, che mi ha permesso di scalfire il complesso argomento delle fluttuazioni superconduttive.
Grazie alla Dott. ssa C. Mozzati, A. Vai e M. Moscardini per il loro supporto tecnico e informatico.
Un ringraziamento sentito va anche alla Dott. ssa C. Milanese, del dipartimento di Fisica-Chimica dell'Universitá Pavia, per la caratterizzazione SEM delle polveri di $NbSe_2$, e per la sua gentilezza.

La mia esperienza "Pavese" é stata arricchita dal confronto con altre figure di grande valore. Ringrazio il Prof. L. C. Andreani per il confronto scientifico e quello personale, e per avermi riavvicinato alla meravigliosa risorsa della lettura.

Grazie ai miei colleghi d'ufficio, a pranzi, ai caffé, e alle "pause sfogo".

Grazie ai colleghi di Parma, che mi hanno dato accesso al loro suscettometro ac. Al Dott. M. Mazzani i miei migliori auguri per la sua nuova famiglia! Ringrazio inoltre la dott. ssa C. Pernechele e il Prof. R. DeRenzi.

Voglio esprimere la mia gratitudine anche verso il Dott. G. Profeta, dell'Universitá de L'Aquila per il calcolo DFT sul composto $Ba(Fe_{1-x}Rh_x)_2As_2$.

Grazie ai miei amici di sempre, Elisa, Cri, Max, Mattia, Gloria, Letizia, Francesca, Daniele... e ai tanti altri (ma a volte troppo pochi) che mi hanno accettato per come sono (diventata). Per non aver giudicato le mie scelte, e avermi sostenuto nei momenti peggiori, che solo loro conoscono.
Grazie a mia zia Gió... ce l'hai fatta di nuovo a convincermi!
Sarah Fontó helped my so much to "polish" the first drafts of my papers. I deeply thank her for the fresh way she teaches English, and for her precious friendship. You're a Volcano!! Keep going!!

The CNISM PhD Program gave me the wonderful opportunity to travel. Even if at the beginning I was quite scared and insecure, by time I realized how much enriching this opportunity was.
Being said that, I wish to thank some of my international collaborators.

On the "European side", Prof. M. Poggio allowed me to realize the cantilever magnetometry experiments, while the NMR group of the Laboratoire National des Champs Magnétiques Intenses of Grenoble hosted me, at the end of the first year of my PhD, to realize the high filed T_1 measurements.
Recently I visited the NMR lab of the IFW of Dresden. I thank Dr. H.-J. Grafe for this opportunity, and his coworkers for the nice welcome.

During my PhD program, I also had the unique occasion to travel overseas. Prof. William Halperin is kindly acknowledged for hosting me at Northwestern University, where I spent three wonderful (although extremely cold!) months. I also thank his enthusiastic collaborators for their help, and Arneyl Reyes and Philip Kuhuns, who "open the doors" of the National High Magnetic Field Lab.

A warm thank is due to the Chicago Ta'leef Collective corporation, that supported me in a delicate transition of my life. Thanks to all the people who "crossed my way", during this journey. Grazie alla mia famiglia per avermi accettato, dopo tutto....

Dominique Lapierre's and Khaled Hosseini's masterpieces have been unique mates of my train trips.

Mahmoud, this thesis is for you, it costed me so much.... as much as staying far from you.

List of publications

- **February 2014**: *Vortex Lattice Melting of a $NbSe_2$ single grain probed by Ultrasensitive Cantilever Magnetometry*
  L. Bossoni, P. Carretta, M. Poggio. To be submitted to Applied Physics Letters.

- **February 2014**: *Non-conventional superconducting fluctuations in $Ba(Fe_{1-x}Rh_x)_2As_2$ iron-based supercondutors.*
  L. Bossoni, A. Lascialfari, L. Romanó, P.C. Canfield, To be Submitted to Journ. Cond. Phys. Matter.

- **September 2013**: *Evidence of unconventional low-frequency dynamics in the normal phase of $Ba(Fe_{1-x}Rh_x)_2As_2$ iron-based supercondutors.*
  L. Bossoni, P. Carretta, W. P. Halperin, S. Oh, A. Reyes, P. Kuhns, P.C. Canfield, Phys. Rev. B (R) **88**, 100503 (2013).

- **April 2013**: *Glassy Transition in the Vortex Lattice of $Ba(Fe_{0.93}Rh_{0.07})_2As_2$ superconductor, probed by NMR and ac-susceptibility.*
  L. Bossoni, P. Carretta, M. Horvatić, M. Corti, A. Thaler, P. C. Canfield, Europhys. Lett. **102**, 17005

- **March 2012**: *NMR investigation of vortex dynamics in the $Ba(Fe_{0.93}Rh_{0.07})_2As_2$ superconductor.*
  L. Bossoni, P. Carretta, A. Thaler, and P. C. Canfield, Phys. Rev. B **85**, 104525;

- **January 2011**: *NMR and μSR study of spin correlations in $SrZnVO(PO_4)_2$: An S=1/2 frustrated magnet on a square lattice.*
  L. Bossoni, P. Carretta, R. Nath, M. Moscardini, M. Baenitz, C. Geibel Phys. Rev. B **83**, 014412;